Alveolar Microfluidic Systems for the Study of Barrier Function, Cell Damage, and Migration at the Air-Blood Barrier

by

Nicholas J. Douville

A dissertation submitted in partial fulfillment
of the requirements for the degree of
Doctor of Philosophy
(Biomedical Engineering)
in The University of Michigan
2011

Doctoral Committee:

Professor Shuichi Takayama, Chair
Professor Richard F. Keep
Associate Professor Paul J. Christensen
Assistant Professor Mohamed E.H. El-Sayed

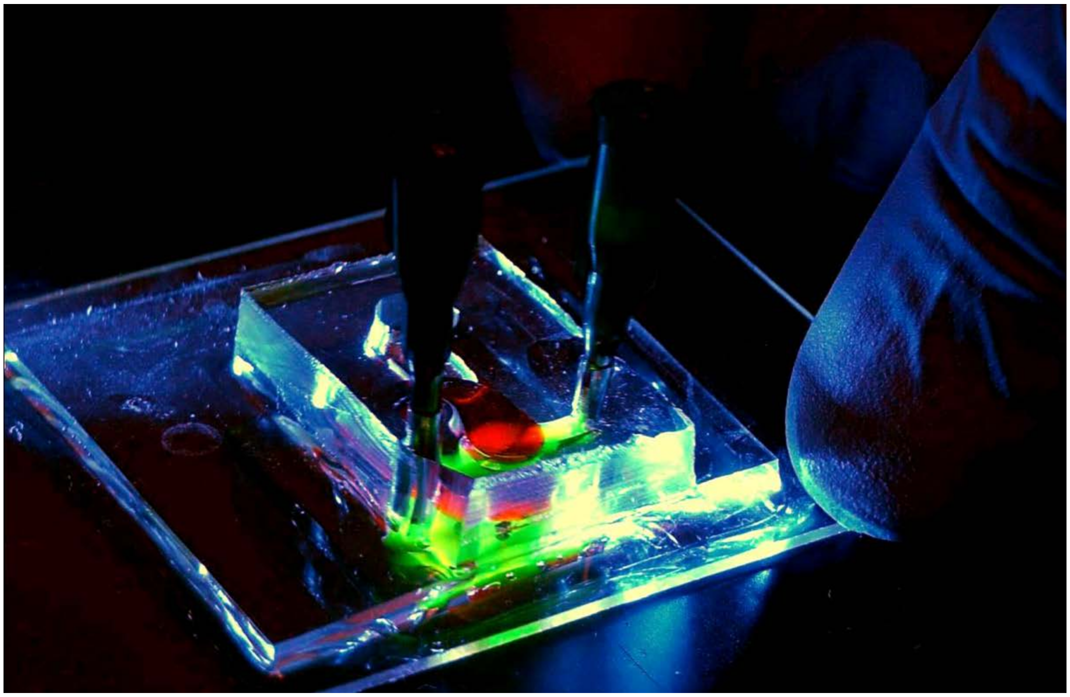

Acknowledgements

I would like to thank my family and friends for support and encouragement through my long and continuing educational journey.

I would also like to thank Dr. Takayama for his help, guidance, and mentorship through my 6 years in his laboratory. In addition to the knowledge and scientific skills directly taught; he has modeled tremendous work ethic, integrity, time-management, and optimism that have influenced my thinking inside and outside of the lab.

During my time at Michigan, I have had the opportunity to collaborate with experts spanning a range of disciplines from fracture mechanics to fluid dynamics to *Microelectromechanical Systems* (MEMS). These collaborations have enabled me to see biomedical problems from vastly different perspectives and are a testament to the educational opportunities within the Biomedical Engineering Department and Medical Scientist Training Program (MSTP) at the University of Michigan. At various times, multiple collaborators have taken the time to educate me (*often in areas far outside my expertise*) and have treated me with the same respect with which they would treat students in their own laboratories. I would like to thank Dr. James Grotberg, Dr. Mohamed El-Sayed, Dr. Paul Christensen, Dr. Michael Thouless, Dr. Yi-Chung Tung, Dr. Dongeun Huh, Dr. Toshiki Matsuoka, Dr. Hossein Tavana, and Dr. Parsa Zamankhan for mentorship in collaborative projects at Michigan. I have also had the opportunity to mentor undergraduate students at an earlier stage in their educational journey. I would like to thank: Ran Li, Chris Park, Steve Cavnar, and Steve Allen for tremendous dedication, insight, and energy in your research efforts within the Takayama Laboratory.

I would like to thank Dr. Ron Koenig, program director of Michigan's Medical Scientist Training Program for helping me to integrate my research interest in the field of Biomedical Engineering with my long term aspiration to advance medical research as a physician scientist. There could be not greater program director than Dr. Koenig!

Thank you to Mayte Brown, Penelope Morris, Ellen Elkin, and Ruth Halsey for ensuring that logistical issues were resolved, deadlines met, and funding awarded - so that I could focus more of my time and energy directly on research. I would also like to thank the wonderful staff members in the Department of Biomedical Engineering, especially Maria Steele, Susan Bitzer, Tonya Brown, Kathy McCrumb, Amanda Nelson, and Katharine Guarino.

Takayama Lab: I consider myself fortunate to have worked with such an intelligent and talented group of friends in the Takayama Lab: Steven Allen, Tommaso Bersano-Begey, Steve Cavnar, Wansik Cha, Bor-Han Chueh, Yao-Kuang Chung, Angela Dixon, Amy Hsiao, John Frampton, Nobuyuki Futai, Yunseok Heo, Dongeun Huh, Andreja Jovic, Yoko Kamotani, Albert Kao, Nobuhiro Kato, Kerim Kaylan, Byoung Choul Kim, Sung Jin Kim, Jason Kuo, Joseph Labuz, Qianyi Lee, David Lai, Ran Li, Yan Chen Liu, Toshiki Matsuoka, Geeta Mehta, Roberto Miguez, Chris Moraes, Bobak Mosadegh, Chris Park, Joong Yull Park, Tejash Patel, Sasha Cai Lesher-Perez, Poorna Ramamurthy, Whi Jae Roh, Amir Sarvestani, Christopher Shah, Young Jae Shin, Arlyne Simon, Jonathan Song, Hossein Tavana, Joshua White, Jonathan Yin, and Ying Zheng.

Barrier Function: This work was supported by NIH (HL084370 and CA136829), the University of Michigan Medical Scientist Training Program (NIGMS T32 GM07863) and National Heart, Lung, and Blood Institute (F30HL095333). We thank Daryl Kipke, John Seymour, and Kip Ludwig of the Neural Engineering Laboratory (NEL) for use of the Autolab potentiostat/galvanostat and assistance

with impedance spectra measurements and analysis. We thank Richard Keep, Paul Christensen, and Jon Song for their helpful discussions.

Experiments to characterize nano- and micro-scale cracking in conductive metal films were partially supported by the National Science Foundation (CMMI-0700232) and the National Institute of Health (R01-HG004653-01). We thank Dr Brian N. Johnson for help with the evaporation of thin metal films in the Chemical Engineering Clean Room at the University of Michigan and Dr Pilar Herrera-Fierro for assistance with imaging within the Lurie Nanofabrication Facility at the University of Michigan.

Cell Death and Detachment from Combined Stresses: This work was supported by The National Heart, Lung, And Blood Institute (NHLBI) (HL084370 and HL85156), as well as, the NHLBI Ruth L. Kirschstein NRSA for Individual Predoctoral MD/PhD Fellows (F30HL095333) and the University of Michigan Medical Scientist Training Program (NIGMS T32 GM07863). We thank Dr Mohamed El-Sayed, Dr David Halpern, and Dr Hossein Tavana for their helpful discussions.

Cell Migration: This work was supported by The National Heart, Lung, And Blood Institute (NHLBI) (HL084370 and HL85156), as well as, the NHLBI Ruth L. Kirschstein NRSA for Individual Predoctoral MD/PhD Fellows (F30HL095333) and the University of Michigan Medical Scientist Training Program (NIGMS T32 GM07863).

Table of Contents

List of Figures

Figure

List of Tables

Table

List of Appendices

Appendix

List of Abbreviations and Symbols

AECs	Alveolar Epithelial Cells
AM	Alveolar Macrophage Cells
AoC	Alveoli-on-a-Chip
Au	Gold
Ca	Capillary Number
Cr	Chromium
d	characteristic dimension of tube or channel
d_o	diameter of trachea (Weibel Model ~ 1.8 cm)
ε	strain
E	Young's modulus
FEA	finite-element analysis
FN	fibronectin
Γ	toughness
h	thickness of stiff film
LEFM	linear-elastic fracture mechanics
μ	fluid viscosity
ρ	density
$P_{alveolar}$	Alveolar Pressure
$P_{arterial}$	Pulmonary Arterial Pressure
P_{venule}	Pulmonary Venule Pressure
PDMS	poly(dimethylsiloxane)
PBS	phosphate buffered saline
Q	Volumetric Flow Rate
Re	Reynolds Number
σ	surface tension
TEER	trans-endothelial (or epithelial) electrical resistance
U	velocity of fluid in channel volumetric flow rate/cross section area
V_o	Functional Residual Capacity
ΔV	Tidal Volume

ABSTRACT

Alveolar Microfluidic Systems for Study of Barrier Function, Cell Damage, and Migration at the Air-Blood Barrier

by

Nicholas J. Douville

Chair: Shuichi Takayama

The exchange of oxygen and carbon dioxide occurs across the *air-blood barrier* (or alveolar-capillary barrier). This barrier must be sufficiently thin to allow the passive diffusion, yet sufficiently strong to maintain a dry alveolar environment. When *solid* and *fluid* mechanical stresses damage the air-blood barrier's integrity, edema fills this normally air-filled alveolar environment and pathology results. The specific mechanisms by which these stresses impact the cells of the air-blood barrier remain poorly understood. The role of *solid* mechanical stress (cyclic stretch) has been explored through traditional, culture techniques, but only recently have microfluidic systems allowed systematic exploration on combined *solid* and *fluid* stresses. Although such systems can be tailored to the biological phenomena being studied, key design parameters include: (i) two-layered channel design (to mimic “alveolar” and “endothelial” compartments), (ii) ability to convey combined *solid* and *fluid* stresses, (iii) co-culture, and (iv) the integration of biological sensors to detect real-time changes.

A microfluidic “Alveoli-on-a-Chip” system was designed and fabricated. By varying the degree of fluid-filling within the “alveolar” channel, differential strain conditions were applied to alveolar epithelial cells. Experiments using this system, demonstrated significant increases in cell death and detachment in alveolar cell populations exposed to fluid and solid mechanical stresses compared to populations exposed solely to solid mechanical stresses.

Because nearly all pathological processes of alveoli alter barrier permeability, detection of changes to the integrity of this barrier is an essential feature in alveolar models. A technique for embedding Ag/AgCl recording electrodes within a two-layered PDMS microsystem, allowing impedance to be measured across a porous cell culture membrane was also developed. This fabrication technique eliminated the need for direct deposition of recording electrodes onto the elastomer, avoiding the frequent and deep cracking pattern resulting from the modulus mismatch between conductive metals and PDMS polymer.

The impact of mechanical stresses on the alveolar immune response was also studied by patterning alveolar macrophages onto confluent monolayers of alveolar epithelial cells using aqueous two-phase (ATPS) printing. Using this

technique, increased migration rates in co-cultures experiencing physiologic stretch levels were demonstrated compared to migration in static cultures.

Chapter I

Introduction

Engineering Alveolar Structures

INTRODUCTION

The exchange of oxygen and carbon dioxide occurs in the terminal divisions of the respiratory tree, across the *air-blood barrier* (or alveolar-capillary barrier). This barrier consists of: (i) type-I alveolar epithelial cells (AECs), lining air-filled alveolar sacs, (ii) capillary endothelial cells, lining blood-filled pulmonary capillaries, and (iii) an interstitial region comprised of fused basement membranes for cell adherence (Figure1.1). In addition to the type-I alveolar epithelial cells and capillary endothelial cells constituting the air-blood barrier, numerous other cell types (and accompanying cell-cell interactions) exist within alveoli and the supporting vasculature, including: (i) type-II alveolar epithelial cells, responsible for production of surfactant lining the alveolus, (ii) alveolar macrophage cells patrolling the alveolar surface to identify foreign material then recruit additional inflammatory cells, and (iii) neutrophils flowing through the pulmonary vasculature, which traverse the air-blood barrier when signaled. The air-blood barrier must be sufficiently thin to allow the passive diffusion of oxygen inward, yet sufficiently strong to maintain a dry alveolar environment [Maina and West, 2005]. When *solid* and *fluid* mechanical stresses damage the integrity of the air-blood barrier, edema-fluid fills this normally air-filled alveolar environment and pathology (such as: *Acute Respiratory Distress Syndrome*) results. The specific mechanisms by which these stresses impact the cells of the air-blood barrier (in both physiologic and pathologic processes) remain poorly understood. The role of *solid* mechanical stress (cyclic stretch) has been explored through traditional, well-based alveolar models, but only recently have advances in microfluidic design allowed the role of *fluid* mechanical stress (and combined stress profiles) to be explored systematically in alveolar models. Although microfluidic systems can be tailored to the specific biological phenomena being studied, many of these *next-generation* microfluidic alveoli share common design parameters including: (i) two-layered channel design (to mimic the “alveolar” and “endothelial” compartments of the air-blood barrier), (ii) ability to convey combined *solid* and *fluid* stresses, (iii) co-culture of multiple cell types, as occurs in the alveolus (shown in Figure 1.1B), and (iv) the integration of biological sensors to detect changes occurring at the air-blood barrier (permeability, gene expression, surfactant condition, etc). As microfluidic control systems continue to decrease in size and increase in complexity, a thorough understanding of the scale, stresses, and interactions occurring at the air-blood barrier, becomes particularly important.

DIMENSIONS AND STRESSES

The structure and geometry of alveoli are dictated by functionality, as the respiratory tree branches into hundreds of millions of alveolar sacs (estimated between 300 million [Weibel, 1963] and 480 million [Ochs *et al*., 2004]) to effectively maximize the surface area (143 ± 12 m^2, in a 74 kg man) available for gas diffusion [Gehr *et al*., 1978]. Successful *Tissue-Engineering and Microfluidic Modeling* of alveolar structures requires key dimensions, stresses, and cell-cell interactions of functioning alveoli to be considered. Existing models have successfully captured some of these elements, while neglecting others based on experimental limitations. For example, when studying the impact of fluid mechanical stresses on alveolar cells it is important to match the Reynolds and Capillary Number between the *in vivo* condition and *in vitro* model – but, not inherently necessary to preserve alveolar diameter and membrane thickness enabling ease of fabrication and actuation [Douville *et al*., 2011]. The dimensions and stresses of the *in vivo* condition are, therefore, an important consideration when designing any microfluidic system. This process is further complicated in the alveolar microfluidic systems, because multiple stresses occur simultaneously (*solid* and *fluid* mechanical stresses) and because of the extremely small scale (~250 μm diameter of alveolar sac; <10 μm diameter of pulmonary capillaries). Approximate dimensions and stresses can be easily calculated by combining elegant models of the lung's branching structure with well-established spirometry data (a commonly administered pulmonary function test). Although these dimensional models are calculated using data from larger conducting airways (first 10 generations) and spirometry data that assumes uniform distribution of stresses through the entire lung; they provide an important *first-order approximation* of key design parameters and illustrate key concepts about the *in vivo* processes. In this section, calculations and assumptions necessary to derive these *first-order approximations* are discussed then the best known estimation derived from direct measurements and specific computational modeling is presented.

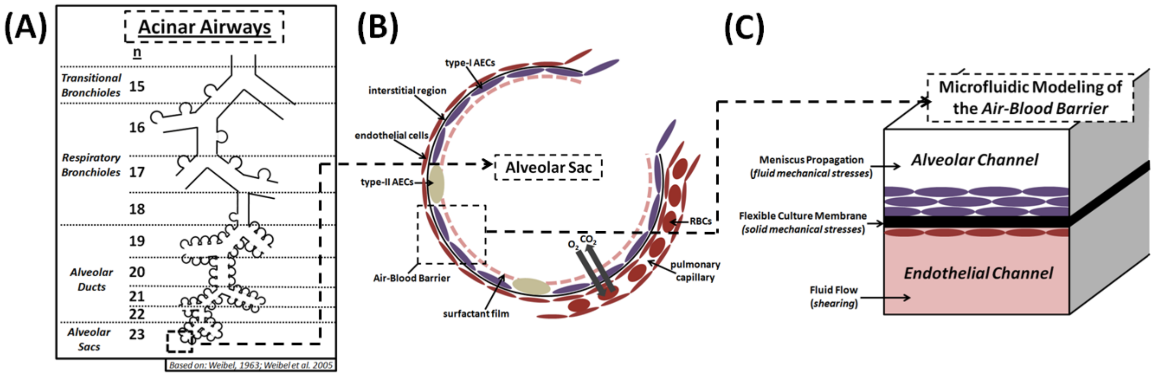

Figure 1.1 Schematic of Alveolar Structures which can be Modeled using Microfluidic Systems. *The Schematic of Acinar Airway branching is based off the Weibel Model of the airway [Weibel et al., 1963] and modified to account for additional information regarding appearance of alveoli [Weibel et al., 2005].*

A. Scale of Alveolar-Sacs.

First-Order Approximation. Although constructed with data from the first 10 branches of the respiratory tree, the Weibel Model can be extended to provide a first-order approximation for the diameter of subsequent respiratory bronchioles and alveolar structures. In this model, the diameter (d_n) of the any branch in the respiratory tree can estimated as a function of the generation number (n) and the diameter of the trachea (n=0; d_o~1.8 cm) according to Equation 1.1. In this model (depicted schematically in Figure 1.1A, terminal bronchioles (n=14) branch into transitional bronchioles (n=15) then into respiratory bronchioles (n=16-18), a region where both conduction and diffusion occurs (N=17-19); and eventually into alveolar ducts (n=19-22) and terminal alveolar sacs (n=23) [Weibel, 1963; Weibel *et al*., 2005].

$$d_n = 2^{(-n/3)} d_o \qquad \text{Equation 1.1}$$

Direct Measurement of Alveolar Diameter and Volume. Measurements of lung reconstructions [Haefeli-Bleuer and Weibel, 1988] and serial histological sectioning [Hansen *et al*., 1975] demonstrate that applying the Weibel model (Equation 1.1) to distal airway generations, leads to an underestimate of the diameter of the pulmonary acinus, the total alveolated region connected to a single respiratory bronchiole where gas exchange occurs. Haefeli-Bleuer and Weibel determined the mean volume of a human acinus to be 187±79 mm^3 with airway diameter falling from 500 μm to 270 μm through 10 generations of acinar branching, with the inner diameter of alveolar sacs consistently about 250 μm, regardless of the generation [Haefeli-Bleuer and Weibel, 1988; Weibel *et al*., 2005]. Development of synchrotron radiation-based X-ray tomographic microscopy has enabled rat alveolar diameters to be imaged showing a typical alveolar diameter as small as 15-40 μm [Tsuda *et al*., 2008; .Sznitman *et al*., 2010; Schittny *et al*., 2008].

B. Thickness and Mechanical Properties of the Interstitial Layer.

Direct Measurements of Interstitial Thickness. The interstitial layer is comprised of the basement membranes of the epithelial and endothelial layer fused together. The thickness of the interstitial layer has been measured in humans (0.2-0.3 μm) [Gehr *et al*., 1978], as well as, a variety of mammals (rabbit: 0.175±0.010 μm; dog: 0.318±0.081 μm; horse: 0.390±0.02 μm) [Birks *et al*., 1994]. In mammals, the interstitium can be as thin as 0.1 μm at the most narrow point and contains four molecules: (i) Type IV collagen from both epithelial and endothelial sides –responsible for tensile strength, (ii) laminins – responsible for cell adherence to the basement membrane, (iii) perlecan – attached to long heparin sulfate glycosoaminoglycan chains, and (iv) entactin/nidogen – bound in a tight complex with laminin and may play role in cell adherence to the extra cellular matrix (ECM). The high strength to thickness ratio of the air-blood barrier is generated by type IV collagen in the basement membranes [West and Mathieu-Costello, 1999]. The tensile strengths of 15 μm thick basement membranes comprised of Type IV collagen (~150x thicker than those found in the air-blood barrier) has been measured at 1.7 x 10^6 N*m^{-2} [Fisher and Wakely, 1976]. Most of the Type IV collagen is located in the thin (~50 nm thick) lamina densa, sandwiched between the epithelial and endothelial ECM regions [West and Mathieu-Costello, 1992]. This tensile strength is crucial because of the enormous circumferential or hoop stress (S) experienced in the walls of a pulmonary capillary [West and Mathieu-Costello, 1999].

First-Order Approximation of Hoop Stress in Pulmonary Capillaries. We can determine an *order-of-magnitude* approximation of circumferential stress experienced by the alveolar basement membrane by using the Laplace Relationship (Equation 1.2) and assuming typical values for some key parameters.

$$S = P \times r/t \qquad \text{Equation 1.2}$$

Where:

- P is the capillary transmural pressure. Assume P=36 mmHg (~4800 N/m^2), estimated from the capillary pressure at the bottom of a human lung during exercise [West *et al*., 1991; Wagner *et al*., 1986].
- r is the capillary radius. Assume r = 3.5 μm; estimated from the radius of pulmonary capillaries in mammals [Birks *et al*., 1994].
- t is the thickness of the interstitial layer. Assume t = 0.25 μm; estimated from the thickness of interstitial layer in humans.

Based on these assumptions, the Law of Laplace indicates a wall stress greater than 6.72×10^4 N*m^{-2} (calculation based on: West and Mathieu-Costello, 1999), and possibly as high as 9×10^5 N*m^{-2} in the central region of the ECM where Type IV collagen is concentrated. Studies on rabbit pulmonary capillaries demonstrate failure of the air-blood barrier (disruption of the capillary endothelium; while basement membrane remains intact) at capillary transmural pressures >40 mmHg (5333 N/m^2), corresponding to circumferential stress of 8.9×10^4 N*m^{-2} (assuming P=40 mmHg, r=5µm,t=0.3µm) [West *et al*., 1991].

The basement membrane holding the cells of the air-blood barrier is much thinner than can be reproduced through cell culture and tissue engineering platforms. In microfluidic platforms, epithelial and/or endothelial cells are routinely cultured on polyester [Huh *et al*., 2007] or poly(dimethylsiloxane) membranes [Huh *et al*, 2010; Douville *et al*., 2011]. It is important to note that these cell culture membranes are often 1-2 orders of magnitude thicker than the basement membranes they are replicating.

C. Dimensions, Flow, and Trans-mural Pressures in Pulmonary Capillaries.

Direct Measurement of Pulmonary Capillary Diameter. The diameter of pulmonary capillaries was measured in humans (7.48 ± 2.31 µm), as well as, other mammals (rabbit: 6.02 ± 1.95 µm; dog: 6.03 ± 1.38 µm) [Doerschuk *et al*., 1993]. When the pressure within a pulmonary capillary increases, such as during exercise or due to gravity, the diameter of the pulmonary capillary also increases. Huang and colleagues approximated the diameter of a capillary cross section as a function of the transmural pressure resulting capillary diameters ranging from ~8µm at a transmural pressure of 18 cmH_2O down to ~5µm at transmural pressures of 2 cmH_2O [Huang *et al*., 2001]. Transmural pressures in a human pulmonary capillaries range from as low as 8.3 mmgHg at rest to greater than 29 mmHg during exercise [West *et al*. 1999].

Pulmonary Blood Flow Depends on Gravitational Pressure Differences. West proposed that differences in blood flow profile occur in different regions (or “zones”) of the lung resulting from gravitational pressure differences [West *et al*., 1964]. In *Zone 1*, alveolar pressure exceeds pulmonary capillary pressure ($P_{alveolar} > P_{arterial} > P_{venule}$), collapsing the pulmonary capillaries and restricting blood flow. In *Zone 2*, alveolar pressure exceeds pressure at the capillary exit but not the capillary inlet ($P_{arterial} > P_{alveolar} > P_{venule}$), enabling capillary flow, independent of venule pressure. In *Zone 3*, pressure across the entire length of the pulmonary capillary exceeds alveolar pressure ($P_{arterial} > P_{venule} > P_{alveolar}$), and constant flow is controlled by the pressure difference between the inlet and outlet to the pulmonary capillaries.

Computational Modeling of Pulmonary Blood Flow. Because pulmonary capillaries are shorter and more narrow than capillaries in systemic circulation, blood flow in pulmonary capillaries is traditionally modeled as a continuous sheet bound on both sides by a compliant endothelium (sheet-flow model), as opposed to a discrete tubule (tube-flow model) used to represent systemic microcirculation [Fung and Sobin, 1969; Burrowes *et al*., 2004]. Burrowes and colleagues expanded upon such models to account for gravity-dependent regional variations in blood flow [Burrowes *et al*., 2004]. Increased pressure in the lower regions of the lung leads to increased capillary diameter, decreased resistance to flow, and consequently an increased flow rate. Conversely, the lower pressure upper regions of the lung, have smaller capillary diameters and slower blood flow rates. This model correctly predicts the expected transition from *Zone 2* to *Zone 3* flow occurring around 22 cm from the base of a 30 cm lung. In this model, gravity-dependent variability in capillary diameter (>8.5 μm at the base to <6.0 μm at the apex), corresponds to variability in flow (> 0.35 mm^3/s at the base to < 0.005 mm^3/s at the apex) [Burrowes *et al*., 2004].

Because the capillaries surrounding a single alveolus are much smaller than can be easily fabricated, engineers may choose to replicate *acinar* (as opposed to *alveolar*) perfusion within the endothelial portion of an alveolar model. By combining existing models of pulmonary capillaries flow (microcirculation) with models for large pulmonary vessels, blood flow through a single acinus can be modeled as a function of the height from the base of a 30 cm lung [Clark *et al*., 2010]:

- in the lower 60% of the lung (*Zone 3*) capillary sheets are fully distended leading to a constant flow ~1.29 mm^3/s independent of height
- in the upper 40% of the lung, flow increases with decreasing height (*Zone 2* and *Zone 3*) beginning at ~0.82 mm^3/s at the apex of the lung [Clark *et al*., 2010].

A Braille-based peristaltic pump was used to generate fluid flows up to 4.9×10^{-2} mm^3/s in a microvasculature model [Song *et al*, 2005]. Endothelial cells aligned and elongated in flow conditions as low as 7.4×10^{-3} mm^3/s (average shear stress ~9 dyn/cm^2). Additionally, there is non-uniform flow within pulmonary vessels. Fluid velocity varies as a function of distance from the center of the vessel with velocity approaching zero at the vessel wall and increasing to maximum velocity in the center of the vessel. This variable flow leads RBCs to move faster than the average velocity of blood [Tawhai and Burrowes, 2008]. The average diameter of pulmonary capillary is smaller than the diameter of both red blood cells (RBC) and neutrophils (PMN). Therefore, RBCs must deform shape to pass through narrow pulmonary capillaries, however, PMNs cannot deform shape, so frequently become trapped leading to a 40-80 fold increase in the concentration of PMNs compared to systemic circulation [Hogg and Doerschuk, 1995]. The resulting RBC aggregation and WBC margination can also be modeled in microfluidic systems [Jain and Munn, 2009].

D. Cyclic Stretch within Alveoli.

First-Order Approximation of Solid Mechanical Stresses. Alveolar epithelial cells are exposed to solid mechanical stresses during the stretching and relaxation cycle of breathing. Cyclic stretching has been found to play a role in the role of pathological states such as ventilator-induced lung injury (VILI). Replicating the cyclic stretch experienced b alveolar epithelial cells in physiologic and pathophysiologic states is an important consideration for any micro-engineered alveolus. A first order approximation of linear stretch (λ) occurring within an alveolus can be calculated using Equation 1.3

$$\lambda = (1 + \Delta V/V_o)^{(1/3)} - 1 \qquad \text{Equation 1.3}$$

Where:

- ΔV is the *Tidal Volume* (physiologic condition). Assume $\Delta V = 0.50$ L during normal breathing in a healthy adult, male [Ganong, 2003]. Assume ΔV within the range between $0.32L < \Delta V < 1.60L$ in conditions of mechanical ventilation [Fretschner, 1993].
- V_o is the *Functional Residual Capacity*. Assume $V_o = 2.20$ L in a healthy adult, male. Assume V_o within the range between $0.77 \text{ L} < V_o < 2.58\text{L}$ in conditions of mechanical ventilation.

Based on the values assumed above, linear strain could range anywhere from approximately 7% in a healthy human, undergoing normal breathing to as high as 45% in pathological ventilation. This *first-order* calculation assumes that all lung tissue stretches evenly, which is obviously incorrect, but provides an estimation to direct microfluidic fabrication and design. In pathologic states, such as Acute Respiratory Distress Syndrome (ARDS), a fraction of the alveoli may be collapsed or fluid-filled, further decreasing the functional residual capacity of the lung (V_o), leading to increased strain and the potential for over-inflation [Hubmayer, 2002].

More Precise Estimation of Solid Mechanical Stresses. The actual degree of cyclic stretch occurring at the level of individual alveoli (the linear strain experienced by alveolar epithelial cells) is more difficult to measure accurately and has not been directly measured *in vivo* [Chapman et al., 2005]; however, studies using *in vitro* cell culture models suggest that linear strain values from 8-12% roughly correspond to physiologic breathing, while linear strain values from 17-22% correspond to pathophysiologic ventilation states which lead to cell death [Tschumperlin *et al*., 2000; Birukov *et al*., 2003]. Changes in the surface area of the epithelial basement membrane were characterized as a function of lung volume. As lung volume increased from 24% of total lung capacity to 42%-60%-82% and 100% of total lung capacity; the surface area of basement membrane increased from by 5%-16%-12% and 40%, respectively [Tschumperlin and Marguiles, 1999]. For ease of comparison, this data can be converted from 2-dimensional strain to 1-dimensional (linear) strain: 2.5%-7.7%-5.8%-18.3%.

D. Fluid Dynamics in an Alveoli.

First-Order Approximation of Fluid Mechanical Stresses. When modeling an edematous (either completely or partially fluid-filled) alveoli, it is important to recreate the surface tension forces that would be experienced by alveolar epithelial cells. This is accomplished by designing the microsystem to match Capillary Number (*Ca*), a comparison of viscous (or elongational) forces relative to surface tension across an interface, and Reynolds Number (*Re*), a dimensionless ratio of *inertial* forces (which induce *turbulent* flow) to *viscous* forces (which induce *laminar* flow) with the physiologic or pathophysiologic state being modeled. *Ca* and *Re* within a microfluidic channel can be easily calculated according to Equations 1.4 and 1.5.

$$Ca = \mu U / \sigma \qquad \text{Equation 1.4}$$

$$Re = \rho U d / \mu \qquad \text{Equation 1.5}$$

Where:

- μ is the fluid viscosity of the growth media in the microchannel. Assume that growth media has the same fluid properties of water, therefore $\mu = 0.01$ Poise [Swindells *et al*., 1952].
- σ is the surface tension of the growth media. Assuming fluid properties of water, σ=72.8 dynes/cm. When growth media is enriched with surfactant, the surface tension in the system can be substantially lowered. In theoretical calculations on growth media enriched with Survanta, a natural lung surfactant, a substantially lower surface

tension state, σ=17.5 dyne/cm, was assumed [Hammer, 1995; Douville et al., 2011].

- ρ is the density of the growth media in the microchannel. Assuming fluid properties of water, ρ = 1 g/cm^3 [Lide, 2009].
- U is the velocity of the fluid in the channel, which can be calculated by dividing the volumetric flow rate (Q) by the cross sectional area (A) of the microchannel or capillary tube.
- d is the *characteristic dimension* of the tube or channel. In a circular tube, such as branch of the pulmonary tree, the characteristic dimension is the diameter of the tube. In rectangular tubes, as with most microfluidic channels, the characteristic diameter, d=(2*width*height)/(width+height).

Fluid velocity is typically a parameter that can be manually set by the microfluidic control system to achieve *Ca* and *Re* that matches the desired model system. For example, in our 0.2cm x 0.6cm microfluidic alveolar model (d=0.3 cm), fluid velocity, U=0.344 cm/s was set by an automated syringe pump [Douville *et al*., 2011]. According to Equation 1.4 and 1.5, this fluid velocity corresponded to a Ca=4.7x10^{-5} and a Re=10.3.

A first-order approximation for *Re* and *Ca* (at any generation within the pulmonary tree, not just alveolar ducts and sacs) can be calculated using Weibel's model for airway diameter as a function of branch generation [Weibel, 1963]. Equation 1.6 and 1.7 show the *Ca* and *Re* as a function of airway generation (trachea is generation, n=0).

$$Ca_n = [4\,Q\,\mu\,] / [\sigma\,(2^{(n/3)}\,\pi\,d_o^2)] \qquad \text{Equation 1.6}$$

$$Re_n = (\rho/\mu)\,[(4Q) / (2^{(-2n/3)}\,\pi\,d_o)] \qquad \text{Equation 1.7}$$

Where:

- Q is the flow rate of an adult lung, estimated at 200 cm^3/s in a healthy adult undergoing normal breathing to as high as 11,000 cm^3/s during Peak Expiratory Flow [Nunn and Gregg, 1989].
- d_o is the diameter of the trachea. Assume d_o =1.8 cm, from Weibel's data.

Based on these assumptions, *Ca* and *Re* can be calculated for a fluid-filled acinus (Weibel Model Dimensions) under conditions of normal breathing (Q~200 cm^3/s) and peak expiratory flow rate (Q~11,000 cm^3/s). These values are listed in Table 1.1

Pulmonary Branch	Gen.	Ca (norm)	Re (norm)	Ca (peak)	Re (peak)
alveolar ducts	20	1.33E-05	0.17	5.84E-03	75.39
alveolar ducts	21	1.05E-05	0.11	4.64E-03	47.49
alveolar ducts	22	8.37E-06	0.07	3.68E-03	29.92
alveolar sacs	23	6.64E-06	0.04	2.92E-03	18.85

Table 1.1. Estimated Values for *Ca* and *Re* under Normal Breathing and Peak Expiration.

Replicating the fluid stresses experienced by the alveolar epithelial cells is a key consideration in the design of an "Alveoli-on-a-Chip". The fluid flow and dimensions of such a microfluidic system can be varied to approximate the *Ca* and *Re* numbers of the system being modeled. Unfortunately, direct measurements of these parameters in alveoli are limited. We have outlined some basic calculations that can be tailored to the specific details of the system being modeled. For example, a system analyzing the impact of surfactant enrichment therapy would calculate *Re* and *Ca* using a much lower value for surface tension (σ) or a system analyzing mechanisms for ventilator-induced lung injury would calculate *Re* and *Ca* using the flow rate (Q) settings of alternative ventilation protocols.

More Precise Estimation of Fluid Mechanical Stresses. Computational modeling has been used to more accurately resolve fluid dynamic parameters within an *air-filled* acinus (as opposed to *fluid-filled*, in the sample calculation above).

Assuming acinar diameter of a few hundred microns, fluid velocity (U) less than a few cm/s, kinematic viscosity of air (μ/ρ) approximately 0.2 cm^2/s; *Re* < 1.0 was estimated in a pulmonary acinus [Karl *et al*., 2004]. When the impact of rhythmic breathing is accounted for , *Re* decreases from ~1.11 in the transitional bronchioles (n=15) to ~ 0.005 in the terminal alveolar sacs (n=23) [Sznitman *et al*, 2007]. Because *Ca* in alveoli depends on the fluid state, this estimation is complicated by the thin film of surfactant-enriched fluid lining the physiologic alveoli. When the surface tension of the surfactant-enriched surface layer is in the range 10 to 1 dyne/cm, the *Ca* of a partially fluid-filled alveolus is estimated between 10^{-5} to 10^{-4} [Wei *et al*., 2005]; however, surface tension gradients (*Marangoni Stress*) generate streaming patterns. A modified alveolar *Ca* (estimated ~ 0.0614) scales inversely with the Marangoni Stresses [Zelig and Haber, 2002]. Analysis of Peclet number suggests that convective flow can be disregarded in distal branches (at rest: Pe < 1.0, for $n \geq 18$) and that the transition from convection to diffusion (*Pe* =1) shifts substantially later in the pulmonary tree during exercise (n=21) [Sapoval *et al*., 2002].

PATHOPHYSIOLOGY OF THE ALVEOLI

When *solid* and/or *fluid* mechanical stresses cannot be effectively mitigated by the usual alveolar mechanisms (for example: reduction of surface tension through surfactants or clearing of over-inflation through elastic recoil); the integrity of the air-blood barrier can be damaged, leading to edema within the alveoli. This inflammatory edema intensifies the stresses occurring and further impairs compensatory mechanisms, launching a positive feedback cycle eventually resulting in alveolar pathology. These pathophysiological processes can be grouped according to the cause of increased stress (for example: mechanical ventilation) or the etiology of impaired compensation (for example: non-functional surfactant due to pre-term delivery or low elastic recoil from smoking). Some major pathological processes impacting the integrity of the air-blood barrier and the types of questions surrounding these diseases that can potentially addressed through microfluidic models are summarized below.

A. Acute Respiratory Distress Syndrome (ARDS). ARDS is a clinical condition characterized by: (i) pulmonary edema, (ii) decreased lung compliance, and (iii) dysfunctional surfactant composition. The etiology of ARDS can range from pneumonia or sepsis to trauma or toxicity. Regardless of underlying cause, all cases of ARDS result from a common pathologic process: cellular damage to the air-blood barrier [Hayes, 2010]. The increased permeability of the air-blood barrier leads to inflammation and edema accumulating within the alveolus, altering and inactivating the surfactant lining the alveolus. Without surfactant to lower surface tension and stabilize them, the alveoli are more prone to collapse which leads to even higher fluid stresses and further cell injury [Halpern and Grotberg, 1992]. Mechanistic studies suggest a positive feedback cycle: fluid stresses damage the air-blood barrier, which leads to surfactant alterations and the collapse of additional alveoli. The collapse of additional alveoli leads to even greater fluid stresses and further damage to the air-blood barrier. The specific interactions and mechanisms by which cyclic stretch and fluid stresses damage the air-blood barrier as well as alter surfactant remains incompletely understood. ARDS can be further complicated by neutrophil infiltration and pulmonary fibrosis. These cell-cell interactions and cellular responses to complex stress profiles can be systematically studied using microfluidic cell culture platforms, potentially revealing insight into the pathology and treatment for ARDS.

B. Neonatal Respiratory Distress Syndrome (NRDS). Respiratory distress in newborns can occur from a variety of causes including fetal head injury, coiling of umbilical cord, and aspiration of blood or amniotic fluid. The most common etiology, however, is lung immaturity from preterm delivery [Kumar, 2009]. NRDS occurs in about 60% of infants born at a gestational age of 28 weeks or less, compared to an incidence of less than 5% after 34 weeks gestation. This results because alveolar type-II epithelial cells increase surfactant production around the 35 week of gestation, to overcome high surface tension forces during the first breath. If delivery occurs before the infant has adequate time for surfactant production, the lungs of this surfactant-deficient newborn will collapse with each breath, leading to atelectasis, hypoxemia, and damage to the air-blood barrier.

The damaged air-blood barrier allows plasma to leak into the alveolus, eventually forming a hyaline membrane which increases the diffusion gradient, further perpetuating the cycle [Kumar, 2009]. The risk and severity of NRDS can be mitigated prior to pre-term delivery through administration of corticosteroids to accelerate surfactant production and tocolytics to delay delivery; however, steroids are only effective after 24 weeks gestation and tocolytics only delay delivery for a few additional days (48 hours). After delivery, surfactant replacement therapy (SRT) and oxygenation (usually through ventilation) are the cornerstones of NRDS-treatment.

The surfactant implicated in NRDS has lower phosphatidylglycerol, higher phosphatidylinositol, and lower percentage of saturated phosphatidylcholine [Warren and Slutsky, 2010] compared to normal surfactant. Furthermore, this NRDS-susceptible surfactant is more sensitive to inactivation from soluble proteins contained in edema fluid. Large-scale clinical trials have shown SRT to be effective in the treatment of NRDS [Chu *et al*., 1967]; but, somewhat surprisingly, failed to show benefit in the treatment of ARDS [Anzueto *et al*., 1996]. Because both diseases share a similar mechanism rooted in dysfunctional surfactant and surface-tension based cellular injury, SRT would seem an attractive and logical treatment for ARDS [Nicholas *et al*., 1997], but a variety of complicating factors including pulmonary fibrosis and neutrophil infiltration limit the efficacy of SRT in ARDS. A microfluidic *in vitro* model could potentially allow these factors to be systematically studied, illuminating key mechanistic differences in the pathology of NRDS and ARDS.

C. Ventilator-Induced Lung Injury (VILI). Because mechanical ventilation promotes gas transport down the pulmonary tree and exchange across the air-blood barrier, it is a critical therapy for patients in extreme respiratory failure, with etiology ranging from ARDS to neurodegenerative diseases. However, in certain ARDS-cases, mechanical ventilation has been shown to promote further cellular-level injury, leading to an exacerbation of the underlying pathology, known as Ventilator-Induced Lung Injury (VILI). This cellular-level damage is occurs through two important mechanisms: (i) *volutrauma*, alveolar distension from excessive tidal volumes, and (ii) *atelectrauma*, the opening/collapse cycle and the accompanying shearing and surfactant disruption [Fisher and Bland, 2007]. The stresses experienced by the epithelium in the pathology of VILI can be decomposed into *solid* mechanical stress (resulting from cyclic stretch) and *fluid* mechanical stresses (generated by the collapse and re-opening of alveoli) [Carney *et al*., 2005]. The role of cyclic stretch in the development of VILI has been confirmed *in vitro* through a variety of flexible membrane cell culture devices, such as the FlexerCell system [Tschumperlin and Marguiles, 1998; Vlahakis *et al*., 1999; Tschumperlin and Marguiles, 2000; Egan, 1980]. The role of fluid mechanical stresses, however, has been suggested by clinical observations that *volutrauma* is insufficient to cause the degree of cell injury seen in VILI [Hirschl *et a*l., 1996; Hirschl *et al*., 1998], but systematic *in vitro* study has been limited. Recent advances in microfluidic fabrication have allowed *fluid* mechanical stresses to be systematically studied in models of *airway* injury [Bilek *et al*., 2003; Huh *et al*., 2007]. These microfluidic studies enable fluid mechanical stresses (specifically: shearing, shear gradients, pressure, and pressure gradients) to be transmitted from a propagating air–liquid meniscus to underlying alveolar epithelial cells. These airway-based studies reveal that fluid stresses can lead to substantial cell death; but were not directly applicable to models of the alveoli where both solid and fluid mechanical stresses occur. Only recently have microfluidic fabrication techniques been developed to incorporate flexible PDMS membranes to expose alveolar epithelial cells to combined stresses. [Huh *et al*., 2010; Douville *et al*., 2011]. Initial studies of combined stresses in alveolar microfluidic models, suggest that cyclic stretch alone is not sufficient to the degree of cell injury seen in VILI. In addition to revealing mechanistic insight on the development of VILI, microfluidic air-blood barriers can potentially be used to test cellular damage and permeability changes in response to different ventilation strategies (high frequency, varied inspiration to expiration ratio, positive end-expiratory pressure, etc).

D. Emphysema and Overinflation. Emphysema is a subset of chronic obstructive pulmonary disease (COPD) characterized by irreversible disruption of the alveolar septa [Boas and Winnie, 2007]. Destruction of the alveolar septa results in decreased elastic recoil and increased compliance, as well as decreased surface area available for gas exchange. These changes in the mechanical properties of the lung cause the lung to easily distend during inspiration (high compliance); but empty poorly during expiration (low elastic recoil). This results in overinflation of the lung, characterized by high total lung capacity, functional residual capacity, and residual volume. When limited to reversible changes of the alveolar septae with no rupture, this process is termed *obstructive overinflation*. When the distension leads to irreversible rupturing of the septae, it is classified as *emphysema*. The over-distension of alveoli can result from smoking, long-term exposure to pollution, or a fibrotic reaction from the accumulation of alpha 1-antitrypsin (secondary to enzymatic deficiency or liver cirrhosis). Foreign bodies, inflammation, thick mucus have all been demonstrated to create a “ball-valve” obstruction, creating localized overinflation [Boas and Winnie, 2007]. The pathologic response to distension from overinflation can be uniquely studied using microfluidic cell culture platforms. Furthermore, the inflammatory response of alveolar epithelial cells to cigarette smoke and pollution can be quantified and systematically studied.

TRADITIONAL ALVEOLAR MODELS

Solid mechanical stretch has been implicated as a central component in nearly all alveolar pathological processes, and the role of stretch has been extensively studied in models of ARDS [Ning and Wang, 2007], NRDS [Copeland *et al*., 2006; Copeland and Post, 2007], and VILI [Tshumperline and Marguiles, 1998; Vlahakis *et al*., 1999]. Solid mechanical stresses have been traditionally recreated by culturing alveolar cells (AECs, macrophages, etc) on the surface of a flexible membrane whose dimensions can be controlled through pressure-based or mechanical actuation. The most widely used technique is the Flexercell (FlexCell International Corporation, Hillsborough, NC) culture systems, a computer-controlled culture well that uses vacuum pressure to strain or compress (either cyclic or static) cells cultured on a flexible membrane [FlexCell International, Corp]. Based on both scale and stress profile, Flexercell and other similar systems, are the first step towards full alveolar modeling within micro-devices. Next generation microsystems attempt to more accurately replicate alveolar: (i) scale (transition from milli- to micro-) and (ii) stresses (transition from solid mechanical stress to combined solid and fluid stresses), as well as, (iii) integrate additional sensors to monitor barrier function and (iv) account for the complex cell-cell interactions occurring at the air-blood barrier. Despite the limitations of traditional alveolar models, such systems have revealed important insight into the response of air-blood barrier cells to mechanical stretch. Specifically, cyclic stretch has been shown to: (i) upregulate key inflammatory cytokines; (ii) increase expression of surfactant proteins; and (iii) activate a variety of signaling molecules like c-fos and MAP-kinase. Although a full review of alveolar response to cyclic stretch is beyond the scope of alveolar microdevices, key genotypic changes are summarized in Table 1.2.

NEXT GENERATION ALVEOLAR MODELS

The next generation of alveolar models will more faithfully replicate: (i) size, (ii) stresses, (iii) gas permeability, and (iv) cell-cell interactions occurring at the air-blood barrier. Additionally, these new models will allow (v) real time quantitative measure of barrier function to pin-point the exact timing and mechanisms by which barrier integrity is destroyed.

A. Combined Stresses. Only recently, have advances in microfluidic design and fabrication allowed the unique fluid and surface-tension effects occurring throughout the lung to be systematically studied. The importance of such fluid mechanical stresses were first demonstrated in small *airway* models [Bilek *et al*., 2003; Yalcin *et al*., 2007; Huh *et al*., 2007]. Although the role of fluid stresses in *alveolar* models could be deduced from such *airway* models, the relative impact of *fluid* as compared to *solid* mechanical stresses could not be resolved.

Gene	**Cell Type**	**Stretch Profile**	**Experimental System**	**Result/Finding**	**Reference**
Inflammatory Cytokines					
IL-8	Macrophage cells (ventilated alveolar macrophages, moncyte-derived macrophages, and promonocytic THP1 cells)	Elongated 7% of initial diameter (12% increase in cell surface) for 8 and 24 hrs (+/- LPS)	Silastic membrane	1. NF-kB activated in ventilated macrophages 2. Mechanical ventilation induced low levels of IL-8 secretion by alveolar type II-like cells 3. Other cell types (fibroblasts, endothelial cells, and bronchial cells) failed to produce IL-8 in response to prolonged cyclic pressure-stretching load 4. TNF-a and IL-6 were produced in response to LPS but not after mechanical ventilation – suggesting a differential response to mechanical ventilation between IL-8 and both TNF-a and IL-6.	Pugin, 1998
IL-8	A549	20/30% stretch and either 20/40 cycles per min for 12/24/48 hrs of applied stretch	Flexercell 2000 – computer controlled pneumatic device;	1. 30% stretch enhanced IL-8 release in all experiments (true after 12,24, and 48 hrs of applied stretch) 2. At the 3 time points, stretched cells released 48, 41, and 56% more IL-8 than matched static controls 3. TNF-α release was not detectable under static stretch conditions	Vlahakis, 1999
IL-8 (p38)	BEAS-2B cells (human bronchial epithelial)	20% maximal equibiaxial elong.; 20 cycles/min; square wave; 1:1 ratio; measured at 8 hrs/24 hrs	Flexercell (Collagen I-coated)	1. Cell stretching results in an increase in IL-8 mRNA expression and IL-8 protein secretion 2. This process is dependent on MAPK activation 3. ERKs, JNKs, and p38 were all rapidly phosphorylated after the initiation of cyclic stretch 4. P38 was detected as early as 5 min after initiation of strain	Oudin, 2002
Surfactant Proteins					
SPC/ tropo-elastin	Mixed fetal rat cells	5% elong; 60 cycles/min, 15 min/hr, 24 hrs,	Gelfoam sponge	1. Mechanical strain (not dexamethasone) significantly increased SP-C mRNA expression 2. Mechanical strain and dexamethasone upregulated tropoelastin mRNA expression 3. No additive or synergistic effect in presence of both mechanical strain and dexamethasone 4. Neither mechanical strain nor dexamethasone had significant SP-A expression	Nakamura , 2000
SP-A,-B,-C	Isolated primary culture of type II epithelial cells and cocultures of epithelial and mesenchymal cells isolated from fetal rats during late development	Equibiaxial elongation of 5% was applied at intervals of 50 cycles per minute for 24 hrs.	Flexercell	1. Cyclic stretch of type II AECs increased SP-C mRNA expression by 150± 30% (day 18) and 130±30% (day 19) 2. Stretch of co-cultures with fibroblasts increased SP-C expression by 170±40 (day 18) and 270±40% (day 19) 3. Stretch of isolated type II cells increased SP-B mRNA expression by 50% (day19) – unlike SP-C, coculature did not produce significant additional effects on SP-B levels 4. Cyclic stretch promotes developmentally timed differentiation of type II cells – expression of SP-C gene appears to be highly responsive to mechanical stimulation	Sanchez-Esteban, 2001

SP-A,-B,-C	Rat alveolar epithelial cells (type II)	21% increase in membrane SA, maintained in distended state for 18 hrs	Silicone membranes – distended by hydrostatic pressure	1. Stretch has no effect on mRNA content of SP-A and GAPDH 2. Stretch causes decrease in mRNA content of SP-B and SP-C 3. Stretch causes increase in rTI$_{40}$ (a marker of type I phenotype)	Guttierrez 1998
EGF, EGFR, SP-A, SP-D, proSP-B, proSP-C, PCNA	Mature and immature dog lung	Lung growth in mature and immature dog lung 3 weeks and 10 months after right pneumonectomy (PNX)		1. Immature lung: alveolar cell proliferation is regionally regulated in parallel with EGF and EGFR levels and inversely correlated with SP-A and proSP-C levels 2. Post-PNX lung growth: not associated with EGF or EGFR upregulation but with markedly increased SP-A level and moderately increased SP-D level; proSP-B and proSP-C levels did not change 3. Post-PNX lung growth is not a simple recapitulation of maturational responses and SP-A/SP-D may modulate post-PNX lung growth	Foster, 2002
Growth/Signaling Pathways					
c-fos	Isolated rat lungs	Submitted to injurious ventilator regimens (*in vivo*)		1. *In vivo* evidence of c-fos activation (important substrate of MAPK and member of activator protein-1 family)	Tremblay, 1997; Oldenhof, 2002
MAP kinase signaling and HB-EGF-like growth factor	Normal human bronchial epithelial (NHBE) cells – cultured at an air-liquid interface	6 hrs of transcellular pressure (30 cmH20)	Silicon plugs with access port were fit on transwells	1. Application of transcellular pressure to differentiated bronchial epithelial cells increased ERK phosphorylation with no measurable change in JNK or p38 phosphorylation 2. Increase in ERK phosphorylation noted as early as 5 min after onset of transcellular pressure and continued to increase over 30 min 3. Compressive stress equivalent to smooth muscle constriction in asthmatic, leads to selective and rapid increase in ERK phosphorylation and HB-EGF gene expression	Tschumperlin, 2002
ERK1/2; EGFR	Lung alveolar epithelial cells (AEC) – isolated from Sprague Dawley rats	5%/30% elongation on flexible bottom membranes at frequency of 30 cycles/min; 1:1 stretch to relaxation ratio.	Flexercell (FX-3000)	1. Cyclic stretch induced a rapid (within 5 min) increase in extracellular signal related kinase 1/2 (ERK1/2) phosphorylation in AEC 2. Cyclic stretch activates MAPK in AEC. 3. ERK1/2 activation was significantly increased after 5 min of stretch – peaked at 10 min – returned to basal levels by 30 min.	Correa-Meyer, 2002
MAP-kinase	U-2 OS cell line (osteosarcoma)	10 dyne/cm^2 at a frequency of 1Hz	Mechanical drag force applied via magnetic beads placed between poles of magnetic device	1. Cytoskeleton senses cellular deformation 2. Mechanical stress of β1 and α2 integrin subunit induce tyrosine phsophorylation of proteins compared with 3. Integrins sense physical forces that control gene expression through the MAP-kinase pathway	Shafrir, 2002; Schmidt, 1998

Table 1.2. Changes in Genetic Expression of Alveolar Cells in Response to Cyclic Stretch.

This is because microfluidic *airway* models all involve a static cell culture membrane (therefore, cannot convey *solid* mechanical stresses) and first generation *alveolar* models all involve an open cell culture well (therefore, cannot convey *fluid* mechanical stresses. Next generation airway models incorporate combined *solid* and *fluid* mechanical stresses, as would be experienced by alveolar cells at the air-blood barrier). A two-layered PDMS microsystem achieved adequate oxygen diffusion to tissue engineering alveolar parenchyma by mimicking flow through the pulmonary microvasculature [Fritsche *et al*., 2009]. Continuous perfusion across a porous polycarbonate membrane ensures that alveolar cells receive a sufficient supply of oxygen and nutrients and led to a 4-fold increase in cell proliferation (with cell viability >96%) compared to static culture. This cell culture technique was extended to sustain alveolar cells grown at an air-liquid interface (ALI) by basal perfusion through a porous, PDMS membrane [Huh *et al*., 2010]. Cells cultured at the ALI exhibited more physiological behavior (increased barrier permeability, surfactant production, and structural integrity) compared to cells cultured under liquid media. In addition to allowing basal perfusion and culture at an ALI, *in vivo* levels of cyclic stretch (5-15%; 0.2 Hz) and fluid shear stress could be controlled in the *in vitro* model of the air-blood barrier (Figure 1.3A) [Huh *et al*., 2010].

Another “Alveoli-on-a-Chip” system uses a non-porous, flexible PDMS membrane actuated via the “endothelial channel” to generate combined stress levels expected under physiologic and pathophysiologic alveolar conditions [Douville *et al*, 2011]. In this system, a “dead-end” alveolar chamber is separated from a “through” endothelial channel by a thin PDMS membrane. By varying the degree of fluid-filling within the “alveolar” channel, differential strain conditions could be applied to alveolar epithelial cells cultured on different regions of the membrane. In Condition 1, (Figure 1.2) cells in region A experience solid mechanical stress from the membrane stretch and cells in region B experience minimal fluid stress since the meniscus does not propagate through region B. In Condition 2, cells in region A experience solid mechanical stretch and cells in region B experience high degrees of fluid mechanical stress from the back and forth propagation of the meniscus. In Condition 3, cells in region A experience combined solid and fluid mechanical stresses, while cells in region B experience neither solid nor fluid mechanical stresses.

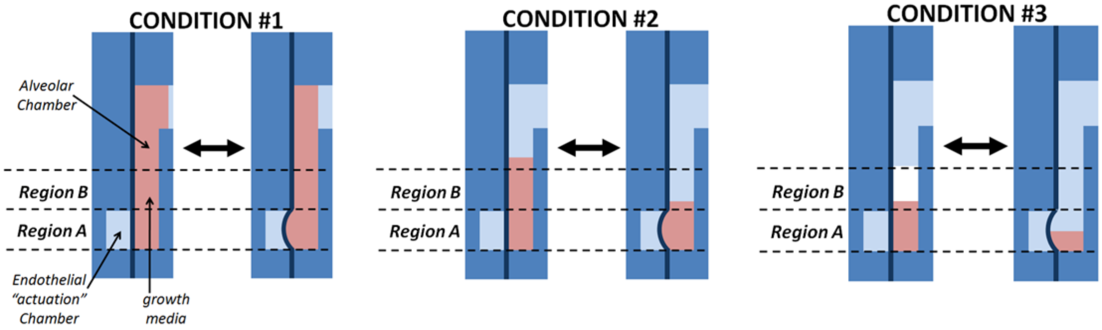

Figure 1.2 Schematic of Stress Profile in "Alveoli-on-a-Chip" as a Function of Growth Media Filling Condition.

Computational analyses of the fluid stresses beneath a meniscus show that this technique allows a more complicated and physiologic fluid stress profile to be generated. It is important to note that inhalation (receding stroke of the meniscus) and exhalation (advancing stroke of the meniscus) have different stress profiles. Our computational model predicts that maximal values for all fluid stresses (shear stress, shear stress gradient, and pressure gradient) occur beneath the transient region of the meniscus and in the receding direction of the meniscus (as opposed to the advancing directing). This computational result was confirmed by experimental results showing preferential cell detachment in the direction of the receding meniscus propagation. Computational modeling of the fluid mechanical stresses generated in this "Alveoli-on-a-Chip" microfluidic system also illustrated the effect of meniscus propagation velocity on fluid stresses, showing that maximum values: (i) wall shear stress increase with increasing propagation speed, (ii) shear stress gradient does not vary with propagation speed, and (iii) pressure gradient decreases with increasing propagation speed. This *in vitro* system enables potential ventilation strategies to be tested against theoretical predictions as well as the cell response to differential stresses (for example: the offsetting effect of increased shear stress; but decreased pressure gradient as meniscus velocity increases) to be potentially resolved. Initial experiments using this system to test combined stresses, demonstrated significant increases in cell death and detachment in alveolar cell populations exposed to fluid and solid mechanical stresses compared to populations exposed solely to solid mechanical stresses.

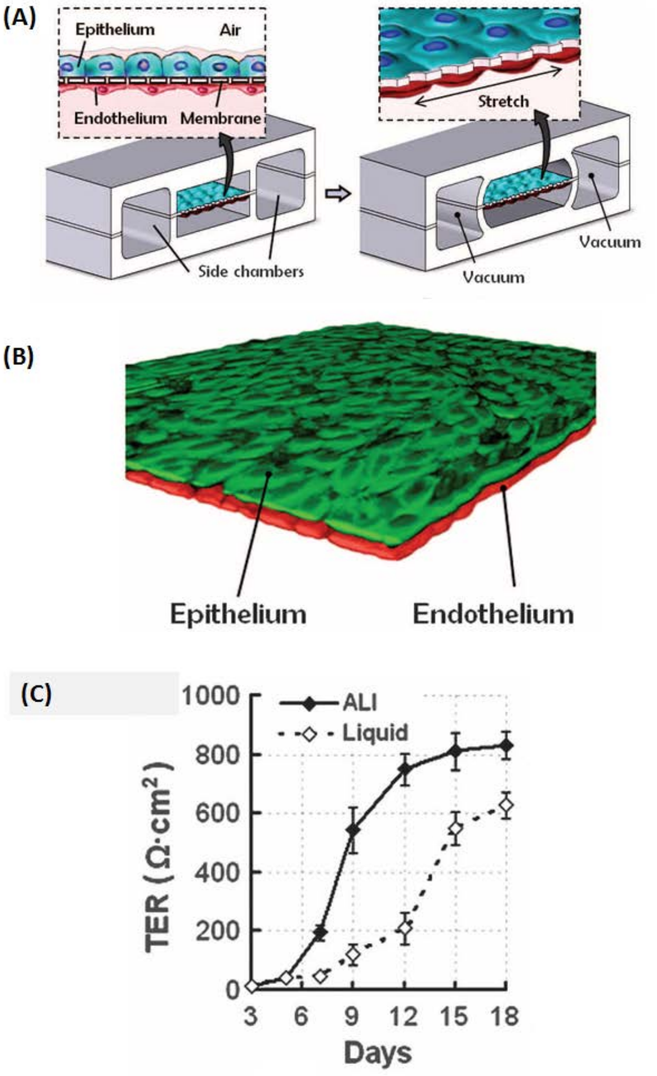

From Huh *et al.*, 2010 (used with permission)

Figure 1.3. Next Generation Alveoli-on-a-Chip Technologies. (A) Physiologic Stresses (B) Co-culture of epithelial and endothelial cells (C) Quantification of Barrier Function by measuring Trans-Epithelial Electrical resistance (TER or TEER) a quantification of paracellular permeability across cells monolayers cultured in: (i) the completely liquid-filled microfluidic channel (Liquid) compared to (ii) cells cultured at an Air-Liquid Interface (ALI) meaning the interface of the air-filled “Alveolar Channel” with basal feeding from the liquid-filled “Endothelial Channel”.

B. Gas Diffusion. The large surface area (143$\underline{+}$12 m^2) and high *diffusion capacity* (125$\underline{+}$18 to 263$\underline{+}$34 mL O_2/min*mm Hg) of the physiologic lung is difficult to replicate *in vitro* [Geher *et al*., 1978]. A variety of microfluidic strategies have emerged to efficiently "oxygenate" blood through thin synthetic membrane, with the objective of implanting an "artificial lung" to assist patients in acute respiratory failure or end-stage pulmonary disease. This design is further complicated by the requirement that direct contact between fluid in the endothelial chamber and the synthetic gas exchange membrane be minimized (due to coagulation and inflammatory responses) [Kniazeva *et al*., 2010]. Microfluidic-based lung assistance devices have achieved adequate levels of oxygenation by (i) stacking multiple layers of microchannels, (ii) in parallel. Alternating "oxygen" and "vascular" bi-layers (3,5, or 10 bilayers), were stacked using soft lithography techniques to achieve high rates of oxygen through the thin (11 μm) PDMS membranes separating these compartments. Such a system maximizes the surface area:volume ratio for oxygenation and minimizes fluid forces in the endothelial channel [Kniazeva *et al*., 2010]. Clotting concerns can be further reduced by culturing endothelial cells within the microvasculature [Burgess *et al*., 2009]. Burgess and colleagues stacked 6 gas-permeable layers (4 gas + 2 blood) attaining an O_2 gas permeance of 9.16 x 10^{-6} mL/s/cm^2/cmHg and a CO_2 value of 3.55 x $^{10-5}$ mL/s/cm^2/cmHg. A compliant housing chamber incorporated into the thoracic artificial lung (TAL) dampens pulsatile blood flow from the right ventricle and microporous, polypropylene membrane hollow fibers enable gas saturations >98% within normal flow ranges [Cook *et al*., 2005].

C. Real-time Monitoring of Barrier Function. Because nearly all pathological processes of alveoli alter the permeability of the air-blood barrier, the ability to detect and quantify changes to the integrity of this barrier is an essential feature of next generation alveolar models. The presence of tight junctions can be qualitatively detected by observing characteristic proteins (occludin, ZO-1, ZO-2) or transmembrane fibrils and quantitatively measured by paracellular permeability markers or trans-epithelial electrical resistance (TEER) [Gumbiner, 1993]. While less representative of the long term character of the tissue than tight junction protein analysis, TEER provides an instantaneous quantification of the tightness of a cell layer [Balda *et al*., 1996]. This instantaneous and continuous monitoring capability is critical in pinpointing exactly at which point during fluid buildup in the alveoli, alveoli closure and reopening, or other steps such as infiltration of leukocytes, the air-blood barrier breaks down. The electrical resistance across a pulmonary endothelial cell barrier in response to physiologic (5% elongation) and pathologic (18% elongation) levels of cyclic stretch was measured in a traditional alveolar model (cyclic stretch; no fluid stresses) [Birukov *et al*., 2003]. This study revealed that pre-treating endothelial cells with 48 hours of pathologic stretch (18% elongation) led to an increased level of barrier disruption (decreased TEER, following addition of thrombin); whereas pre-treating with physiologic levels of stretch (5% elongation) had a protective effect on the barrier (increased TEER, following barrier disruption) [[Birukov *et al*., 2003]. Because impedance can be quantified in real-time and does not damage or alter the character of the cell monolayer, TEER sensing is an ideal feature to incorporate in *next generation* microfluidic alveolar models.

Direct current resistance measurements have been conducted in microfluidic channels to approximate barrier function (or nano-scale dimensional analysis); however, such techniques are generally limited by: (i) the small microfluidic cell culture area, high electrical resistance along the length of the microchannel, and (iii) measurement-to-measurement variance resulting from changes in electrode placement. Cells cultured under an air-liquid interface (air filled alveolar channel, with basal feeding through a porous membrane from the endothelial channel) demonstrated increased electrical resistance (Figure 1.3C) compared to epithelial monolayers cultured with media in both alveolar and endothelial channels [Huh *et al*., 2010]. A technique for embedding Ag/AgCl recording electrodes within a two-layered PDMS microsystem, allows impedance to be measured across a porous cell culture membrane [Douville et *al*., 2010]. This fabrication technique eliminates the need for direct deposition of recording electrodes onto the elastomer, avoiding the frequent and deep cracking pattern resulting from the modulus mismatch between conductive metals and PDMS polymer [Douville *et al*., 2011; Thouless *et al*., 2011]. Furthermore, this system was utilized for impedance spectroscopy, a technique that measures complex impedance (real and imaginary components) across a spectra of frequency values (10 Hz to 1.00 MHz), allowing a more physiologic circuit model to be used to resolve TEER values across epithelial and endothelial monolayers through one week in culture.

Decreased barrier function was also quantified by measuring an increase in the transport of nanoparticles across the air-blood barrier (from the alveolar channel to the endothelial channel) in response to solid mechanical stretch [Huh *et al*., 2010]. This effect was significantly reduced when an antioxidant was added to the cell culture, suggesting that increased production of reactive oxygen species (ROS) stimulated by the stretch may be responsible for increased permeability of the air-blood barrier. Fluid mechanical stress (shearing; physiologic level of 15 dyne/cm^2) was also shown to increase barrier permeability (in the presence of solid mechanical stresses). Radio-labeled molecules provide the most specific and sensitive quantification of barrier function, even allowing different methods of transport (paracellular, transcellular, etc) to be resolved, although the applicability of such techniques to PDMS-based microfluidic cell culture is currently limited by the differential absorption of small, hydrophobic molecules into the bulk substrates [Wang *et al*., 2011].

D. Co-Culture. In addition to replicating the complex stress profile, *next generation* alveolar models potentially recreate some of the complex cell-cell interactions of the air-blood barrier. The most basic cell-cell interaction occurs at the interface between the alveolar side of the model and the endothelial side of the channel and can be controlled by varying the pore size of the membrane separating each compartment. Most cell culture studies have analyzed each compartment separately; for example: studying the impact of stretch on the alveolar epithelial monolayer without incorporating the endothelium into the model. Microfluidic-based co-culture systems offer an opportunity to resolve how cell-cell interactions across the air-blood barrier impact permeability. Human alveolar epithelial cells and microvascular endothelial cells were co-cultured on opposing sides of a porous PDMS membrane (Figure 1.3B) [Huh *et al*, 2010]. In this co-culture system, fluorescently labeled human neutrophils were incorporated into media flowing through the endothelial channel, allowing: (i) adhesion, (ii) diapedesis, and (iii) transmigration across the air-blood barrier into the alveolar channel to be monitored. Furthermore, bacteria could be incorporated into the alveolar channel activating neutrophils flowing through the endothelial channel.

The impact of mechanical stresses on the alveolar immune response was also studied using a co-culture system printed via an aqueous two-phase system (ATPS) [Tavana *et al*., 2009]. By patterning rings of mouse alveolar macrophage cells (AMJ2-C11) on confluent monolayers of mouse alveolar epithelial cells, increased migration rates in cultures experiencing a physiologic (5% linear strain) degree of stretch compared between static cultures were resolved [Douville *et al*., 2011]. Single cell migration studies show that cyclic stretch decreases the migration of alveolar epithelial cells [Crosby *et al*., 2008] and increases the migration of vascular endothelial cells [Sweeney *et al*., 2005]. Because stretch-dependent migration is a function of: (i) cell type (ie: epithelial, endothelial, macrophage) and (ii) cell culture condition (ie: co-culture with a cells expressing ICAM-1) [Paine *et al*., 2002]; migration is another experimental parameter with the potential to be uniquely studied using *next-generation* alveolar models.

CONCLUSIONS

When the alveolar cells are unable to mitigate the solid and fluid mechanical stresses experienced, the integrity of the air-blood barrier is compromised and pathology results. The mechanisms by which these stresses impact the cells of the air-blood barrier (in both physiologic and pathologic processes) remain poorly understood. First-generation alveolar models have revealed important insight how (i) a single cell-culture responded to (ii) a single stress type. These studies showed significant changes in the expression of surfactant proteins, inflammatory cytokines, and signaling markers in response to stretch. Next-generation alveolar models have taken advantage of recent advancements in microfluidic design and fabrication to expand upon these earlier models. These next-generation systems allow the effects of combined solid and fluid mechanical stresses to be studied in two-layered co-cultures modeling the interaction of epithelial cells from the alveolar side of the air-blood barrier and endothelial cells from the vasculature side. Additionally, the incorporation of sensors within the microfluidic channels allows real-time quantification of barrier function at the air-blood barrier. As microfluidic control systems continue to decrease in size and increase in complexity, a thorough understanding of the scale, stresses, and interactions occurring at the air-blood barrier, becomes particularly important. We have not only highlighted the most up-to-date measurements and computational modeling available for ease of reference when designing microfluidic alveolar models; but also provided the computational framework necessary to logically estimate unforeseen variants where no direct measurements exist. As the physiologic relevance of such systems increases and the level of quantitative changes that can be detected increases in resolution, the scope of problems that can be systematically studied, disease mechanisms that can be resolved, and clinical outcomes that can be potentially screened expands exponentially.

Chapter II

Barrier Function

Fabrication of Two-Layered Channel System with Embedded Electrodes to Measure Resistance Across Epithelial and Endothelial Barriers

Nicholas J. Douville, Yi-Chung Tung, Ran Li, Jack D. Wang, Mohamed E.H. El-Sayed, and Shuichi Takayama

ABSTRACT

This chapter describes a straightforward fabrication process for embedding Ag/AgCl electrodes within a twolayer poly(dimethylsiloxane) (PDMS) microfluidic chip where an upper and a lower channel are separated by a semiporous membrane. This system allows for the reliable real-time measurement of transendothelial and transepithelial electrical resistance (TEER), an accepted quantification of cell monolayer integrity, across cells cultured on membranes inside the microchannels using impedance spectroscopy. The technique eliminates the need for costly or specialized microelectrode fabrication, enabling commercially available wire electrodes to easily be incorporated into PDMS microsystems for measuring TEER under microfluidic environments. The capability of measuring impedance across a confluent cell monolayer is confirmed using (i) brain-derived endothelial cells(bEND.3), (ii) Madin Darby Canine Kidney Cells (MDCK-2), and mouse myoblast (C2C12) (all from ATCC, Manassas, VA). TEER values as a function of cell type and cell culture time were measured and both agree with previously published values from macroscale culture techniques. This system opens new opportunities for conveniently resolving both transendothelial and transepithelial electrical resistance to monitor cell function in real-time in microfluidic cell cultures**.**

INTRODUCTION

Transmembrane electrical resistance offers a quantitative technique to measure the integrity of the tight junctions that govern solute transport across the paracellular space of endothelial and epithelial monolayers [Reichel *et al*., 2003]. Because impedance values can be recorded in real time without damaging cells, it is expected to be particularly useful for dynamic microfluidic experiments. Existing systems for measuring transendothelial/epithelial electrical resistance (TEER), however, are limited to static or macroscopic cell environments and difficult to adapt to microchannels. The challenge arises because of (i) the small cell culture area for TEER measurement, (ii) the high electrical resistance along the length of the microchannel, dictating electrode placement in immediate proximity of the cell culture area, (iii) and measurement-to-measurement variances if the recording electrodes are not secured within the channel. A convenient and robust channel design and fabrication procedure for embedding electrodes within a poly(dimethylsiloxane) (PDMS) microsystem for the purpose of taking TEER measurements within microfluidic systems is presented. The system is characterized by measuring impedance across monolayers of three common cell lines (i) C2C12, (ii) bEND.3 (brain-derived endothelial cells), and (iii) MDCK-2 (Madin Darby canine kidney cells, epithelial) over 7 days of static growth.

Technologically, measurement of electrical properties within microfluidic systems or other small scale systems has previously been reported for applications ranging from flow cytometry [Cheung *et al*., 2005; Yao *et al*., 2004; Simonnet and Groisman, 2006] to patch clamping [Pantoja *et al*., 2004; Farinas *et al*., 2001; Sinclair *et al*., 2003] to electrophoresis [Sia and Whitesides, 2003; Lagally *et al*., 2000] to electrochemical detection [Pai *et a*l, 2009]; however, these techniques require electrode deposition onto a rigid substrate such as silica which greatly limits the diffusion of oxygen and carbon dioxide required for cell culture [Ayliffe *et al*., 1999; Iliescu *et al*., 2007]. Embedding and immobilizing TEER recording electrodes directly within the microfluidic channel, in close proximity to the cell monolayer, eliminates the systemic electrical resistance of growth media within the microchannel and reduces signal noise resulting from electrode motion. Efforts to deposit recording electrodes (Au, Pt, and Ag) directly onto a PDMS substrate were limited by frequent cracking due to Modulus differences between conductive metals and elastomeric PDMS polymer and attempts to directly integrate macroscale recording devices resulted in noise obscuring the signaling value [Douville *et al*. *Soft Matter*, 2011]. Deposition-free integration of metallic electrodes into two-layered microfluidic channels [Chueh *et al*., 2007; Wu *et al*., 2005] would enable upper and lower channels to be to be fabricated entirely from PDMS without the presence of a rigid silica substrate. This could potentially improve gas diffusion and allow co-culture of multiple cell types on opposing sides of a membrane.

Biomedically, microfluidic systems are emerging as useful platforms for modeling cellular barriers. This is because these systems offer precise control over physiologic stresses [Walker *et al*., 2004; Song *et al*., 2005; Huh *et al*., 2007],chemical signaling [Atencia and Beebe, 2005], and the degree of cell-cell interaction [Ayliffe *et al*., 1999]. One challenge has been the development of convenient and quantitative measures of the integrity of the cell barrier in microfluidic devices. Barrier integrity, specifically tight junctional control over the paracellular permeability of an endothelial or epithelial monolayer, can be characterized in vitro through quantitative techniques including (i) transendothelial/epithelial electrical resistance (TEER) and (ii) measuring the permeability of radiolabeled paracellular permeability markers like mannitol and qualitative tests including (i) freeze-fracture electron microscopy of transmembrane fibrils and (ii) immunostaining for proteins characteristic of tight junctions (occludin, ZO-1, and ZO-2). Because TEER offers quantitative monitoring of the monolayer integrity without damaging or altering the cell phenotype, it is expected to be particularly useful for time-lapse analysis of microfluidic experiments.

EXPERIMENTAL SECTION

Materials and Reagents. Poly(dimethysiloxane) (PDMS) (Sylgard 184) was purchased from Dow Corning (Midland, MI). SU-8 2150 for two-step positive photoresist features was purchased from MicroChem Co. (Newton, MA). Polyester membranes were purchased from Corning Inc. (Corning, NY). All cell lines were purchased from ATCC (Manassas, VA). Ag/AgCl electrodes of 500 *μ*m diameter were purchased from World Precision Instruments (Sarasota, FL).

Device Design and Fabrication. The device is composed of two layers of PDMS microfluidic channels, which are designed with integrated microgrooves that permit the physical registration of two electrodes on opposite sides but in immediate proximity to a porous membrane on which cells are cultured for impedance measurement [Tung *et al*., 2004]. The porous membrane on which cells attach and grow (initial diameter 24 mm and with a thickness of 10 *μ*m) is first cut from the TransWell casing using a scalpel and trimmed to a size slightly larger than the area of overlap between the upper and lower channels (2 mm × 2 mm). The cut membrane was then sandwiched between two PDMS channels. The elastomeric nature of the PDMS material combined with sealing of any crevices by PDMS mortar [Chueh *et al*., 2007], allows sealing of the channel despite the 10 *μ*m thickness of the membrane. Figure 2.1 provides an overview of the device design. The deposition-free integration of metallic electrodes alleviates the delaminating problem between metallic thin films and PDMS surfaces. Moreover, the fabrication process can be performed in the ambient environment without using sophisticated thin film deposition instruments in environment-controlled cleanrooms. Such microfluidic device design is capable of providing more functionalities and robust measurement results without increasing fabrication complexity.

The microfluidic channels on each PDMS layer were designed to have cross sectional areas of 2000 *μ*m (width) by 200 *μ*m (height) and an additional channel groove (500 *μ*m × 500 *μ*m) intersecting the main channel at a 45° angle for the measurement electrodes as shown in Figure 2.2. The fabrication of the PDMS chips was conducted using a soft lithography technique. A silicon wafer with two step positive relief features fabricated using negative tone photoresist (SU-8 2150, MicroChem Co., Newton, MA) patterned by two separate photolithography steps was used as a mold. The mold was then silanized with tridecafluoro-1,1,2,2-tetrahydrooctyl-1-trichloro-silane (United Chemical Technologies, Bristol, PA) in a desiccator for more than 30 min at room temperature to prevent unwanted bonding. PDMS (Sylgard 184, Dow Corning) prepolymer mixed at a weight ratio of 12 (prepolymer)/1 (curing agent) was poured on the mold and cured overnight. The cured PDMS layers were removed from the wafer, and reservoir holes were punched within the upper PDMS layer allowing access to both the upper and lower channels (Figure 2.2). Ag/AgCl recording electrodes with a diameter of 500 *μ*m (World Precision Instruments, Sarasota, FL) were fit into the 500 *μ*m × 500 *μ*m side channel and held by elastomeric tension through the sealing process. The electrodes were loaded through the entire length of the side channel but did not completely enter the main channel so that the confluency of the cell monolayer could be easily imaged. A 24 mm diameter (10 *μ*m thickness) semiporous polyester membrane with pore size of 400 nm (Corning Inc.,Corning, NY) was cut into square sheets slightly greater than the overlapping area between the upper and lower channels (2 mm × 2 mm) to completely cover the overlapping region. A PDMS mortar solution (3 toluene/2 PDMS by weight) was spun onto a glass microscope slide at 500 rpm for 5 s followed by 1500 rpm for 60 s to spread the mortar evenly along the entire surface of the glass slide. The upper and lower slabs of PDMS were contact printed onto the glass slide contact spreading the PDMS/toluene mortar onto the flat substrate while sparing the recessed channel features. The edges of the polyester membrane were also “stamped” onto the PDMS/toluene mortar before being placed over the overlapping region between the upper and lower slabs of PDMS to seal the channels [Chueh *et al*., 2007]. After sealing the layered channels, PDMS prepolymer at a weight of 3 (prepolymer)/1 (curing) agent was injected into the side channel using an 18 gauge blunt syringe needle. PDMS flow from the syringe was limited only to the side channel and flow was stopped before the PDMS prepolymer could flow into the main "cell culture" channels or immerse the tip of the electrodes. Flow was discontinued by holding pressure constant within the loading syringe containing PDMS prepolymer (sealed via elastomeric tension with the inlet reservoir punched into the PDMS). To further restrict PDMS flow into the main channels, the chip was elevated so that the main channel (and electrode tip) remained at a higher point than the side channel. The PDMS was allowed to cure for 24 h at room temperature, and the process was repeated for the second electrode.

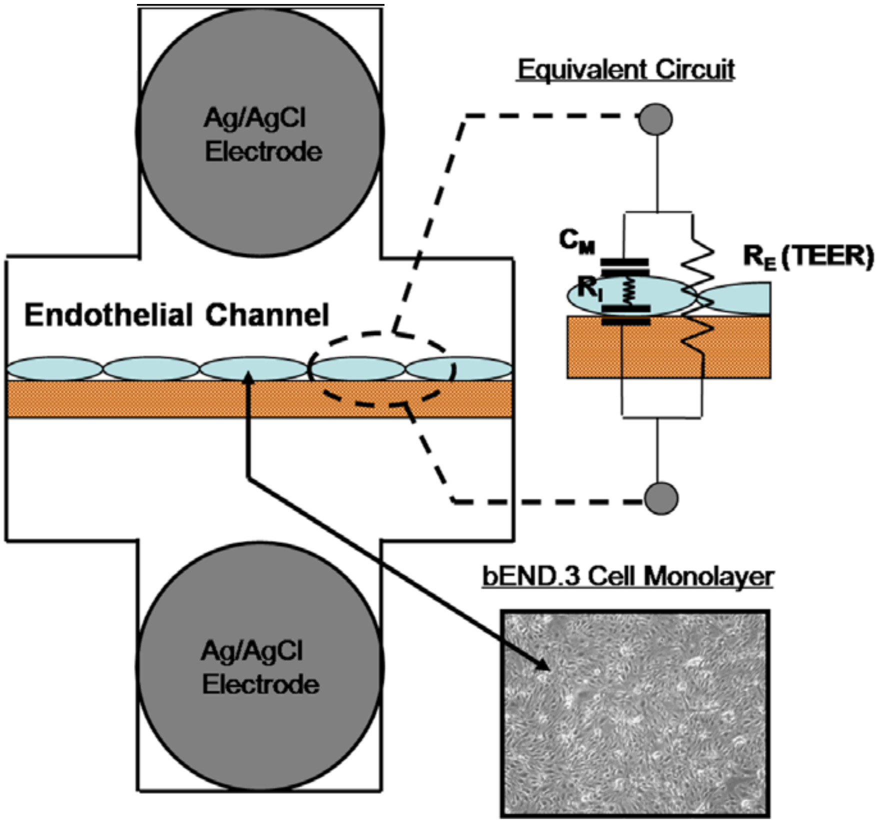

Figure 2.1. System design with equivalent circuit model. Ag/AgCl recording electrodes were embedded on opposing sides bEND.3 cells cultured on a polyester porous membrane. Electrical current has two parallel paths through a confluent cell monolayer. The transcellular path can be modeled by the internal resistance of a cell (RI) in series with the capacitance of the cell membranes (C_M). The paracellular path is modeled by the resistor R_E and represents the transendothelial electrical resistance (TEER) of the experiment.

Cell Seeding and Culture. Epithelial (MDCK-2) and endothelial (bEND.3) cell lines were selected because they offered well characterized and accepted TEER values to compare the experimental results. Since mouse myoblast cells (C2C12) are not expected to form tight junctions, they were selected as a control cell line to demonstrate measurement variability inherent to the system or any impedance drift resulting from prolonged cell culture. All cell lines were cultured in endothelial growth media (DMEM with 10% fetal bovine serum and 1% penicillin/streptomycin) prior to seeding in the microfluidic chip. The microfluidic chip was exposed to plasma oxygen for 5 min to make hydrophilic. Prior to cell seeding, fibronectin solution (Invitrogen) at a concentration of 100 μg/mL in phosphate buffered saline (PBS) was injected into the upper (endothelial) channel to promote cell adhesion. The lower channel was preloaded with growth media. Since the fibronectin solution adheres to the porous membrane as well as the surrounding PDMS microchannel walls, cells have the potential to adhere and divide along the channel walls; however, due to the orientation and geometry of the system and gravity-driven pumping mechanism, the vast majority of cells adhere directly to the porous membrane. The fibronectin solution remained in the upper channel for 30 min at 25 °C under ultraviolet light to sterilize the system. After UV sterilization, sterile techniques and conditions were maintained. Following 30 min of fibronectin coating, the channel was completely washed with growth media to remove the nonadsorbed fibronectin and filled with growth media until seeding. Cells were trypsinized, centrifuged, and resuspended in 1 mL of growth media (to a concentration ~10^5 cells/mL). The cell suspension was then flowed through the upper channel until pressure gradient between the inlet and outlet equilibrated, eliminating flow. The cells were allowed to adhere under this static condition (no flow) for ~12 h before fresh media was flowed through the channel. The growth media was completely replaced with fresh media.

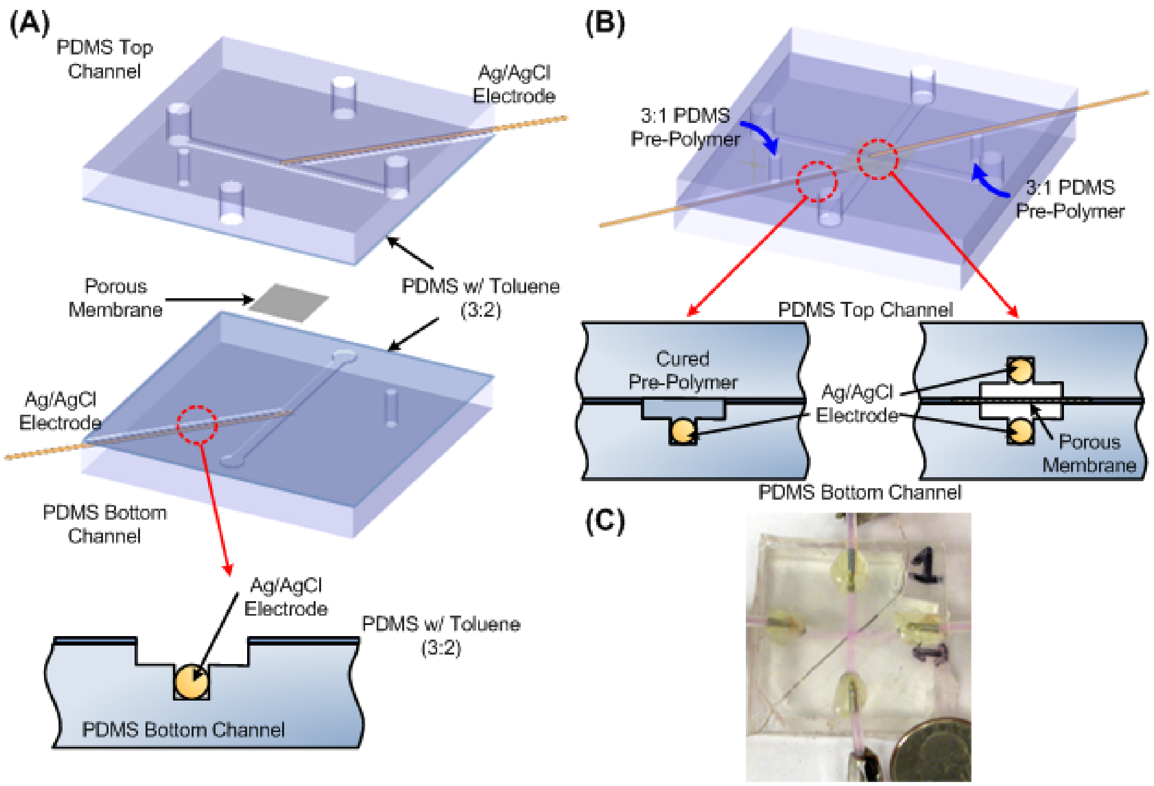

Figure 2.2. Fabrication overview. (a) Device bonding. Ag/AgCl wire electrodes were set into grooves of the same diameter fabricated within side channels. Upper and lower slabs were bonded using a PDMS/toluene stamping procedure. Chip was cured overnight at 60 °C tightly bonding upper and lower slabs. (b) Securing embedded electrodes. 3 (PDMS prepolymer)/1 (PDMS curing agent) was injected into the side channels. Flow was discontinued before PDMS prepolymer immersed the tip of the electrode or entered the main channel. Chip was elevated slightly during curing to prevent liquid polymer from draining into the main channel. Steps were repeated for the opposite electrode (orientation of the elevation was also switched). (c) Photograph of fabricated device.

approximately every 12 h for the duration of the experiment. Immediately after seeding and for the duration of the culture time, the entire microfluidic system was kept in an incubation chamber (37 °C, 5% CO2). After successful cell seeding, cells rapidly divided until confluence. After reaching confluence, cells were successfully maintained within the microfluidic system for over 7 days of experimental measurement.

Impedance Spectroscopy. Impedance spectra were taken using an Autolab potentiostat/galvanostat (EcoChemie). Alternating current of amplitude 0.1 V was passed between the two embedded Ag/AgCl electrodes in the frequency range from 10 Hz to 1.00 MHz, yielding a total of 64 impedance measurements (8 per decade spaced logarithmically). The total time for a single frequency scan was approximately 7 min.

Resolving TEER from Circuit Model. In order to resolve the TEER value from the experimental impedance spectra, the control impedance spectra (taken from the same chip just before cell seeding) was subtracted from the measured impedance spectra (with cells) to eliminate the effect from electrolyte, membrane, and electrode-electrolyte interfaces and simplify the analysis. An equivalent lumped element circuit model (as shown in Figure 2.1) was used to simulate the cell monolayer electrical behavior. The circuit is constructed by three components, where R_E, R_I, and C_M represent extracellular (TEER) and intracellular resistances and a membrane capacitance, respectively [Kunni and Kinouchi, 1998; Kim *et al*., 2004; Lewis and Wills, 1982]. In order to resolve the value of each component, a MATLAB (The MathWorks, Inc., Natick, MA) code using its optimization tool box to estimate the values (Chapter 2, Supporting Information) was developed. In the MATLAB code, the objective minimized the absolute difference between the simulated and experimental impedance values under various frequencies. The TEER value determined by the MATLAB algorithm was then normalized for surface area of the cell monolayer (specifically 0.04 cm^2) by multiplying the total impedance yielding reported values in units of Ωcm^2.

RESULTS AND DISCUSSION

Characterization of System. Prior to seeding cells, the baseline impedance of the system (electrodes, electrolyte, and polyester membrane) was characterized. In initial experiments, the electrolyte solution contained within the microchannel as well as switched from a low-impedance polyester membrane to a high impedance PDMS membrane was varied. Increasing the concentration of the KCl electrolyte from 0.1 to 1.0 M resulted in a frequency-independent impedance decrease of greater than 1.5 kΩ (Figure 2.3A). Replacing the porous polyester membrane with a PDMS membrane of similar thickness but without pores (~10 *μ*m) increased the impedance of the system from 100 kΩ (polyester) to the MΩ (PDMS) range. The PDMS membrane also contributed a capacitive effect to the impedance spectra (Supporting Information, Figure 2.6). These experiments verified that the system correctly detected expected impedance changes. The impact of fibronectin (FN) treatment on the baseline impedance of the system was also tested. Baseline system impedance was recorded for three chips filled with PBS. Next, fibronectin in PBS (at a concentration of 100 *μ*g/mL) was loaded into the system, allowing the fibronectin to deposit for 30 min, before the channel was flushed with fresh PBS. These results showed that FN treatment had a minimal impact on the impedance of the system (Supporting Information, Figure 2.7). The impedance of a channel filled with endothelial growth media (DMEM), phosphate buffered saline (PBS), and 0.1 M KCl (no fibronectin was added to the system during these comparison controls) was also measured. The impedance of the system containing 0.1MKCl had the lowest impedance; the PBS had intermediate impedance, and the growth media had the highest impedance (Figure 2.3B). This experiment demonstrated the feasibility of recording through channels containing endothelial growth media, eliminating the need for a specifically conductive electrolyte solution for cell recordings. Traditional recording systems record impedance values at either DC current or a limited number of a AC frequencies [Cereijido *et al*., 1978; Giaever and Keese, 1984; Stamatovic *et al*., 2009].

Measuring at high frequency minimizes but does not completely eliminate impedance resulting from the capacitive cell membrane. While sufficient for taking TEER measurements across a large area such as in TransWell cultures particularly when the TEER values are large, measuring impedance across the full spectrum of AC frequencies enables the characteristic of the cell monolayer to be more accurately modeled and resolved [Kottra and Fromter, 1984; Erben *et a*l., 1995; cellZscope; Wegener *et al*., 1996]. The smaller microfluidic system is inherently prone to lower signal-to-noise ratios. For example, the surface area of

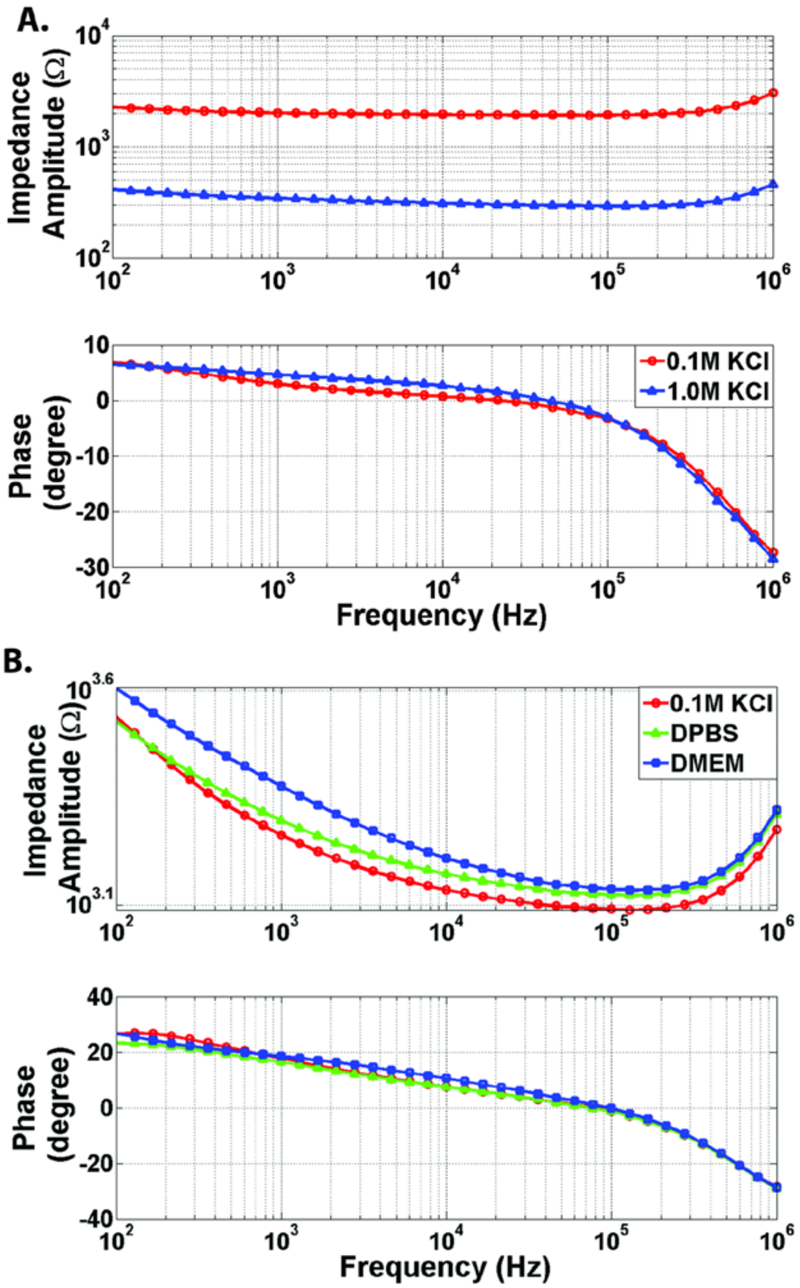

Figure 2.3. System characterization. (a) Impact of varying KCl concentration on impedance spectra. As the concentration of KCl is increased from 0.1 to 1.0 M, the resistivity of the electrolyte solution decreases, leading to decreased resistance. Change in the concentration of KCl is expected to yield a purely resistive change (no impact on capacitance of the system). The frequency independent impedance change confirms this expected result. (b) Impact of varying electrolyte solution on impedance spectra. KCl (0.1 M) has the lowest impedance. Phosphate buffered saline has intermediate impedance. Endothelial growth media has the highest impedance. Endothelial growth media (DMEM) is suitable for electrical recordings.

the system is 0.04 cm^2 compared to a surface area of 4.91 cm^2 in the 6-well TransWell culture systems most commonly used for TEER measurements (and 0.143 cm^2 even in 96-well TransWell cultures which are considered very small). Thus, in addition to placing and immobilizing electrodes close to the cells, we measure impedance at over 64 frequency points and use this data to find the best fit to the entire equivalent circuit (Figure 2.1) and resolve out factors that can vary independently of TEER. A relatively large variability in impedance between different chips was found, most likely due to variance in the distance between the two electrodes caused by alignment variations of the upper and lower channel. It is estimated that for every millimeter difference in the distance between the two recording electrodes, the resistance changes by approximately 2.5 kΩ [Lee *et al*., 2008]. Variability between different measurements within a single chip (where the electrodes remain fixed), however, was minimal. Thus, in the experimental TEER measurements, the baseline impedance of each individual chip was characterized prior to endothelial cell seeding and subtracted from the impedance of the cell monolayer within the chip. This allowed a circuit model to be fit that accounted for contribution of the cell monolayer.

Establishing a Baseline Measure. As an experimental control and to establish a baseline measure, we measured the impedance of the system for 1 week under two conditions: (i) without cells (acellular) and (ii) with cells not expected to form tight junctions (C2C12 cell culture). In both conditions, the media was replaced with fresh media twice per day. Although no cells were cultured in the first control, TEER values were fit using the MATLAB algorithm and the experimental data was normalized to total membrane surface area. The data are summarized in the Supporting Information. Measurements of the system containing growth media without cells (Supporting Information, Figure 2.8) showed relatively minimal change in TEER [<10 Ωcm^2 in either the positive or negative direction] when compared to the magnitude of TEER changes which result from tight junction formation in endothelial and epithelial cell lines [~100

Ωcm2 in the positive direction]. Furthermore, the absence of either a positive trending TEER (as expected from protein deposition on the electrodes) or negative trending TEER (as expected if the Ag/AgCl electrodes were being reconditioned during testing) through 7 days of measurements (the first day is the baseline) indicate that the system is stable for long-term experimental measurements in serum-containing media. Because the TEER fluctuations do not trend in either the positive or negative direction, we hypothesize that these changes indicate the baseline level of noise or error in the system resulting from recording equipment as well as other variables that could not be perfectly controlled such as temperature fluctuation in the incubator, precise attachment of system to recording equipment, or resistivity of the DMEM solution. Next, changes in TEER resulting from culturing a cell line not expected to form tight junction were measured. The electrical resistance across a C2C12 monolayer (Figure 2.4C) displayed a minimal increase [<20 Ωcm^2 in the positive direction] indicating that the physical presence of cells or cellular byproduct results in a nontrivial increase in monolayer resistance despite the theoretical absence of tight junctions which is able to be resolved from TEER changes resulting from tight junction formation.

TEER as a Function of Time with Epithelial and Endothelial Cells. MDCK-2 and bEND.3 cells were seeded onto the fibronectin-treated membrane. Impedance spectra were taken each day for seven consecutive days. Because temperature influences the impedance of the growth media, measurements were consistently taken 30 min after fresh media was loaded into the system and the system was kept incubated at 37 °C before and between all measurements. TEER values were resolved from the impedance spectra taken on each day following seeding using a best-fit circuit algorithm (Supporting Information). Data showed that TEER values increased with each day of growth from day 1 to day 3 to 4 before reaching a plateau and even decreasing slightly. The error bars depicted in Figure 2.4A,B,C are the standard deviation of the nine TEER values that can be resolved on each day, for each cell type. The experimental data agreed with the accepted TEER range of 150-200 Ωcm^2 for bEND.3 cells [Koto *et al*., 2007] and 50-150 Ωcm^2 for MDCK-2 cells [Richardson *et al*., 1981]. Additionally, both cell lines followed an increase-plateau-decrease pattern similar to previously published models, and significant differences between each of the three chosen cell lines could be resolved (Figure 2.4).

Dynamic Impedance Changes in Response to Chemical/Protein Treatment. To demonstrate that our system can detect dynamic impedance changes in response to chemical factors, the impedance of a bEND.3 cell monolayer was measured; then, the cell monolayer was treated for 30 min with TritonX-100 (0.1% in DMEM) [van de Ven *et al*., 2009], before the system was flushed with fresh DMEM and the impedance was remeasured. Our experimental results showed that the impedance of the entire system decreased significantly at all frequency points following treatment with TritonX-100 (Supporting Information, Figure 2.9). The change in TEER (paracellular resistance) was also resolved using the MATLAB circuit fitting algorithm and found decrease from 161.5 ± 0.8 Ωcm^2 to 39.7 ± 1.9 Ωcm^2 (Supporting Information, Figure 2.9A). Furthermore, a change in the impedance at all frequency points following trypsinization was demonstrated (Supporting Information, Figure 2.5). The decrease in impedance amplitude shows that the system and technique are capable of detecting changes in response to chemical or protein treatment in real time.

The Potential Impact of Fluid Flow. All of the experimental data were taken in the static case (absence of fluid flow). Readings taken during fluid flow may impact TEER measurements, but we envision that the flow can always be stopped during short durations of measurements.

Comparison to Existing TEER Measurement Systems. To enable reliable TEER measurement across the small cell culture area within microfluidic channels, the system incorporates features adapted from multiple advances that have been made over the years for macroscopic TEER measurement systems

[Deli *et al*., 2005]. The most widely used system for measuring TEER in vitro is the commercially available TransWell culture environment and the “chopstick-style” recording electrode [Mishler *et al*., 1990; Hurst and Fritz, 1996]. For more reproducible and stable TEER measures of leaky cell barriers with lower TEER values, improved recording chambers with embedded electrodes have been constructed. An example is the Endohm chamber, where electrodes are placed immediately above and beneath the membrane to minimize resistance from the media and allow a more uniform current density to flow across the membrane. The microfluidic chamber incorporates a similar concept by embedding electrodes immediately above and below the cell culture membrane inside the channels. Another enhancement in measurement is represented by the cellZscope [CellZscope] which can measure the impedance across a wide spectrum of frequencies, rather than the typical one frequency, to give more detailed measures of barrier properties. The microfluidic TEER measurement system also acquires impedance spectra at 64 frequencies to obtain more accurate TEER values [Seebach *et al*., 2000]. Giaever and colleagues developed an alternative system that does not use porous membranes to measure endothelial barrier function of cells directly grown on gold electrodes [Giaever and Keese, 1984]. This system has the advantage of enabling measurements of cell barrier functions over very small areas. We initially attempted to mimic this system by forming gold electrodes inside PDMS microchannels but found that the flexibility of PDMS led to cracking of gold and limited the conductivity [Tiruppathi *et al*., 1992]. The membrane embedded microfluidic TEER system we describe, however, still enables measurements to be made over relatively small cell culture areas. Additionally, by keeping the membrane sandwiched multilayer channel structure, our system enables basal cell treatment that is critical for optimal signaling in some cellular systems [Song *et al*., 2009]. Perhaps the most related device setup is that reported by Harris and Shuler where TEER was measured across a small area of cells cultured on a thin silicon nitride membrane with a custom electrode-embedded chamber [Harris and Shuler, 2002]. The reported TEER values from this device, however, were very low due to cell culture problems making it difficult to validate functionality or make comparisons. Hediger and colleagues have also developed microfabricated systems for characterizing epithelial cell tissues [Hediger *et al*., 2000; Hediger *et al*., 2001]. Their design allows transepithelial resistance to be measured in a glass or PDMS microsystem; however, it was limited by multiple fabrication steps and a multilayered modular arrangement. Further advances in microfluidically analyzing the electrical properties of cells are reviewed by Bao, Wang, and Lu [Bao *et al*., 2008].

Comparison to Existing Techniques for Taking Electrical Recordings with Microfluidic Systems. There have been several reported methods for integrating electrodes within microfluidic systems [Siegel *et al*., 2007; Gray *et al*., 2004; Lacour *et al*., 2004]. In a method developed by Garcia and Henry, a gold wire was aligned within a perpendicular microfluidic channel and sealed using superglue and conducting paint [Garcia and Henry, 2003; Garcia and Henry 2004]. Electroplating and electroless deposition have been used to fabricate recording electrodes within microfluidic systems but are limited by multiple slow and costly lithographic steps and the requirement for a smooth rigid substrate [Polk *et al*., 2006]. Die, impression, and injection molding have also proven useful for very specialized approaches but are limited by the high cost and complexity of the system [Martin *et al*., 2000]. The systems described in this manuscript can be easily fabricated using standard soft-lithography techniques and utilize readily available and standardized electrodes which should enable this technique to be easily expanded to other models and systems.

The procedure described in this paper combines recent advances from a variety of scientific disciplines including cell biology (impedance spectroscopy), microfluidic fabrication, and electrical engineering (flexible electronic circuits) to create cell culture microenvironments with real time, nondamaging read outs of cell functions. The procedure described in this paper has six advantages to exiting fabrication techniques, which makes it especially useful and versatile: all

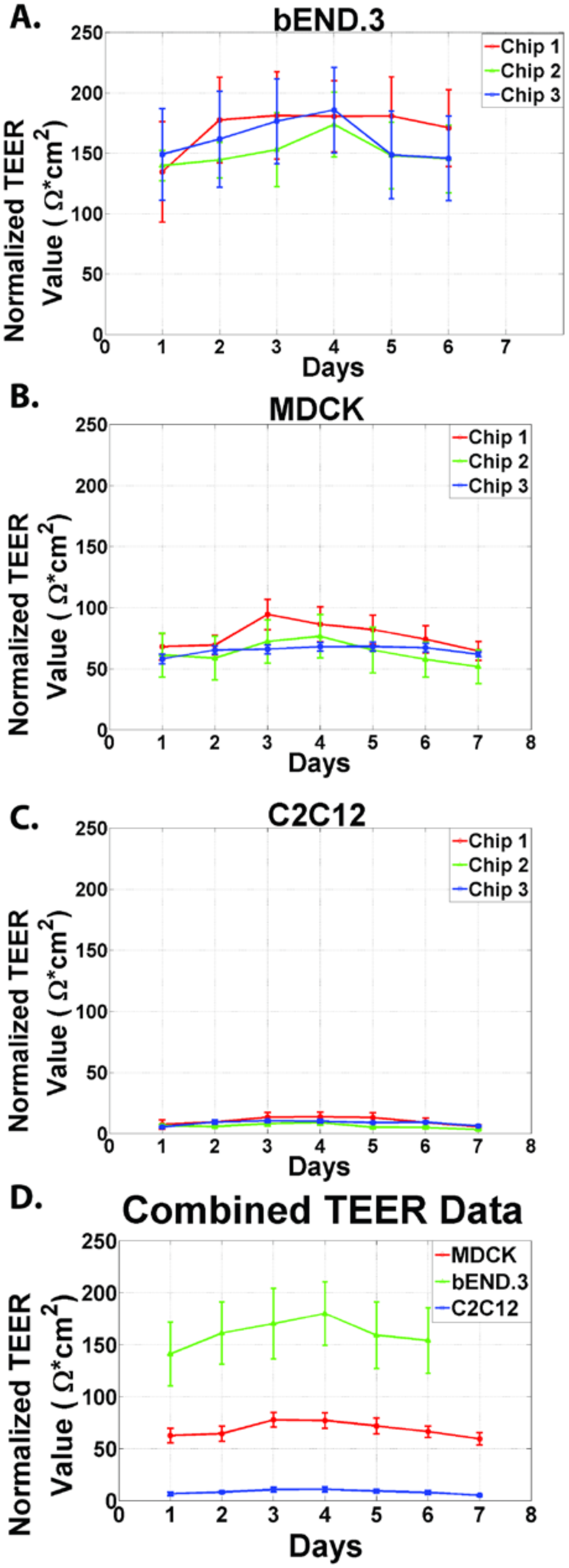
A.
bEND.3
Normalized TEER Value (Ω*cm^2)
Days
Chip 1
Chip 2
Chip 3
0
50
100
150
200
250
0
1
2
3
4
5
6
7
B.
MDCK
Normalized TEER Value (Ω*cm^2)
Days
Chip 1
Chip 2
Chip 3
0
50
100
150
200
250
0
1
2
3
4
5
6
7
8
C.
C2C12
Normalized TEER Value (Ω*cm^2)
Days
Chip 1
Chip 2
Chip 3
0
50
100
150
200
250
0
1
2
3
4
5
6
7
8
D.
Combined TEER Data
Normalized TEER Value (Ω*cm^2)
Days
MDCK
bEND.3
C2C12
0
50
100
150
200
250
0
1
2
3
4
5
6
7
8

Figure 2.4. Resolved TEER as a function of days since confluence for different cell lines. We seeded endothelial (bEND.3) and epithelial (MDCK-2) cell lines with well characterized barrier properties into our microfluidic system. For all cell lines, TEER increases for approximately 3 to 4 days following seeding before plateauing and decreasing slightly. Our data agreed with the accepted TEER range of 150-200 Ωcm^2 for bEND.3 cells48 and 50-150 Ωcm^2 for MDCK-2 cells. Additionally, both cell lines followed an increase-plateau-decrease pattern similar to previously published models and significant differences between each of the three chosen cell lines could be resolved (a, b). Changes in TEER resulting from culturing a cell line not expected to form a tight junction were also measured. The electrical resistance across a C2C12 monolayer (c) displayed a minimal increase [<20 Ωcm^2 in the positive direction] indicating that the physical presence of cells or cellular byproduct results in a nontrivial increase in monolayer resistance despite the theoretical absence of tight junctions. The data from the individual chips are combined in (d). Error bars represent standard deviations. In their system, a nanoporous polycarbonate membrane is glued between two microscale reservoirs.

(i) all steps are based in traditional soft-lithography procedures and do not require unique metal deposition components; (ii) the electrodes utilized are inexpensive, well-characterized, and commercially available; (iii) the cell culture membrane is taken directly from TransWell culture wells, the membrane most commonly used in TEER systems; (iv) the recording electrodes are close to the permeable membrane and positioned appropriately to reliably measure TEER in real time, from cells cultured over a small surface area without disrupting the integrity of cell membrane; (v) the fitting algorithm utilizing a full impedance spectra provides a more accurate representation of the TEER than traditional DC measurement or single frequency impedance measurement systems; (vi) the entire system is fabricated from PDMS polymer (no glass substrate) allowing gas exchange convenient for long-term cultures. The system design can continue to be improved by standardizing the fabrication protocol which will eliminate the chip-to-chip variance currently seen. The inclusion of an additional reference electrode could also potentially eliminate the system variance characterized in the Supporting Information. The size of the electrode, relative to channel dimensions, can also continue to be reduced.

CONCLUSION

A convenient channel design and fabrication procedure for measuring endothelial and epithelial cell barrier function within a PDMS microfluidic system is presented. This method for embedding Ag/AgCl recording electrodes within a side microfluidic channel can be easily replicated by any lab with soft lithography capabilities utilizing widely available, well-characterized, and commercially available electrodes and membranes. Because our system is composed of an upper and lower channel fabricated entirely from PDMS polymer, many of the limitations of existing microfluidic electrical recording systems, specifically the need for rigid, nonpermeable substrate or a costly and slow fabrication protocol, can be avoided. Our fabrication method enables placement and immobilization of recording electrodes in close proximity to cells growing on a polyester membrane. Additionally, by combining this fabrication technique with circuit fitting using impedance spectroscopy, TEER values can be resolved from microfluidic cell culture platforms with much smaller surface areas compared to conventional culture systems. The biological utility of the electrode-embedded microfluidic system by noninvasively resolving endothelial and epithelial barrier function in 1 week of cell culture is demonstrated. Our TEER results agreed with expected results in both value and profile (increase plateau). This system is expected to provide a valuable, real-time, quantitative measure of the effects of microfluidic cultures on cells under unique physiological two-layer microfluidic environments such as exposure to laminar flow and air-liquid two-phase flows, combined with basal signaling and basal side co-cultures [Song *et al*., 2005; Huh *et al*., 2007].

SUPPORTING INFORMATION

circuit_fun.m: Matlab function that imports the experimental data (in ASCII formated) exported from the Autolab potentiostat/galvanostat, calculates the impedance spectrum using the equivalent circuit, and defines the objective value to be optimized (minimized). The experimental data generated by Autolab contains two initial lines of non-numerical data. The first line is the frequency (Hz), the second line is real component of the impedance data, and the third line is the imaginary component of the impedance data.

```
function F = circuit_fun (rc_component)
%%%%%%%%%%%%%%%%%%%%%%%%%%%%%%%%%%%%%%%%%%%%%%%%
% Import data from autolab output .dfr file (experimental)
autolab_data1 = importdata ('Experimental File Name.dfr');
% Extract numerical data part from the data structure
autolab_data1 = autolab_data1.data;
% Import data from autolab output .dfr file (baseline data)
autolab_data2 = importdata ('Baseline File Name.dfr');
% Extract numerical data part from the data structure
autolab_data2 = autolab_data2.data;
% Number of measurement points in each impedance spectrum
point_num = 64;
% Number of impedance measurement sets
data_set = autolab_data1 (1)/point_num;
data_set = autolab_data2 (1)/point_num;
% Number of lines containing numerical non-impedance data
head_line = 2;
for a = 1:1:point_num
for b = 1:1:data_set
frequency (a,b) = autolab_data1 (head_line + (a-
1)*data_set*9 + (b-
1)*9 + 1);
impedance_rel1 (a,b) = autolab_data1 (head_line + (a-
1)*data_set*9 +
(b-1)*9 + 2);
impedance_img1 (a,b) = autolab_data1 (head_line + (a-
1)*data_set*9 +
(b-1)*9 + 3);
frequency (a,b) = autolab_data2 (head_line + (a-
1)*data_set*9 + (b-
1)*9 + 1);
impedance_rel2 (a,b) = autolab_data2 (head_line + (a-
1)*data_set*9 +
(b-1)*9 + 2);
impedance_img2 (a,b) = autolab_data2 (head_line + (a-
1)*data_set*9 +
(b-1)*9 + 3);
end
end
```

```
impedance1 = impedance_rel1 + j*impedance_img1;
impedance_amp1 = abs (impedance1);
impedance_phase1 = angle (impedance1) * (180/pi);
impedance2 = impedance_rel2 + j*impedance_img2;
impedance_amp2 = abs (impedance2);
impedance_phase2 = angle (impedance2) * (180/pi);
%%%%%%%%%%%% Use data set 2 as background
Z_exp_amp = impedance_amp1 - impedance_amp2;
Z_exp_phase = impedance_phase1- impedance_phase2;
%%%%%%%%%%%%%%%%%%%%%%%%%%%%%%%%%%%%%%%%%%%%%%%%%%%
frequency = frequency(:,1);
omega = 2*pi*frequency;
R1 = rc_component (1)*1000;
R2 = rc_component (2)*1000;
C1 = rc_component (3)*1.E-9;
Z_R1 = R1;
Z_R2 = R2;
Z_C1 = 1./(j*omega*C1);
Z = Z_R1 + (Z_C1.*R2)./(Z_C1+R2);
S 4
Z_amp = abs(Z);
Z_phase = angle(Z)*180/pi*-1;
if or(or((R1 < 0),(R2 < 0)),(C1<0))
F = 1.e12;
else
F = sum(((log10(Z_amp) - log10(Z_exp_amp))).^2);
End
```

circuit_fit.m: Matlab program that allows the user to input the initial estimate of the circuit parameters and performs the optimization using the objective function defined in the first program. In this specific program, the optimization function (fminsearch) finds minimum objective value of unconstrained multivariable function using derivative-free method starting at the initial estimate.

```
clear all;
R1 = 1; % KOhm
R2 = 3; % KOhm
C1 = 1000; % nF
rc_component0 = [ R1 R2 C1 ];
options = optimset('MaxIter',1.E4,'MaxFunEvals',1.E4);
[rc_component,F] =
fminsearch(@circuit_fun,rc_component0,options)
r1 = rc_component(1)*1000
r2 = rc_component(2)*1000
c1 = rc_component(3)*1.e-9
```

Figure 2.5 Representative Impedance Spectra for bEND.3 cells over One Week Growth

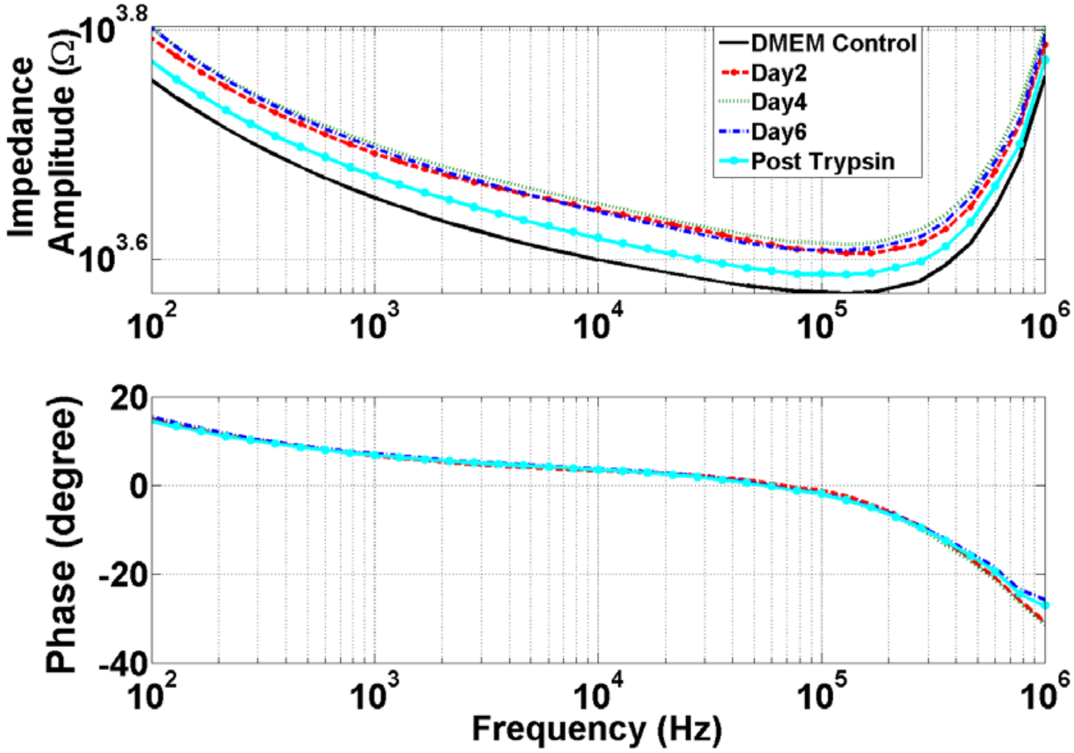

Representative Impedance Spectra for bEND.3 cells over One Week Growth. The impedance increases from baseline chip (DMEM control) to Day 2 and again from Day 2 to Day 4. The impedance plateaus near Day 4 before decreasing slightly on Day 6. Trypsinization decreases the impedance below Day 2 levels but remains higher than the baseline chip (DMEM control). Note, only every other day graphed for clarity.

Figure 2.6 Comparison of Impedance Spectra for Porous Polyester Membrane (400 nm Pore Size) and PDMS membrane.

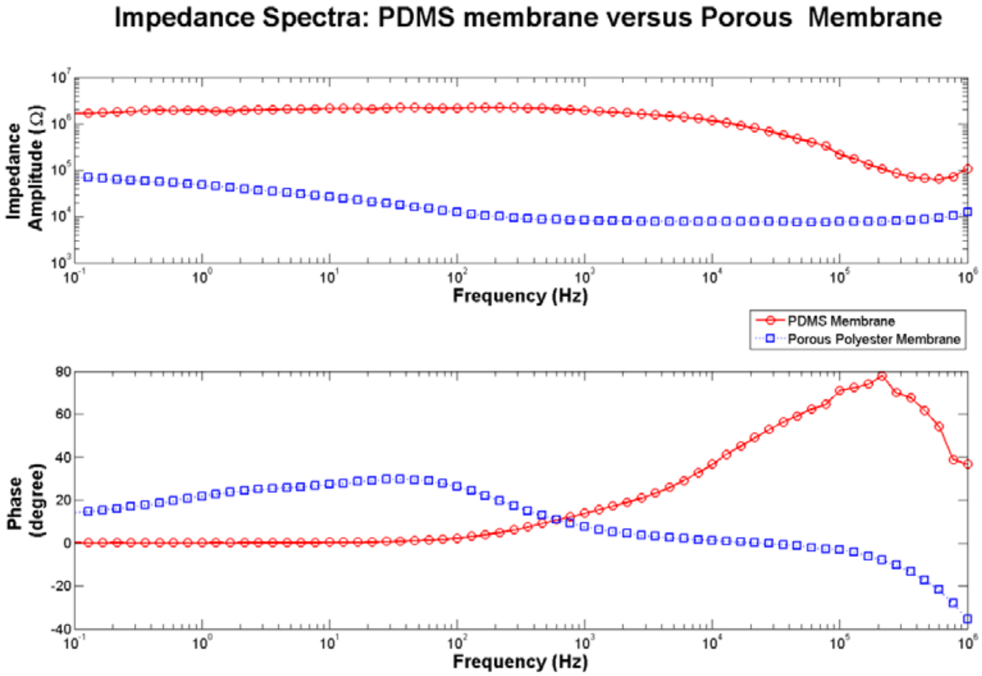

Impact of Membrane Material on Impedance Spectra. To verify that our system was capable of detecting large changes in impedance, we tested the impact of membrane material on impedance. First we characterized the standard system (polyester membrane with 400 nm pore size) sandwiched between the upper and lower PDMS channels. We compared this impedance to impedance measured in a system fabricated with a PDMS membrane in the place of the polyester membrane. Because PDMS is an insulator, we expected the resistance at low to intermediate frequencies to be much greater than the baseline (porous system). Our experimental results agreed with the expected results: the impedance amplitude was an order of magnitude greater in the system containing the PDMS membrane compared to the standard, porous membrane. Furthermore, at high frequencies, the impedance gap decreased (as the phase of the chip containing the PDMS membrane rose). This indicates that the PDMS membrane has a capacitive effect on the net impedance of the system.

Figure 2.7 The Impact of FN treatment on Impedance Spectra

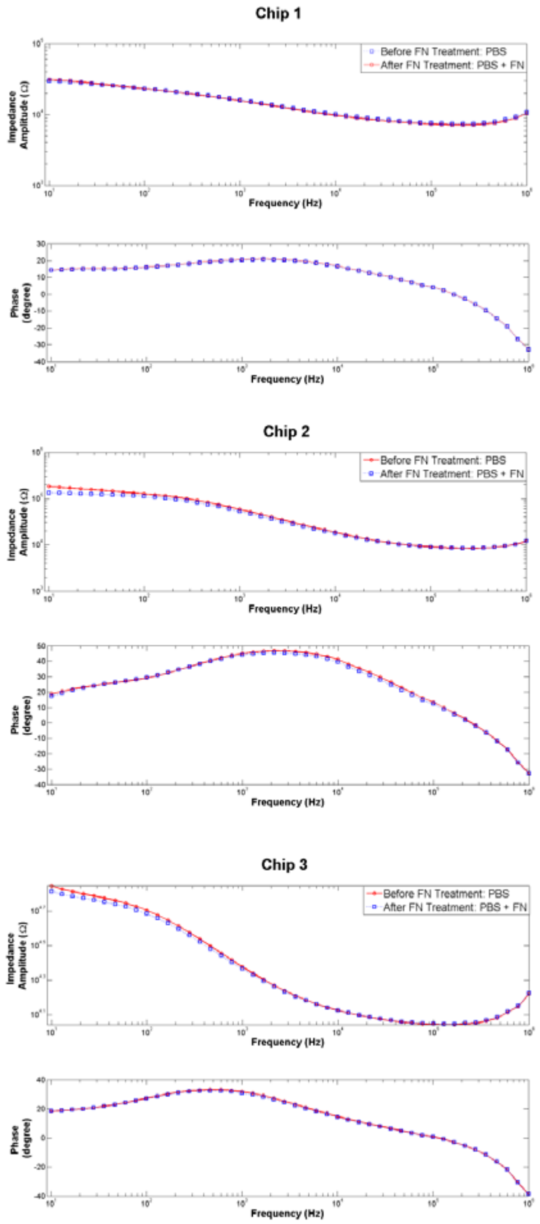

Impact of FN Treatment on Impedance Spectra. To test the impact of FN treatment on the baseline impedance of our system, we measured the impedance of 3 different Chips filled only with PBS. We then treated the system with fibronectin using an identical protocol to the one used in preparation for cell culture (30 minutes of 100 µg/mL FN in PBS under UV light). After 30 minutes of treatment, fresh PBS (without FN) was flowed into the system and the impedance was re-measured. We found that FN treatment had a minimal impact on the impedance spectra, actually decreasing amplitude slightly at low frequencies.

Figure 2.8 Inherent Measurement Variance

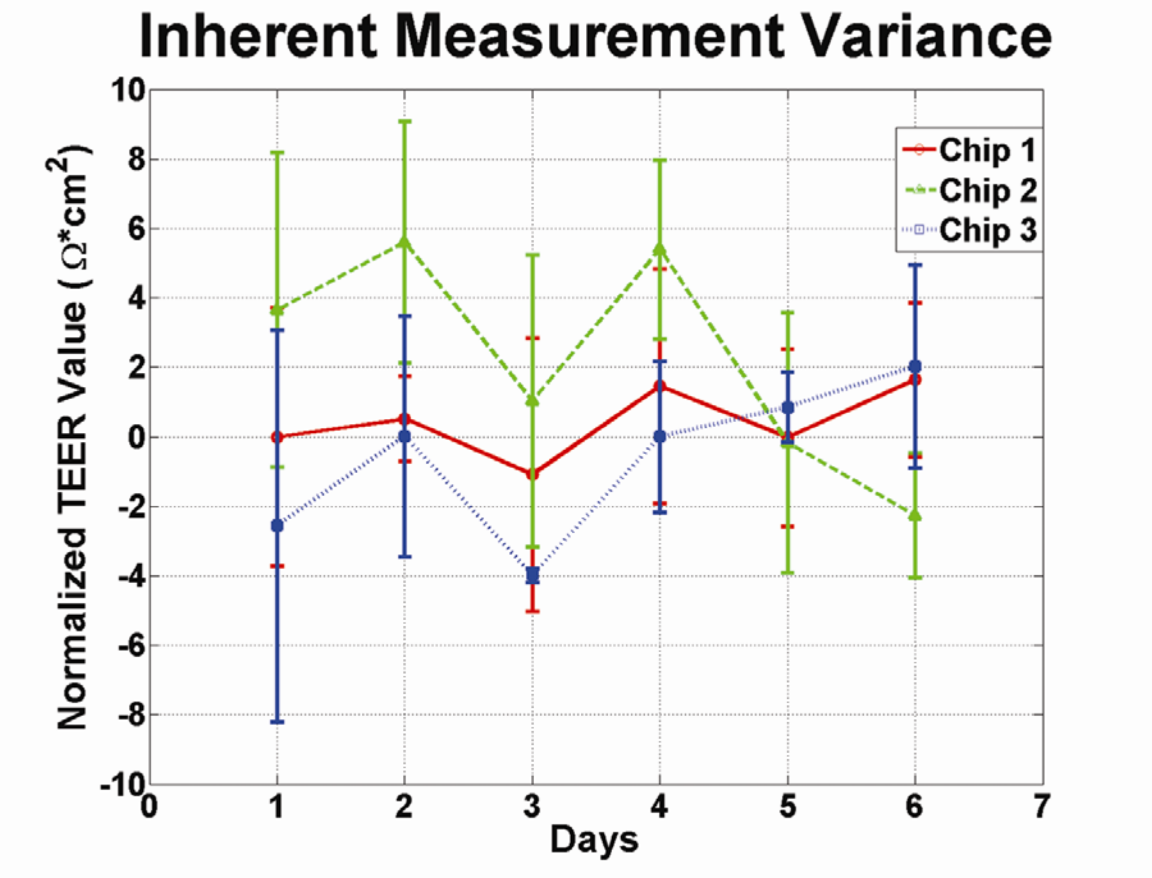

Inherent Measurement Variance. As a control experiment, an identical protocol to the cell culture experiment was maintained for the acellular condition. Growth media was loaded into the system, changed twice per day, and stored in the incubator at 37 ° C. Impedance measurements were resolved daily for 6 days. The data show that trans-membrane resistance values fluctuate between +6 Ω*cm^2 and -4 Ω*cm^2. The resistance measurements do not appear to trend either upward or downward as a function of time. The small measurement variance provides a window where TEER values as opposed to system drift can be resolved.

Figure 2.9 Impact of Treatment with TritonX-100

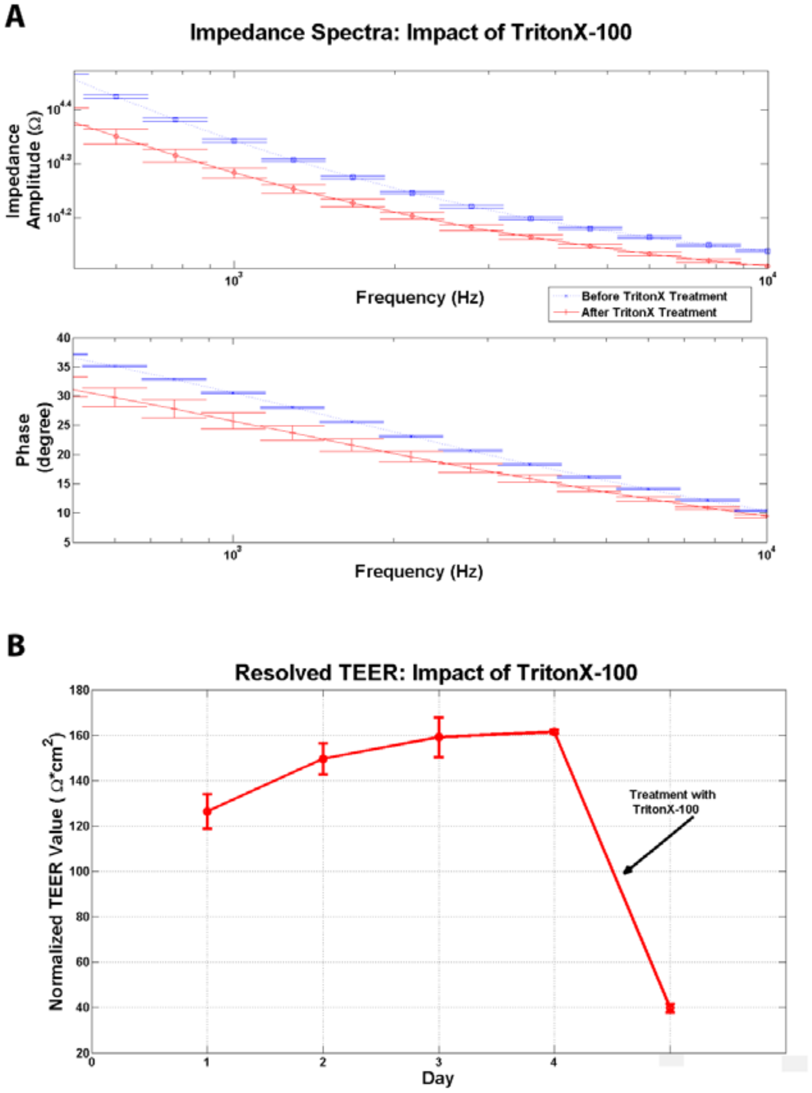

Impact of Treatment with TritonX-100. Treatment with the non-ionic surfactant, TritonX-100 is expected to increase the permeability of an endothelial cell monolayer. To demonstrate that this microfluidic system can detect dynamic changes in impedance, a confluent bEND.3 cell monolayer was treated for 30 minutes with 0.1% TritonX-100 then completely flushed with fresh growth media. The impedance amplitude decreased significantly at each frequency point (partial spectrum shown in the Figure 2.9A) and the TEER decreased from a maximum value of 161.51 ±0.755 Ω*cm^2 to 39.73 ± 1.925 Ω*cm^2 (shown in Figure 2.9B) demonstrating that treatment with TritonX-100 increases the permeability of the cell monolayer.

Fracture of Metal Coated Elastomers

Nicholas J. Douville, Zhengyu Li, Shuichi Takayama, and M.D. Thouless

ABSTRACT

Polydimethylsiloxane (PDMS) substrates were coated with thin layers of gold varying in thickness between 40 nm and 160 nm. Arrays of parallel cracks formed when a tensile strain was applied to the coated system, with the spacing between the cracks being approximately inversely proportional to the strain. When the crack profiles were examined, it was noted that the cracks extended deep into the substrate—to depths up to two orders of magnitude greater than the film thickness. This extension of the cracks into the substrate is the result of the large mismatch in elastic properties between the metal and soft substrate, and plays a role in the development of the cracking pattern. Despite the relatively large strains that can be applied through the elastomeric substrate, there was no evidence of macroscopic plasticity in the metal films, and numerical analyses showed that the crack profiles were consistent with elastic deformation of the metal. A quantitative comparison of the crack depth and spacing with the predictions of a companion mechanics analysis indicated that the observed spacing and depth were consistent with the metal film being much tougher than the elastomeric substrate. However, for this level of toughness to be exhibited in a metal film would require plastic deformation over a scale much larger than would be expected in such a geometry. This inconsistency may be resolved by recognizing that rupture of a thin metal film can be associated with shear localization that results in a mode-II failure, rather than by classical mode-I crack propagation. This results in a failure mechanism for a metal film that is a high-strain, but low-energy process, with substrate cracking absorbing the excess elastic energy available upon rupture of the film. Such a failure mechanism is consistent with earlier observations for the failure of thin metal films, and this work suggests that failure of an elastomeric substrate may contribute to an additional loss of constraint enhancing this localization.

INTRODUCTION

Understanding the mechanics of deformation and failure of a stiff film supported on an elastomeric substrate is important for a number of potential applications. These include the design and fabrication of flexible electronics [Lewis, 2004; Douville *et al*., 2010], sensitive skins for machines [Lumelsky *et al*., 2001; Lacour *et al*., 2004], elastomeric actuators [Pelrine *et al*., 2000; Begley *et al*., 2005], and the use of patterns for fabrication systems [Zhu *et al*., 2005; Mills *et al*., 2010; Chung *et al*., 2008]. Under a compressive loading, it is well known that the stiff film deforms by a surface-buckling phenomenon [Moon *et al*., 2007; Bowden *et al*., 1998; Chen and Hutchinson, 2004]. Conversely, the film can rupture in response to a tensile strain [Lacour *et al*., 2003; Li *et al*., 2004; Begley and Bart-Smith, 2005; Jansson *et al*., 2006; Tsubone *et al*., 2007; Mills *et al*., 2008; Akogwu *et al*., 2010; Cordill *et al*., 2010]. Two basic mechanisms for the rupture of stiff films on elastomers have been discussed in the literature: one based on instabilities (flow instabilities associated with plastic deformation of a ductile film) [Li *et al*., 2005; Li and Zuo, 2006]; and the other based on fracture of brittle films (with or without accompanying delamination) [Begley *et al*., 2005; Jansson *et al*., 2006; Tsubone *et al*., 2007]. The discussions of these models have all been predicated on the assumption that the failure process does not extend into the substrate. In this paper we have identified and characterized a new failure mechanism in which failure of the film is coupled with fracture of the substrate. We have shown that when a metal film on an elastomeric substrate fractures, the cracks can extend into the substrate to depths up to two orders of magnitude greater than the film thickness. In other words, a metal film that is only 100 nm thick can control cracks extending 10 μm into the substrate.

Linear-elastic fracture mechanics can be used to show that a crack can channel across a film supported on a substrate upon the application of a critical tensile strain [Hu *et al*., 1988; Beuth *et al*., 1992]. If the crack remains in the film, the critical strain, ε_c, required to introduce a single crack into a stiff film of thickness *h*, toughness Γ_f and plane strain modulus E_f on a very thick compliant substrate of modulus E_s is approximately given by [Beuth, 1992; Dundurs,1969]:

$$\varepsilon_c \approx 1.17\,(E_s/E_f)^{0.885}\,(\Gamma_f/(E_s h))^{0.05} \qquad \text{Eqn 2.1}$$

Above this critical strain, a series of approximately periodic parallel cracks can channel across the film [Thouless, 1995; Thouless, 1990; Thouless *et al*., 1992; Hutchinson and Suo, 1992]. While details of the spacing between the cracks often depend on stochastic effects [Thouless, 1995], fracture-mechanics analyses indicate that the characteristic spacing between the cracks in these arrays is approximately inversely proportional to the strain and increases with film thickness [Thouless, 1990; Thouless *et al*., 1992; Hutchinson and Suo, 1992]. It also increases as the stiffness of the film increases, since the length over which strains build up from a crack surface increases with modulus-mismatch ratio [Shenoy *et al*., 2000].

When the surface of an elastomer such as polydimethylsiloxane (PDMS) is oxidized, a stiff brittle layer is formed. The periodic channel cracks that can be formed upon the application of a tensile strain have been shown to be useful for various nano- and biological applications [Zhu *et al*., 2005; Mills *et al*., 2010; Huh *et al*., 2007; Kim *et al*., 2011; Rand *et al*., 2008]. However, the ambiguity associated with the parameters of an oxidized surface layer (thickness, modulus, property gradients, and variability of oxidation conditions) prompted an interest in exploring the fracture behavior of a film with relatively well-controlled properties. For this reason, a system consisting of PDMS coated with gold was chosen for study. Gold films are also of practical interest as they have the advantage of providing additional control of the surface chemistry for biomedical applications such as using self-assembled monolayers (SAMs) for controlled cell adhesion [Mrksich *et al*., 1996].

While the modulus mismatch between gold and PDMS is about two orders of magnitude greater than the range studied in any studies of thin-film cracking, the observations in this study were superficially consistent with what would have been expected by extrapolation from the analyses based on fracture mechanics, with crack spacings up to four orders of magnitude greater than the film thickness. However, a more careful examination of the experimental results indicated that the PDMS also fractured as the crack arrays channeled across the gold film. In this paper we give experimental details of this phenomenon, and discuss it in the light of a general fracture-mechanics analysis presented in a companion paper that was originally motivated by the observations described here [Thouless *et al*., 2011].

EXPERIMENTAL METHODS

An elastomeric substrate was made for these studies using polydimethylsiloxane (PDMS) (Sylgard 184, Dow Corning) mixed at a ratio of 3 parts polymer base to 1 part curing agent by weight. The pre-polymer was poured into a dish to form a slab of thickness 3.5 mm, and cured in an oven at 60°C for 4 hours. After curing, the slab was cut into strips 50 mm long and 10 mm wide. The strips were placed onto silanized glass slides covered by a thin spin-coated film of PDMS pre-polymer (Figure 2.10A). This PDMS pre-polymer was cured at 60°C for 4 hours (to give a total curing time of 8 hours for the slabs). This step allowed the slabs to be held flat during handling and coating, but permitted relatively easy removal for subsequent testing. The PDMS was then coated by 10 nm of evaporated Cr to function as an adhesion layer; this was followed by evaporation of an Au layer that was either 40, 80 or 160 nm thick (Figure 2.10B). The thickness of the two layers was controlled to within 2 nm using an Inficon XTC/2 film deposition controller, calibrated according to the procedures specified by the manufacturer. In addition, we also verified the calibration process by using a Dektak 6M stylus profiler to measure directly the thickness of a 10 nm Cr/80 nm Au bi-layer deposited on a PDMS substrate along an edge formed by shielding from the deposition process. While the results presented in this chapter were taken from systems with evaporated films, similar results were obtained with sputtered films, although it was noted that a higher compressive stress existed with the sputtered films, as demonstrated by the increased tendency of sputtered films to buckle.

The modulus and toughness of the PDMS substrate were determined using tension and compact-tension tests [Mills *et al*., 2008], ensuring that the test specimens had undergone the same total curing cycle as the substrates used in the tests. The modulus of the PDMS was found to be 3.8 ± 0.5 MPa. With the assumption of incompressibility for an elastomer, this is equivalent to a plane strain modulus of Es = 5.1 ± 0.7 MPa. The mode-I toughness of the PDMS, Γ_s, was found to be 460 ± 50 J m^{-2}.

The gold-coated samples were removed from the glass slide using ethanol to wet the interface between the spin-coated PDMS film and glass slide. The samples were then fastened into a mechanical micro-tensile tester, mounted in an optical microscope (Figure 2.10C) that enabled the system to be stretched at a nominal-strain rate of approximately 0.005 per second. Periodic cracks were observed to channel across the system during these tensile tests. The spacing between neighbouring pairs of cracks was measured as a function of strain using in situ optical microscopy. At pre-determined levels of applied strain, the strain was held fixed and replicas of the surface were made using PDMS prepared by mixing the curing agent and polymer base in a ratio of 1:3 by weight. Prior to replica formation, the surface (thin metal film and exposed PDMS cracks) of the system was silane treated according to a protocol described by Mills and colleagues [Mills *et al*., 2008]. This silane treatment prevented the PDMS replica from cross-linking with native PDMS and ensured complete removal following polymerization. These replicas were stripped from the cracked surface after being cured at room temperature for 24 hours, and sectioned in a longitudinal direction. Optical microscopy was used to determine the crack profiles from these sections for the 80 and 160 nm thick Au films (Figure 2.11A). However, the limitations of optical resolution required the profiles for the 40 nm Au films to be determined by atomic-force microscopy (AFM) of the top surfaces of the replicas

(Figure 2.11B). The profiles obtained by these techniques were subsequently summarized in terms of a crack opening (distance between the peaks on either side of the crack) and crack depth (distance from peak to trough). The three points used for these definitions are indicated on the AFM trace of Figure 2.11B.

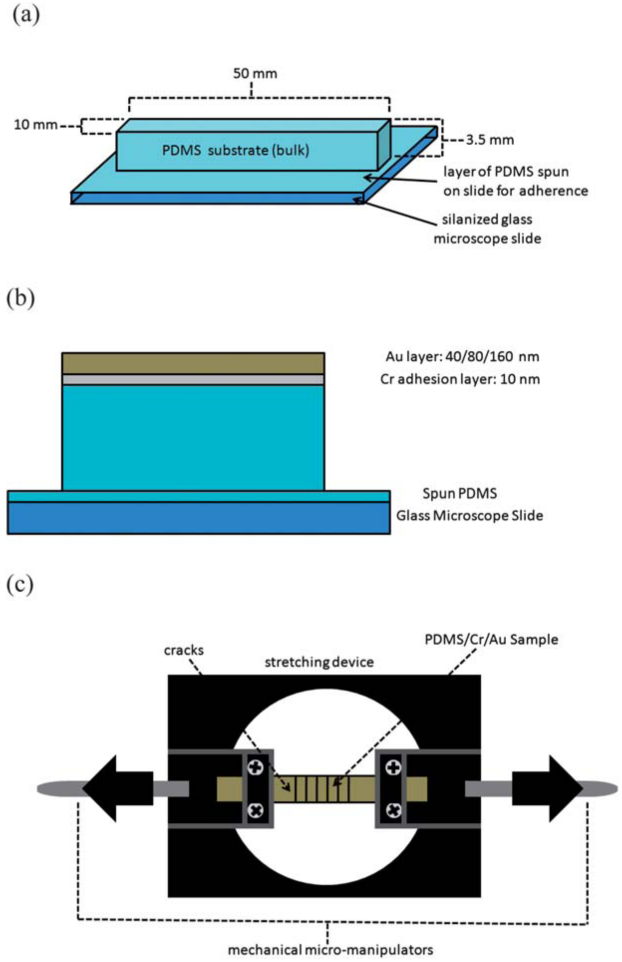

Figure 2.10. Schematic of Cracking System. (a) PDMS substrate fastened to silanized glass slide with a thin layer of spin-coated PDMS. (b) Coated system with 3.5 mm thick PDMS substrate, 10 nm Cr bonding layer, and 40/80/160 nm thick Au layer. (c) System in mechanical testing device results in a series of cracks upon the application of tensile strain.

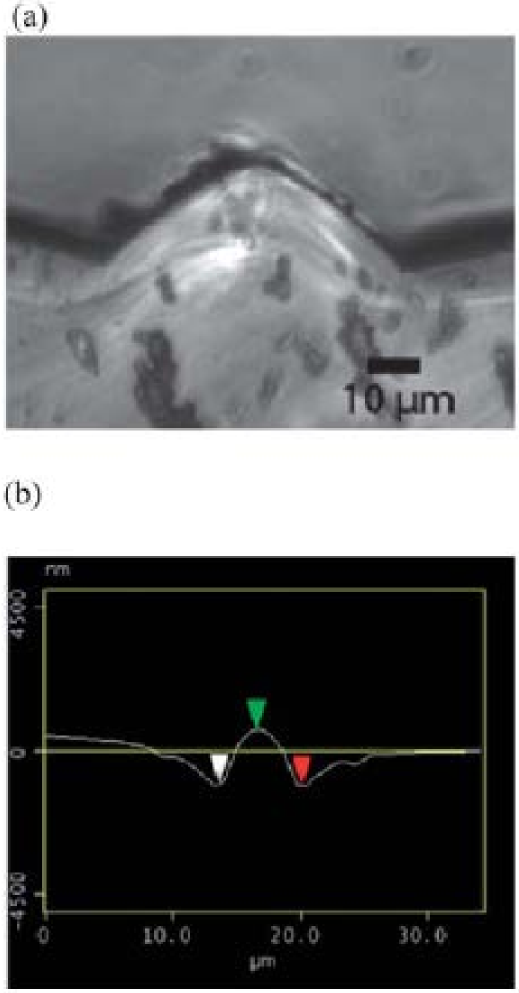

Figure 2.11. Cross Sectional Profile of Cracks. (a) Optical micrograph of sectioned replica showing typical profiles of a crack generated at a strain of 25% for a specimen with a 160 nm Au layer. The replica is at the bottom of the image. (b) AFM images of a replica showing a typical profile of a crack generated at a strain of 10% for a specimen with a 40 nm Au layer. In subsequent figures, the crack opening is defined as the distance between the points of maximum rise at the crack mouth, and the crack depth is defined as the distance between these two points and the crack tip. The crack spacing is defined as the distance between neighbouring crack tips in a relaxed state.

EXPERIMENTAL RESULTS

It was noted that there was a small residual compression in the film, as indicated by a periodic array of buckles, before beginning the tensile tests. As the buckles appeared only after the PDMS was released from the glass slide, it is believed that this compressive stress was induced by the thermal-expansion mismatch between the PDMS substrate and the glass slide to which it was bonded before the evaporation of the metal film. For a system with 80nm Au and 10nmCr, the wavelength of these buckles was very regular and equal to about 45 μm. The buckles were aligned perpendicular to the tensile axis of the specimen (the long axis of the specimens— the presence of free surfaces appears to have relaxed the compression in the orthogonal, narrower, direction). Upon the initial application of a tensile strain, these buckles disappeared. However, after the cracks formed, a different set of buckles were formed. These new buckles were parallel to the tensile axis and perpendicular to the cracks (Figure. 2.12), as has been observed in earlier studies for oxidized PDMS [Mills *et al.*, 2008]. It is believed that these buckles formed from an induced compressive stress arising from the interaction between the Poisson contraction of the substrate below the cracks and the relaxation of the applied strain in the region between the cracks. The average wavelength for these buckles was about 32 μm. A difference in wavelengths between the buckles associated with a relaxed tension and the buckles associated with cracking was a very consistent feature of these studies, and earlier studies on oxidized PDMS [Lee, 2008]. Furthermore, both sets of wavelengths were much larger than that which is predicted by standard results for buckling on a compliant substrate, in which the wavelength, λ, is related to the film thickness, h, by [Allen, 1969]:

$$\lambda = 2\,\pi h(E_f/3E_s)^{1/3} \qquad \text{(Eqn. 2.2)}$$

which would indicate a wavelength of about 9μm for a gold film of 80 nm (compared to the experimentally observed wavelength of approximately 45 μm for the uncracked system). Even recognizing that the experimental configuration is a bi-layer, this discrepancy is outside the range of what can reasonably be explained by experimental uncertainty, precluding the use of these buckling equations in further analysis, such as estimation of residual compression.

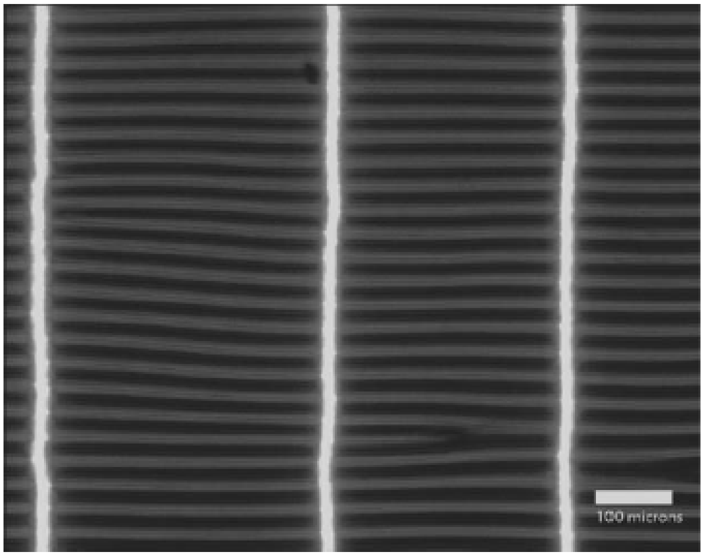

Figure 2.12 Optical Micrograph Showing Formation of Periodic Cracks. An example of an optical micrograph showing the formation of periodic cracks in a sample with an 80 nm evaporated Au and 10 nm Cr adhesion layer on PDMS at a nominal strain of 15%. Periodic buckles, induced by Poisson contraction, run perpendicular to the direction of the cracking.

Figure. 2.13 shows a plot of the average crack spacing as a function of applied nominal strain. The average spacing at a given strain ε_o was determined from the average of in situ optical measurements of the distance between individual pairs of neighbouring cracks, and corrected by a factor $1/(1 + \varepsilon_o)$ to compensate for the stretching. The error bars represent one standard deviation in the crack spacing from multiple pairs of cracks. At high strains, each datum point in the figure corresponds to an average from up to 100 crack pairs. Cracks were observed down to nominal strains of just below 1%. However, at these lower strains, the number of cracks in the gauge length was so low that the use of distances between neighbouring cracks to determine the average crack spacing had a statistical effect of slightly under-estimating the average spacing that would be observed in a longer specimen. There was also some ambiguity in these very low strain ranges as to whether any cracks had been introduced by handling prior to straining. Datasets corresponding to less than five observed cracks have not been included in Figure 2.13.

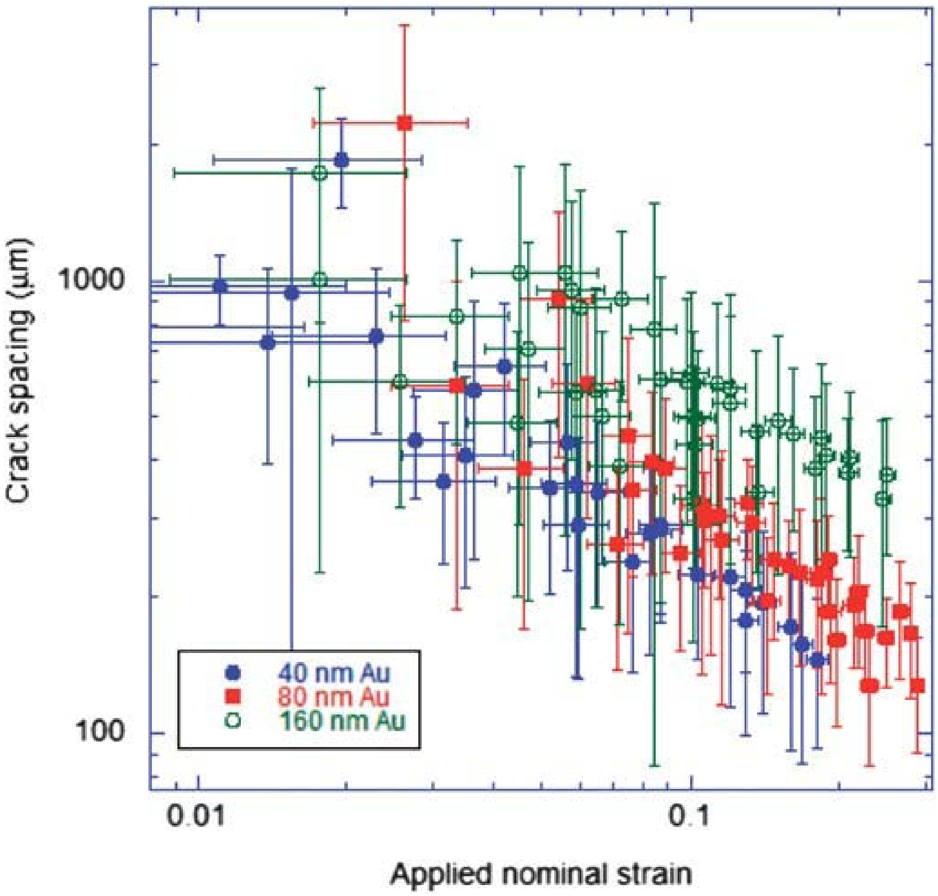

Figure 2.13. Average Crack Spacing as a Function of Applied Normal Strain. The error bars represent one standard deviation in the crack spacing.

Figure 2.14 shows a plot of the average crack depth as a function of nominal strain. These values were determined from between 10 and 20 crack profiles obtained from replicas taken at each strain, as described in the previous section. Of particular significance is that the depth of the cracks is in the range of 5 to 15 µm, compared to a total film thickness of between 50 nm and 170 nm. Since the replicas were taken under strained conditions (so the cracks were relatively open) the crack profiles were probably fairly faithfully replicated. Direct images of the cracks were obtained using a 3D measuring laser microscope (Olympus OLS4000) at 50x magnification to validate that these crack profiles were not artifacts of the replica process.

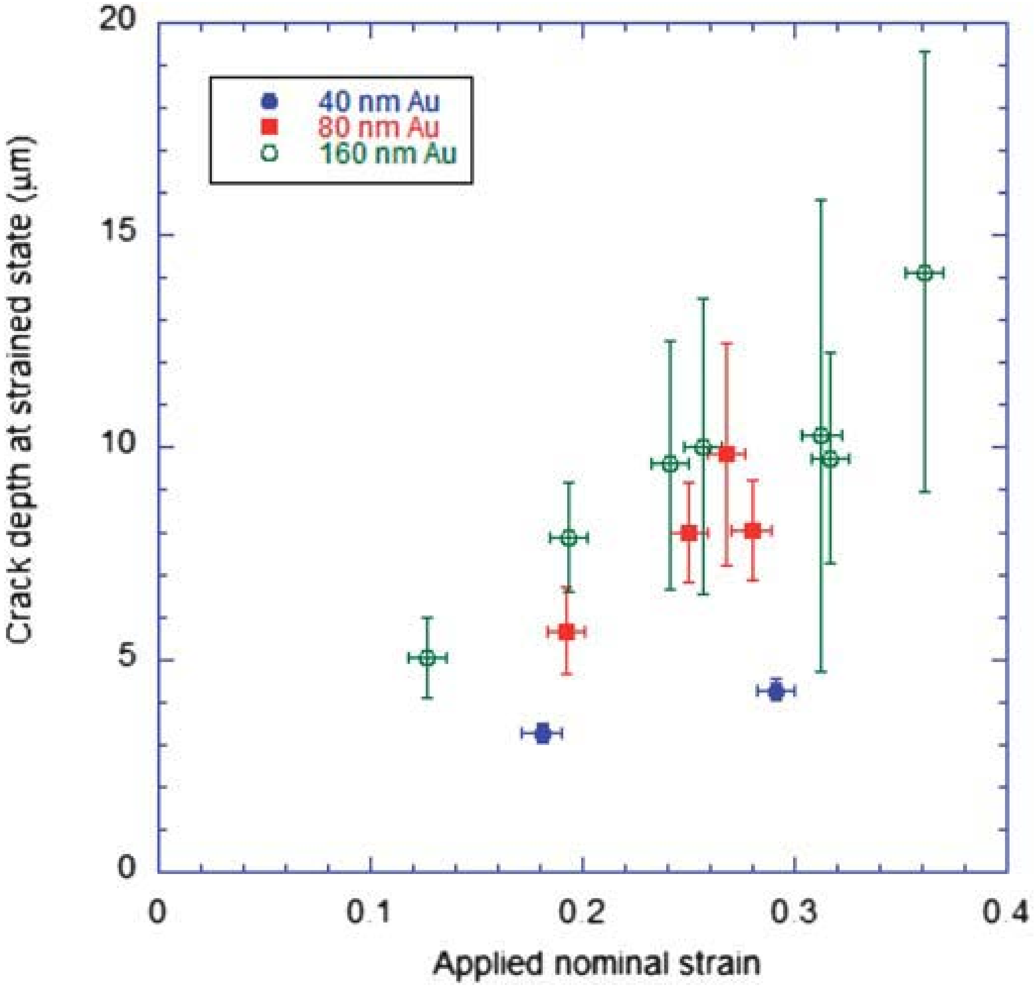

Figure 2.14. Average Crack Depth as a Function of Applied Nominal Strain. The uncertainties represent one standard deviation of depths from all. The crack depth is an underestimate, because it has not been corrected for the applied strain (which makes the cracks wider and shallower).

While an average crack spacing could be determined for a given strain, the stochastic nature of the cracking process meant that the cracks were not uniformly spaced across the film. Furthermore, there was no uniformity in the depth and opening of the cracks. This is illustrated by the data plotted in Figure 2.15. The profiles of a series of cracks were measured from the replicas along with the distance to the nearest neighbouring cracks on both sides. The depth and opening of the cracks is plotted in Figure 2.15 as a function of this average spacing, with the width of the error bars indicating the distance to the nearest crack (so a small error bar in this figure corresponds to a more symmetrical crack). It should be noticed that openings of many tens of microns are consistent with the fact that the cracks are clearly visible by low powered optical microscopy (Figure. 2.12), and is consistent with the very deep cracks. Had the cracks remained within the metal layer, with the layer bonded to the substrate, the crack openings would have been much smaller than actually observed.

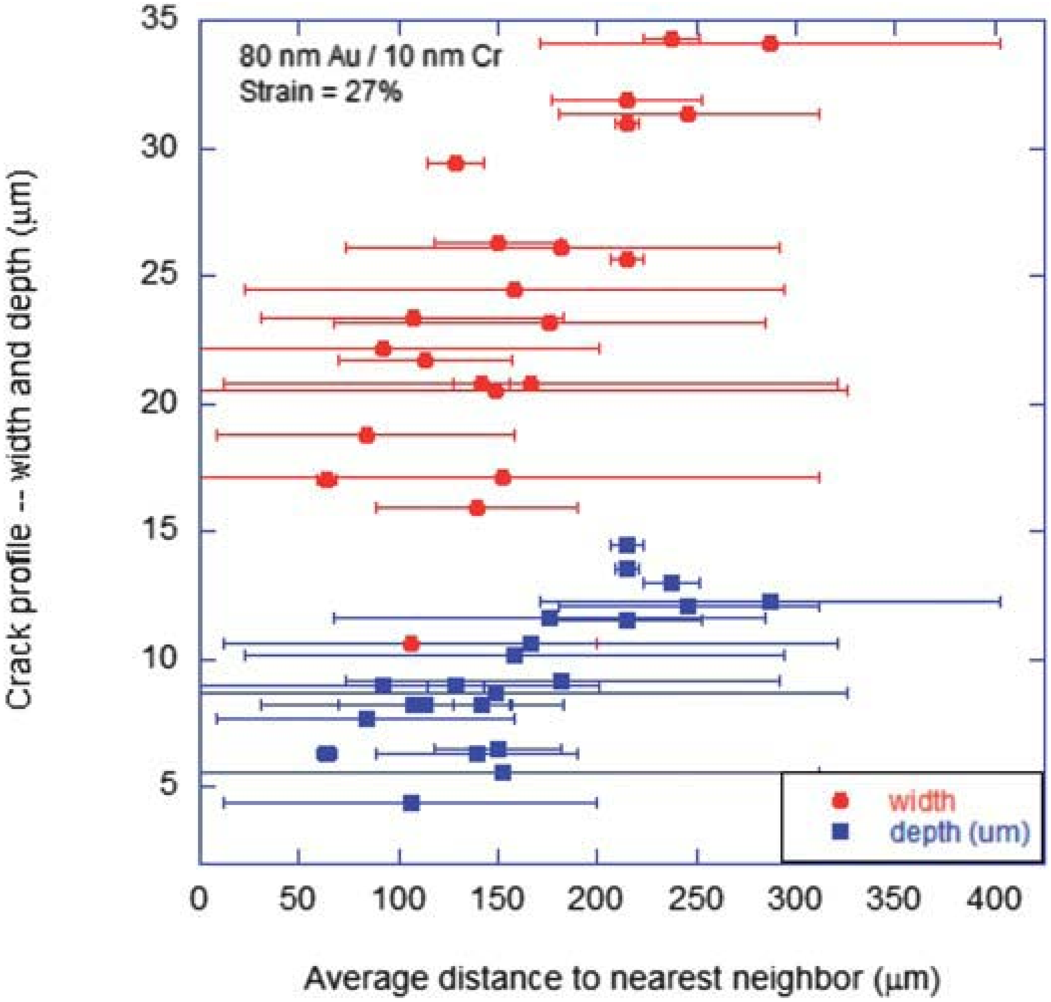

Figure 2.15. Dependence of the Crack Opening and Crack Depths on the Average Distance to the Nearest Neighbour for One Particular Value of Applied Nominal Strain. The range of the uncertainties for the spacing in this plot represents the maximum and minimum distances to the nearest crack. A small uncertainty indicates a crack more nearly in the middle of two neighbours.

DISCUSSION

The most striking aspect of the experimental results was the relatively great depth to which the cracks propagated within the substrate. This was apparent from the replica studies and from the optical observations of the crack opening.

As discussed below, finite-element calculations showed that the profile of the crack surface could only be explained by these deep cracks. Furthermore, it should be noted that it is actually a well-known mechanics result that a crack within a stiff layer should be drawn across an interface into a more compliant material [Beuth, 1992; Zak and Williams, 1963]. However, despite the fact that, in retrospect, crack propagation in an elastomeric substrate might be expected, this phenomenon has not been previously noted or analyzed. Prompted by the observations described in this paper, a general linear-elastic fracture mechanics analysis of cracking in stiff films on compliant substrates was developed and has been presented elsewhere [Thouless *et al*., 2011]. Here, the experimental results presented above are discussed in the light of the insight provided by this general analysis.

Strain level in the metal film

The nominal strains applied to the substrate are sufficiently large, being in excess of 20%, that there is an immediate question about the validity of a linear-elastic analysis. As detailed elsewhere [Mills *et al*., 2008] and verified again for this study, the PDMS itself behaves in a linear fashion at nominal strains up to about 40%. The cracks, and the depth to which they propagate, reduce the strain in the film to a level well below the nominal strain applied to the substrate. The extent of this reduction can be deduced by a finite element calculation that accurately includes the crack spacing, depth, and elastic properties. The PDMS was modeled with a modulus of 3.8 MPa and an assumed Poisson's ratio of 0.4995 using hyper-elastic elements in the commercial finite-element program ABAQUS. The metal films were modeled using incompatible-mode elements. The modulus and Poisson's ratio of Cr were assumed to be 279 GPa and 0.21; the elastic properties of Au were assumed to be 78 GPa and 0.44 [Zak and Williams, 1963]. Initially, the films were assumed to deform only in an elastic fashion. Owing to the huge modulus mismatch between the PDMS and metallic layer, the full depth of 3.5 mm for the substrate was modeled (along with the correct thickness of the Cr and Au layers). A segment of the system containing a set of cracks that had been observed experimentally was modeled. While periodic boundary conditions were used at either end of this segment, the crack spacing within the segment was set according to the experimental observations. The mesh was reduced to 10 nm around the crack tips within the PDMS, and a mesh-sensitivity analysis was conducted to assure that any uncertainties from the numerical procedure were less than the uncertainties from the experimental observations. The calculations were done for a number of different sets of data that formed the plot given in Figure 2.14 to verify consistency between the results, but one particular set will serve for illustrative purposes. Table 2.1 lists experimental details of a set of five contiguous cracks, with the measured spacing, depth and opening at a nominal strain of 25%. The periodic boundary conditions were imposed on the plane at the centre of the first and last cracks of the series, and the appropriate level of strain was introduced by the imposition of a uniform displacement between these boundaries under planes strain conditions.

Figure 2.16 shows the deformed mesh that results from the crack distribution given in Table 2.1. While the crack depths and spacings were chosen *a priori* to match the experimental measurements, the crack openings were left as parameters to be determined as outputs from the numerical calculations. A subsequent comparison with the experimental observations (Table 2.1) shows that these completely elastic calculations describe the openings very well. The fact that the crack profiles predicted from an elastic calculation matched the experimental observations so well, indicates that the metal film does not deform plastically to any significant extent. (Plastic deformation of the film would have reduced the crack opening.) The calculations indicated that the strain in the film increased with distance from the cracks, and reached a maximum of between about 0.4% and 0.6% halfway between neighbouring cracks. This maximum level of strain was obtained in a reproducible fashion from several related calculations with different experimental datasets, and was therefore taken to be an approximate measure of the strain required to rupture the film.

		Observed (±1 μm)	Calculated
crack 1	opening (μm)	19	16
	depth (μm)	8	8
space (μm)		68	70
maximum computed strain			0.45% ± 0.05%
crack 2	opening (μm)	15	13
	depth (μm)	7	7
space (μm)		46	49
maximum computed strain			0.41% ± 0.05%
crack 3	opening (μm)	14	15
	depth (μm)	6	5-6
space (μm)		129	123
maximum computed strain			0.60% ± 0.05%
crack 4	opening (μm)	17	21
	depth (μm)	7	7
space (μm)		86	88
maximum computed strain			0.50% ± 0.05%
crack 5	opening (μm)	18	18
	depth (μm)	7	7

Table 2.1. Comparison between Observed Crack data and FEA shown in Figure 2.16. This was used to estimate the strain level in the metal film (nominal strain applied to the system = 25%;10 nm Cr and 80 nm Au).

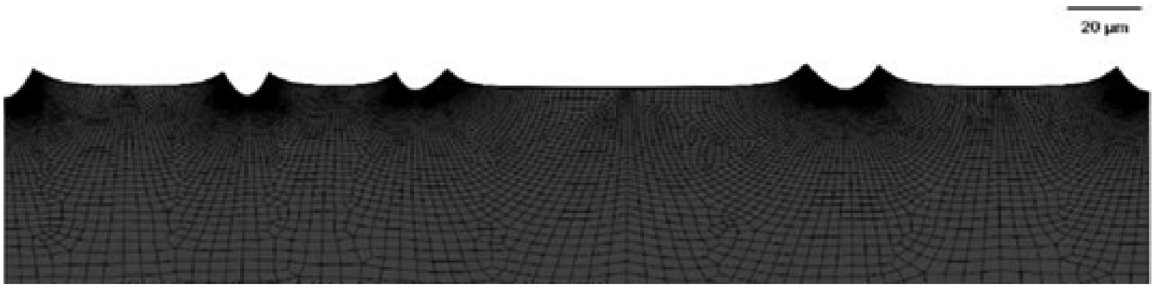

Figure 2.16. Output from a FEA calculation for a system with 10 nm of Cr, 80 nm of Au, and a nominal strain of 25%, with crack depths and spacing set by experimental observation. The peaks to either side of the cracks (which match the experimental profiles as shown in Figure 2.16) are the result of a Poisson's ratio effect. The stress is relaxed near the crack surfaces, causing the out-of-plane displacement to be relaxed.

Comparison of observations with related elastic fracture mechanics analysis. A major conclusion of the finite-element calculations described above is that the metal film deforms elastically up to strains of about 0.6% before fracture occurs. This level of elastic strain, indicating a yield stress of 475 MPa or more, is consistent with what might be expected for gold films of this thickness.40 Furthermore, elastic deformation of the metal film indicates that the problem should be amenable to a linear-elastic fracture mechanics (LEFM) analyses, which allows one to invoke the concept of a fracture toughness for the thin metal film and substrate, as described in the companion analysis [Thouless *et al*., 2011].

The LEFM analysis of our companion manuscript is a general one appropriate for a single film of modulus E_f, toughness Γ_f, and thickness h on a compliant substrate of modulus E_s, toughness Γ_s, subjected to a nominal applied tensile strain of ε_o. This analysis indicates that cracking of the substrate enhances failure of the system in that it reduces the critical strain for propagating a channel crack to below that given by Equation 2.1. Furthermore, above this critical strain, the crack spacing, *S*, is predicted to be approximately inversely proportional to the applied strain:

$$S/h \propto (1/\varepsilon_o)\,(\Gamma_s/(E_s h))^{1/2} \qquad \text{Eqn. 2.3}$$

In this relationship, the constant of proportionality is a function of the ratio of Γ_f/Γ_s, with the normalized crack spacing increasing as the toughness ratio increases [Thouless *et al*., 2011]. As can be seen in the nondimensional plot of Figure 2.17, the experimental data is quite well described by the functional form of Equation 2.3, despite the fact that the experiments involved a bilayer consisting of two different metals. It is noted that the use of a slightly more compliant substrate with a 10:1 ratio of polymer:curing agent resulted in a slightly larger crack spacing for a given nominal strain. This is consistent with Equation 2.3.

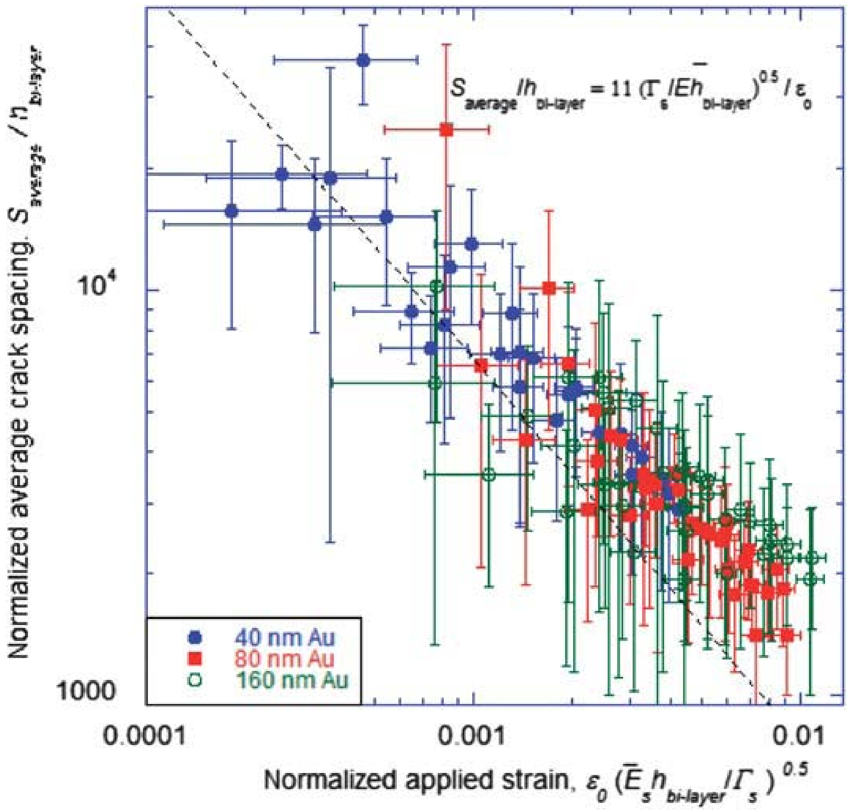

Figure 2.17. The Experimental Data Replotted in a Non-Dimensional Form, to Make Comparison with the LEFM Analysis.

The LEFM results indicate that the crack spacing is dependent on both the modulus mismatch and the toughness ratio between the film and substrate [Thouless *et al*., 2011]. Specific examples of the general results from the mechanics calculation are given in Figure 2.18, which shows how the predicted crack spacing varies with applied strain for different levels of toughness ratio between film and substrate. The calculations of Figure 2.18 were computed for a modulus mismatch ratio of 2 x10^4, which is a good approximation for the mismatch between Au and PDMS. It will be observed that the crack spacing increases for a given level of strain as the toughness ratio film increases. The depth of the crack has also been shown to increase with this ratio [Thouless *et al*., 2011].

Superimposed on Figure 2.18 is the approximate range for the experimental data for the Au/Cr bi-layers on PDMS. It will be see that the LEFM models provide a reasonable agreement with the experimental results for the crack spacing if the toughness of the metal film is taken to be about 10–50 times greater than that of the substrate. While this toughness of about 4.5–22 kJ m^{-2} (corresponding to a fracture toughness, K_{Ic}, of about 21–46 MPa√m) is reasonable for bulk metal specimens, it is considerably in excess of what might be expected for a thin film because it would require a plastic zone size much larger than the film thickness. An approximate estimate for the toughness of a thin film is given by the product of the thickness and yield strength [Hutchinson, 2010]. Such a calculation would indicate a toughness of no more than about 50 J m^{-2} for a Au film of 80 nm. This is only about 10% of the toughness of the PDMS. Such a low value of toughness would correspond to a very ‘‘brittle’’ film, and the cracks would be expected to penetrate only a little distance into the substrate. Furthermore, the predicted spacing would be considerably more than an order of magnitude less than observed, and the onset of cracking would occur at a relatively low strain.

The apparent paradox where a thin metal film on a soft substrate that should behave in a relatively brittle fashion, but actually exhibits cracking behaviour consistent with a much tougher material, may perhaps be resolved by recognizing that there is evidence thin gold films do not rupture by a classical mode- I fracture mechanism. In 1960, Pashley performed in situ tensile tests of thin gold films in a transmission electron microscope [Pashley, 1960]. These experiments revealed that free-standing thin gold films deform elastically until failing at relatively high strains by rupture associated with shear localization. For thin films, this rupture mechanism dissipates much less energy than a mode-I fracture mechanism. It is probably related to the well-known fracture mechanics phenomenon that, while the toughness of metals increases from plane-strain values to plane-stress values as the thickness decreases, the fracture mechanism changes to a shear mode and the toughness drops with sample thickness below a critical thickness [Brock, 1982]. Furthermore, it has been shown for metal films on polymeric substrates that while this shear localization

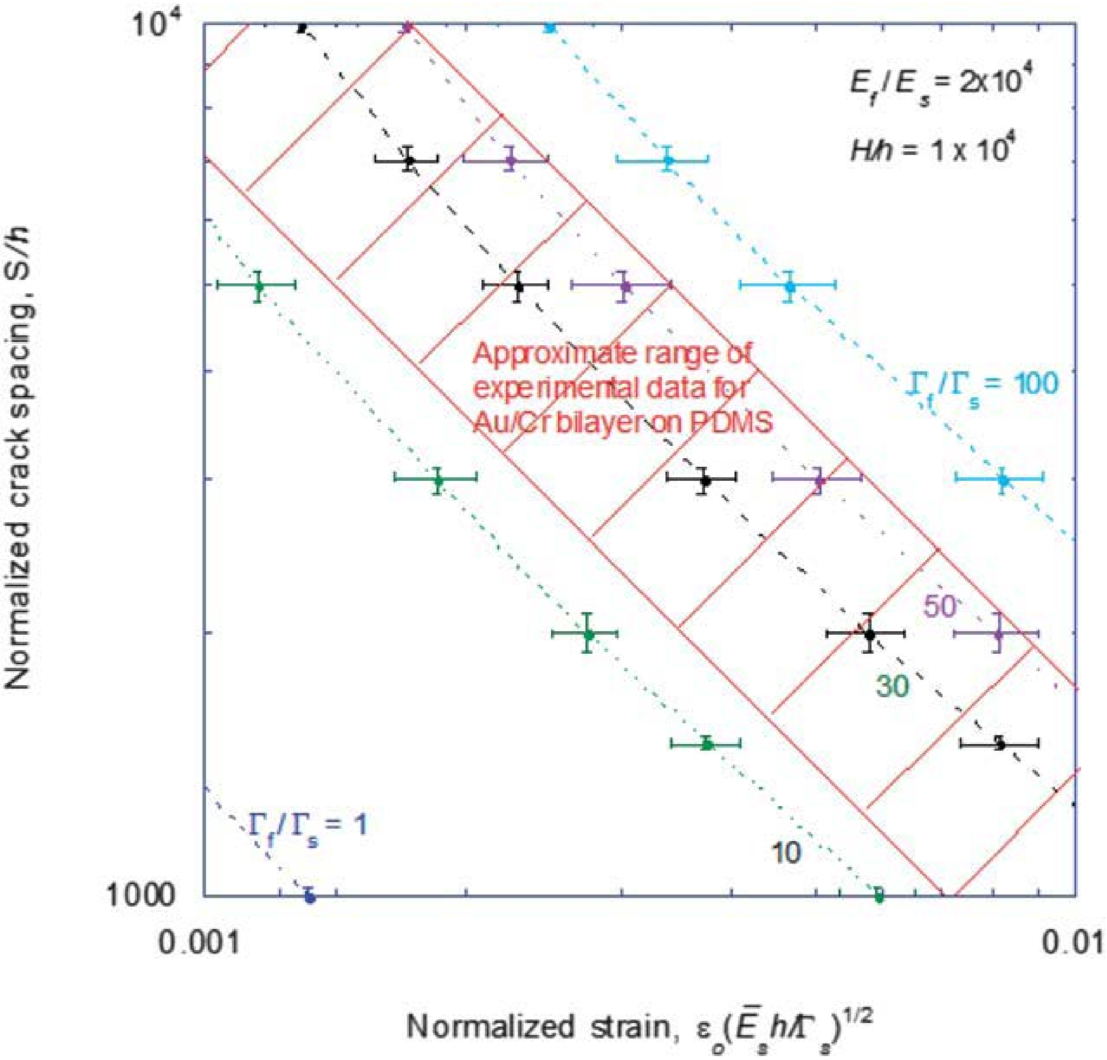

Figure 2.18. The Results of the LEFM Analysis Calculated for a bi-layer, with a modulus mismatch ratio between the film and substrate comparable to the value appropriate for Au on PDMS. Results for different values of the ratio of the film toughness to the substrate toughness, Γ_f/Γ_s, are presented. A comparison to the range of experimental results indicates that they match the LEFM model for a toughness ratio in the range of 10 to 50.

can be suppressed if the substrate is reasonably stiff [Li *et al*., 2005], the constraint may not be sufficient to suppress the localization if the substrate is an elastomer such as PDMS [Li and Suo, 2006]. The results presented in the present work are consistent with these results from the literature. Furthermore, we have shown that there may be an additional loss of constraint suppressing this localization mechanism associated with fracture of the substrate.

CONCLUSIONS

When metal films supported on a very compliant substrate such as PDMS rupture, they can induce fracture of the underlying substrate, with the cracks growing to significant depths below into the substrate. It has been shown in an accompanying paper that this reduces the critical strain at which crack propagation can occur [Thouless *et al*., 2011]. Despite the large nominal strains that can be imposed on the Au/PDMS system, the strain in the metal film may remain in the elastic regime. This is both because thin films tend to have relatively high yield strengths, and because cracking limits the strain transfer from the substrate to the film. While elastic deformation of the film and substrate implies that the techniques of fracture mechanics may be a valid means to analysis the fracture, the results reinforce the notion that the concept of toughness for such a thin metal layer is ambiguous. The observed strains required for fracture and the corresponding crack spacing seem to be consistent with toughness much higher than is appropriate for an elastic thin film. Rupture of the metal appears to be controlled not by the toughness of the film, but also by a critical stress or strain level in the film. Once the film has ruptured, then the cracks can propagate into the substrate. This view of the process is consistent with existing results in the literature that metal films fail by shear localization, and that while a stiff polymer may provide a constraint to suppress this mode of failure, a soft polymer such as PDMS does not provide a sufficient constraint. Fracture of the substrate further reduces any constraint on this failure mod

Chapter III

Cellular Level Damage

Combination of Fluid and Solid Mechanical Stresses Contribute to Cell Death and Detachment in a Microfluidic Alveolar Model

Nicholas J. Douville, Parsa Zamankhan, Yi-Chung Tung, Ran Li, Benjamin L. Vaughan, Cheng-Feng Tai, Joshua White, Paul J. Christensen, James B. Grotberg and Shuichi Takayma

ABSTRACT

Studies using this micro-system demonstrated significant morphological differences between alveolar epithelial cells (transformed human alveolar epithelial cell line, A549 and primary murine alveolar epithelial cells, AECs) exposed to combination of solid mechanical and surface-tension stresses (cyclic propagation of air–liquid interface and wall stretch) compared to cell populations exposed solely to cyclic stretch. We have also measured significant differences in both cell death and cell detachment rates in cell monolayers experiencing combination of stresses. This research describes new tools for studying the combined effects of fluid mechanical and solid mechanical stress on alveolar cells. It also highlights the role that surface tension forces may play in the development of clinical pathology, especially under conditions of surfactant dysfunction. The results support the need for further research and improved understanding on techniques to reduce and eliminate fluid stresses in clinical settings.

INTRODUCTION

We hypothesize that ventilator-induced lung injury (VILI) results from a combination of solid mechanical stresses, occurring as alveolar epithelial cells cyclically stretch and relax, and fluid mechanical (or surface tension) stresses, occurring as an air-liquid interface propagates over airway and alveolar epithelial cells. Previous mechanistic studies in vitro using cell-attached, deformable membranes have shown that cyclic stretch plays a role in the development of ARDS-like cell injury [Tschumperlin and Margulies, 1998; Egan, 1980; Fu *et al*., 1992; Tschumperlin *et al*., 2000; Vlahakis *et al*., 1999]. In addition, *in vitro* models of air-liquid interface flow over cells on rigid, non-stretching, substrates have demonstrated that the related stresses and stress gradients can injure underlying epithelial cells [Bilek *et al*., 2003; Yalcin *et al*., 2007; Huh *et al*., 2007; Tavana *et al*., 2009]. In our study, we present combined stretch and fluid/interface flows to examine their total and individual effects.

Difficulty recreating the complex shear stress and pressure fields experienced by alveolar cells has limited the understanding of the role of surface tension stresses. Advancements in microfluidics have only recently allowed fluid mechanical stresses to be systematically studied in models of airway injury. But these techniques have not been extended to in vitro modeling of an alveolus, which necessitates both solid and fluid mechanical stresses. Here, we describe a micro-engineered, cell-lined alveolus where physiological and pathophysiological levels of both fluid and solid mechanical stresses can be recreated over alveolar epithelial cells.

Mechanical ventilation is a critical therapy for patients with acute respiratory distress syndrome (ARDS). However, mechanical ventilation has also been shown to promote further cellular-level injury, leading to an exacerbation of ARDS-like symptoms, known as VILI. This cellular-level damage is hypothesized to result from a combination of cyclic and fluidic mechanical stresses generated by the collapse and re-opening of alveoli [Carney *et al*., 2005]. Solid mechanical stress occurs as epithelial cells are exposed to the cyclic stretching and relaxation of the alveolus during over-expansion and contraction. Fluid mechanical stresses are transmitted through the propagation of an air-liquid meniscus exposing underlying alveolar cells specifically to: shearing, shear gradients, pressure, and pressure gradients. Traditionally, research has focused on the cyclic stretch as the primary mechanism for VILI development. This focus on solid mechanical stress exists because: (i) solid mechanical stresses play a clinically and mechanistically important role in the development of VILI, but also, because (ii) models of stretching are much easier to engineer, whereas replicating physiological fluid mechanical stresses in vitro has been limited by a lack of appropriate tools and model systems.

While cyclic stretching plays a critical and well-established role in the development of VILI [Tschumperlin and Margulies, 1998; Egan, 1980; Fu *et al*., 1992; Tschumperlin *et al*., 2000; Vlahakis *et al*., 1999], the contribution of combined fluid mechanical stresses has not been systematically studied. The limitations of existing alveolar and airway models are described in Figure 3.1, highlighting the unmet need for an alveolar model capable of conveying combined fluid and solid stresses. Figure 3.1A shows previous alveolar stretching models which expose alveolar epithelial cells to cyclic stretch but lack the ability to apply fluid mechanical stresses[Tschumperlin and Margulies, 1998; Tschumperlin *et al*., 2000; Vlahakis *et al*., 1999]. Figure 3.1B shows in vitro airway models which recreate fluid mechanical stresses via a constant velocity air finger propagating into a liquid-filled chamber. This rigid substrate cannot be stretched limiting extension of these techniques to alveolar models [Bilek *et al*., 2003; Yalcin *et al*., 2007; Huh *et al*., 2007; Tavana *et al*., 2009]. Figure 3.1C explains how the cyclic propagation of a meniscus over a flexible, PDMS membrane recreates combined stresses within our microsystem. This novel technique provides a more physiologic model of the stresses occurring in a variety of surface-tension related-diseases including ARDS, neonatal respiratory distress syndrome (NRDS), and VILI.

Clinical therapies for surface-tension-related diseases that reduce or eliminate surface-tension effects without altering solid mechanical stretch have led to significant reduction in cell injury and improved clinical outcomes. Such clinical observations suggest that stretching alone is not sufficient to cause damage to

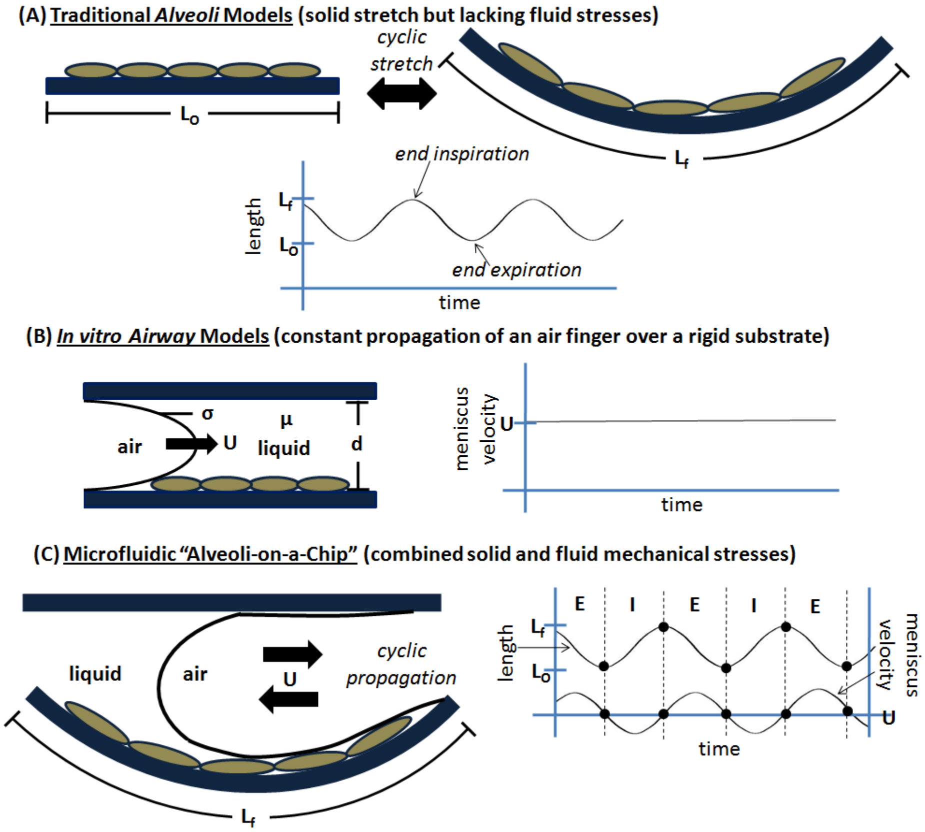

Figure 3.1 Limitations of existing models. (a) Previous alveolar models recreate stretch but lack the ability to model fluid stresses. (b) Previous airway models recreate fluid mechanical stresses via propagation of a constant velocity ‘‘air-finger’’ over a rigid substrate, limiting extension of these techniques to alveolar models. (c) Our microfluidic ‘‘alveoli-on a- chip’’ incorporates cyclic propagation of a meniscus over a flexible, PDMS membrane to recreate combined stresses providing a more physiologic recreation of the stresses occurring in a variety of surface tension diseases including ARDS, NRDS, and VILI.

the degree of air-blood barrier damage seen and that the high fluid mechanical stresses generated at the air-liquid interface play a critical role in pathology and mechanisms of the specific disease. Furthermore, large-scale clinical trials have shown surfactant replacement therapy (SRT) to be effective in the treatment of NRDS [Chu *et al*, 1967]; but, somewhat surprisingly, failed to show benefit in the treatment of ARDS [Anzueto *et al*., 1996].

While ARDS can be complicated by a variety of factors including neutrophil infiltration, pulmonary fibrosis, and increased barrier permeability (when compared to NRDS, which is usually limited to surfactant deficiency); the fact that both diseases share a similar mechanism rooted in dysfunctional surfactant and surface-tension based cellular injury makes SRT an attractive and logical treatment for ARDS [Nicholas *et al*., 1997]. The absence of a suitable *in vitro* model capable of recreating both solid and fluid stresses has made systematic study on factors potentially limiting the success of SRT in the treatment of ARDS, but not NRDS, difficult.

Another clinical therapy for reducing surface tension forces is liquid ventilation, a technique where the alveolus is filled with perfluorocarbon (PFC) liquid, effectively eliminating the air-liquid interface. Liquid ventilation studies have shown improved pulmonary gas exchange in ARDS models, further suggesting that fluid mechanical stresses play some role in the development of ARDS-pathology [Hirschl *et al*., 1996; Hirschl *et al*,. 1998]. Despite these clinical observations and substantial evidence of the role fluid mechanical stresses play in the development of airway injuries [Bilek *et al*., 2003; Yalcin *et al*., 2007; Huh *et al*., 2007; Tavana *et al*., 2009], no *in vitro* studies of fluid mechanical effects in an alveolar model have been conducted.

We designed a novel microfluidic system enabling the study of the unique combination of fluid and solid stresses found within alveoli. The system is significantly different from macroscopic cell stretching systems in terms of size and ability to create air-liquid interfaces over cells. Our system also differs from recently described two layered microchannel models [Chueh *et al*., 2007; Douville *et al*., 2010]. Key functional differences that enable our new microfluidic systems to model the alveoli include: (i) a ‘‘cell culture’’ chamber that mimics an alveolus (instead of micro-channels that mimic airways) allowing fluid stresses to be propagated, (ii) a curved, flexible PDMS membrane (instead of rigid polyester or rectangular flexible membrane [Huh *et al*., 2010]) for transmitting stretch to alveolar epithelial cells, (iii) automated actuation of respiration profile including: tidal volume, breathing frequency, and meniscus velocity. By creating the back and forth movement [Smith and Gaver, 2008] of an air-liquid meniscus as opposed to air-fingers or liquid plugs, as described in previous models [reviewed by Grotberg and Jensen, 2004] through our partially liquid-filled microfluidic alveoli, the impact of individual and combined stresses on cell viability and adherence was resolved. We observed morphological as well as quantifiable differences in cell death and detachment in cell alveolar epithelial cell populations exposed to the combined solid and fluid mechanical stresses compared to cells exposed solely to solid mechanical stresses, suggesting that fluid mechanical stresses play a crucial role in cell injury and pathology seen in ventilator-induced lung injury.

EXPERIMENTAL

‘‘Alveoli-on-a-chip’’ microfluidic device

The device consists of two microchannels separated by a flexible, PDMS membrane (Figure 2.2). The three component layers - (i)‘‘alveolar chamber’’ for cell culture, (ii) flexible PDMS membrane for transmitting stretch, and (iii) ‘‘actuation channel’’ for controlling stretch and meniscus propagation - are each fabricated independently. Meniscus propagation rates and membrane stretch characteristics were selected to match linear strain values(see Supporting Information, Figure 3.13) and surface tension forces (determined by Capillary number and Reynolds number, see Supporting Information, Figure 3.12) experienced within an edematous alveolus [Weibel *et al*., 1963; Johnson *et al*., 2003; Hinds *et al*., 1999]. Using the actuation settings standardized for our experimental conditions (optimized to 35-40% cyclic strain and 3.44 mm s^{-1} meniscus velocity), we were able to match the capillary number estimated to occur within an edematous (fluid-filled) alveolar sac (generation n=23) and the Reynolds number estimated to occur within a respiratory bronchiole (generation n=17), the location in the respiratory tree where architecture begins to transition from terminal airway to alveolar structures. These estimations of *Ca* and *Re* indicate that our system is capable of recreating the types of stretching and surface tension forces experienced by alveoli during mechanical ventilation.

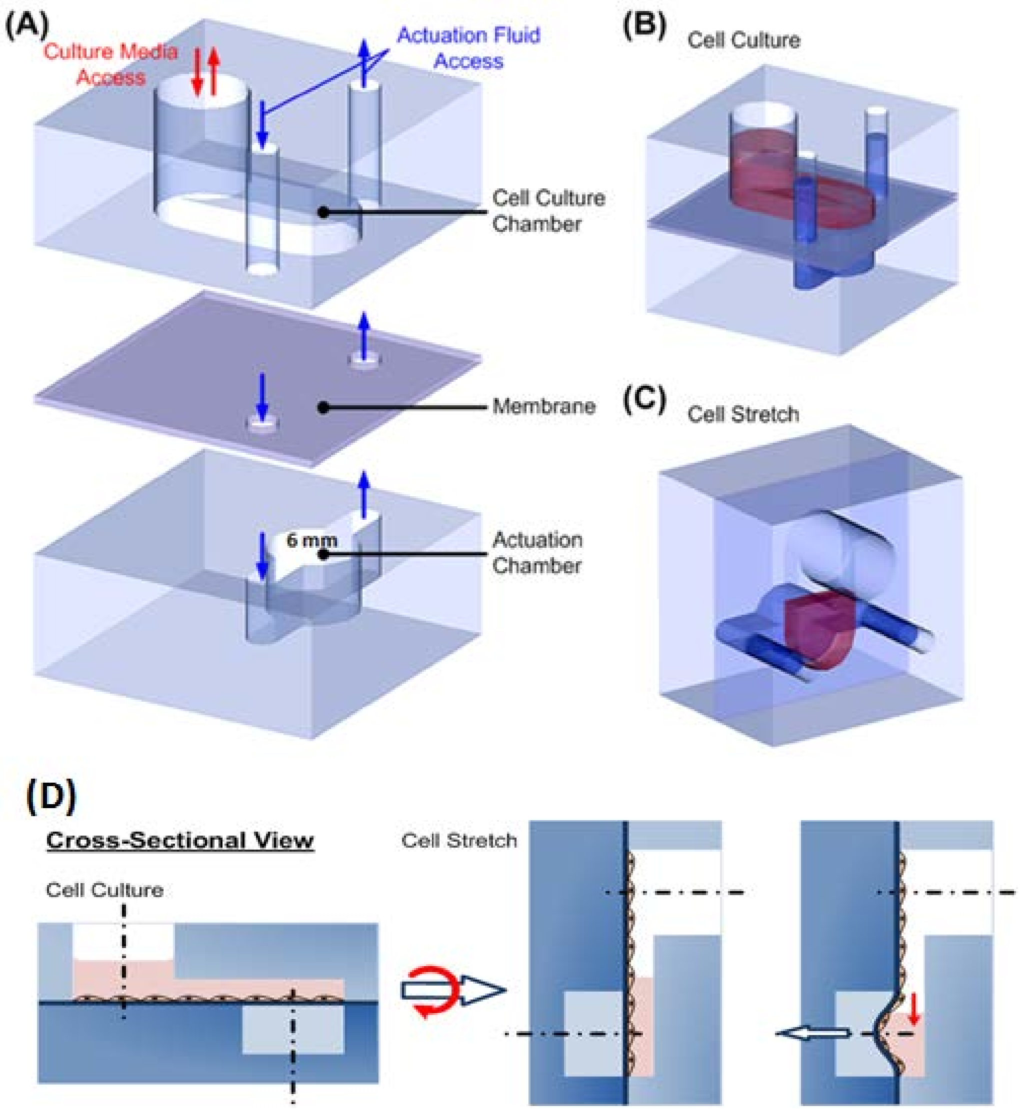

Figure 3.2. Microfluidic ‘‘Alveoli-on-a-Chip.’’ (a) Three components are assembled to form a two-layered microfluidic model. An ‘‘alveolar chamber’’ enables culture of alveolar epithelial cells (A549). A thin PDMS membrane separates the alveolar chamber from the actuation channel allowing deformation of the cell culture chamber. The ‘‘actuation channel’’ can be interfaced with a programmable syringe pump to control the degree of stretch (amplitude) as well as the velocity of the meniscus propagation (velocity). (b) The ‘‘alveolar chamber’’ can be filled with F-12K growth media and positioned in the horizontal orientation to allow for optimal cell adherence and growth. (c) During experiments, the ‘‘alveolar chamber’’ can be partially filled with fluid and positioned in the vertical configuration to establish a meniscus at the interface of fluid and air. (d) A cross-sectional view of the microfluidic device shows the horizontal orientation for cell culture and the vertical configuration for experimentation. By withdrawing fluid from the ‘‘actuation channel’’, the membrane can be forced to deform and relax stretching cells and propagating the meniscus over a specified cell region.

Although fluid stresses are replicated with this microfluidic device, it is important to note that the size-scale of the system (6 mm) does not correspond to the dimensions of typical alveoli (~200 μm).

The flexible PDMS membrane was fabricated by spinning PDMS pre-polymer (10 base: 1 curing agent, by weight) onto a silanized glass slide at 300 rpm for 90 seconds. Following spinning, the membrane was allowed to cure for 4 hours at 60 °C forming a membrane with a thickness of ~100 μm (although 100 μm is the thinnest membrane we can fabricate and still easily handle, it is important to note that this scale is still two orders of magnitude thicker than the physiologic alveolar-blood barrier). Access holes to the ‘‘actuation channel’’ were punched into the surrounding substrate of the ‘‘alveolar chamber’’ (as depicted in Figure 3.2A) to align with the inlet and outlet of the ‘‘actuation channel’’.

The ‘‘alveolar chamber’’ was irreversibly bonded to the PDMS membrane, still secured to the silanized glass slide, using a handheld corona treater for approximately 30 seconds on both substrate and membrane, as previously described [Haubert *et al*., 2006]. The membrane was cut from the slide around the area of the substrate and removed. The un-treated bottom of the membrane and substrate surrounding the ‘‘actuation channel’’ were then corona treated and bonded using the previously described technique [Haubert *et al*., 2006].

18 gauge blunt syringe tips were secured within the inlet and outlet access ports allowing the entire device to easily interface with a standard syringe pump.

Cell culture-A549

Human alveolar basal epithelial (A549; CCL-185, ATCC) cells were cultured in Kaighn’s Modification of Ham’s F-12 Medium (F-12K Medium; 30-2004, ATCC) containing 10% v/v fetal bovine serum (FBS; 10 082; Gibco), 100 U mL^{-1} penicillin, and 100 U mL^{-1} streptomycin. The microfluidic chip was exposed to plasma oxygen for 5 min to make hydrophilic. Prior to cell seeding, fibronectin solution (Invitrogen) at a concentration of 10 µg mL^{-1} in phosphate buffered saline (PBS) was injected into the ‘‘alveolar chamber’’ to promote cell adhesion. The ‘‘actuation channel’’ was preloaded with deionized water immediately following exposure to plasma oxygen. Fibronectin solution was kept in the alveolar chamber for 30 min at 25°C under ultraviolet light to sterilize the system. After UV sterilization, sterile techniques and conditions were maintained. Following 30 min of fibronectin coating, the channel was completely washed with growth media to remove the non-adsorbed fibronectin and filled with F-12K growth media until seeding.

A549 cells nearing confluence in a flask were trypsinized, centrifuged, and resuspended in F12-K growth media (to a concentration of ~200 cells per µL). The growth media of the upper chamber were completely exchanged for 200 µL of cell suspension. The device was temporarily elevated to the vertical position during cell seeding to allow uniform distribution of cells along the entire surface of the PDMS culture membrane, before being returned to the horizontal orientation for the duration of cell adhesion and cell growth. Cells were allowed to adhere in the static, horizontal orientation for 12 hours. Fresh growth media (200 µL) were exchanged 12 hours after the initial seeding and every subsequent 24 hours for the duration of the experiment. Cells were allowed to grow for 6 days before beginning experiments (see Supporting Information, Figure 3.9 for images of cell growth).

Cell culture-primary, murine AECs

Specific pathogen-free male C57BL6 mice were purchased from Jackson Laboratories. Mice were kept in isolated cages and received water and food *ad libitum*. The animal care committee at the Ann Arbor Veterans Administration Medical Center approved all protocols. AECs were isolated from the mice as previously described [Christensen *et al*., 2004]. Following pentobarbital anesthesia and heparinization, the mouse was exsanguinated and the pulmonary vascular perfused free of blood. The trachea was cannulated and the lungs filled with 1-2 ml of Dispase (Worthington). Subsequently, 0.45 ml of low melting point agarose was infused via the trachea and the lungs were placed in iced PBS for 2 min to harden the agarose. The lungs were incubated in 2 ml of Dispase and incubated for 45 min at 24 ° C. The lung tissue was teased from the airways and minced in DMEM with 0.01% DNase. The lung mince was gently swirled for 10 min, and passed successively through nylon mesh filters. The cells were incubated with biotinylated anti-CD32 and anti-CD45 followed by streptavidin-coated magnetic particles, before magnetic removal of leukocytes. Mesenchymal cells were removed by overnight adherence in a Petri dish.

Fibronectin solution was kept in the alveolar chamber for 2 h at 25 ° C under ultraviolet light to sterilize the system. After UV sterilization, sterile techniques and conditions were maintained. Cells were plated at a density of 2 x 10^5 cells per device (~2000 cells per μL) in DMEM plus 10% FBS, 1% penicillin/streptomycin. Fresh growth media (200 μL) were exchanged every 24 hours for the duration of the experiment. Cells were maintained in culture for 4 days before beginning experiments.

Actuation programming

A variety of experimental parameters were controlled using a programmable syringe pump including: amplitude (tidal volume), frequency (respiratory rate), and the total number of cycles (duration of the experiment). Experimental parameters were selected to mimic typical ventilation settings (12-20 respiratory cycles per minute) [Esteban *et al*., 2000], cyclic strain found in pathologic ventilation [Chapman *et al*., 2005], and meniscus rates linked to cell death [Huh *et al*., 2007; Tavana *et al*., 2009]. Because the syringe pump (Chemyx, Fusion) had a lag as the pump transitioned from withdrawal to infusion; the meniscus moved at a faster velocity than would be expected if the meniscus moved continuously with no lag period. The position of the meniscus and velocity of the meniscus at our experimental condition are depicted in the Supporting

Information, Figure 3.10 showing an ‘‘off’’ period of 1.2 seconds at the top and bottom of each cycle. We experimentally optimized dimensions of our system and selected a pumping rate yielding a respiratory rate of 12.5 cycles per minute, within the range of frequently used ventilation settings. We used slow motion video of the propagating meniscus to precisely determine the velocity of the meniscus (3.44mm s^{-1}) and distance (4.13 mm) at all time points (meniscus position and velocity are shown in the Supporting Information, Figure 3.10).

Modeling of fluid mechanical stresses

Figure 3.3A shows an air finger advancing into a liquid-filled tube or channel, with a forward-facing meniscus indicated by red-filled squares. This type of system has been used by Bilek *et al*. to study the fluid mechanics and cell injury of airway reopening. They found that cell damage increased with decreasing propagation velocity and that surfactant enrichment protected from cellular injury [Bilek *et al*., 2003]. Yalcin *et al*. also studied the impact of a propagating air finger on epithelial monolayers [Yalcin *et al*., 2007]. They showed that decreasing channel height and decreasing velocity both increased the percentage of cell death, predicting that distal lung regions are more susceptible to lung injury. Figure 3.3B shows an air finger receding from a liquid filled tube or channel, with a backward-facing meniscus indicated by blue-filled circles. We are unaware of any experiments examining cell injury for this flow. However, our current study involves oscillation of the air-liquid interface so that both advancing and receding air fingers are realized. Figure 3.3C shows a liquid-plug propagating into a liquid-lined, air-filled tube. It has both a forward-facing meniscus (red-filled squares) and a backward-facing meniscus (blue-filled circles). This system was used by Huh *et al*. to study liquid-plug propagation over human airway epithelial cells [Huh *et al*., 2007].

From their experiments and computations, they demonstrated that the backward-facing meniscus imposes significantly higher stresses on the cells than a forward-facing one. They also showed that rupture of the plug, which creates a

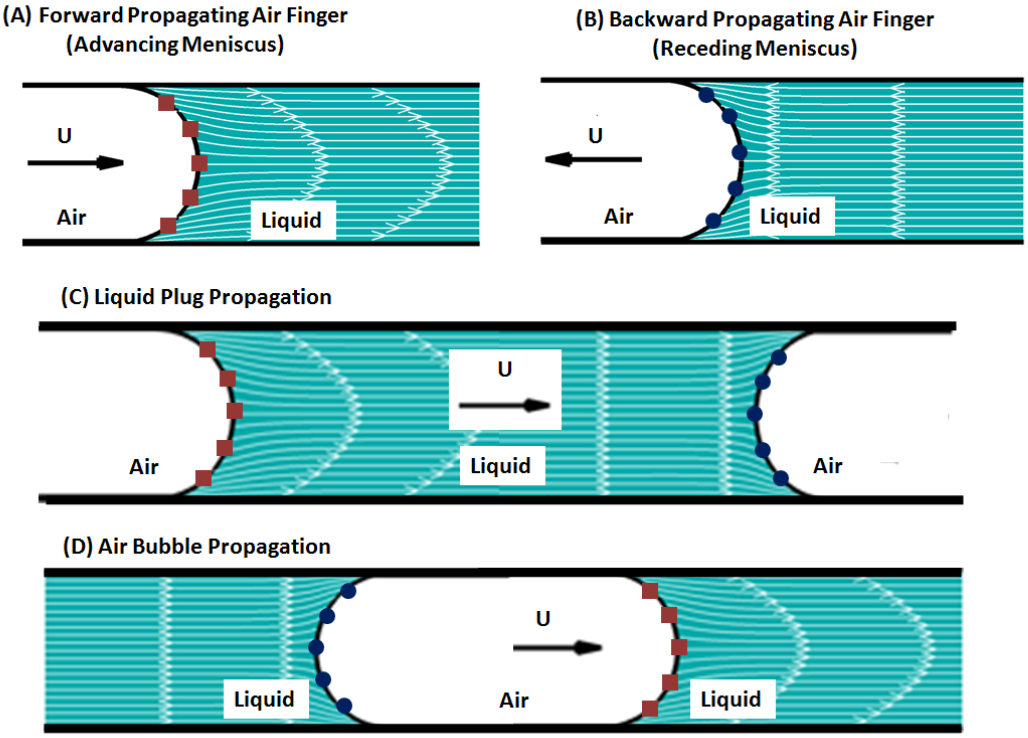

Figure 3.3. Schematic representation of fluid stress models. (a) The advancing (inhalation) stroke of our system can be modeled by the forward-facing meniscus (red squares) of a semi-infinite bubble propagating within a fluid filled channel. (b) The receding (exhalation) stroke of our system can be modeled by the backward-facing meniscus (blue circles) of a semi-infinite bubble propagating within a fluid filled channel. (c) Liquid plugs contain both forward- and backward-facing menisci, however, the backward-facing meniscus (blue circles) is responsible for the highest degree stress profile and majority of cell death. (d) Finite bubble propagating within a fluid filled channel contains both forward facing meniscus (red squares) and backward-facing meniscus (blue circles).

crackle sound in the lung, is the most damaging event. Figure 3.3D shows a finite-bubble propagating in a liquid-filled tube or channel. It also has both a backward-facing meniscus (blue-filled circles) and a forward-facing meniscus (red-filled squares). Computational fluid dynamics of this bubble are used in the present paper. Shear stress, shear stress gradients, pressure, and pressure gradients on the wall are calculated for the forward-facing and backward-facing menisci of the bubble shown in Figure 3.3D and applied to our system, which oscillates between the condition depicted in Figure 3.3A and that depicted in Figure 3.3B.

Therefore, for better understanding of the fluid related phenomena in the oscillatory motion, the steady displacement of a finite size bubble with different propagation speed, *U* (0.5, 1, and 2 cm s^{-1}), was simulated numerically (the details of the numerical procedure are described by Zamankhan *et al*. for a 2D channel with a width of 2 mm [Zamankhan *et al*., 2011]. The density, viscosity and the surface tension of the filling liquid were assumed to be 1 g cm^{-3}, 1 cp, and 70 dyne per cm, respectively. For these inputs, Reynolds number is less than 20, even for the highest propagation speed. Therefore the effects of inertia are neglected in the computations. The effect of the propagation speed on the meniscus profile, the distributions of wall shear stress and its gradient, and pressure gradient are presented below. In all of the cases the location of the tip is at y = 0.

Figure 3.4B shows the half profile of the meniscus for both phases of the motion when the propagation speed is 1 cm s^{-1}. It is seen that in both phases, the meniscus is constituted from a transient and a flat part. During the advancing motion, the transient and the flat regions merge together smoothly, however, in the receding direction, the meniscus is wavy in the region where the two regions meet. As detailed below, this wavy region has significant effects on the distribution of the wall shear stress and the pressure gradient. It is also seen from Figure 3.4B that the flat part the meniscus is separated from the wall through a liquid film. These trends are held for the other propagation speeds as well.

In the absence of the fluid inertia and for a planar channel, the dimensionless thickness of the liquid film, scaled by the half width of the channel, was deduced as 1.3375 $Ca^{2/3}$ for $Ca \rightarrow 0$ by Reinelt and Saffman [Reinelt and Saffman, 1985] from the analytical analysis of Bretherton [Bretherton, 1961], where $Ca = \mu U/\sigma$ is the capillary number. In the definition of capillary number μ represents fluid viscosity and σ represents surface tension. Figure 3.4C shows the computed

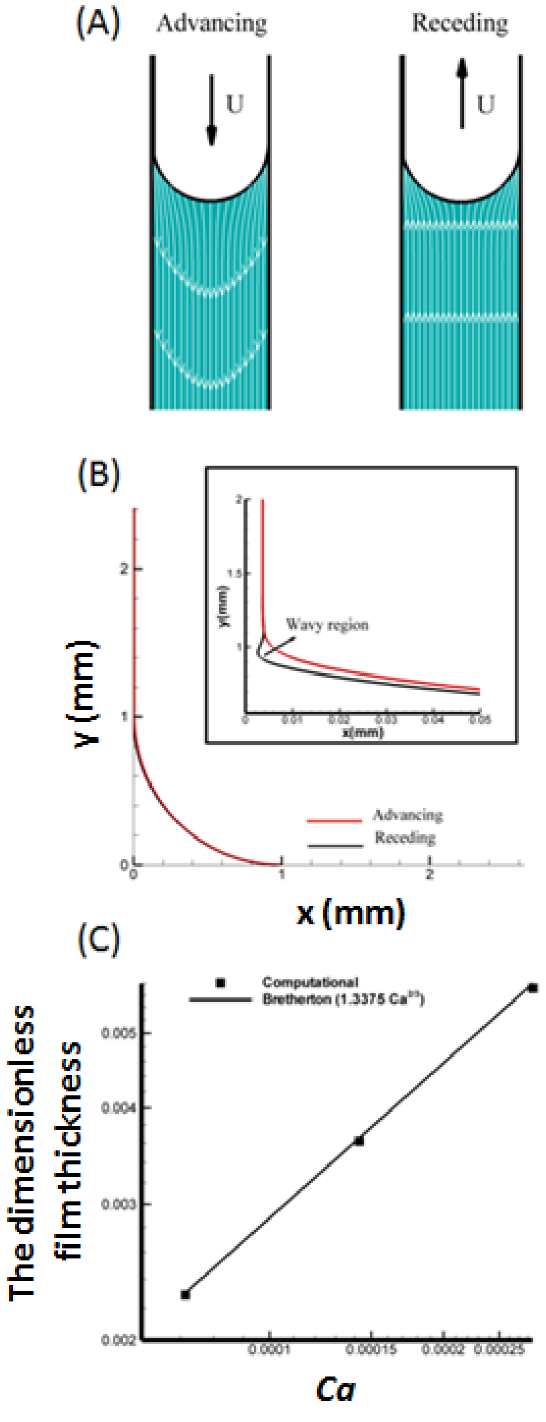

Figure 3.4. Modeling fluid mechanical stresses. (a) Streamlines around the advancing and receding phase meniscus for a propagation speed of 1 cm s^{-1}. (b) Meniscus profile during the advancing and the receding motions when the propagation speed is 1 cm s^{-1}. The inset magnifies the region where the transient and the flat regions meet. The wall is along x = 0. (c)The computed film Thickness for different propagation speed along with Bretherton analytical relation.

dimensionless thickness for the three propogation speeds in terms of *Ca* along with Bretherton analytical relation [Bretherton, 1961]. It is seen that the agreement is excellent. Since the fluid properties and the channel dimensions remain unchanged, *Ca* and the (dimensionless and dimensional) film thickness both increase with the propagation speed as it is seen from Figure 3.4C.

Figure 3.5 shows the distribution of the shear stress, shear stress gradient, and the pressure gradient along the wall for both phases of the motion when the propagation speed is 1 cm s^{-1}. It is seen from the figures that during both phases, the maximum of the magnitude of all the three quantities is located beneath the transient region of the meniscus. This is consistent with the experimental observations, showing a concentration of cell injuries in the same area. It is also seen from the figures that the maximum of the magnitude of the three quantities is significantly larger during the receding motion compared to the advancing one. This is also consistent with the experimental results, showing more damages during the receding motion compared to the advancing one. The wavy distribution for the three quantities during the receding motion is due to the wavy profile of the meniscus in the transient region (shown in the inset of Figure 3.4B) during this phase of the motion.

Figure 3.6 shows the shear stress, the shear stress gradient, and pressure gradient along the wall during the receding phase (directionality where the magnitude of all three quantities is maximum) at different propagation speeds. It is seen that the maximum of the magnitude of the wall shear stress and the pressure gradient increases and decreases with propagation speed, respectively, while that does not vary for the shear stress gradient with the propagation speed. From Bretherton analytical analysis [Bretherton, 1961] it can be deduced that for Ca → 0 the maxima of magnitude of the wall shear stress and the pressure gradient are proportional to $U^{1/3}$ and $U^{-1/3}$, respectively, while that remains unchanged with *U* for the wall shear stress gradient. By examining the presented

(A) Shear Stress

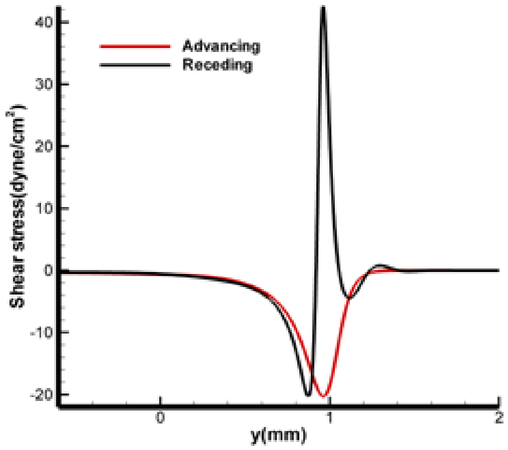

(B) Shear Stress Gradient

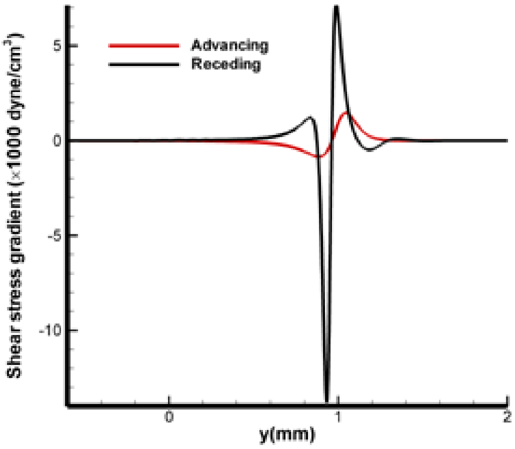

(C) Pressure Gradient

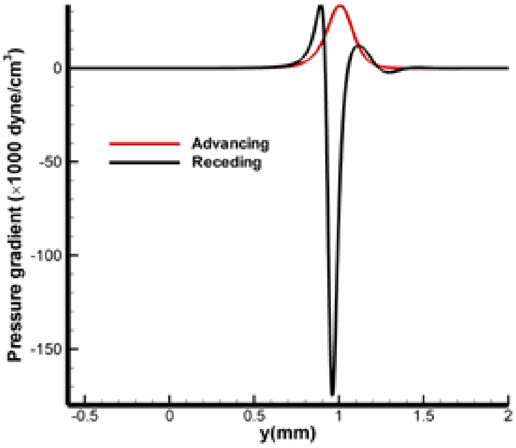

Figure 3.5. Effect of directionality on fluid mechanical stresses (at 1cm*s^{-1}). (a) Wall shear stress for advancing and receding motions. (b) Gradient of wall shear stress for advancing and receding motions. (c) Wall pressure gradient for advancing and receding motions.

.

(A) Shear Stress

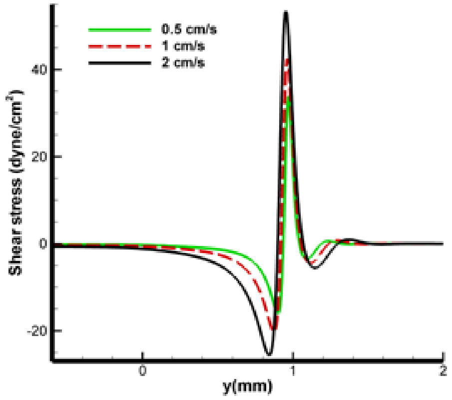

(B) Shear Stress Gradient

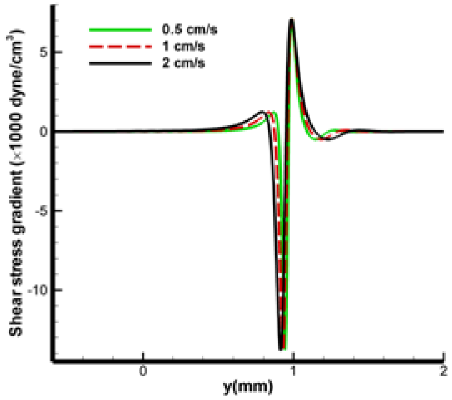

(C) Pressure Gradient

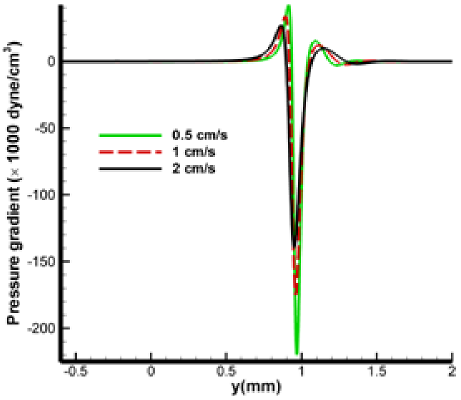

Figure 3.6. Effect of meniscus velocity on fluid mechanical stresses (in the receding direction). (a) Wall shear stress for meniscus velocity = 0.5 cm s^{-1}; 1.0 cm s^{-1}; and 2.0 cm s^{-1}. (b) Gradient of wall shear stress for meniscus velocity = 0.5 cm s^{-1}; 1.0 cm s^{-1}; and 2.0 cm s^{-1}. (c) Wall pressure gradient for meniscus velocity = 0.5 cm s^{-1}; 1.0 cm s^{-1}; and 2.0 cm s^{-1}.

results in Figure 3.5 and 3.6, it is observed that the computed maxima match with Bretherton analysis quantitatively.

Mechanism of protective effect of surfactant enrichment

Damage to the underlying alveolar epithelial cells is a function of the stresses and strains that they experience when an air-liquid interface, in the form of an advancing meniscus (forward propagating air finger), a receding meniscus (backward propagating air finger), or a liquid plug (both types of menisci), propagates over them. The jump in pressure across the air-liquid interface (meniscus) leads to large stress differences over a short distance, a mechanical perturbation which tears at cell membranes since different parts of the cell see very different stress levels. One can think of the Law of Laplace locally along the interface, so that the pressure jump is proportional to the local interfacial curvature and surface tension: $\Delta p \approx k\, \sigma$ where k is the curvature and σ is the surface tension. A way to reduce Δp is to lower the surface tension σ. This decreases the pressure jump across the meniscus so that all stresses, and particularly their spatial gradients, are reduced. Introducing surfactants into the system achieves this surface tension reduction. Likewise, replacing the gas-liquid interface with a liquid-liquid interface, as in liquid ventilation using perfluorocarbons, reduces the surface tension. We have repeated the previous simulation of finite bubble propagation at two reduced surface tension conditions (35.0 and 17.5 dyne per cm compared to the original model at a surface tension of 70.0 dyne per cm). These values were selected to correspond to the range of surface tension resulting from surfactant-enrichment and surfactant-replacement therapy [Hamer, 1995]. Supporting Information, Figure 3.16 compares shear stress, shear stress gradient, and pressure gradient for the receding motion with a propagation speed of 0.5 cm s^{-1} in our original DMEM model ($\sigma = 70$ dyne per cm) with two reduced surface tension conditions ($\sigma = 35.0$ dyne per cm and $\sigma = 17.5$ dyne per cm). From Bretherton analysis, it can be deduced that for limit of $Ca \rightarrow 0$, the maxima of magnitude of shear stress, shear stress gradient, and pressure gradient are proportional to $\sigma^{2/3}$, σ, and $\sigma^{4/3}$, respectively. The computational results are in quantitative agreement. Therefore, all of these fluid mechanical stresses and gradients are decreased in the surfactant-enriched (decreased surface tension) experimental condition.

Furthermore, liquid filling of the alveolar cross-section cannot occur without an initial loading event. When the naturally occurring liquid lining becomes too thick, it experiences an instability due to surface tension forces which leads to closure of the airway or alveolar region by forming a plug or finger [Halpern and Grotberg, 1992; Halpern and Grotberg, 1993]. During inspiration this liquid is reapplied to the wall and the region reopens. However, the plug can reform at the end of expiration and the process repeats itself. We have shown that the creation of the finger or plug subjects the tissue wall (i.e. epithelium) to similarly high values of stresses and stress gradients as finger or plug propagation [Bian *et al*., 2010; Tai *et al*., 2010]. Reducing the surface tension with surfactants, for example, stabilizes the system and allows thicker films to exist without forming a plug [Halpern and Grotberg, 1993]. We have also modeled plug formation for the surfactant-enriched and non-enriched experimental conditions. In this airway closure model, the following dimensional parameters were adopted: $a^* = 0.065$ cm, $L^* = 0.44$ cm, $\rho^* = 1.0$ g cm^{-3}, $\mu^* = 0.13$ Poise, and $\sigma^* = 20$ and 70 dyne per cm. Where a^* and L^* are the radius and length of the airway, ρ^* is the density of liquid, μ^* is the viscosity, and σ^* is the surface tension. $\sigma^* = 20$ dyne per cm can represent the surfactant-enriched experimental case and 70 dyne per cm the standard, non-enriched DMEM case. The initial film thickness is 23% of the radius of the airway.

Supporting Information, Figure 3.17 shows streamline plots at different instants for plug formation in the surfactant-enriched case ($\sigma^* = 20$ dyne per cm). These plots show that liquid is pushed from two ends of the airway to the bulge area around $x \approx 0$ and the deformation of the liquid film is very tiny at the initial stage. Supporting Information, Figure 3.18 plots R_{min} (distance from tip of bulge to centreline of the airway) *versus* time for surfactant-enriched and non-enriched cases. This figure shows that the interface is almost stationary during most of the closure and that the closure event happens rapidly in a very short period of time. Furthermore, the closure in the surfactant-enriched/low surface tension case (σ^* = 20 dyne per cm) takes longer than the closure in the standard surface tension case (s^* = 70 dyne per cm). Supporting Information, Figure 3.19 shows wall stresses and their gradients for the surfactant-enriched and non-enriched experimental conditions. The magnitude of both shear and normal stresses and their gradients are smaller in the surfactant-enriched case compared to the standard case. The growth rate in the surfactant-enriched case is much slower than the non-enriched case (Supporting Information, Figure 3.18) and lower stresses and gradients are induced along the wall of the airway (Supporting Information, Figure 3.19) . Overall, we can see that the surfactant delays airway closure and decreases the wall stresses and the gradients, which should further protect the cells.

Modeling of solid mechanical stresses

In order to estimate the surface strain generated on the membrane, we constructed a three-dimensional (3-D) finite element analysis (FEA) model using the commercial software ANSYS (ANSYS Inc.). A circular plate meshed with 3-D 10-node tetrahedral elements was exploited for the model. Fixed boundary conditions were applied at the periphery of the circular plate, and a constant pressure was applied at the one side of the plate. To accurately simulate the plate deformation, the simulation was conducted with nonlinear large deformation option. The constructed model and the simulation results are shown in the Supporting Information, Figure 3.11. The results show the von Mises strain at the center of the membrane under various membrane deformations. As can be seen in the Supporting Information, Figure 3.11, while applying pressure to cause the membrane deformed more than 1.6 mm, it generates approximately 35% strain on the membrane surface, on which the cells attached. We can reach the stress level more than 30% in our device to simulate the real stress in real alveolus *in vivo*, which can range from approximately 6.5% for healthy lung in physiologic respiration to as high as 45.4% for an atelectatic lung during mechanical ventilation (assumptions and calculations shown in the Supporting Information, Figure 3.13) [Fretschner *et al*., 1993]. Exploiting the simulation results, the surface strain profile can be estimated by measuring the maximum deformation of the plate in the experiments.

Algorithm for quantification of cell detachment

To quantify the amount of cell death and detachment, we stained the cells using the Live/Dead viability/cytotoxicity assay and imaged the cell membrane with fluorescent microscopy. To the fluorescent micrographs, we first applied the Sobel method for edge detection to generate a binary image where the edges divide the image into regions of live/dead cells compared to empty space. The resulting binary image is then dilated to improve the edge connections and any holes are filled. The percent of live or dead cells is estimated as the fraction of white pixels divided by the total number of pixels in the image. We ran an ANOVA test and both Tukey's Studentized Range (HSD) and Bonferroni t-test *post hoc* tests on data obtained from the four experimental conditions using the commercially available statistical analysis software, SAS/STAT (SAS Institute, Inc., North Carolina, USA).

RESULTS AND DISCUSSION

Alveoli-on-a-chip microfluidic model

We have designed a novel microfluidic system to recreate the unique stress conditions occurring over a cellular air-blood barrier of a human alveolus. By varying the degree of fluid loading within our alveoli-on-a-chip, we can mimic a variety of physiologic (air-filled) and pathophysiologic (edematous*) in vivo* conditions. Our system utilizes a flexible, PDMS membrane separating an ''alveolar chamber'' from an ''actuation channel'' to create both cyclic stretch and fluid mechanical stresses. The degree of chamber filling also enables the user to isolate individual stresses. The ''alveolar chamber'' provides a robust microenvironment for cell culture, while the ''actuation channel'' easily interfaces with a commercially available, programmable syringe pump to control the breathing profile. Solid stresses have been studied in alveolar models using stretchable membranes; however, the open, reservoir structure makes establishing fluid stresses difficult. Fluid mechanical stresses have been studied in airway models by the progression of liquid plugs or air fingers; however, the rigid membrane structure limits their extension to alveolar models which require stretching to mimic the large volume changes of the alveoli. We report the first alveolar model capable of replicating both fluid and solid mechanical stresses for the cell culture of epithelial cells.

We have also modeled fluid mechanical stresses in our microfluidic alveolar model. This analysis showed that for both directions of meniscus motion, the maxima for the magnitude of wall shear stress, shear stress gradient, and the pressure gradient occur beneath the transient region of the meniscus and that the maxima for the magnitude of wall shear stress, shear stress gradient, and pressure gradient are significantly larger during the receding motion compared to the advancing one. The maxima of the magnitude of the wall shear stress and the pressure gradient increase and decrease with propagation speed, respectively. However that remains unchanged with the propagation speed for the shear stress gradient. The numerical results are in a good quantitative agreement with Bretherton analysis, valid for $Ca \rightarrow 0$ and no fluid inertia effect.

Morphological response to fluid mechanical stress

By varying the amount of fluid loaded into the ‘‘alveolar chamber’’, we control the type of mechanical stresses experienced by the cells on the flexible PDMS membrane. We tested cells’ responses to increasing levels of linear strain under the following conditions: (i) fluid-filled, (ii) air-filled, and (iii) air-liquid meniscus. Completely filling the chamber to a volume of 200 μL establishes an environment where cells on the culture membrane experience cyclic stretch but minimal fluid mechanical stress. Complete removal of fluid from the chamber exposes cells solely to cyclic stretch eliminating all fluid mechanical stresses. Partial filling of the channel with a volume of 40 μL fluid exposes cells to combination of solid and fluid mechanical stresses as the meniscus propagates over top of the deforming cell culture membrane. All experiments were conducted for a total of 60 cycles of stretch (288 seconds). In initial experiments, we tested six different strain levels, beginning at approximately 15% linear strain and continuing to the maximum strain tested (approximately 50% linear strain) on A549 cell populations. A549 cells were allowed to grow for 6 days before beginning experiments. After 6 days of culture, cells demonstrated near complete confluence (quantified as 97.2% with a standard deviation of 2.2% using our MatLAB algorithm). Since A549 cells do not exhibit contact inhibition, overconfluence and cell stacking was a concern, however, the characteristic detachment profile (folding in the ‘‘receding’’ direction of the meniscus) of still adherent cell ‘‘sheets’’ was most prominent at very high cellular densities and could not be clearly visualized at lower cell densities.

We also repeated these experiments with primary, murine alveolar epithelial cells cultured for 4 days (quantified as 73.3% confluence with a standard deviation of 3.7% using our MatLAB algorithm), to confirm these findings in a primary cell population as well as a more physiologically relevant cellular density. In both cell populations, clear morphological differences were observed between cell populations exposed solely to the solid mechanical stress (in either the completely air-filled or completely liquid-filled case) versus cell populations experiencing combined stresses in the partially filled case. Finite element analysis was used to determine maximum von Mises strain values occurring at the centre of the circular membrane. Strain values cited are averages assuming uniform, linear strain across the entire membrane surface area, as calculated from volumetric deformation. After 60 cycles of stretch, a large degree of cell detachment can be seen in cells exposed to combination of stresses, whereas the cell monolayer is more intact in populations exposed solely to solid mechanical stress. These morphological changes can be visualized in the 10x micrographs depicted in the Supporting Information, Figure 3.14 and Figure 3.15.

Additionally, the adherent cells have a decreased projected surface area indicative of a partial loss of adherence. In the A549 experiments, periodic pockets of cell detachment can be seen in the air-filled condition (Supporting Information, Figure 3.14A) and the liquid-filled (Supporting Information, Figure 3.14B) condition indicating that cyclic stretch impacts on cell morphology; however, clear qualitative differences between these two experimental conditions could not be assessed. In the AEC experiments, substantial cell detachment can be seen (Supporting Information, Figure 3.15A/B) in the presence of cyclic stretch, however, a greater degree of cell detachment occurs when a meniscus propagates in conjunction with the stretch.

To better visualize macro-scale changes in cell detachment and death, we stained A549 cells using Live/Dead viability/cytotoxicity assay (Invitrogen) and imaged at 2x magnification (Figure 3.7). These low-magnification, fluorescent micrographs provide insight on global behaviour of cells within the microdevice. The data show substantial cell detachment after as few as 10 cycles of combination of stresses and a significant cell death beginning as early as 20 cycles of combination of stresses. Cells exposed solely to solid mechanical stresses in either the air-filled or fluid-filled case did not demonstrate significant cell detachment or cell death at any of the test conditions. Additionally, cell detachment in the combined stress condition, appeared in the receding direction of the meniscus (see Figure 3.7), consistent with our model of meniscus propagation which predicted greatest shear stress (absolute value), shear stress gradient, and pressure gradient in the receding (exhalation) direction of meniscus movement.

Quantitative differences in cell death and detachment result from fluid mechanical stresses

For quantitative analysis on cell detachment, we selected: frequency of 12.5 cycles per minute, meniscus propagation of 3.44 mm s^{-1}, membrane deformation of ~38% linear strain. Using a Matlab algorithm, we analyzed the percentage of

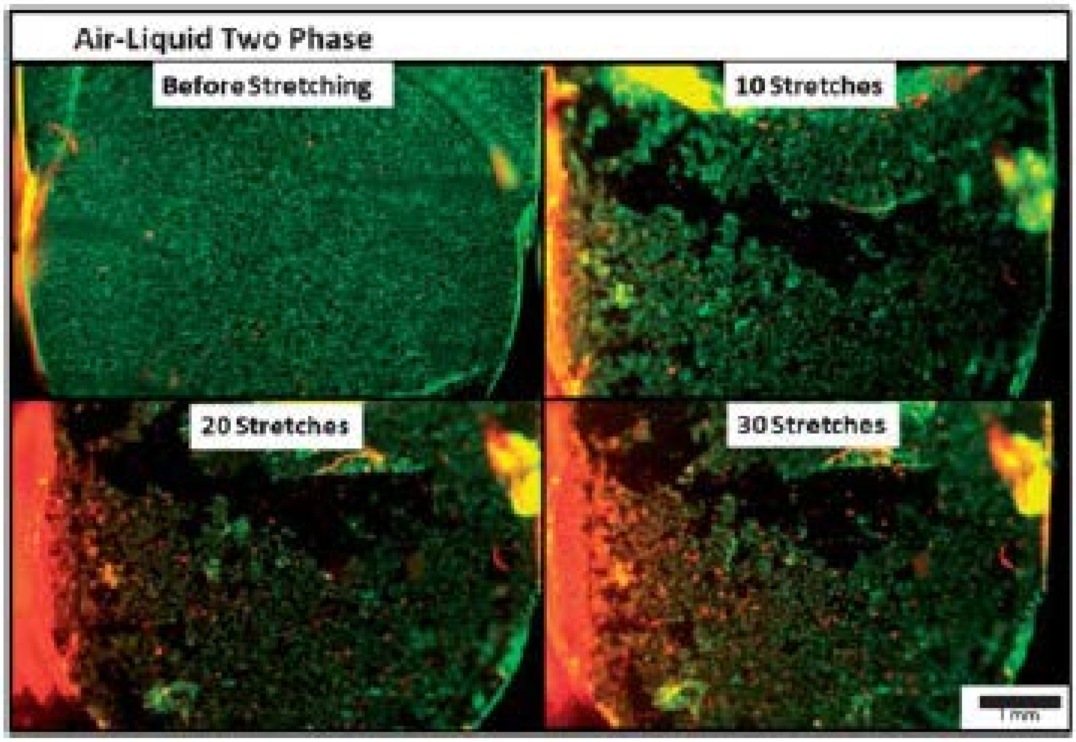

Figure 3.7. Impact of mechanical stress type on A549 cell morphology. Low magnification (2x) fluorescent micrographs enable visualization of cell death (red stain) and cell detachment on a membrane-wide scale. Cell detachment is visible after as few as 10 cycles of stretch and significant cell death begins as early as 20 cycles. These qualitative images highlight the detachment characteristics, since after further cycling, death and detachment become too prevalent that visualization of mechanism is impossible. Note the triangular cell sheet appears to fold upward indicative of detachment in the receding direction of the meniscus.

the total culture area covered with living cells using the live portion of the Live (Calcein AM)/Dead (Ethidium homodimer-1) viability/cytotoxicity assay. For A549 experiments, five chips were used for each of the experimental conditions. For murine AECs, three chips were used for each of the experimental conditions. Within each chip, five 10x fluorescent micrographs were imaged (one from each quadrant and a central image—as shown in the Supporting Information, Figure 3.14 and 3.15) with additional 4x images analyzed to account for potential selection bias resulting from non-uniformity across membrane surface.

A549. Following exposure to an air-liquid meniscus in combination with cyclic stretch, an average of 16.8% of the cell culture membrane contained viable A549 cells. This was significantly different than the percent of the culture membrane containing living cells in either the air-filled (80.6%) or the liquid-filled (68.0%) stretch-only condition (data summarized in Figure 3.8A). Image analysis of control A549 cell populations exposed to neither fluid, nor solid mechanical stresses resulted in 97.2% (SD = 2.2%) of the membrane containing living cells. This suggests that stretch alone is responsible for the change in membrane confluence from 97.2% confluence to 80.6% confluence (~17% change in the amount of membrane containing living cells); while combined stresses result in the increased cell detachment from the air-filled case (80.6% confluent) to the combined stress case (16.8% confluent). We hypothesized that the fluid-filled condition (minimal shearing, very small pressure gradient) would have less cell detachment compared to the air-filled condition (shearing and pressure gradient); however, this difference was shown not to be significant by experimental data. These data show that the fluid mechanical stresses transmitted by an air-liquid meniscus contribute to a substantial increase (16.8% compared to 80.6%) in the amount of cell detachment compared to the physiologic ‘‘air-filled’’ condition undergoing the same magnitude, frequency, and duration of cyclic stretching.

We also verified the protective effect of surfactant by enriching partially filled (air-liquid interface condition) F-12K growth media with Survanta, a natural lung surfactant, to a final concentration of 1.0 mg mL^{-1}. Repeating the experiment under identical conditions showed substantially less cell detachment than the un-enriched partially filled condition (63.9% of total surface area covered with viable cells) indicating that surfactant-enrichment is a feasible mechanism for reducing the fluid mechanical stresses transmitted to the underlying cell population.

AEC. Following exposure to an air-liquid meniscus in combination with cyclic stretch, an average of 32.5% of the cell culture membranes contained viable AECs. This was significantly different than the percent of the culture membrane containing living cells in either the air-filled (47.0%) or the liquid-filled (48.2%) stretch-only condition (data summarized in Figure 3.8B). Image analysis of control AEC cell populations exposed to neither fluid, nor solid mechanical stresses resulted in 73.3% (SD = 3.7%) of the membrane containing living cells. This suggests that stretch alone is responsible for the change in membrane confluence from 73.3% confluence to 47.0% confluence (~26.3% change in the amount of membrane containing living cells); while combined stresses result in the increased cell detachment from the air-filled case (47.0% confluent) and the liquid-filled case (48.2% confluent) to the combined stress case (32.5% confluent). These data show that the fluid mechanical stresses transmitted by an air-liquid meniscus contribute to a substantial increase (32.5% compared to 47.0%) in the amount of cell detachment compared to the physiologic ‘‘air-filled’’ condition undergoing the same magnitude, frequency, and duration of cyclic stretching.

In the completely air-filled case, primary alveolar epithelial cells are more susceptible to cyclic stretch than the adenocarcinoma epithelial cells (change of 26.3% from control to air-filled in AEC compared to a change of 16.6% from control to air-filled in A549). This agrees with previous studies showing A549 cells to be resistant to stretch-induced injury [Vlahakis *et al*., 2002]. In both cellular populations, significant changes in cell death and detachment could be detected following exposure to combination of stresses compared to stretch-only in either an air-filled or liquid-filled system.

CONCLUSIONS

Traditional in vitro models of ventilator-induced lung injury (VILI) have focused on the role of cyclic stretch (solid mechanical stress) in lung damage. Only recently, have advancements in microfluidic technology allowed the role of fluid mechanical stresses, like pressure gradients and shearing, to be systematically studied; but have been limited to airway models. We have designed and fabricated a microfluidic alveolar model capable of recreating fluid and solid mechanical stresses independently and in combination and used this model to study cell damage under conditions similar to those found in mechanical

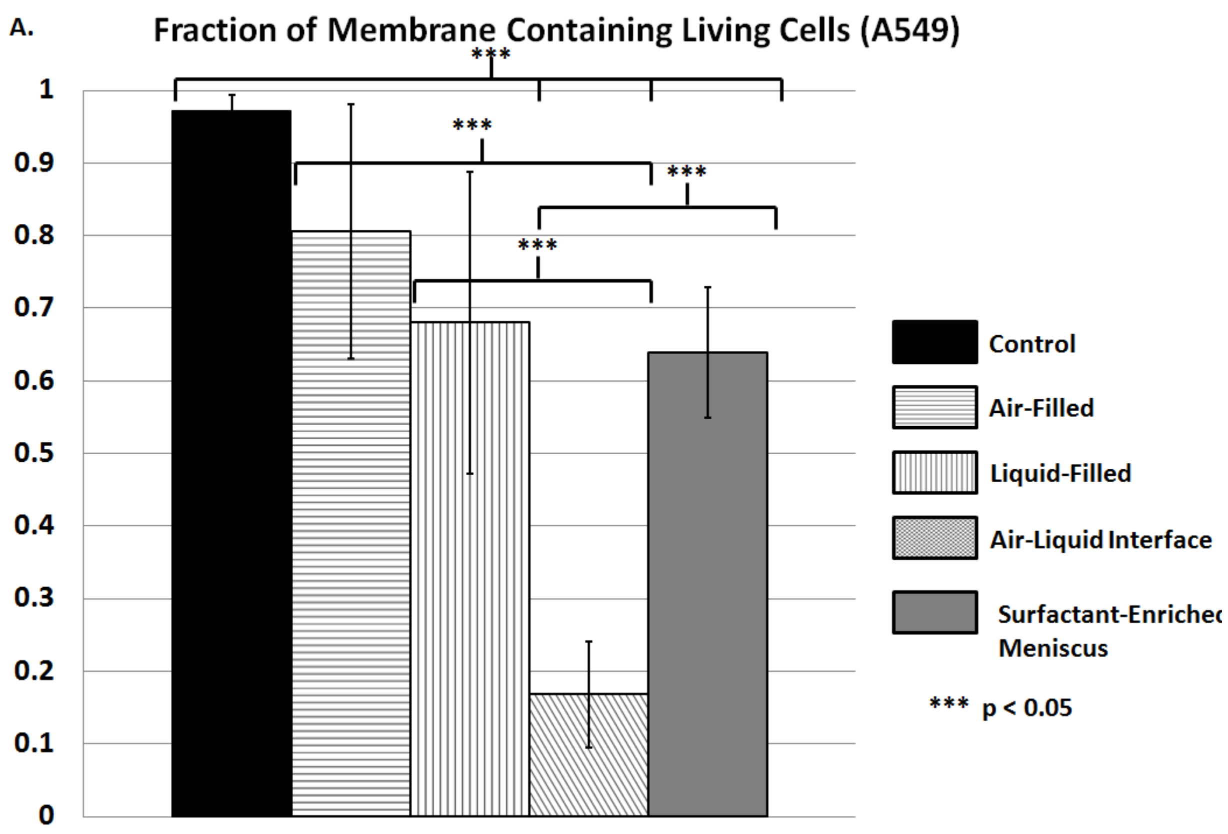
A.
Fraction of Membrane Containing Living Cells (A549)
***
***
***
***
1
0.9
0.8
0.7
0.6
0.5
0.4
0.3
0.2
0.1
0
Control
Air-Filled
Liquid-Filled
Air-Liquid Interface
Surfactant-Enrichec Meniscus
*** p < 0.05

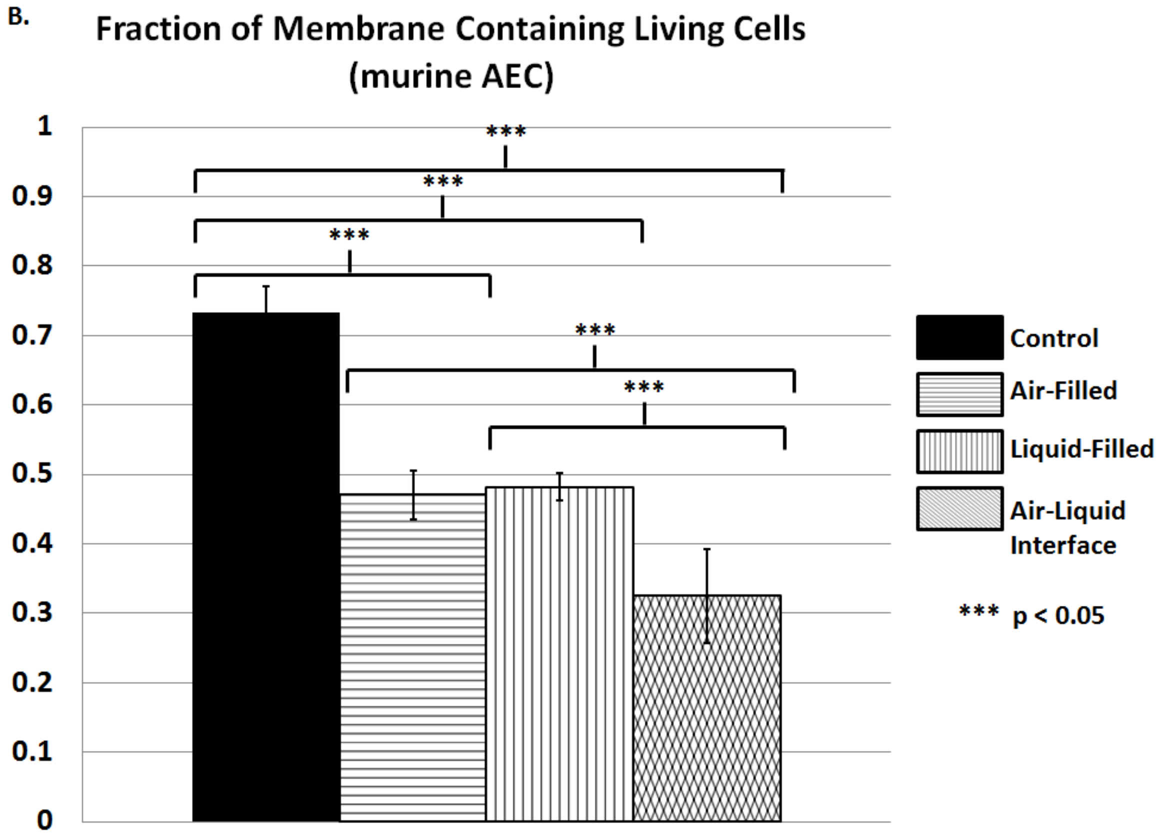
B.
Fraction of Membrane Containing Living Cells (murine AEC)
***
***
***
***
***
1
0.9
0.8
0.7
0.6
0.5
0.4
0.3
0.2
0.1
0
Control
Air-Filled
Liquid-Filled
Air-Liquid Interface
*** p < 0.05

Figure 3.8. Impact of fluid mechanical stress on cell detachment. Using a Matlab algorithm that quantified the percentage of a total area containing living cells (stained by Calcein AM), we determined the percent attachment of cells in two cell populations (a human cell line: A549 (a) and a murine primary cell alveolar epithelial cells: AEC (b) exposed to 3 experimental stress conditions (air-filled, liquid-filled, and air-liquid interface). Following 60 cycles of stretch in the air-filled condition, viable cells remained over 80.6% (SD = 17.5%) of the membrane in the A549 experiments and 47.0% (SD = 3.5%) of the membrane in the AEC experiments. In the liquid-filled experimental condition, viable cells remained over 68.0% (SD = 20.8%) of the membrane in the A549 experiment and 48.2 (SD = 2.0%) of the membrane in the AEC experiment. 16.8% (SD = 7.3%) of the A549 cells exposed to an air-liquid interface remained after 60 cycles of stretch and 32.5% (SD = 6.7%) of the AECs remained. Adding surfactant to the air-liquid meniscus condition displayed a protective effect increasing the percentage covered by viable A549 cells to 63.9 (SD = 9.0%). Analysis using both Tukey's Studentized Range (HSD) test and Bonferroni t-test for the four experimental conditions showed that significant differences in the percentage of viable cells (p-value < 0.05) result from cyclic stretch (both air-filled and liquid-filled) compared to control populations. Further significant changes occurred with the addition of fluid stresses (air-liquid interface compared to either air-filled or liquid-filled). The addition of surfactant to the A549 cell populations also yielded significant differences in percentage of membrane covered with viable cells compared to the air-liquid interface condition.

ventilation. Cell populations experiencing combination of fluid and solid mechanical stresses displayed significantly increased cell death and detachment compared to those experiencing solid stretch with minimal or non-existent fluid stresses. This deleterious effect (on A549 cells populations) was significantly reduced by the protective effect of surfactant-enriched growth media, suggesting continued research on surfactant therapy as a potential treatment for numerous surface-tension pathologies including ARDS and neonatal respiratory distress syndrome.

This research supports clinical observations that cyclic stretch alone is not sufficient to cause the degree of cell injury seen in VILI, and that surface tension forces, resulting from the propagation of moving meniscus within an alveoli, contribute to cell death and detachment. Our microfluidic system provides the first *in vitro* technique to systematically study the role of both solid and fluid mechanical forces in VILI. Additionally this system can be easily modified to study other surface tension diseases affecting alveoli. Furthermore, the precise control over respiration profile, as well as ease with which forces can be studied independently and in combination, allows investigation on the efficacy of a variety of ventilation strategies (varying velocity, inhalation/exhalation profile, and frequency) as well as potential clinical therapies (surfactant replacement, liquid ventilation) to deliberately minimize fluid stresses at the phase and location where they are most concentrated (exhalation).

SUPPORTING INFORMATION

Figure 3.9. A549 Cells over 1 week of Growth

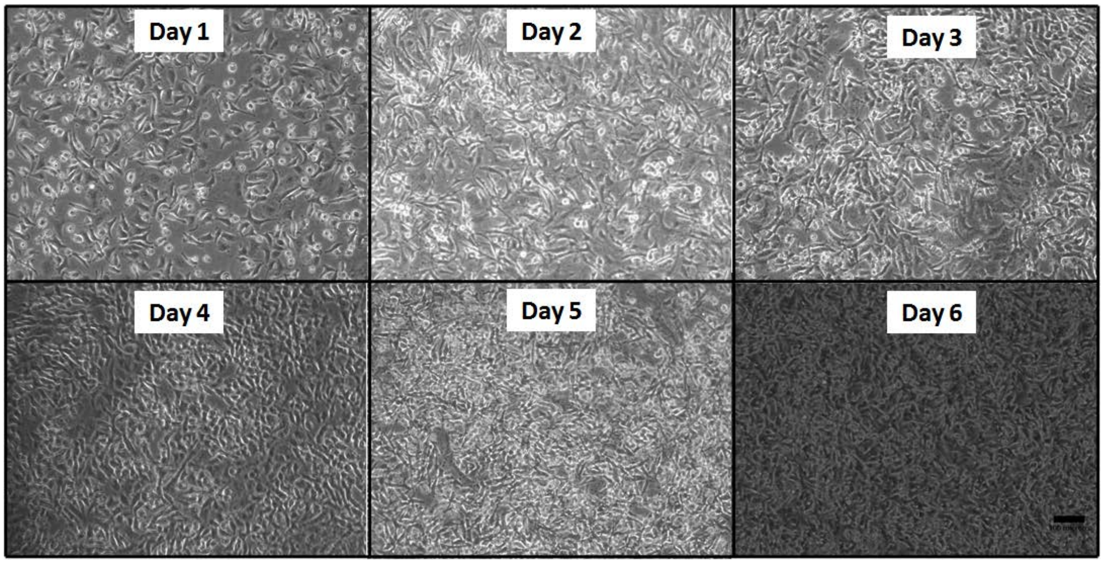

Figure 3.10. Velocity and Position of Meniscus

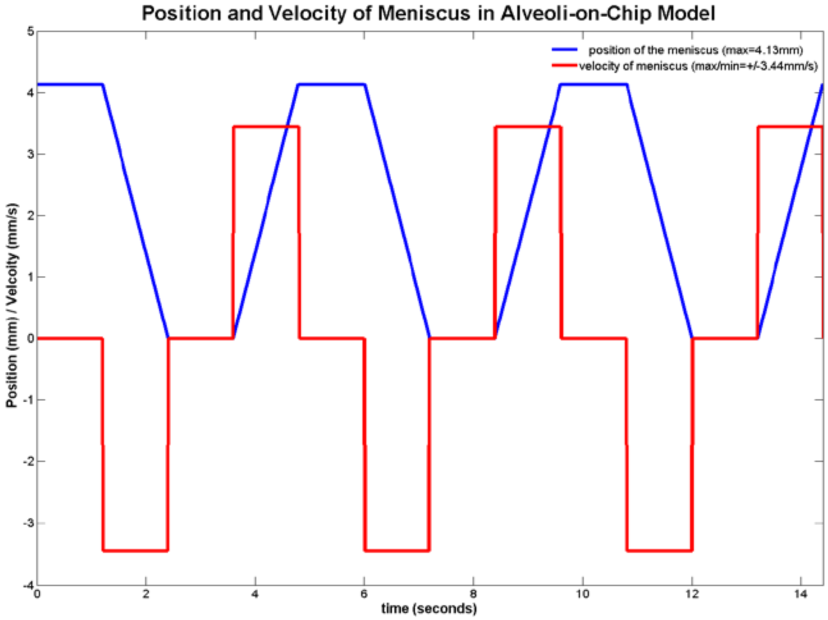

Figure 3.11. Modeling the Solid Mechanical Strain in the System

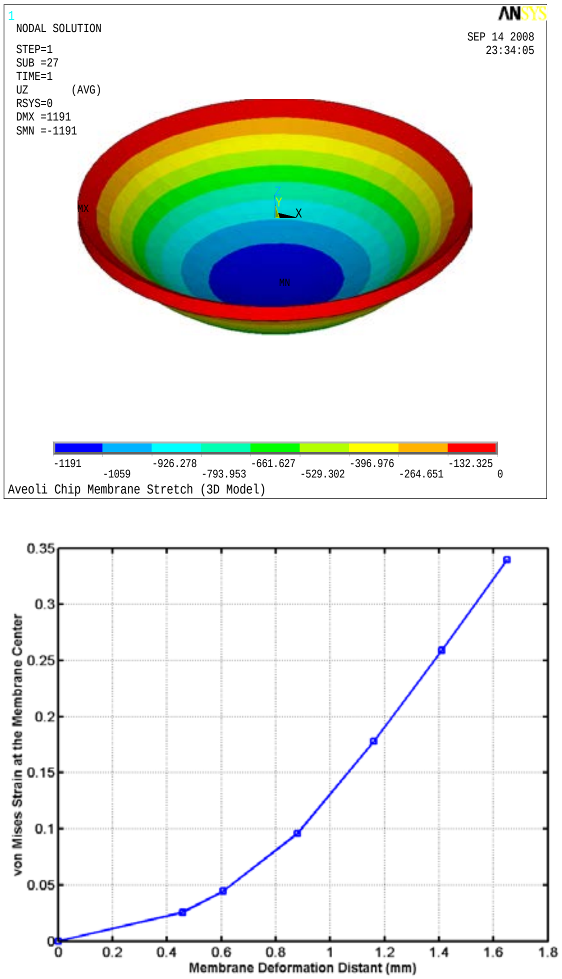

a. Three-dimensional (3-D) finite element analysis (FEA) model of von Mises Strain

b. The von Mises strain at the center of the membrane under various membrane deformations (horizontal displacements)

Figure 3.12. Designing and Automating “Alveolus-on-a-Chip” to Replicate Fluid stresses within an Alveolus

Assumptions (all calculations assume F-12K growth media has same properties as H_2O):

- μ (fluid viscosity) = 0.01 Poise
- σ (surface tension) = 72.8 dynes/cm
- ρ (density of fluid) = 1 g/cm^3
- d_o = 1.8 cm (diameter of trachea)
- d_n = diameter of a nth generation airway (Weibel Model)
- Q (flow rate of adult lung) = 250-500 cm^3/s

	Human Lung	***Alveoli-on-a-Chip***
Dimensions	$d_n = 2^{\left(\frac{-n}{3}\right)} d_o$	0.2 cm x 0.6 cm
Cross-Sectional Area	$2^n \frac{\pi d_n^2}{4} = 2^{\frac{n}{3}} \frac{\pi d_o^2}{4}$	0.12 cm^2
U (Velocity of Fluid)	$U_n = \frac{Q}{A_n} = \frac{4Q}{(2^n \pi d_n^2)} = \frac{4Q}{(2^{\frac{n}{3}} \pi d_o^2)}$	0.344 cm/s
Ca (Capillary Number)	$Ca_n = \frac{\mu U}{\sigma} = \frac{4Q\mu}{\sigma(2^{\frac{n}{3}} \pi d_o^2)}$	$Ca = \frac{\mu U}{\sigma} = 4.7x10^{-5}$
Re (Reynolds Number)	$\mathrm{Re}_n = \frac{\rho}{\mu} \frac{4Q}{(2^{\frac{n}{3}} \pi d_o^2)} d_n = \frac{\rho}{\mu} \frac{4Q}{(2^{(\frac{-2n}{3})} \pi d_o)}$	$\mathrm{Re} = \frac{\rho U d}{\mu} = 6.8$

Airway	Generation	Dimensions (cm)	Cross-Sectional Area (cm^2)	U (Velocity of Fluid) (cm/s)	Ca (Capillary Number)	Re (Reynolds Number)
trachea	0	1.8	2.544690047	98.24379214	0.013495026	17683.88259
bronchi	1	1.428660947	3.206108555	77.9761495	0.01071101	11140.14796
bronchi	2	1.133928945	4.039443657	61.88971087	0.008501334	7017.853455
bronchi	3	0.9	5.089380093	49.12189607	0.006747513	4420.970646
bronchioles	4	0.714330473	6.41221711	38.98807475	0.005355505	2785.036989
bronchioles	5	0.566964472	8.078887313	30.94485544	0.004250667	1754.463364
bronchioles	6	0.45	10.17876019	24.56094804	0.003373757	1105.242662
bronchioles	7	0.357165237	12.82443422	19.49403737	0.002677752	696.2592473
bronchioles	8	0.283482236	16.15777463	15.47242772	0.002125333	438.6158409
bronchioles	9	0.225	20.35752037	12.28047402	0.001686878	276.3106654
bronchioles	10	0.178582618	25.64886844	9.747018687	0.001338876	174.0648118
bronchioles	11	0.141741118	32.31554925	7.736213859	0.001062667	109.6539602
bronchioles	12	0.1125	40.71504074	6.140237009	0.000843439	69.07766635
bronchioles	13	0.089291309	51.29773688	4.873509344	0.000669438	43.51620296
bronchioles	14	0.070870559	64.63109851	3.86810693	0.000531333	27.41349006
bronchioles	15	0.05625	81.43008149	3.070118505	0.00042172	17.26941659
terminal bronchioles	16	0.044645655	102.5954738	2.436754672	0.000334719	10.87905074
respiratory bronchioles	17	0.03543528	129.262197	1.934053465	0.000265667	6.853372515
respiratory bronchioles	18	0.028125	162.860163	1.535059252	0.00021086	4.317354147
respiratory bronchioles	19	0.022322827	205.1909475	1.218377336	0.00016736	2.719762685
alveolar ducts	20	0.01771764	258.524394	0.967026732	0.000132833	1.713343129
alveolar ducts	21	0.0140625	325.720326	0.767529626	0.00010543	1.079338537
alveolar ducts	22	0.011161414	410.381895	0.609188668	8.36798E-05	0.679940671
alveolar sacs	23	0.00885882	517.0487881	0.483513366	6.64167E-05	0.428335782

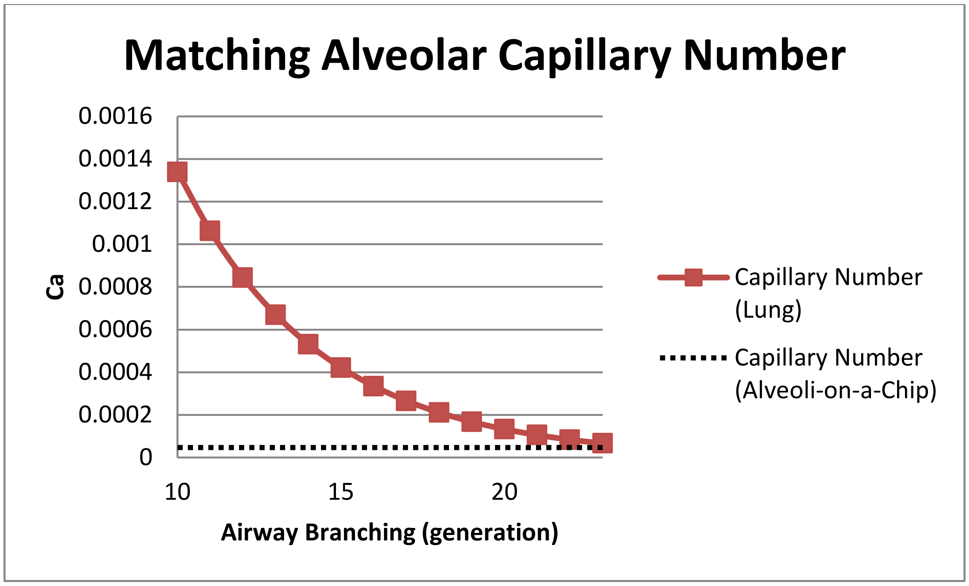
Matching Alveolar Capillary Number
0.0016
0.0014
0.0012
0.001
0.0008
0.0006
0.0004
0.0002
0
Ca
10
15
20
Airway Branching (generation)
Capillary Number (Lung)
Capillary Number (Alveoli-on-a-Chip)

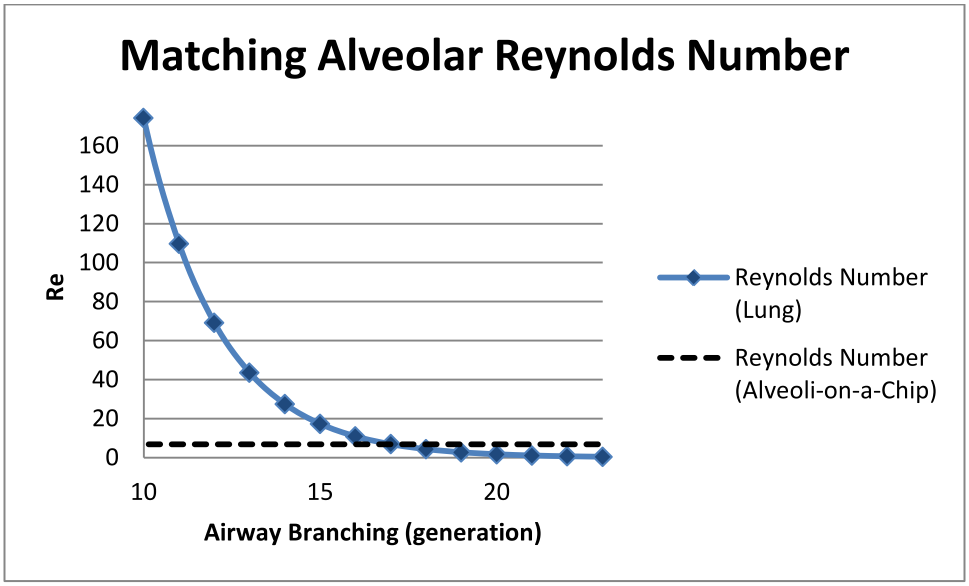
Matching Alveolar Reynolds Number
160
140
120
100
80
60
40
20
0
Re
10
15
20
Airway Branching (generation)
Reynolds Number (Lung)
Reynolds Number (Alveoli-on-a-Chip)

Figure 3.13. Determining Linear Strain in Alveolus under Normal Breathing and Pathologic Ventilation

$$\lambda = (1 + \Delta V/V_o)^{(1/3)} - 1$$

Assumptions:

- Tidal Volume (physiologic condition) = ΔV = 0.50 L
- Functional Residual Capacity (physiologic condition) = V_o = 2.40 L
- Range of Tidal Volumes (mechanical ventilation) = 0.32 – 1.60 L
- Range of functional Residual Capacities (mechanical ventilation) = 0.77 – 2.58 L
- $\lambda_{\text{physiologic}}$ = 0.065
- $\lambda_{\text{pathologic ventilation}}$ = 0.454 (upper range)

Figure 3.14. A549 Morphological Changes

A549 Cells exposed to cyclic stretch (60 cycles) in: (A) completely air-filled or (B) completely liquid-filled condition demonstrated isolated pockets of cell detachment, but remained mostly confluent over the entire culture area. Cells exposed to (C) cyclic stretch (60 cycles) in the presence of a propagating air-liquid meniscus demonstrated significant cell detachment as well as decreased size and surface area of the still adherent, viable cells indicative of a stressed condition. All images (A,B,C) are taken from the central region of the membrane.

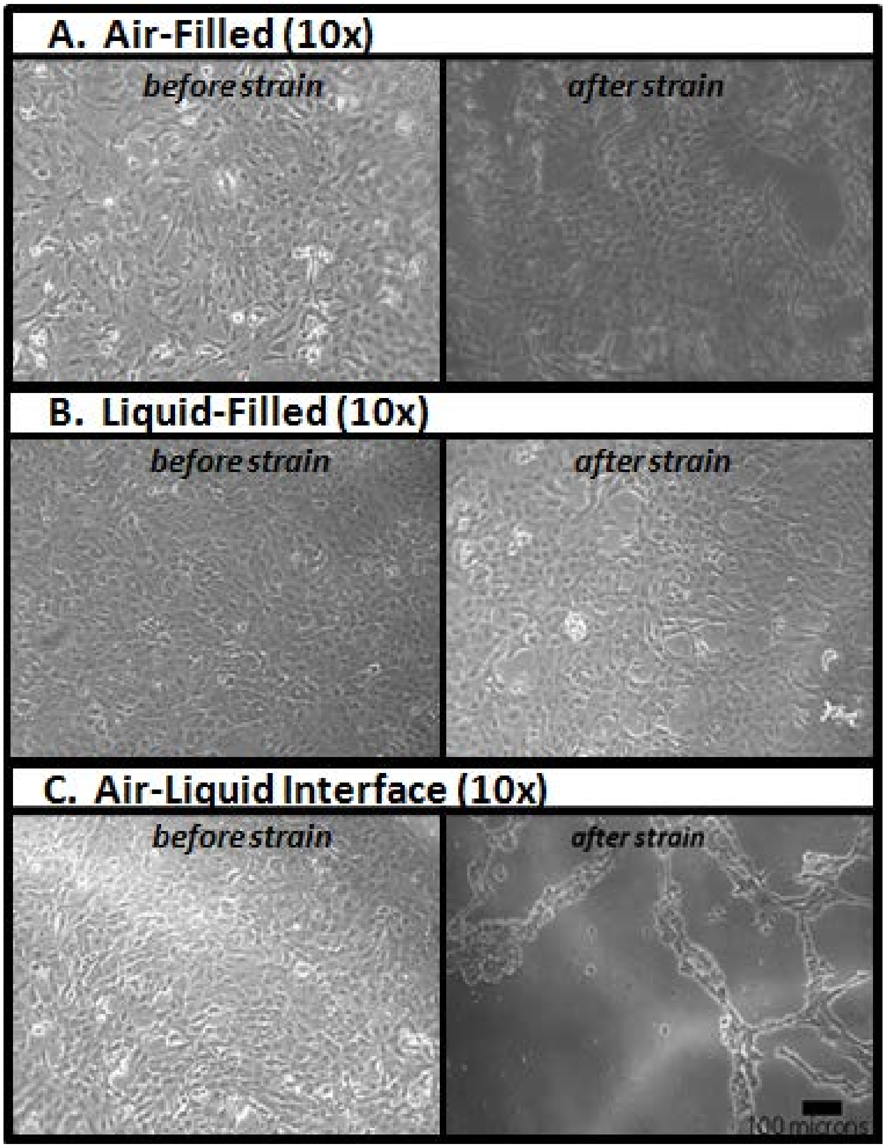

Figure 3.15. Primary, murine AECs Morphological Changes

Primary, murine AECs cultured for 4 days demonstrated substantially lower degree of confluence compared to A549 cells cultured for 6 days. AECs exposed to 60 cycles of cyclic stretch in the presence of a propagating air-liquid meniscus (C.) demonstrated a greater degree of cell detachment compared to cells exposed solely to cyclic stretch in the air-filled (A.) or liquid-filled (B.) condition. AECs experiencing cyclic stretch with no meniscus (A./B.) still showed substantial death and detachment. All images (A,B,C) are taken from the central region of the membrane.

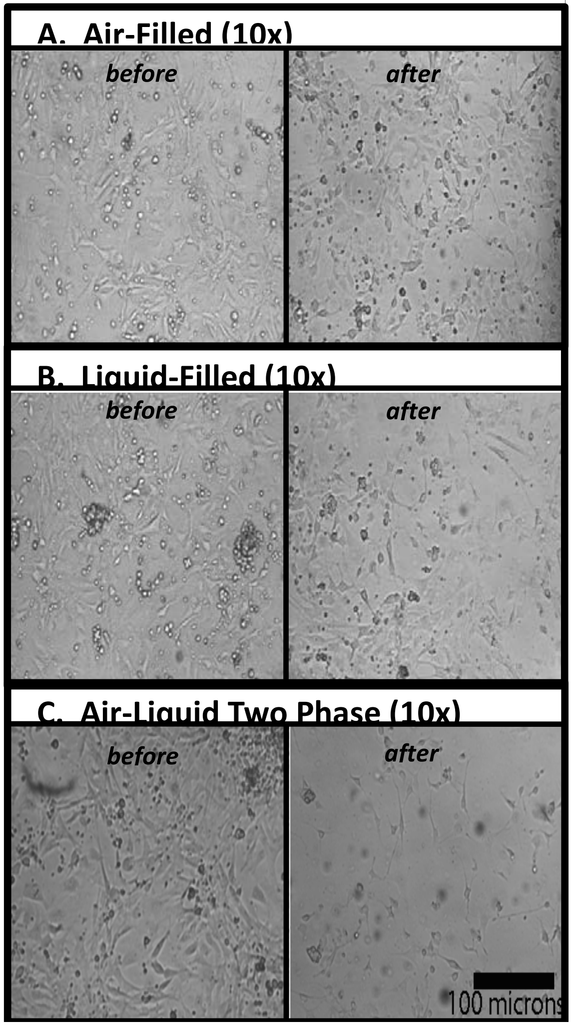

Figure 3.16. Effect of Surface Tension on Fluid Mechanical Stresses (at 0.5 m/s meniscus velocity, receding direction). The attached graphs show the effects of the surface tension on stresses and their gradients, for propagation speed of 0.5 m/s, receding meniscus at three surface tension values: 70.0,35.0, and 17.5 dyne/cm. It can be deduced from Bretherton analysis that at the limit of Ca--->0, the shear stress, its gradient and the pressure grad are proportional with $\sigma^{2/3}$, σ, and $\sigma^{4/3}$, respectively, which our results capture very well. Therefore the surface tension reduction of surfactant enrichment brings down all the three fluid mechanical stresses responsible for the cell damage.

(A) Shear Stress

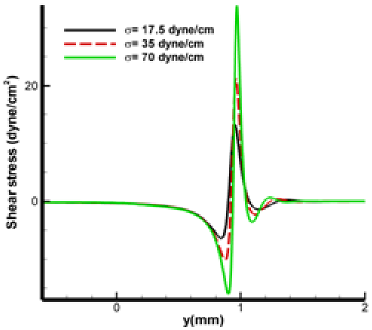

(B) Shear Stress Gradient

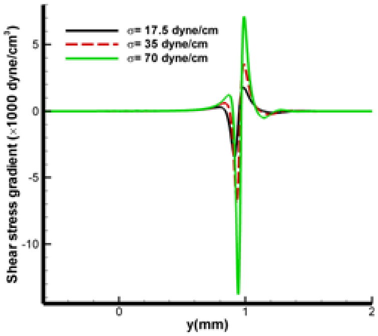

(C) Pressure Gradient

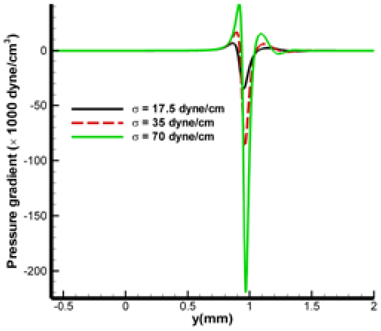

Figure 3.17. Streamline Plots at different instants during *surfactant-enriched* Plug Formation

(A) Plug Formation – Surfactant Enriched (t=0.0058 sec)

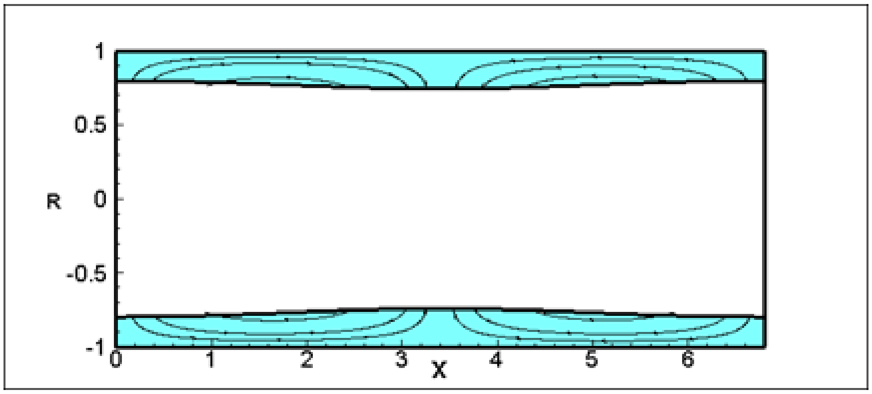

(B) Plug Formation – Surfactant Enriched (t=0.0115 sec)

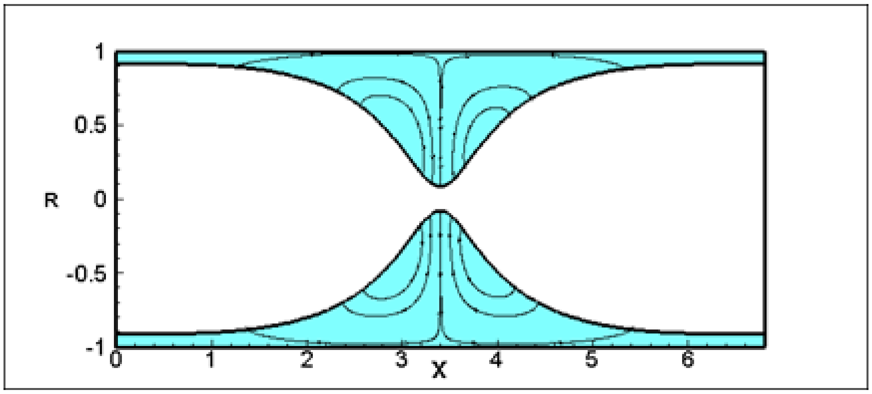

Figure 3.18. Distance (R_{min}) from Tip of Bulge to Airway Centerline as a function of Time for *surfactant-enriched* and *non-enriched* Experimental Conditions

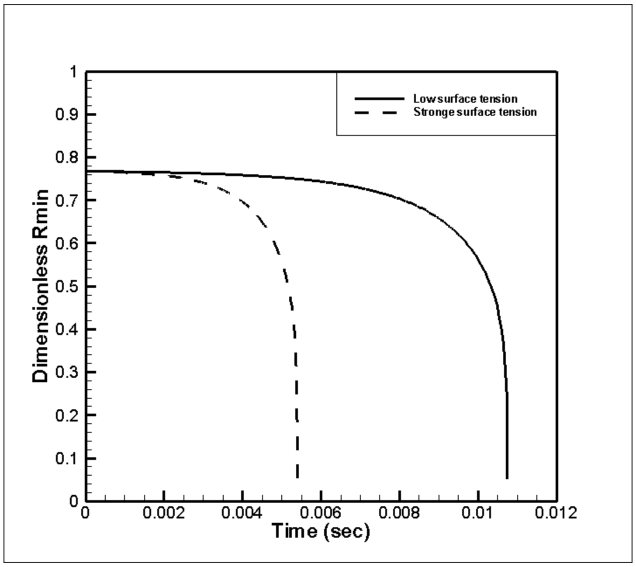

Figure 3.19. Wall Stresses and Wall Stress *Gradients* for surfactant-enriched and non-enriched Experimental Conditions.

(A) Wall Stresses

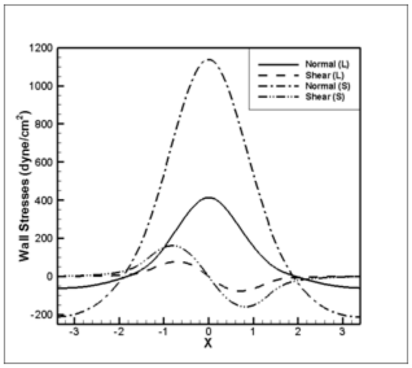

(B) Wall Stress Gradients

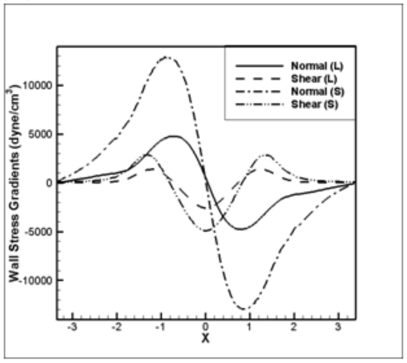

<u>L = Low *surface tension*</u>
σ^*=20 dyne/cm
surfactant-enriched case

<u>S = Strong *surface tension*</u>
σ^*=70 dyne/cm
non ***surfactant-enriched case***
DMEM

Chapter IV

Cell Migration

Cyclic Stretch Increases Alveolar Macrophage Migration and Alters Expression of Key Inflammatory Chemokines and Receptors

Nicholas J. Douville, Chris Park, Christopher Moraes, Joshua White, Amanda Kinney, Arlyne Simon, Kerim Kaylan, Paul Christensen, Shuichi Takayama

ABSTRACT

The lung has a large epithelial surface area, constantly exposed to microbial pathogens and particulate material via inhalation and microaspiration. To defend the host from these challenges, alveolar macrophages (AM) act as sentinel cells, patrolling the alveolar surface, not only to identify foreign material, but also to recruit and activate additional inflammatory cells. Adhesion and migration across this epithelial surface likely plays an important role in host defense, but the cell-cell interactions and stresses impacting this migration are poorly understood. As alveoli expand and contract with each breath, epithelial cells and macrophages located in different lung regions are exposed to different amounts and types of strain. A model system capable of measuring migration while these variables are manipulated could provide important insights into these events. We have designed and fabricated an *in vitro* model that recreates the solid mechanical stresses experienced by alveolar macrophages migrating across the pulmonary epithelial cell surface. Using this model, we have shown macrophage movement across the AEC monolayer to be significantly influenced by stretch. We have also demonstrated the upregulation of some key inflammatory cytokines and receptors in response to cyclic stretch. These experimental results suggest that cyclic stretch impacts the speed and efficacy with which AM patrol the epithelial surface of alveoli.

INTRODUCTION

Repeated branching of the respiratory tree into bronchioles of decreasing diameter which eventually terminate into alveolar sacs, maximizes the epithelial surface area available for the diffusion of O_2 and CO_2. Alveolar Macrophages (AM) patrol this alveolar surface flagging microbial pathogens or foreign particulate which reach the alveoli through inhalation and aspiration, for removal by phagoctyosis. Additionally, these sentinel cells recruit and activate additional inflammatory cells through the secretion of inflammatory cytokines. The migration of AM across a monolayer of Alveolar Epithelial Cells (AEC) has only recently been studied using *in vitro* models [Paine *et al*., 2002]. These models illustrated the critical importance of intercellular adhesion molecules in the planar chemotaxis of AM over an AEC surface, as well as provided a system to quantify cell migration in response to chemotactic stimuli, however, were limited by: (i) the inability to recreate the dynamic microenvironment of the physiologic alveoli and (ii) the inability to co-culture AM and AEC in geometric configurations which would potentially allow more quantitative characterization of migration.

The alveolar epithelial surface expands and contracts with each cycle of inspiration and expiration. Surface tension effects resulting from air-liquid interfaces and mitigated by surfactant films, further complicate study of migration in physiologically relevant models of alveoli [Huh *et al*., 2010; Douville *et al*., 2011]. Mechanical disturbances to the respiratory environment can impact a variety of cell signaling pathways, including inflammatory cytokines specifically involved with cell activation and migration [Pugin *et al*., 1998; Vlahakis *et al*., 1999; Oudin *et al*., 2002]. Furthermore, cyclic stretch (solid mechanical stress) has been shown to impact cellular migration: (i) increasing migration of vascular endothelial cells [Sweeney *et al*., 2005], while (ii) decreasing migration of airway epithelial cells [Savla *et al*.,1998] . To our knowledge, no studies have currently analyzed the role cyclic stretch plays in macrophage migration within an alveolar model.

Additionally, ICAM-1 interactions between AEC and AM are necessary for AM migration [Paine *et al*., 2002]. Recent advancements in the cell patterning using aqueous two-phase systems (ATPS) allow multiple cell types to be co-cultured in controlled geometric patterns [Tavana *et al*., 2009; Tavana *et al*., 2011]. Printing in geometric patterns enables better quantification of cellular migration. Using ATPS micropatterning techniques, we printed AM (AMJ2-C11: ATCC, Manassas, VA) over a confluent monolayer of AEC (primary, murine AEC). ATPS printing allows migration to be measured in the *inward* direction (ideal for chemotaxis) [Supplementary Information, Figure 4.4A] or migration to be measured in the *outward* direction (ideal for chemokinesis) [Supplementary Information, Figure 4.6B].

We report increased rates of AM migration across an AEC monolayer in response to physiologic levels of cyclic stretch. Using ATPS printing techniques we demonstrate the ability to co-culture AM and AEC in geometric configurations on a flexible PDMS membrane. This PDMS membrane was stretched using a custom-designed negative pressure actuator exposing the co-cultured cells to solid mechanical stress of amplitude and frequency controlled to match physiologic alveolar conditions. Additionally, we analyzed changes in the gene expression for both AECs and AMs (as well as, co-culture system) using a murine, *inflammatory cytokines and receptors* PCR array (PAMM-011E, SABiosciences) following 6 hours of cyclic stretch (5% linear strain). These experimental results suggest the substantial impact stretch could have on the speed and efficacy with which AM patrol the epithelial surface of alveoli, potentially explaining clinical observations of differential phagocytosis and clearance between regions of the lung that experience differential stretch conditions.

MATERIALS AND METHODS

Cyclic Stretch via PDMS Wells. A PDMS system consisting of similar dimension wells to those of a standard polystyrene 96-well plate was designed and fabricated. These dimensions were selected to allow compatibility with nano-litre printing equipment and high throughput imaging techniques. Key dimensional modifications, including: (i) well diameter of 6 mm in PDMS system, compared to 6.35 mm in polystyrene plate and (ii) 6 x 5 grid structure in the PDMS system compared to 8 x 12 grid structure in the polystyrene plate enabled robust, repeatable, inexpensive fabrication. Holes were punched through the entirety of a rectangular slab of PDMS using a 6 mm biopsy punch (Delasco, Council Bluffs, IA). The slab of PDMS containing “through” holes was irreversibly bonded to a PDMS membrane secured to the silanized glass slide (75 mm x 50 mm) using a handheld corona treater for approximately 30 seconds on both substrate and membrane [Haubert *et al*., 2006; Douville *et al*., 2011]. The membrane was removed from the glass slide and the entire device was exposed to plasma oxygen for 60 seconds prior to cell seeding to make the PDMS hydrophilic. A rigid polystyrene barrier, with “through” holes machined to match the well array separated the vacuum chamber from the PDMS system ensuring displacement was localized to the membrane region and not the bulk substrate.

Radial and circumferential strain was calculated as a function of vertical displacement (ΔZ – Figure 4.1B) at different distances from the center of the membrane [Supplementary Information, Figure 4.7]. Relatively consistent strain values occur within the region patterned with cells (region of diameter < 2 mm, located centrally within each 6 mm diameter well). Negative pressure was applied from a vacuum-sealed chamber located beneath the PDMS system and controlled using a regulator valve. A solenoid valve controlled the fraction of time in the strained and un-strained condition (Figure 4.1B) by alternating between negative pressure and ambient pressure. Using the regulator and solenoid control system, a wide range of membrane deflection values and breathing frequencies could be applied. A respiration rate of 15 cycles per minute and 5%

linear and circumferential strain (ΔZ ~ 1.2 mm) was selected to allow for quantifiable changes in migration and gene expression, with no detectable changes in cell death and detachment [Douville *et al*., 2010].

ATPS Co-Culture. Cells were printed using an Aqueous Two-Phase System (ATPS) formed from the non-ionic polymer polyethylene glycol (7% PEG, MW: 35K) and dextran (7% DEX, MW: 500K) dissolved in Dulbecco's Modified Eagle Medium (DMEM). Due to density differences between the PEG and DEX-phase solutions, the well is filled with PEG-phase solution completely *immersing* the AEC monolayer. Droplets of the more dense DEX solution can be used as *patterning phase* maintaining pre-determined configurations within the PEG *immersion phase*. The interfacial tension between the PEG and DEX solutions, ensures that DEX patterns are maintained for extended periods of time. 250 nL DEX-phase droplets were dispensed into wells containing PEG-phase solution using an automated liquid-handler (Cybio, Jena, Germany). The protocol for patterning AM on a AEC monolayer using a PEG-DEX ATPS system is depicted in Figure 4.1A. The PDMS wells were exposed to plasma oxygen for 5 minutes to make the surface membrane hydrophilic. Following oxidation step, the membranes were treated with 10 μg mL^{-1} fibronectin in PBS overnight. The FN-solution was removed from the wells before partial filling with ~75 μL of PEG-phase DMEM (7% PEG in DMEM w/w) (Figure 4.1A). Next, a 250 nL droplet of DEX-phase DMEM (7% DEX in DMEM w/w) was deposited centrally in each well using the liquid handler. Alveolar macrophage cells (AMJ2-C11) fluorescently labeled with CellTracker (5-chloromethylfluorescein diacetate, Invitrogen), were trypsinized and resuspended in PEG-phase DMEM. An additional amount (~40 μL) of thePEG-phase resuspension was carefully pipetted into each well, so as not to disturb the DEX-phase droplet. The AM cells were allowed to adhere for 4 hours, then contents of the wells was removed and replaced with regular DMEM solution.

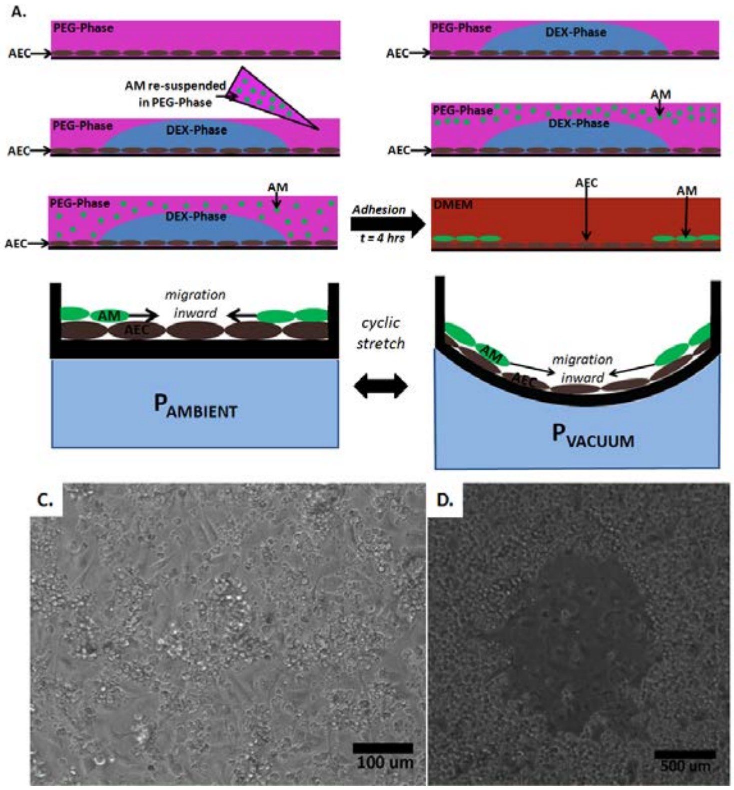

Figure 4.1. Experimental Set-Up.

(A) **ATPS Co-Culture**. Cells were printed using an Aqueous Two-Phase System (ATPS) formed from 7% PEG (MW: 35K) and 7% DEX (MW: 500K). Droplets of the more dense DEX solution can be used as *patterning phase* maintaining pre-determined configurations within the PEG *immersion phase*. Fluorescently labeled AM cells are suspended within PEG-phase solution, adhering in a central exclusion pattern.

(B) **Cyclic Stretch via PDMS Wells**. Negative pressure was applied from a vacuum-sealed chamber. Vertical displacement of the membrane was calibrated using a regulator valve. A solenoid valve controlled the fraction of time in the un-strained and strained condition by alternating between ambient pressure and vacuum pressure, respectively.

(C) **AEC Cell Culture**. Primary, murine AEC cells were isolated and seeded on PDMS membranes within our system. They were grown in culture for 3 days prior to co-culture with AM.

(D) **AM and AEC Co-culture**. AMJ2-C11 cells were deposited in an exclusion pattern using ATPS and allowed to adhere for 4 hours, before PEG-DEX media was removed, and the wells re-filled with standard growth media (DMEM +10% FBS and 1% penicillin/streptomycin). A decreased droplet size enables the entire region of cell patterning, as well as individual AM and AEC cells, to be visualized on a single 10x micrograph.

AEC Cell Culture. Murine, primary AEC were isolated according to a protocol described by Christensen and colleagues and approved by the animal care committee at the Ann Arbor Veterans Administration Medical Center [Christensen *et al*., 2004]. Briefly, following pentobarbital anesthesia and heparinization, specific pathogen-free male C57BL6 mice were exsanguinated and the pulmonary vascular perfused free of blood. The trachea was cannulated and the lungs filled with 1–2 ml of Dispase (Worthington). Subsequently, 0.45 ml of low melting point agarose was infused via the trachea and the lungs were placed in iced PBS for 2 min to harden the agarose. The lungs were incubated in 2 ml of Dispase and incubated for 45 min at 24 °C. The lung tissue was teased from the airways and minced in DMEM with 0.01% DNase. The lung mince was gently swirled for 10 min, and passed successively through nylon mesh filters. The cells were incubated with biotinylated anti-CD32 and anti-CD45 followed by streptavidincoated magnetic particles, before magnetic removal of leukocytes. Mesenchymal cells were removed by overnight adherence in a Petri dish. An optical micrograph showing AEC cells cultured on a PDMS membrane within our system, prior to ATPS cell patterning is showing in Figure 4.1C.

AM Cell Culture. Depending on the desired macrophage pattern (Supplementary Information, Figure 4.5), AM cells were tryspinized and re-suspended in either the PEG or DEX-solutions at a final concentration of $1x10^6$ cells/µL. The commercially available cell line AMJ2-C11 (ATCC, Manassas, VA) was selected because this line retains many characteristics of alveolar macrophages. These cells are phagocytic and express Fc receptors and Mac-1 (CD-11b) antigens The latter is necessary for interaction with ICAM-1 known to be expressed on primary AEC. Figure 4.1D shows an optical micrograph of AM cells patterned on a AEC monolayer within our PDMS system using ATPS printing.

Inflammatory Cytokines and Receptors PCR Array. AMs and AECs were cultured independently to confluence and AMs were co-cultured in a ring configuration over a confluent monolayer of AECs. The cells were exposed to

5% cyclic stretch for 6 hours, before being lysed and RNA-purified. The gene expression was compared to that of a static control of the same culture condition using a PCR array for murine inflammatory cytokines and receptors.

Phagocytic Index. *S. aureus* is a common lung pathogen which frequently causes pneumonia in the lungs of hospitalized patients. *S aureus* conjugated to pH-sensitive dye was used to measure the phagotyic rate in response to cyclic stretch (Invitrogen, Carlsbad, CA). AMs were patterned in an outer ring configuration surrounding a central droplet of DEX-phase media containing the conjugated *S. aureus*. Following 4 hours in ATPS-culture, both the AM cells and the conjugated bacteria adhered to the PDMS membrane. The percent of macrophages undergoing phagocytosis of a bacteria cell will be calculated using random sampling at 20x magnification around the PDMS membrane (to account for increased migration in the experimentally stretched wells compared to the control, static wells). The printed region was visualized in Figure 4.4 by increasing the acidity of the Opti-MEM growth media (Invitrogen, Carlsbad, CA); however, it is important to note that in experimental conditions the beginning pH of media was 7.4 and the microscope settings zeroed to eliminate the slight baseline fluorescent of unphagocytoses bacteria in neutral pH conditions. The percent of macrophage cells undergoing phagoctyosis of *S. aureus* conjugates will be measured in the stretched and static case at multiple time points.

RESULTS

Migration of AM Across an AEC Monolayer. AM cells labeled with CMFDA CellTracker green fluorescent stain (Invitrogen, Carlsbad, CA) were patterned via ATPS exclusion (Suporting Information, Figure 4.5A and 4.6A) on the surface of a confluent AEC monolayer within the PDMS device. PDMS devices were exposed to 5% cyclic strain and the area of the cell free region was measured each hour. PDMS co-cultures not exposed to cyclic stretch maintained clear cell boundary for greater than 16 hours (Figure 4.2A). In PDMS co-cultures exposed to cyclic stretch, AM cells migrated centrally, completely closing the ring within 4 hours (Figure 4.2B). Figure 4.3 shows the area of the cell free region (normalized to initial printing area) for a total of 5 hours.

The rate of AM migration was quantified by measuring the area “cell free” region in each well. To account for discrepancies in the cell patterning process, the area was normalized for each well (at t = 0 hours, the area of each well = 1). As cells migrated into the excluded region, the area decreased until area = 0, when no cell boundary could be resolved. The wells not exposed to cyclic stretch (static) maintained clear cell boundaries at measurements taken up to 16 hours after adherence. Cells exposed to cyclic stretch completely filled the region within 4 hours after the application of cyclic stretch. The large error in the t=3 hour measurement occurs because in some wells no cell free region remained (area = 0), while in other wells a cell free region could still be resolved. The migration data is shown in Figure 4.3. At all time points, the cells exposed to cyclic stretch migrate at a faster rate than the cells in the static system, however, after 2-3 hours of cyclic strain the migration rate in the cyclic stretched condition increases rapidly, so that the excluded region completely disappears in all wells by 4 hours after the application of cyclic strain. Macrophage cells also demonstrated increased migration in response to stretch when printed directly on PDMS membranes treated overnight with fibronectin (100 µg/mL in PBS). The Migration of AM across a FN-treated PDMS membrane in static and stretched conditions are compared to migration across an AEC monolayer in the Supplementary Information, Figure 4.8. We could not resolve a difference in the rate macrophages migrated across an AEC monolayer compared to FN-treated PDMS membrane, although the error was significantly higher in the AEC-monolayer due to more precise ATPS printing on a cell-free surface.

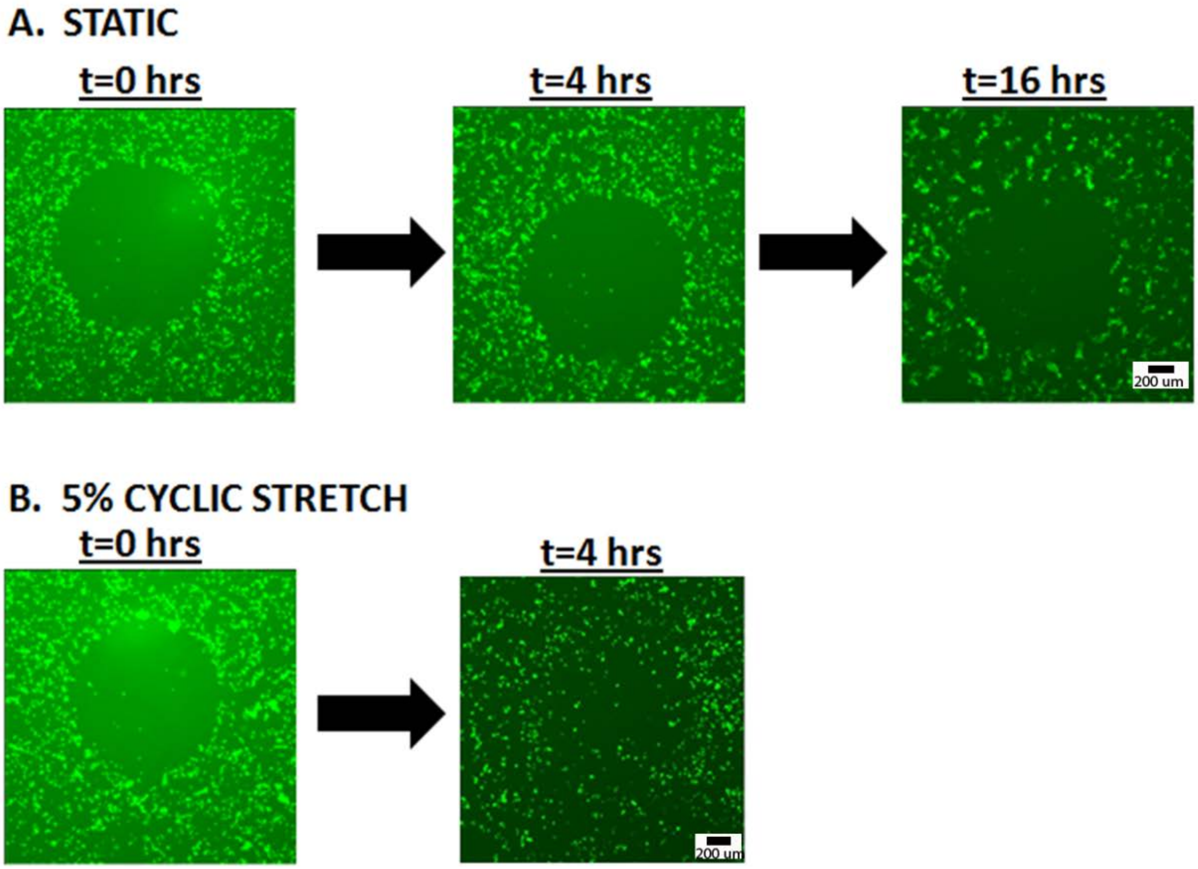

Figure 4.2 Fluorescent Micrographs showing the Migration of AM into the "Cell Free Region".

(A) In PDMS wells not exposed to cyclic stretch (static), the AM maintained clear cell boundary for greater than 16 hours.
(B) In PDMS wells exposed to cyclic stretch, AM cells migrated centrally, completely closing the ring within 4 hours.

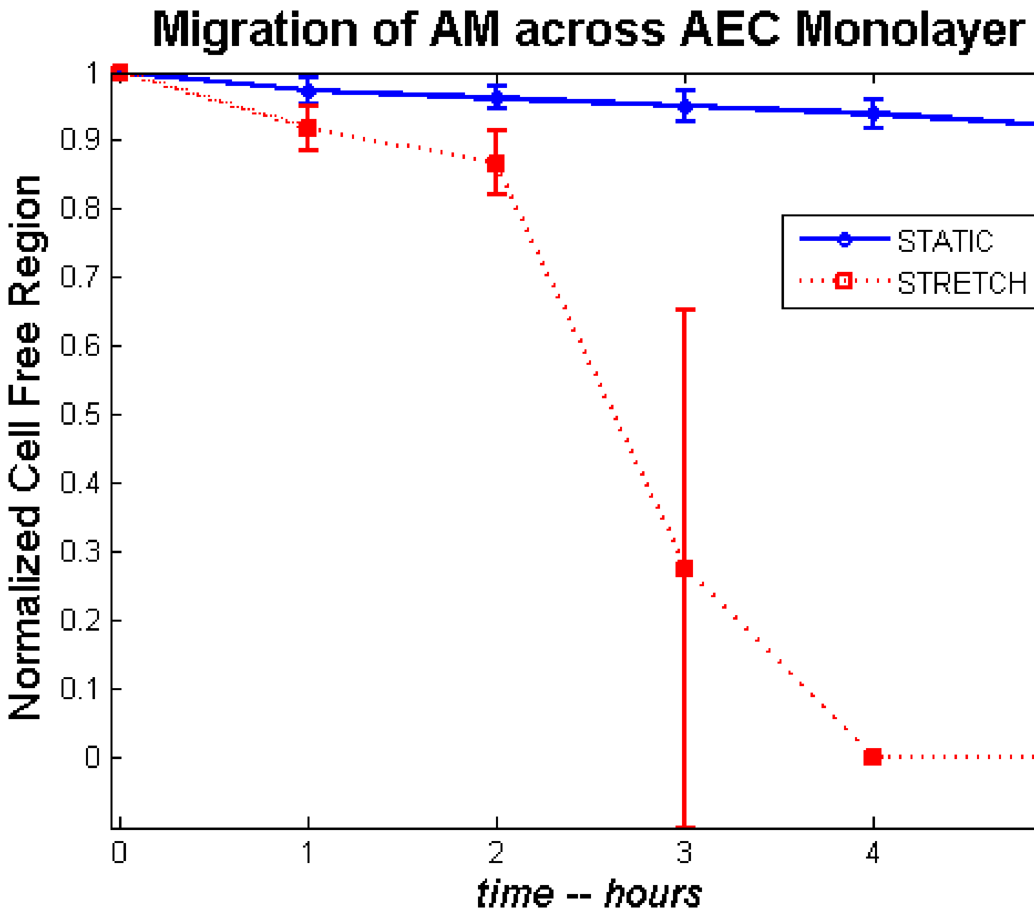

Figure 4.3. Migration of AM across AEC Monolayer under Stretched vs. Static Condition. The area of the "Cell Free" Region was measured (and normalized to the initial area of each well to account for discrepancy in the cell patterning process). As cells migrated into the excluded region, the area decreased. The wells not exposed to cyclic stretch (static) maintained clear cell boundaries at measurements taken up to 16 hours after adherence. Cells exposed to cyclic stretch completely filled the region within 4 hours after the application of cyclic stretch. The large error in the t=3 hour measurement occurs because in some wells no cell free region remained (area = 0), while in other wells a cell free region could still be resolved. All error bars are standard deviations.

Targeted Migration. 10x fluorescent imaging allowed the migration pattern of individual macrophage cells to be tracked over-time. The drawbacks to this technique (compared to imaging at 2x/4x magnification) are that: (i) the geometric configuration of the "cell-free region" cannot be completely visualized, (ii) the interface between the AM and cell-free region appears much less pronounced than in lower magnification images, and (iii) minor variations in microscope focus result from residual negative pressure, despite timing imaging sequences to coincide with the “fully ventilated” expiration breathing cycle. In this higher magnification technique, the interface between the macrophage region and the “cell-free zone” is imaged enabling visualization of two-dimensional migration towards the central region of the membrane (where circumferential strain values are highest, Supplementary Information, Figure 4.7). We compared macrophage migration in response to 5% cyclic strain to macrophage migration in a static, control PDMS reservoir. In the static control, macrophage migration is minimal and is limited to non-directed movements (no net movement over 3 hours). Additionally, in the static case, the boundary between the cellular region and “cell-free zone” is still apparent after 3 hours in culture. In wells exposed to cyclic strain, macrophages migrate from the exterior regions filling the central “cell-free zone”. These AM cells migrated in targeted manner towards to the central region of the PDMS well, while remaining adherent to the PDMS reservoir and remained in the same configuration following PBS wash and addition of fresh media, addressing our concern that migration was occurring through cell detachment and central aggregation.

Inflammatory Cytokine and Receptor Microarray. Significant changes in gene expression were detected in all three cell populations (single culture: AM, single culture: AEC, and co-culture: AEC + AM) exposed to cyclic stretch compared to static controls. Specifically, multiple *C-C motif* Chemokines and Interleukins/Interleukin-receptors were upregulated in all cell populations, as well as, other inflammatory factors such as Tumor Necrosis Factor in the AM population. The results of this microarray experiment are summarized in Table 4.1.

primary AECs			
up	Gene	Name	Fold-change
	Bcl6	B-cell leukemia/lymphoma 6	3.15
	Cxcr5	Chemokine (C-X-C motif) receptor 5	19.8
	Ccl6	Chemokine (C-C motif) ligand 6	2.02
	Cxcl1	Chemokine (C-X-C motif) ligand 1	2.31
	Cxcl5	Chemokine (C-X-C motif) ligan 5	3.58
	IL2rb	Interleukin 2 receptor, β chain	4.69
down	Cc11	Chemokine (C-C motif) ligand 11	2.18
	Ccl19	Chemokine (C-C motif) ligand 19	17.94
	Cxcl10	Chemokine (C-X-C motif) ligand 10	3.62
	Cxcr3	Chemokine (C-X-C motif) receptor 3	3.93
AMs			
up	Abcf1	ATP-binding cassete, subfamily F	2.97
	Bcl6	B-cell leukemia/lymphoma 6	5.32
	Ccl2	Chemokine (C-C motif) ligand 2	2.26
	Ccl3	Chemokine (C-C motif) ligand 3	2.73
	Ccl5	Chemokine (C-C motif) ligand 5	29.44
	Ccl7	Chemokine (C-C motif) ligand 7	3.03
	Ccr1	Chemokine (C-C motif) receptor 1	13.91
	Cx3cl1	Chemokine (C-X3-C motif) ligand 1	3.54
	Pf4	Platelet factor 4	3.26
	Il15	Interleukin 15	4.98
	Il18	Interleukin 18	2.2
	Il1r1	Interleukin 1 receptor, type I	8.55
	Il1r2	Interleukin 1 receptor, type II	3.7
	Itgb2	Integrin β2	2.85
	Mif	Macrophage migration inhibitory factor	4.32
	Spp1	Secreted phosphoprotein 1	4.8
	Tnf	Tumor necrosis factor	2.24
down	Cxcr5	Chemokine (C-X-C motif) receptor 5	2.31
	Tnfrsf1b	TNF receptor superfamily, member 1b	3.01
Co-Culture			
up	Bcl6	B-cell leukemia/lymphoma 6	2.36
	Ccl11	Chemokine (C-C motif) ligand 11	2.4
	Ccl19	Chemokine (C-C motif) ligand 19	3.11
	Ccl2	Chemokine (C-C motif) ligand 2	2.00
	Ccl3	Chemokine (C-C motif) ligand 3	4.97
	Cxcl1	Chemokine (C-X-C motif) ligand 1	2.18
	Cxcl5	Chemokine (C-X-C motif) ligand 5	3.27
	Il11	Interleukin 11	4.43
	Il15	Interleukin 15	2.99
	Il16	Interleukin 16	5.55
	Il1a	Interleukin 1α	2.39
	Il1r2	Interleukin 1 receptor, type II	2.77
	Il4	Interleukin 4	2.15
	Il6st	Interleukin 6 signal transducer	2.6
	Ltb	Lymphotoxin B	2.93
down	Cxcr5	Chemokine (C-X-C motif) receptor 5	10.37
	Ccl24	Chemokine (C-C motif) ligand 24	47.74
	Ccr2	Chemokine (C-C motif) receptor 2	2.34
	Ccr4	Chemokine (C-C motif) receptor 4	6.46
	Ccr9	Chemokine (C-C motif) receptor 9	3.06
	Il18	Interleukin 18	2.09

Table 4.1. Summary of Inflammatory Cytokines and Receptors Microarray Data. Gene expression changes greater than 2x the static value in either the positive or negative direction are listed.

DISCUSSION AND CONCLUSION

The lung is subjected to cyclic stretch during tidal breathing. These changes in epithelial cell surface area may provide new ‘foot holds’ for macrophages patrolling the surface. As a result, areas of the lung with more or less stretch may present different environments for macrophage function. Lung tissue that is partially or completely collapsed (atelectasis) may provide macrophages less opportunity for migration and thus be more susceptible to infection. In addition, ventilation of the lung in is inhomogeneous with more ventilation (stretch) in the lower lung zones when compared to the upper lung zones. It is possible that this may play a role for infections that have a predilection for the upper lung zones (e.g. *M. tuberculosis* or *P. jirovecii*).

Confirmation of Migration from Active Cellular Process. Our experiments strongly suggest increased cell *movement* and increased filling of the central, cell-free zone in response to stress. To verify that the observed migration was not predominantly the result of a physical phenomenon, such as: (i) *detachment and gravity-based central accumulation* or (ii) *convective flow fields* generated within the reservoir, we repeated our experimental protocol (5% linear strain) with a *convex* – as opposed to *concave* – membrane deformation. This membrane deformation was generated by the application of positive pressure in the lower actuation compartment and required an additional polystyrene brace to be fabricated with holes matching the configuration of the PDMS reservoir. This brace was necessary to clamp the PDMS reservoir to the actuation chamber forming a tight seal necessary for pressure-based membrane actuation (note: in negative pressure actuation the PDMS forms a tight casket to the underlying actuation chamber solely on pressure effects and no brace is necessary). If *stretch-actuated migration* were the result of a physical phenomenon, we would expect to see cells accumulate in an outer ring around the edge of the reservoir – because the outer ring is lower than the central region during stretch. In our experimental set-up (negative pressure) the central, cell-free region of the membrane is pulled to a lower point than the outside of the ring during stretch depositing any detached cells centrally.

We confirmed that cells migrate centrally in both the positive and negative pressure stretch condition. Cells migrated inwardly, completely filling the central, cell-free zone within 6 hours of positive-pressure cyclic stretch. A comparison of macrophage migration rate under *positive pressure* conditions to: (i) macrophages patterned on a *static* membrane and (ii) macrophage under *negative pressure* experimental condition can be found in the Supplementary Information, Figure 4.8. Representative fluorescent micrographs from the *positive pressure* control at various time points are shown in the Supplementary Information, Figure 4.9. Macrophage cells migrate more slowly in the *positive pressure* stretch condition (completely filling the central, cell-free region in approximately 6 hours of positive pressure stretch as compared to ~4 hours in the negative pressure experiment. This suggests that while physical forces are *not* the primary mechanism of stretch-actuated cell migration, forces such as gravity and convection may contribute to a non-negligible change in migration rate.

To further confirm that movement is occurring predominantly from an active cellular process, we need to show that migration is impaired when key components of the cellular machinery are blocked. In migration: (i) First, the cell polarizes, (ii) then reorganizes its actin cytoskeleton - (iii) next, integrin mediated adhesion leads to the (iv) formation of a protrusion and (v) traction via actomyosin-mediated contraction - (vi) finally, the rear cell machinary disassembles. The small molecule inhibitor, *blebbistatin* (which interferes with cellular actomyosin cross-bridging) has been used in previous migration studies [Tavana *et al*., 2011] to confirm an active cell process. We are in the process of verifying an active cell process through the negative control inhibition of stretch-based migration via blebbistatin.

While our experimental results suggest that migration is occurring through an active cell process – the fact that we could not resolve a difference in migration rate between macrophages travelling across an AEC monolayer and

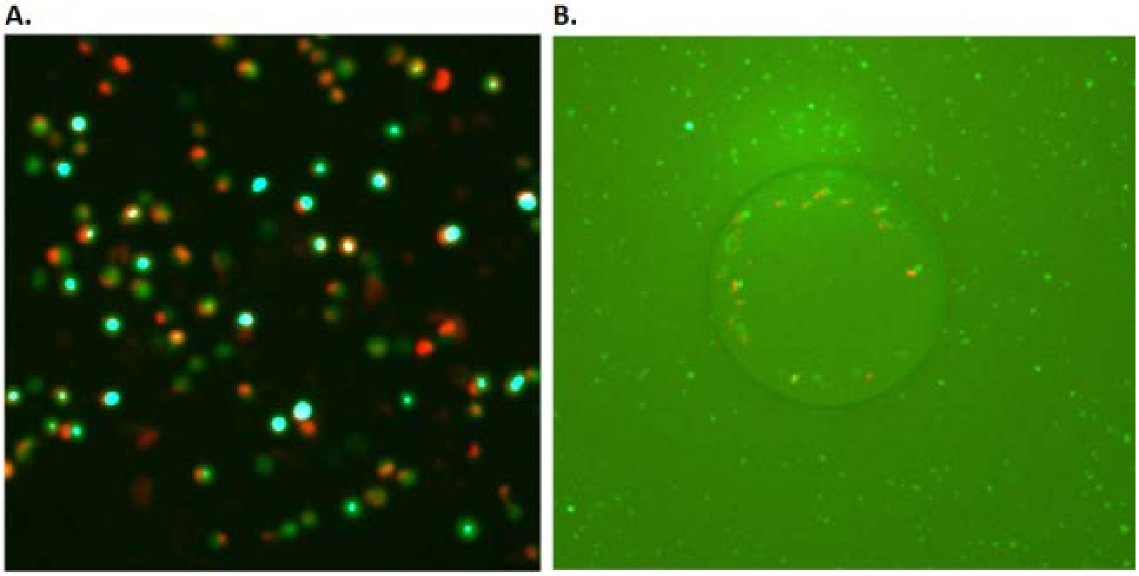

Figure 4.4. Future Directions. Our experiments suggest that stretch impacts the speed with which macrophages patrol the epithelial surface of the lung – but offer no insight into the rate at which they can phagocytosis a foreign particle or bacteria once encountered. Using our ATPS-based system we can pattern bacteria (or bacterial conjugates) in a central ring enabling phagocytic rate in response to stretch to be easily measured. (A) *S. aureus* bacterial conjugates fluoresce red in a pH-dependent manner – allowing the number of conjugates being phagocytosed by green-fluorescent AMJ2-C11 cells to be counted. (B) These bacterial conjugates can be partitioned to the central DEX-droplet allowing combined effect of migration and phagocytosis to be quantified.

those migrating across a FN-treated PDMS (acellular) [Supplementary Information, Figure 4.8] suggests AMJ2-C11 cells migrate in response to stretch via a different mechanism of action than primary AM migrate in response to a chemotactic stimulus such as GM-CSF [Paine *et al*., 2001].

Future Work – Measure of Phagocytic Index. We have shown the stretch impacts the speed with which macrophages patrol epithelial surface, but have not measured the efficacy with which they can clear encountered bacteria. In future experiments, we propose patterning bacterial conjugates that fluoresce in a pH-dependent manner within the central DEX-phase droplet, then measuring the rate of phagocytosis in stretched compared to static wells. Figure 4.4A shows AMJ2-C11 macrophage cells (stained green with CFMDA CellTracker) phagocytosing *S. aureus* conjugated to pH sensitive red-fluorescent dye and Figure 4.4B shows ATPS-patterning of both bacterial conjugates (red) with our fluorescent AMJ2-C11 cells (green).

Conclusion. We have designed and fabricated an *in vitro* model that recreates the solid mechanical stresses experienced by AMs migrating across the pulmonary AEC surface. We have also shown that macrophage migration is significantly influenced by stretch – however the specific mechanism of this movement remains unresolved. Preliminary studies show that cyclic stretch substantially changes the expression of many inflammatory cytokines and receptors in all three cell populations (single culture AM; single culture AEC; and co-culture AEC and AM). Based upon (i) evidence of adherent macrophages post-washing, (ii) movies tracking the migration of individual macrophages, (iii) a positive control showing migration against physical forces, and (iv) the upregulation of multiple chemokines in response to stretch -- we believe that cell *movement* is occurring through *active cell migration*. As the final confirmatory step, we are currently conducting negative controls to inhibit components of the cellular machinery involved in active migration. Combining the presented experiments with proposed future works (specifically: further experimental characterization of the gene regulation response to stretch and measurement of phagocytic rate in response to stretch) should reveal how cyclic stretch impacts the speed and efficacy with which AM patrol the epithelial surface of alveoli as well as suggesting techniques for increasing immune response. The current *in vitro* system could also be used to test the role of stretch in phagocytosis of specific organisms.

SUPPORTING INFORMATION

Figure 4.5. Comparison of Protocols for Patterning Cells Using ATPS Droplets.

(A) Alveolar Macrophage (AM) cells resuspended within the PEG-phase following trypsinization, can be excluded from a region protected by a central DEX-phase droplet.
(B) AM cells resuspended within the DEX-phase droplet following trypsinazation can be deposited within the confines of a central ring.

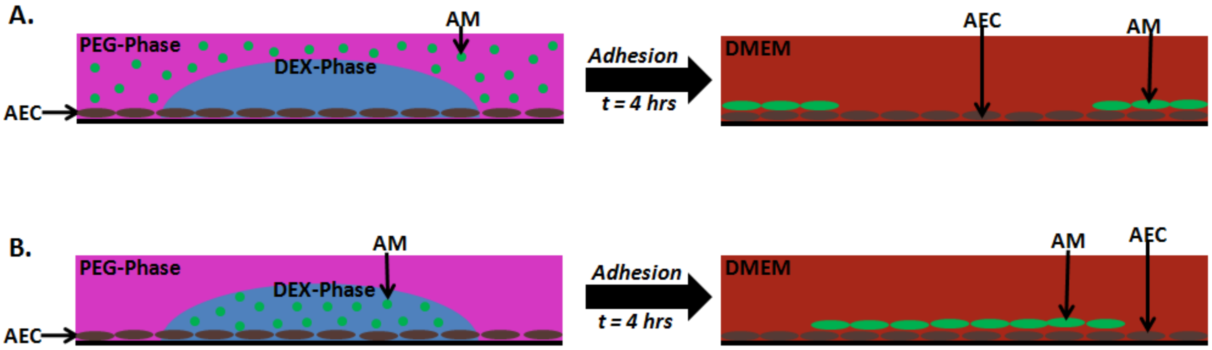

Figure 4.6 Fluorescent Micrographs of Geometric Printing Configurations.

(A) This printing configuration is ideal to measure chemotactic migration inward.
(B) This configuration is ideal for measuring cell migrated outward.

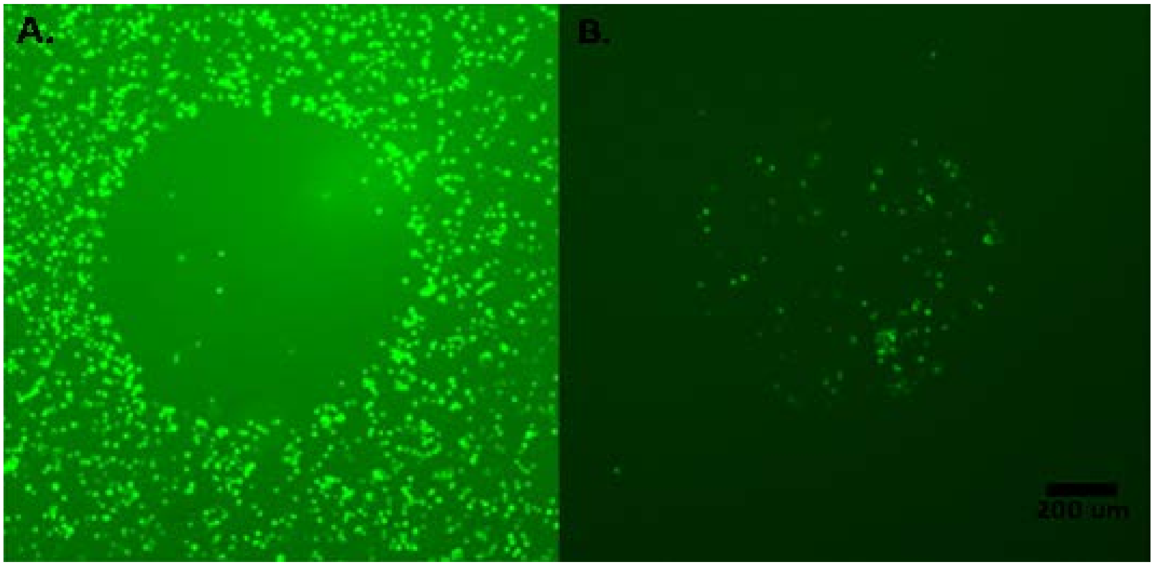

Figure 4.7. Finite Element Analysis of Radial and Circumferential Strain as a Function of Distance (µm) from Center of the Well. *Radial* and *circumferential* strain as a function of distance from the center of the PDMS well at approximate experimental pressure (14 kPa) and membrane thickness (300 µm). Each well in our PDMS system has a total diameter of 6 mm. The dimensions of the printed cell area depends on the volume of DEX-phase droplets dispensed into each well, as well as the hydrophobicity of the printing surface (for example: oxidation of PDMS membrane and whether droplets are printed directly onto the PDMS membrane or on a confluent cell monolayer). Experimental conditions using 250 nL droplets typically result in cell patterning with diameter ~ 2.0 mm. Finite Element Analysis shows relatively consistent strain values within the region patterned with cells (Radial Distance < 1000).

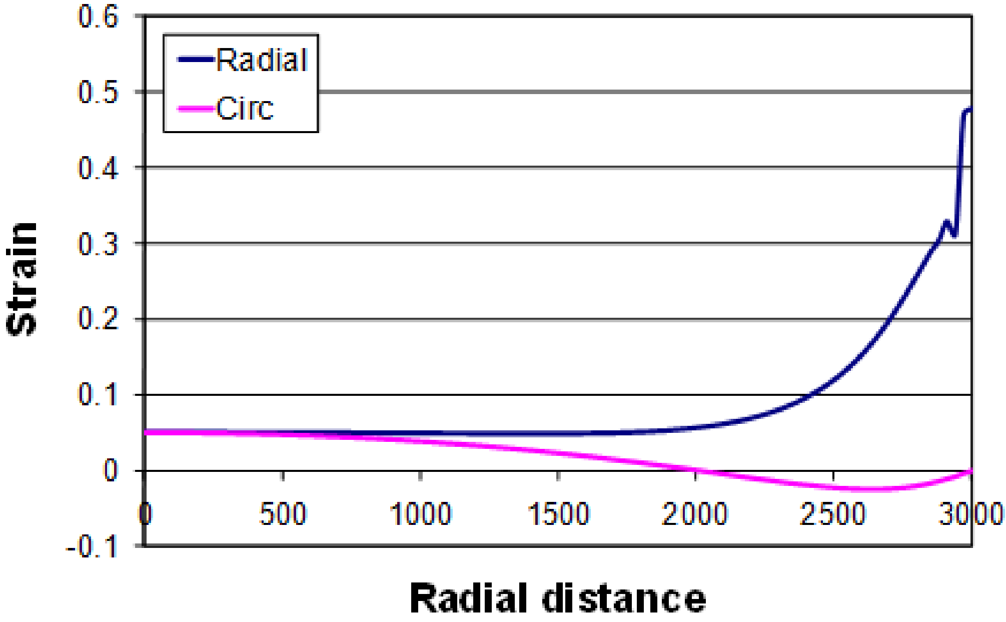

Figure 4.8. Migration Rate in Additional Control Experiments. Increased migration in response to cyclic stretch (compared to the static control) was seen across both AEC monolayers and FN-treated PDMS. We could not resolve a statistically significant difference between the rate macrophages migrate across an epithelial monolayer and the rate macrophages migrate across a FN-treated PDMS membrane. The error (standard deviation) was much higher when ATPS printing on a cell monolayer compared to PDMS membrane containing no cells which is to be expected because the epithelial cells pin contact lines preventing the DEX-phase droplet from reaching stable equilibrium configuration. We also found that positive pressure induced increased migration in macrophages compared to static controls – however, the rate of migration during positive pressure was found to be slower than the rate of migration in the negative pressure experimental set-up (taking approximately 6 hours to completely close the cell-free region under positive pressure compared to 4 hours in the negative pressure condition). This control suggests that while physical mechanisms are not the primary mechanism of stretch-actuated cell migration, they do contribute to a non-negligible change in migration rate.

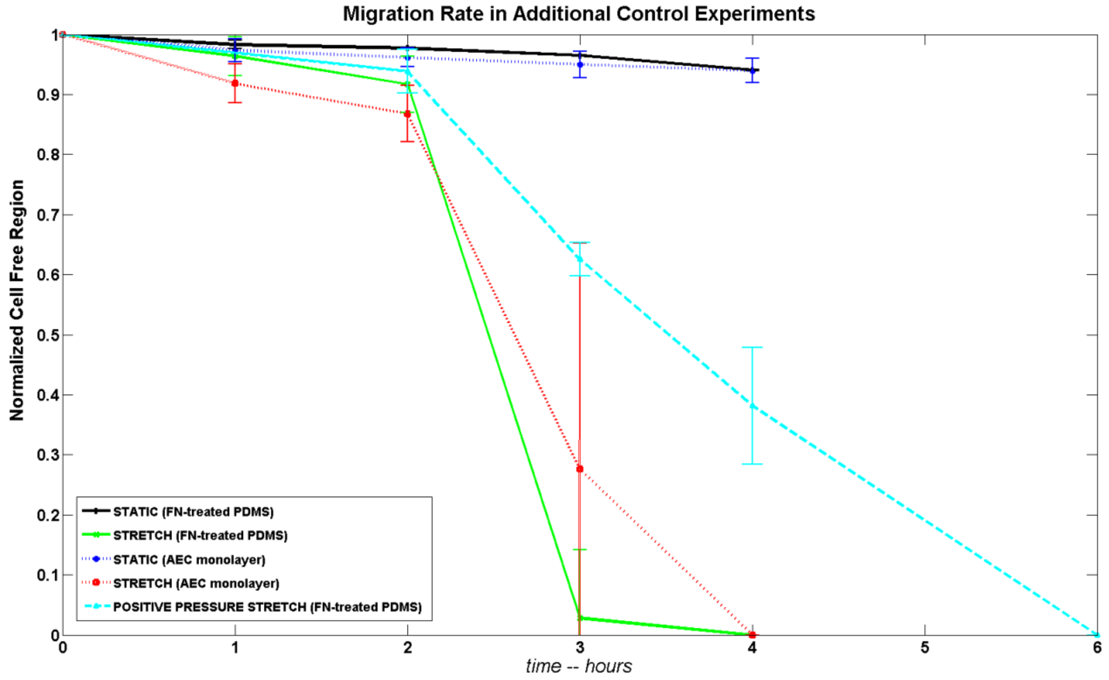

Figure 4.9 Positive Pressure Control. To verify that the observed migration was not predominantly the result of a physical phenomenon (such as *detachment and gravity-based central accumulation* or *convective flow fields* generated within the reservoir) we repeated our experimental protocol with a *convex* – as opposed to *concave* – membrane deformation. This membrane deformation was generated by the application of positive pressure – as opposed to negative pressure – in the lower actuation compartment. If stretch-actuated migration is the result of a physical phenomenon, we would expect to see cells accumulate in an outer ring around the edge of the reservoir. If migration is the result of a cellular process in response to stretch – the cells would migrate centrally (as they had done in the previously described negative pressure system) against gravity and flow fields. This positive pressure control demonstrated a similar outcome to the negative pressure experimental system, completely filling the central, cell-free region. We observed a slightly decreased migration rate (approximately 6 hours for complete filling compared to 4 hours in the negative pressure system) which would be expected because cells are migrating *against* physical forces of gravity and convection. Note: Positive pressure control was conducted on FN-treated PDMS membrane (not across an AEC-monolayer).

A. Static Control

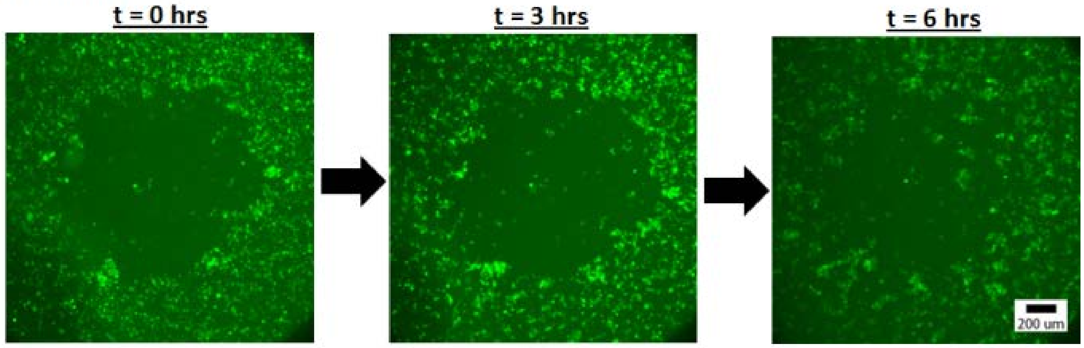

B. 5% Cyclic Stretch (Positive Pressure – *Convex Membrane Deformation*)

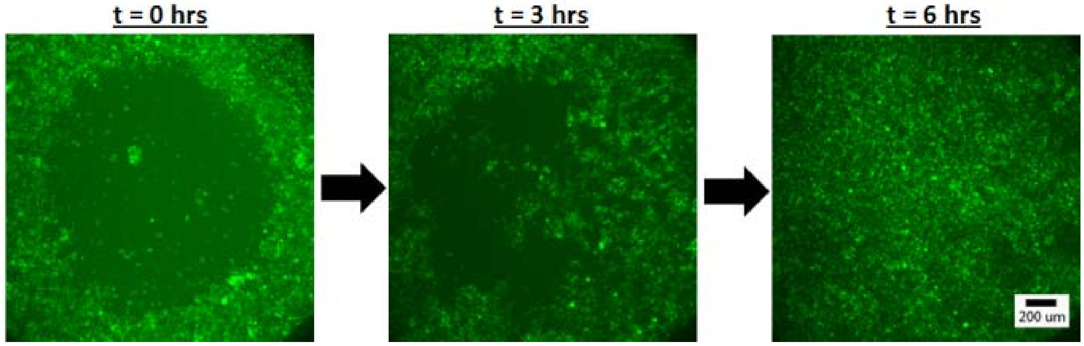

Chapter V

Conclusions and Future Directions

CONCLUSIONS

Next-Generation alveolar models more faithfully replicate the properties of the air-blood barrier, including: (i) size, (ii) stresses, (iii) permeability, and (iv) cell-cell interactions. Additionally, these models incorporate sensors to quantify the integrity of the air-blood barrier in real-time. Because alveoli have small dimensions (~250 μm diameter) a, combined *fluid* and *solid* stress profile that cannot be replicated in traditional alveolar models, and complicated cell-cell interactions; microfluidic systems are the ideal platform to model the *air-blood barrier*.

We have made multiple technological breakthroughs in microfluidic design and fabrication necessary for alveolar modeling, then utilized these novel microsystems to reveal cell behavior and gain insight into the pathology of *air-blood barrier* breakdown.

A. Technological Breakthroughs. We have developed a convenient fabrication procedure for incorporating Ag/AgCl recording electrodes directly within a two-layered microfluidic system [*Analytical Chemistry*, 2010]. Because this method utilizes commercially available recording electrodes and eliminates the need for direct deposition of thin films onto the PDMS substrate, it can be replicated by any lab with soft-lithography capabilities. By using this fabrication technique to embed electrodes directly within a microfluidic channel, we reported the first TEER measurements taken within a microfluidic system. We measured impedance over the frequency spectra from 10 Hz to 1.0 MHz then resolved a best-fit resistance value from an accepted equivalent circuit model yielding a more accurate TEER than single frequency or direct-current resistance measurements. We demonstrated the biological utility of the system by confirming accepted TEER magnitude and pattern for both endothelial and epithelial cells over 1 week in culture. Additionally, we verified the ability of our microfluidic system to detect dynamic changes in barrier integrity by treating a confluent monolayer with TritonX-100, a non-ionic surfactant know to increase permeability, then measuring the subsequent drop in resolved TEER values. In the process of developing our novel fabrication technique, we also discovered that potentially surprising, mechanics occurs when thin metal films are deposited onto an elastomeric substrates [*Soft Matter*, 2011]. Because these findings are broadly useful in the design of flexible electronics, we extensively characterized the cracking of metal-coated elastomers. Our experimental results-combined with a general fracture mechanics analysis presented in a companion manuscript [Thouless et al., 2011] -- provide a comprehensive description of the mechanics governing this cracking phenomenon.

We have also designed and fabricated a microfluidic alveolar model capable of recreating fluid and solid mechanical stresses independently and in combination and used this model to study cell damage under conditions similar to those found in mechanical ventilation [*Lab Chip*, 2011]. This microfluidic system provides the first *in vitro* technique to systematically study the role of both solid and fluid mechanical forces in VILI. Additionally this system can be easily modified to study other surface tension diseases affecting alveoli. Furthermore, the precise control over respiration profile, as well as ease with which forces can be studied independently and in combination, allows investigation on the efficacy of a variety of ventilation strategies (varying velocity, inhalation/exhalation profile, and frequency) as well as potential clinical therapies (surfactant replacement, liquid ventilation) to deliberately minimize fluid stresses at the phase and location where they are most concentrated (exhalation).

We have also developed an ATPS-based *in vitro* system for recreating solid mechanical stresses experienced by alveolar macrophages as they migrate a pulmonary epithelial surface. This system allows multiple cell-lines to be printed in complex geometric patterns, allowing a more quantitative measure of migration across cell monolayers than in previous models [manuscript in preparation].

B. Cell Behavior and Pathology. Using our two-layered microfluidic, Alveoli-on-a-Chip, we demonstrated significant morphological differences between epithelial cells exposed to combination of solid mechanical and surface-tension stresses compared to cell populations exposed solely to cyclic stretch. We also measured significant differences in both cell death and cell detachment rates in cell monolayers experiencing combination of stresses. This deleterious effect was significantly reduced by the protective effect of surfactant-enriched growth media, suggesting continued research on surfactant therapy as a potential treatment for numerous surface-tension pathologies.

Using our ATPS-macrophage patterning model, we have shown macrophage movement across the AEC monolayer is significantly influenced by stretch. Cyclic stretch during tidal breathing increases the epithelial surface area of alveoli potentially providing new ‘foot holds’ for macrophages patrolling the surface. As a result, areas of the lung with more or less stretch may present different environments for macrophage function. For example: lung tissue that is partially or completely collapsed (atelectasis) may provide macrophages less opportunity for migration and thus be more susceptible to infection while the lower lung zones (which experience greater cyclic strain compared to upper lung zones) can clear bacterial infection with higher success. Additionally, we have demonstrated the upregulation of some key inflammatory cytokines and receptors in response to cyclic stretch. These experimental results suggest that cyclic stretch impacts the speed and efficacy with which AM patrol the epithelial surface of alveoli.

FUTURE DIRECTIONS

A. Short Term. In the near-term, future research will focus on resolving the immune response of macrophages to cyclic strain. Based upon our completed research, we are confident that macrophage movement is significantly influenced by cyclic stretch; however, the exact mechanism remains unresolved. Preliminary studies show that cyclic stretch substantially upregulates the expression of key inflammatory cytokines and receptors in: (i) single-culture macrophages, (ii) single-culture epithelial cells, and (iii) co-cultures of macrophages and epithelial cells. This led us to hypothesize that the specific migration mechanism is cytokine dictated. Additional experiments and controls are necessary to hone on the specific mechanistic pathway as well as eliminate some additional mechanisms of cell movement. Figure 5.1 highlights possible mechanisms of cell movement and lists the test/controls necessary to verify or disprove the particular mechanism. The potential significance of our macrophage movement findings increases if we verify that the migration does indeed result from an active cellular process and is *not* the result of a physical process such as gravity-based accumulation or convective fluid flow. Confirming the specific pathway and mechanism also will substantially increases the complexity of our biological study; however, we believe that additional trials using the murine, *Inflammatory Cytokine and Receptor PCR Array* will reveal potential cytokines and receptors for further targeted-blocking studies.

We are also interested in resolving the phagocytic response of macrophages to stretch. We plan on using *S. aureus* conjugates that fluoresce in a pH-dependent to determine the percentage of fluorescent labeled macrophages in the (i) static as compared to the (ii) stretched condition. We have previously verified the ability to selectively pattern bacteria (centrally within the DEX-phase droplet) surrounded by macrophages (peripherally within the PEG-phase droplet). Phagocytosis could operate through the same mechanism as migration (potentially upregulated by inflammatory cytokines and receptors) or through an independent mechanism.

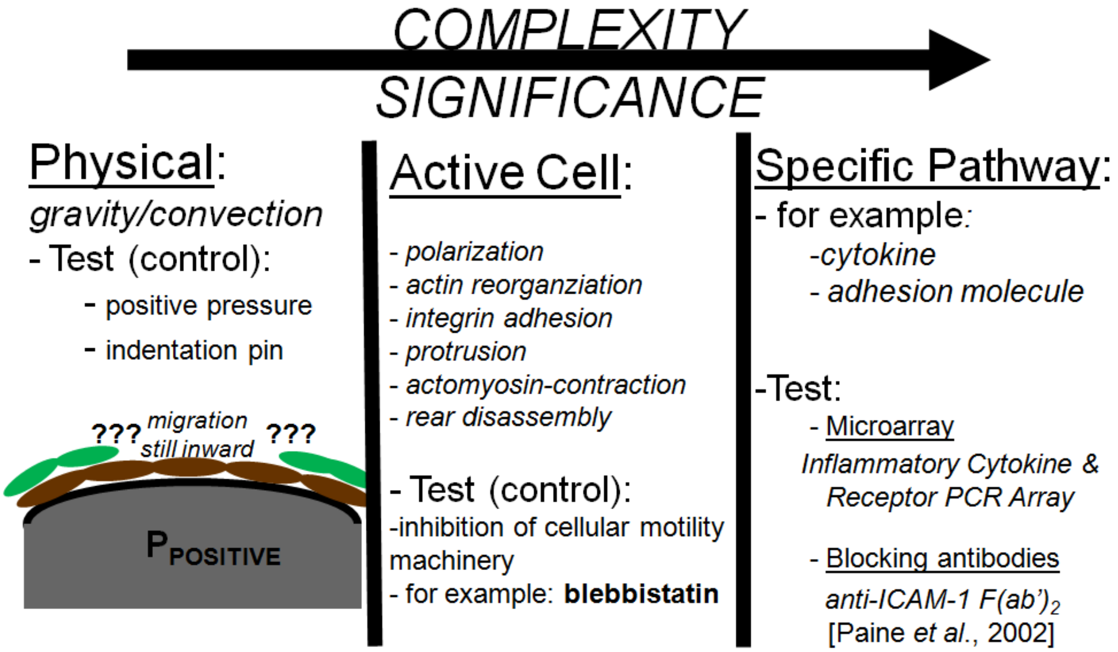

Figure 5.1. Short Term Future Work. Immediate short term studies will focus on resolving the mechanisms of macrophage migration. The significance of the stretch-dependent macrophage migration increases, if we can confirm that the movement results from an active cell process (as opposed to a physical process such as gravity or convection). The specific mechanism will be further targeted based upon continued microarray data.

B. Long Term.

Microfluidic. We have developed microfluidic fabrication and tissue-engineering techniques necessary to model the air-blood barrier. We have verified the feasibility and studied cellular response via independent, stand-alone (non-integrated) devices. For example: (i) in our electrode-embedded microsystem, dynamic detection to barrier disruption was verified using a permeability-altering reagent (TritonX-100) and (ii) in our combined stress microsystem, death and detachment was verified using a live-dead fluorescent stain. The long-term utility of our technological breakthroughs will result from *continued integration* (for example: a microdevice where TEER can be measured in real-time in response to combined fluid and solid mechanical stresses). At the present time, the fabrication techniques are in place for such an integrated microsystem, however, additional issues (*highlighted below*) must be overcome.

An example of a limitation that must be overcome for full integration of the microfluidic technologies described: *membrane surface*. All published TEER recordings have occurred across a cell monolayer cultured on a porous, polyester membranes (pore sizes ~ 400nm). Mechanical stresses have always been actuated through a flexible PDMS membrane (non-porous). The electrical impedance across such a non-porous PDMS membrane has been measured in the MΩ-range (full order of magnitude higher than across the 400nm polyester membrane) – making resolution of TEER across such a PDMS membrane impossible. Studies to fabricate porous PDMS membranes have focused on the selective removal of space-saving particles; however, currently pore size has been too large for consistent cell-culture.

The long-term goal for a Microfluidic “Alveoli on a Chip” can be visualized in Figure 5.2. This system will involve a two-layered microfluidic system. Fluid mechanical stresses in the alveolar region will be controlled through the propagation of menisci. Cyclic stretch will be generated via a flexible cell culture membrane separating the alveolar and endothelial channels. Endothelial cells, cultured on the opposing side of the flexible PDMS membrane will be exposed to shearing from a completely fluid-filled (no air-liquid two-phase flow) endothelial channel. Cell-cell interactions beyond the alveolar-endothelial interface (for example: macrophages across the alveolar surface) or RBCs travelling through the endothelial channel) could also be potentially controlled. Further electrical sensors, (i) such as the TEER recording electrodes presented from our work or (ii) oxygen sensors monitoring the hemoglobin state of RBCs traveling through the endothelial will allow increased understanding of physiologic and pathologic processes, as they occur.

Medical. This research supports clinical observations that cyclic stretch alone is not sufficient to cause the degree of cell injury seen in alveolar pathology, and that surface tension forces, resulting from the propagation of moving meniscus within an alveoli, contribute to cell death and detachment. The microfluidic techniques presented in this research can be easily modified to study other

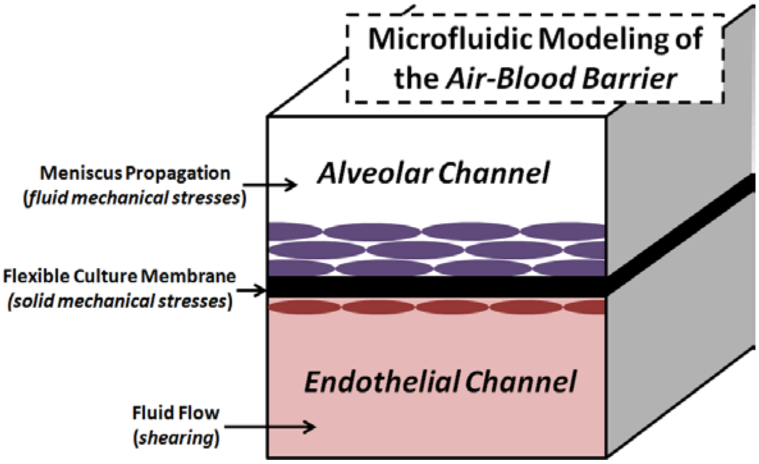

Figure 5.2. Integration of "Alveoli-on-a-Chip" Technologies. Future, microfluidic alveolar devices will incorporate and integrate these technological breakthroughs: (i) two-layered channel, (ii) combined physiologic stress profile, (iii) co-culture, and (iv) recording sensors.

surface tension diseases affecting alveoli. Furthermore, the precise control over respiration profile, as well as ease with which forces can be studied independently and in combination, allows investigation on the efficacy of a variety of ventilation strategies (varying velocity, inhalation/exhalation profile, and frequency) as well as potential clinical therapies (surfactant replacement, liquid ventilation) to deliberately minimize fluid stresses at the phase and location where they are most concentrated (exhalation).

Surfactant Replacement Therapy. Clinical therapies for surface-tension-related diseases that reduce or eliminate surface-tension effects without altering solid mechanical stretch have led to significant reduction in cell injury and improved clinical outcomes. Such clinical observations suggest that stretching alone is not sufficient to cause damage to the degree of air-blood barrier damage seen and that the high fluid mechanical stresses generated at the air-liquid interface play a critical role in pathology and mechanisms of the specific disease. Furthermore, large-scale clinical trials have shown surfactant replacement therapy (SRT) to be effective in the treatment of NRDS; but, somewhat surprisingly, failed to show benefit in the treatment of ARDS. While ARDS can be complicated by a variety of factors including neutrophil infiltration, pulmonary fibrosis, and increased barrier permeability (when compared to NRDS, which is usually limited to surfactant deficiency); the fact that both diseases share a similar mechanism rooted in dysfunctional surfactant and surface-tension based cellular injury makes SRT an attractive and logical treatment for ARDS. The absence of a suitable *in vitro* model capable of recreating both solid and fluid stresses has made systematic study on factors potentially limiting the success of SRT in the treatment of ARDS, but not NRDS, difficult.

Liquid Ventilation. Another clinical therapy for reducing surface tension forces is liquid ventilation, a technique where the alveolus is filled with perfluorocarbon (PFC) liquid, effectively eliminating the air-liquid interface. Liquid ventilation studies have shown improved pulmonary gas exchange in ARDS models, further suggesting that fluid mechanical stresses play some role in the development of ARDS-pathology. Despite these clinical observations and substantial evidence of the role fluid mechanical stresses play in the development of airway injuries, no *in vitro* studies of fluid mechanical effects in an alveolar model of liquid ventilation have been conducted.

Pulmonary Immune Response. The lung is subjected to cyclic stretch during tidal breathing. These changes in epithelial cell surface area may provide new ‘foot holds’ for macrophages patrolling the surface. As a result, areas of the lung with more or less stretch may present different environments for macrophage function. Lung tissue that is partially or completely collapsed (atelectasis) may provide macrophages less opportunity for migration and thus be more susceptible to infection. In addition, ventilation of the lung in is inhomogeneous with more ventilation (stretch) in the lower lung zones when compared to the upper lung zones. It is possible that this may play a role for infections that have a predilection for the upper lung zones (e.g. *M. tuberculosis* or *P. jiroveci*). The current *in vitro* system could be used the role of stretch in phagocytosis of specific organisms.

Appendix I

DNA Linearization through Confinement in Nanofluidic Channels

Nicholas J. Douville, Dongeun Huh, Shuichi Takayama

ABSTRACT

Stretching DNA has emerged as a vital process for studying the physical and biological properties of these molecules. Over the past decade, there has been increasing research interest in utilizing nanoscale fluidic channels to confine and stretch single DNA molecules. Nanofabricated systems for linearizing DNA have revealed new and important insights into the conformation changes of DNA molecules. They also have emerged as innovative techniques for efficiently separating DNA molecules based on size and for physically mapping genetic information along the genome. This review describes physical theories of DNA linearization, current DNA stretching techniques based on nanofabricated channels, and breakthroughs resulting from the use of nanofluidic channels for DNA linearization.

INTRODUCTION

DNA is a long-chain polymer comprising nucleotide monomers linked by phosphodiester bonds. Despite its unusually high mechanical stiffness provided by the double stranded nature and double-helical structure, DNA undergoes dramatic conformational changes such as bending, twisting, and compression [Bustamante *et al*., 2003]. The ability of DNA to change its three-dimensional structure is crucial for packing the extremely long molecule into chromosomes and also serves as a template for encoding and transferring genetic information during transcription and replication. This naturally folded structure of DNA, however, can also complicate mapping, sequencing, and other types of structural analysis of DNA. It is of great fundamental scientific interest as well as of practical importance to study and utilize the physical properties of DNA for separations [Vivoy, 2000], analysis [Heller, 2002], and nanoengineering [Rothemund, 2006; Seeman and Belcher, 2002]. In this review, we will particularly focus on the methods and applications that involve linearization of DNA by confinement.

The mechanical properties of DNA have been studied through a variety of techniques including optical tweezers, magnetic beads, hydrodynamic fluid flow, and, most recently, nanoconfinement [Bustamante, 2003]. Nanoconfinement is a process that constricts DNA molecules within a narrow structure, lowering the entropy of the molecules and forcing the DNA molecule into a stretched configuration. As a result of improved fabrication techniques and incorporation with existing biological research techniques, nanoconfinement is emerging as a promising tool for studying the biophysical properties of DNA and for analyzing genetic information contained therein.

Genetic information is organized linearly along the length of DNA. This information, however, is difficult to "read off", in part, because of extensive folding. DNA stretching facilitates access to this genetic information for a variety of biological research purposes, such as physical gene mapping. Physical gene mapping is the process of determining the relative positions of genes or DNA clones along a chromosome without having to sequence the entire chromosome. The most widely employed approach is restriction mapping. In this technique, DNA clones are digested into smaller fragments using restriction enzymes which cut DNA at specific sequences. The size of the resulting DNA fragments from each clone is then determined by gel electrophoresis. The overlap and relative location of the clones can be modeled by analyzing the patterns of fragments created by digestions using multiple restriction enzymes [Brown *et al*., 1999]. This technique is very useful but limited in that although the size distribution of the fragments from restriction digests of each clone can be obtained, the order of the fragments is lost.

New techniques, most notably molecular combing, have resolved some of the limitations of restriction mapping by allowing analysis of longer DNA segments (up to ~150 kilobases) with retention of DNA fragment order and use of much smaller samples, with an eventual goal of single cells. In molecular combing, one end of the genomic DNA is anchored to a silanized coverslip. The other end is stretched by the hydrodynamic forces exerted on the molecule by a moving meniscus. This stretched, surface-bound DNA can be analyzed using restriction or fluorescence in situ hybridization (FISH) techniques [Michalet *et al*., 1997]. The ability to use molecular combing to analyze long DNA molecules is currently limited by the linearization step. Molecular combing techniques stretch DNA by use of a moving meniscus, which fragments DNA segments larger than a few hundred kb. Inconsistencies in the degree of stretching introduce further variability. These limitations of traditional linearization techniques have impeded various studies including those that require long range mapping. Nanoconfinement offers the ability of linearizing DNA much more precisely and opens the possibility of linearizing much longer DNA molecules than is currently possible.

Another useful application of DNA confinement is the separation of DNA molecules based on length or charge. Gel electrophoresis is currently the most widely used method for separating biological molecules, however, it is limited in its ability to separate molecules greater than 40 kbp. Pulsed-field gel electrophoresis (PFGE) and pulsed field capillary gel electrophoresis (PFCGE) are variations of standard gel electrophoresis that allow separation of longer DNA samples, however, these techniques are generally slow and difficult to perform [Han and Craighead, 2000]. Entropic trapping systems utilize DNA confinement to rapidly separate long DNA molecules. Entropic traps are nanofabricated arrays of alternating thick and thin regions. Large DNA molecules have a greater area in contact with the boundary between thick and thin regions than small DNA molecules, therefore they have a greater probability of escaping confinement.

Consequently, large DNA molecules move more rapidly through the entropic trap. In thick regions, with dimensions near its radius of gyration, dsDNA assumes a relaxed configuration and in thin regions, with dimensions less than its radius of gyration, dsDNA is forced into a stretched configuration [Han *et al*., 1999]. Entropic traps and other confinement-based sieving techniques use DNA linearization to drive the more rapid separation of longer DNA than is possible with current electrophoresis techniques Figure A.1.

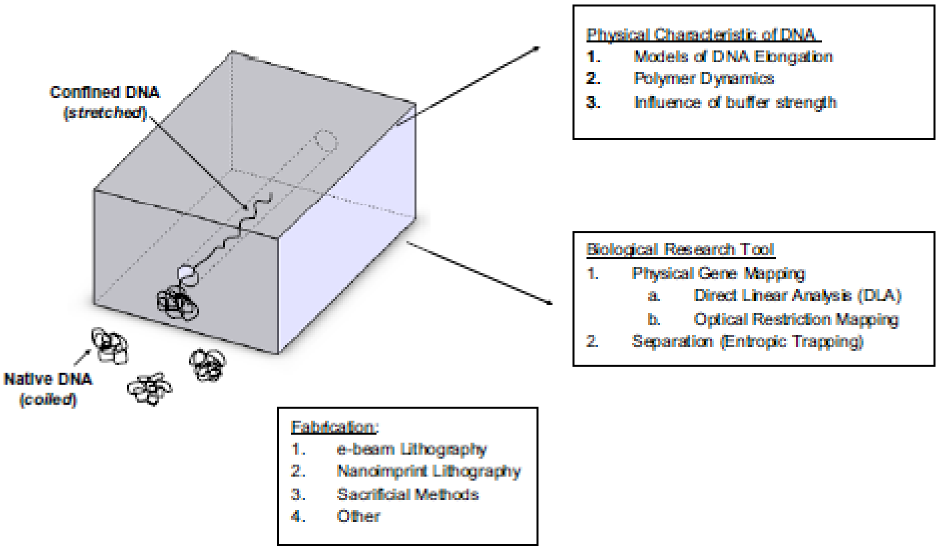

Figure AI.1. Overview of DNA Linearization.

As the ability to rapidly process and analyze large volumes of genetic information has expanded, the need to reliably stretch long DNA molecules has also grown. Applications for DNA nanoconfinement have spread from primarily biophysical research to new, previously unexplored areas, including gene mapping, long-range haplotyping, and separations. This review will:

1. describe the basic principles and techniques for confining DNA in nanochannels;
2. summarize the resulting biological and physical advances;
3. point out existing limitations; and
4. emphasize areas for future study.

BACKGROUND

Lengths of DNA, gene mapping, and importance of DNA linearization

In addition to aiding sequencing, physical gene mapping reveals useful information on genome variation, genetic mutations, and replication dynamics. An overview of typical steps involved in physically mapping the genome is highlighted in Figure AI.2. The longest human chromosome comprises over 250 Mbp, giving a fully stretched length of approximately 8.5 cm. To map the genome, DNA is first sheared or enzymatically digested into DNA fragments with a maximum length of only a few millimeters. These fragments are then incorporated into a bacterial artificial chromosome (BAC) or yeast artificial chromosome (YAC) to amplify their genetic information. The relative order of fragments can be determined by analyzing overlapping sequences of restriction enzymes. Libraries of BAC/YAC fragments can be further digested to fragments of the order of 1000 bp (less than a micron long), which can be directly sequenced. Current techniques for physical gene mapping include restriction digest and optical mapping [Schwartz *et al.*, 1993].

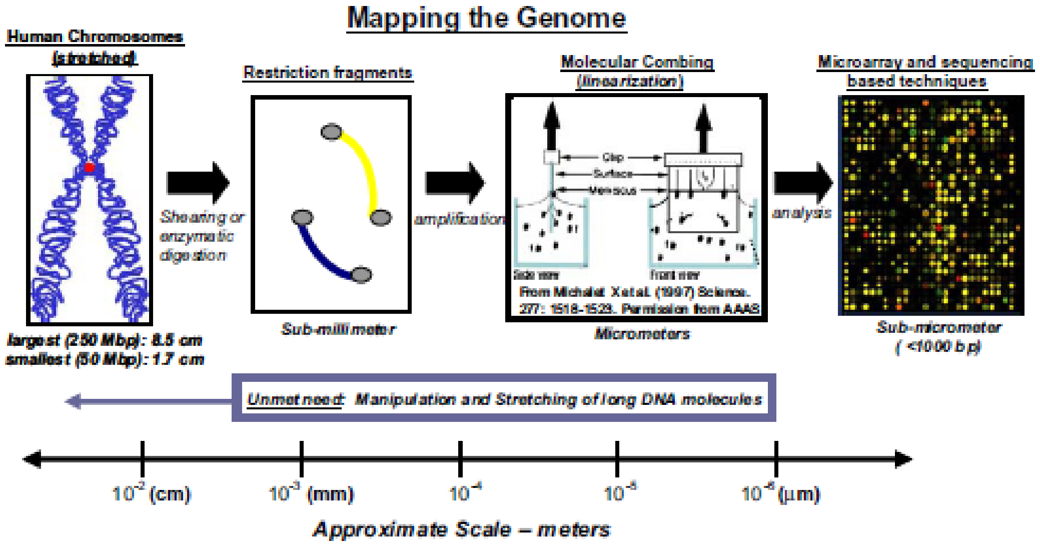

From Michalet X et al. (1997) Science. 277: 1518-1523. Permission from AAAS

Figure AI.2. Mapping the genome. A stretched human chromosome can be as long as 8.5 cm, however, there are no reliable tools to manipulate and stretch DNA molecules of these lengths. Genomic DNA must be fragmented multiple times, amplified by incorporation into a bacterial artificial chromosome (BAC) or yeast artificial chromosome (YAC), and then sequenced or analyzed with microarrays. Traditional techniques for stretching DNA, such as molecular combing, do not allow the reliable manipulation of DNA fragments longer than a few hundred micrometers. Nanoconfinement is a potential mechanism to fill the gap in single-molecule manipulation of long DNA

Physical gene mapping has relied on hydrodynamic forces to linearize DNA. For example, molecular combing linearizes DNA on a silanized coverslip by means of a moving meniscus, allowing the DNA molecule to be analyzed by restriction or fluorescence techniques [Michalet *et al*., 1997]. In another technique, direct linear analysis (DLA) DNA is stretched by the shearing of an accelerating fluid in a microchannel. Chan and colleagues at US Genomics developed a DLA technique capable of mapping DNA molecules as large as 48.5 kbp [Chan *et al*., 2004]. Their technique unwound and stretched DNA in the laminar flow of a tapered microfluidic system.

In many of these techniques, DNA linearization is crucial. The quality and consistency of the linearization, the length of DNA that can be linearized, the amount of sample required, and the user-friendliness determine the usefulness of the techniques. Some areas where enhancements to these traditional techniques are desired include more precise and accurate linearization and ability to stretch longer fragments of DNA. Nanoconfinement-based techniques for DNA linearization offers promise for these types of capability. Such advances would enhance a variety of applications including long-range haplotyping and mapping dynamics of replication over long distances [Zhang *et al*., 2006].

Progression of DNA stretching

A variety of methods have been employed to manipulate and study the structure of DNA. Smith and colleagues were the first to successfully stretch DNA molecules. They chemically attached one end of a DNA molecule to a glass surface and the other end to a magnetic bead that was then exposed to known magnetic and hydrodynamic forces. Their work illustrated the limitations of modeling DNA molecules with the “freely jointed chain” (FJC) model [Smith *et al*., 1992]. Perkins and colleagues used a similar technique to physically stretch a molecule of DNA. They anchored one end of the DNA molecule by optical trapping of a latex microsphere and allowed the other end to elongate with hydrodynamic flow [Perkins *et al*., 1995]. While these methods were useful for understanding the physics of DNA as a polymer, they were not practical for many biological applications, such as gene mapping. A linearization technique that enabled DNA to be easily stretched and read is molecular combing. In this method, DNA molecules are straightened and aligned on a coverslip by a moving meniscus [Michalet *et al*., 1997]. Another technique elongates DNA molecules in a microfluidic channel parallel to the direction of flow, allowing fluorescently labeled DNA molecules to be easily analyzed [Dimalanta *et al*., 2004; Larson *et al*., 2006; Kim *et al*., 2007; Namasivayam *et al*., 2002]. Bakajin and colleagues studied the elongation of single DNA molecules in a confined slit between two planar surfaces [Bakajin *et al*., 1998]. This review will further explore research employing this final confinement technique to stretch DNA.

Theory

Double stranded DNA (dsDNA) has a semi-rigid structure, forcing it to behave in a similar fashion to a uniform rod having linear elasticity. Consequently it can be modeled using the “worm-like chain” (WLC) model that describes the DNA molecule as a continuously flexible, as opposed to the freely joint chain model used to describe polymers that can only bend between discrete segments [Flory, 1953]. The radius of gyration of the DNA molecule is the theoretical measure of the molecule’s size based upon the root-mean-square distance from the molecules center of mass and, therefore, depends on the number of base pairs comprising a fragment of DNA. Thus, consistent with this theory, when DNA is confined within a channel whose diameter is less than its radius of gyration, the DNA molecule extends into a series of non-interpenetrating blobs as a result of self-exclusion. DeGennes’s theory on polymer dynamics further predicts that:

1. monomer density will be uniform along the channel, and

2. DNA extension in the nanochannel will scale linearly with contour length, according to Equation A.1 [deGennes, 1979; Tegenfeldt *et al*., 2004]:

$$L_z = [L(\omega P)^{1/3}] / [D^{2/3}]$$

- L_Z is the extended length of the DNA molecule.
- P is the persistence length, a basic mechanical property quantifying the stiffness of a macromolecule which varies inversely with ionic strength. It is approximately 50-60 nm under physiological conditions but has been shown to be greater than 250 nm at low salt concentrations [Jo *et al*., 2007]. Staining with intercalating dye increases persistence length.
- ω is the DNA width. The effective width varies with ionic environment, owing to electrostatic repulsion between DNA segments. It is approximately 2 nm under physiological conditions but has been shown to be as high as 20 nm at low salt concentrations [Reisner *et al*., 2007].
- L is the contour length, the theoretical length of a totally stretched DNA molecule. The value depends on the number of base pairs in a specific DNA strand, usually calculated assuming 0.34 nm per base pair. Staining with intercalating dye increases contour length.
- D is the diameter of the confining channel
-

Thus, the percentage of total contour length that DNA can be stretched is contingent on the diameter of the confining channel. For example, according to the deGennes's equation presented above, a 100-nm diameter channel is capable of stretching DNA to ~20% of its total contour length, when the persistence length is assumed to be 50 nm. While there are methods to modify these variables, for example high ionic strength buffer can increase DNA's persistence length, basic theory mandates dimensions less than DNA's radius of gyration for confinement-induced elongation [Jo *et al*., 2007]. DeGennes's theory is valid only when the channel diameter is greater than the persistence length of

DNA (~50-60 nm). When the channel diameter is less than the persistence length the interplay between confinement effects and the intrinsic elasticity of DNA determines the extension and extension must be modeled by the Odijk regime, an alternative model which accounts for the intrinsic elasticity of DNA [Reisner *et al*., 2004].

OVERVIEW OF NANOFABRICATION TECHNIQUES

As described in the theoretical considerations, nanoconfinement-based DNA linearization requires channels with dimensions on the sub-micron scale. Because traditional photolithographic techniques lose resolution and softlithographic materials collapse at dimensions this small, innovative nanofabrication techniques were devised to allow DNA linearization via nanoconfinement. Several of the major fabrication principles are outlined below with a brief discussion of the advantages and disadvantages of each method.

Sacrificial methods

Sacrificial techniques refer to a series of fabrication steps that enable a specific layer to be preferentially removed by using chemical etchants. Figure AI.3 depicts a typical sacrificial fabrication technique. A sacrificial layer is uniformly deposited on to a wafer, then patterned using optical lithography, essentially holding the position of the future nanochannel. Next, the sacrificial layer is coated with a ceiling layer and then selectively removed using chemical etchants that do not remove the floor or ceiling layers. The Craighead group has employed sacrificial fabrication techniques to fabricate channels with different specifications for a variety of applications [Foquet *et al*., 2002; Turner *et al*., 2002; Stavis *et al*., 2005]. Stavis and colleagues used polycrystalline silicon for the sacrificial layer, fused silica for the surrounding ceiling, walls, and base, and tetramethylammonium hydroxide (TMAH) as the chemical etchant. Polysilicon was deposited on the glass wafer using low pressure chemical vapor deposition (LPCVD) and then patterned using optical lithography. Glass was selected for the surrounding material because it was optically transparent, chemically inert, and minimized background fluorescence. TMAH was selected because it preferentially removes polysilicon over fused silica. Polysilicon was selected as the sacrificial layer, but materials ranging from polymer coatings to organic solvents could also have been used. Sacrificial methods provide the ability to create ultrasmall microfluidics systems with very tight dimensional tolerance; for long fluidic channels with cross-sectional dimensions less than 1 μm, however, removal can take an extremely long time, and be difficult.

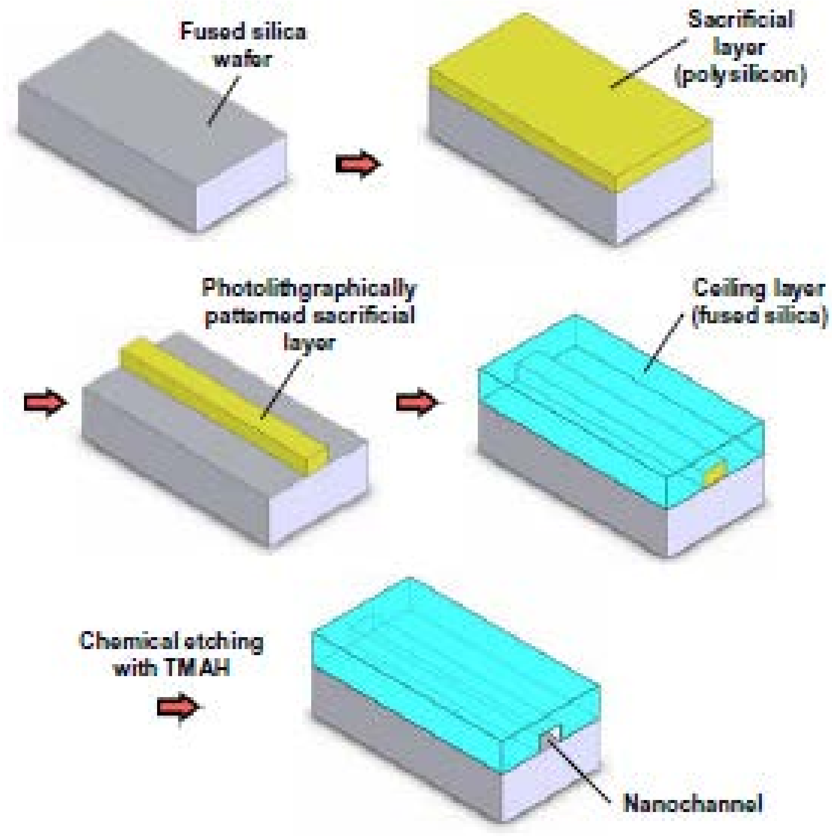

Figure AI.3. Sacrificial Technique for Fabricating a Nanofluidic Channel [Foquet *et al*., 2002]

Harnett, Coates, and Craighead fabricated nanochannels using temperature increases to depolymerize a sacrificial layer of polycarbonate [Harnett *et al*., 2001]. The polycarbonate layer was first patterned using e-beam lithography then capped with an oxide layer using a low-temperature sputtering procedure. When the system was heated to 300 °C, the polycarbonate layer depolymerized leaving channels with dimensions 140 nm×1 μm.

Li and colleagues used a similar technique, patterning the sacrificial polymer poly(butylnorbornene) (PNB) instead of polycarbonate and using nanoimprint lithography (NIL) instead of e-beam lithography to pattern the channel features [Li *et al*., 2003]. After the PNB sacrificial layer was patterned, SiO2 was deposited using PECVD, sealing the channel features. The PNB was then decomposed by heating the system to 440 °C leaving open channels with dimensions less than 100 nm which were used to image elongated DNA molecules. This technique could be modified by decreasing the molecular weight of the sacrificial polymer and modifying the deposition process, allowing channels with even smaller dimensions to be fabricated.

Electron beam lithography

Electron beam lithography is a technique that patterns nanoscale features on a reactive surface with a single beam of electrons. In e-beam lithography electrons are emitted from a conductive source by applying sufficient heat or electric field. The emitted electron beam is then focused through magnetic and electrostatic forces to the desired diameter [McCord and Rooks, 1997]. Since minimum e-beam width is on the nanometer-scale, this technique provides the highest resolution and avoids many of the limitations of photolithography, for example diffraction of light. The major limitation is that e-beam lithography is lower throughput and a much more expensive than photolithography. Using electron beam lithography, Chou and colleagues patterned a silicon dioxide mold with features less than 25 nm. Next they etched away the SiO_2 with a fluorine-based reactive ion etchant. This mold was reproduced quickly and inexpensively in a PMMA polymer using nanoimprint lithography (NIL) which is discussed in more detail in the next section [Chou *et al*., 2002].

Nanoimprint lithography (NIL)

Extending traditional lithographic techniques to the submicron level was a crucial advance with applications in fields ranging from integrated circuitry and optics to

DNA linearization. Although lithography holds the potential to fabricate multiple, complex systems quickly and inexpensively, traditional lithographic techniques are theoretically limited by the wavelength of light used for exposure to minimum dimensions near 100 nm [Cao *et al*., 2002]. This theoretical dimension limit has been lowered in a variety of different ways. X-ray lithography has been used to successfully produce channels as small as 20 nm. Chou and colleagues developed an alternative lithographic technique capable of achieving 25 nm sized with a period of 70 nm [Chou *et al*., 1996]. They incorporated compression molding techniques with traditional lithographic techniques. A layer of PMMA polymer spun on to a silicon substrate was first heated above the glass transition temperature of PMMA. A mold containing nanofeatures fabricated via electron beam lithography was imprinted into the PMMA. Finally, oxygen-based reactive ion etching was used to anisotropically etch the features through the entire reactive layer. At room temperature, the relatively rigid PMMA polymer retains nanoscale features much better than the PDMS elastomers used in soft lithography, which readily deform and collapse. The technique of Chou and colleagues resulted in smooth surfaces, sharp corners, and high aspect ratios that conformed well to the original mold.

UNCONVENTIONAL NANOFABRICATION TECHNIQUES

Organic nanotubes

Karlsson and Orwar demonstrated the ability to fabricated networks of phospholipid nanotubes with controllable connectivity, nanotube length, and nanotube extension angle [Karlsson *et al*., 2001]. They used multi-lamellar and uni-lamellar liposomes as the starting material to build liposome networks with various lipid composition, wettability, and functionality. The nanotubes were formed by mechanical fission of surface-immobilized liposomes with flexible carbon fibers. These initial liposomes were then drawn into lipid nanotubes by micromanipulation of the carbon fibers. The dimensions of these liposome nanotubes could be controlled to a range of several hundred μm in length and diameters of 200-400 nm. Although organic nanotubes have potential for use in

DNA linearization, applications have been limited because of their high of flexibility.

Brochard-Wyart and colleagues examined the behavior of polymers within a lipid bilayer tubule, modeled as a soft, deformable tube with surface tension (σ) and curvature energy (K) [Brochard-Wyart *et al*., 2005]. Their model showed that when the curvature energy exceeds thermal energy two conformations dominate:

1. the extended chain within an unperturbed tube, or
2. the spherical coil within a globular deformation of the tube.

For most conditions soft-tubes assume a “globular” as opposed to “snake-like” configuration, which agrees with the experimental observations of DNA confined within lipid tubes.

Inorganic nanotubes

A final fabrication method attempts to confine DNA within inorganic nanotubes. Inorganic nanotubes hold a number of advantages over traditional nanopore devices. These nanotubes have a high aspect ratio allowing confinement of the entire DNA molecule. Additionally, the planar geometry allows simultaneous optical and electrical probing in a structure that can easily be incorporated into lab-on-chip systems or microelectronics. Fan and colleagues translated silicon nanowires into silica nanotubes through oxidation/etching [Fan *et al*., 2005]. They demonstrated the capability of fabricating nanotubes with an inner diameter of 50 nm and a controlled wall thickness and pore size as small as 10 nm, which theoretically would fully stretch dsDNA (persistence length ~50 nm). They used these nanotubes to measure changes in electrical current that result from ionic blockage after the introduction of λ-phage DNA. Because the current change was shown to be narrow and non-reversible, the authors hypothesized that these current changes corresponded to individual, identical translocation events through the nanotube.

Nanocracking

Adelung and colleagues introduced a novel technique for molding nanoscale wires (<16 nm diameter) from cracks induced within a carbon thin film [Adelung *et al*., 2004]. These cracks resulted from thermal cycling or swelling of the base layer beneath the thin film. Zhu and colleagues developed a technique for inducing cracks within an oxidized thin film layer of poly (dimethylsiloxane) (PDMS) [Zhu *et al*., 2005]. They demonstrated the ability to dynamically modulate crack diameter by adjusting mechanical strain on the system-enabling the possibility of dynamically transitioning from a “loading” and “stretching” channel diameter. Adelung and colleagues used the nanocrack as a template for patterning a Pt or Au nanowire, while Zhu and colleagues used their nanocracks a scaffold for cell growth; both demonstrated the capability of repeatedly fabricating nanoscale structure on a much smaller scale than previously described, however, Huh and colleagues built upon the nanocracking research of Zhu and colleagues to develop a technique to fabricate tunable nanochannels capable of DNA linearization.

Huh and colleagues first generated an ordered array of cracks by mechanically stretching plasma-oxidized (PDMS) [Huh *et al*., 2007]. The resulting cracks were transferred to ultraviolet-curable epoxy then cast using soft lithography techniques into PDMS prepolymer. When this was sealed against another flat slab of oxidized PDMS, Huh and coworkers were able to form a channel with an isosceles triangle profile, the dimensions of which could be dynamically modulated by applying perpendicular force. In the relaxed state these nanochannels had an average base length of 688 nm and average height of 78 nm. When perpendicular force is applied, the channel reversibly narrows. The ability to dynamically modulate channel dimensions overcomes one of the major limitations of DNA nanoconfinement-loading in channels <100 nm. DNA can be effectively loaded into a channel with large dimensions and after it is contained within the channel, can be linearized by decreasing channel dimension.

Other

Other nanofabrication techniques have been developed to overcome specific limitations of the above techniques and have been successfully incorporated into a variety of system for DNA linearization. Devoe and colleagues used thermal deformation techniques commonly employed by the telecommunications industry for fiber optic fabrication to construct parallel arrays of nanochannels with critical dimensions as small as 400 nm [Sivanesan *et al*., 2005]. In their work, Devoe and colleagues fabricated microchannels into rectangular polycarbonate (PC) performs. The PC was then heated above its glass transition temperature ($T_g \approx 150$ °C) and drawn under constant uniaxial tension to form nanochannels with repeatable final dimensions (<5% deviation in dimensions) [Sivanesan *et al*., 2005]. The non-uniform stress field transferred to the channels during the thermal deformation technique changes the cross section of the channels from a trapezoidal initial shape to a more circular or elliptical final channel. Fabrication is limited by non-uniform stress and strain fields during fabrication, resulting from rectangular pre-forms. Detailed modeling of both temperature transition and mechanical stretching also remains a problem limiting fabrication techniques. Although scaling down these techniques remains feasible, thermal deformation has only been shown to produce channels with critical dimensions 400 nm (stretched from an initial size of 20 μm), successful DNA linearization in channels formed by thermal expansion will require critical dimensions to decrease and many of these potential problems to be overcome. Figure AI.4 shows DNA linearization in different devices. The type of nanostructure used in the research described is specifically highlighted in Tables A.1 and A.3.

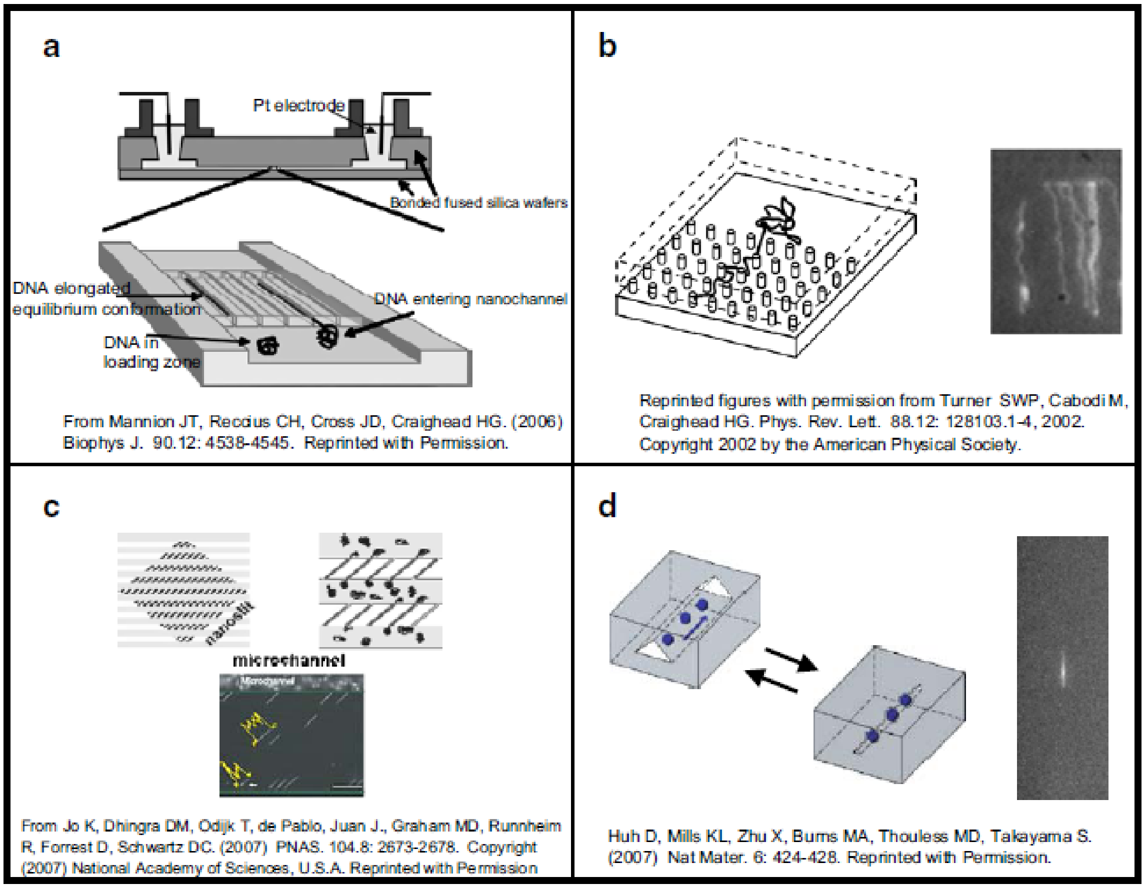

From Mannion JT, Reccius CH, Cross JD, Craighead HG. (2006) Biophys J. 90.12: 4538-4545. Reprinted with Permission.

Reprinted figures with permission from Turner SWP, Cabodi M, Craighead HG. Phys. Rev. Lett. 88.12: 128103.1-4, 2002. Copyright 2002 by the American Physical Society.

From Jo K, Dhingra DM, Odijk T, de Pablo, Juan J., Graham MD, Runnheim R, Forrest D, Schwartz DC. (2007) PNAS. 104.8: 2673-2678. Copyright (2007) National Academy of Sciences, U.S.A. Reprinted with Permission

Huh D, Mills KL, Zhu X, Burns MA, Thouless MD, Takayama S. (2007) Nat Mater. 6: 424-428. Reprinted with Permission.

Figure AI.4. Devices for DNA nanoconfinement. A variety of systems have been used to linearize DNA by nanoconfinement. (a) Nanochannel arrays. Channels with nanoscale dimensions used to confine and elongate DNA molecules. (b) Nanopillar arrays. A system of densely packed pillars between a ceiling and floor layer function as an artificial gel or mesoporous solid. (c) Nanoslits. Diagonal nanoslits overlay a series of horizontal microchannels and force DNA elongation as the nanoslits are electrokinetically loaded from the microchannels. (d) Reconfigurable—tuneable/elastomeric. Applying compressive force to an elastomeric (PDMS) channel reversibly decreases the cross-sectional area of the channel, allowing DNA to be easily loaded in larger channel dimensions and stretched in a smaller channel

DNA LINEARIZATION AND STRETCHING IN NANOCHANNELS

DNA molecules assume a linearized state when confined to nanochannels, because of self-exclusion [Tegenfeldt *et al*., 2004]. The major advantage of nanoconfinement over traditional linearization techniques is that the entire confined DNA molecule is theoretically exposed to the same confinement force, allowing a uniform stretch. This contrasts with traditional linearization techniques which exert a high stretching force at the anchored or confined end which decreases along the length of the molecule. In addition to improved consistency, nanoconfinement offers the ability to integrate images of the DNA in its stretched state over long periods.

The ability to linearize DNA through nanoconfinement is a relatively recent advance combining breakthroughs from nanotechnology and genetic analysis. Table A.1 describes some of the breakthroughs which enabled DNA linearization and highlights some of the biophysical properties revealed by this research.

In one of the earliest studies, Bakajin and colleagues studied the elongation and polymer dynamics of single DNA molecules in a novel environment-a confined slit between planar surfaces [Bakajin *et al*., 1998]. The authors stretched individual DNA molecules into a U-shaped conformation around nanofabricated posts varying in height from 0.1 to 10 μm and measured the corresponding degree of elongation. These experiments demonstrated that the transient extension depends on the degree of confinement, a basic premise for future studies of DNA linearization in nanochannels.

Turner, Cabodi, and Craighead demonstrated polymer motion resulting from a confinement entropic force as opposed to the stretching entropic force [Turner *et al*., 2002]. In their work they stretched T2 phage DNA to approximately 35% of its contour length and proved that DNA confinement could be used to study polymer dynamics. They also demonstrated the potential for separating long polyelectrolytes, such as DNA, based upon length, using the principles of nanoconfinment-induced entropic force.

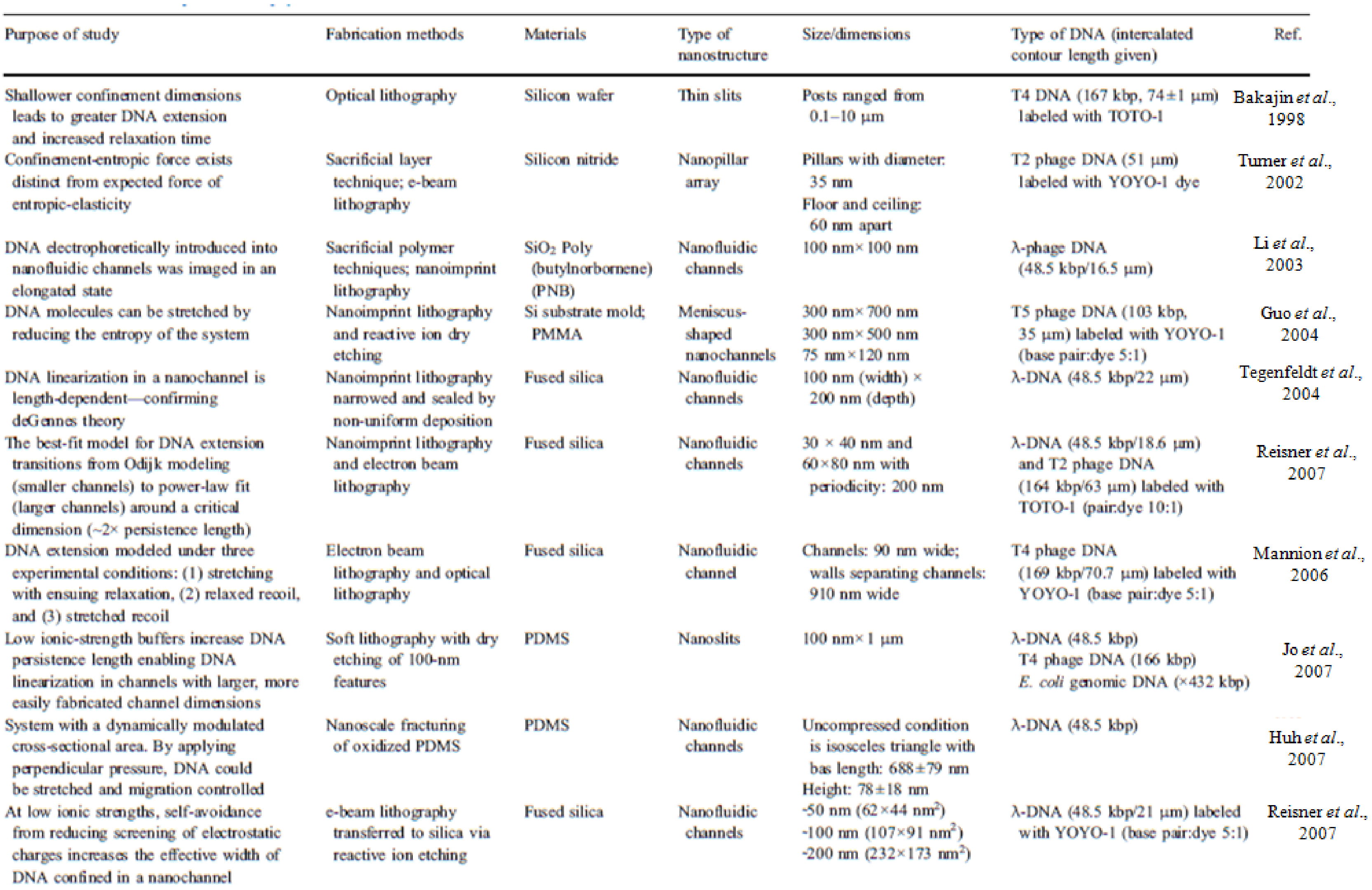

Purpose of study	Fabrication methods	Materials	Type of nanostructure	Size/dimensions	Type of DNA (intercalated contour length given)	Ref.
Shallower confinement dimensions leads to greater DNA extension and increased relaxation time	Optical lithography	Silicon wafer	Thin slits	Posts ranged from 0.1–10 μm	T4 DNA (167 kbp, 74±1 μm) labeled with TOTO-1	Bakajin *et al.*, 1998
Confinement-entropic force exists distinct from expected force of entropic-elasticity	Sacrificial layer technique; e-beam lithography	Silicon nitride	Nanopillar array	Pillars with diameter: 35 nm Floor and ceiling: 60 nm apart	T2 phage DNA (51 μm) labeled with YOYO-1 dye	Turner *et al.*, 2002
DNA electrophoretically introduced into nanofluidic channels was imaged in an elongated state	Sacrificial polymer techniques; nanoimprint lithography	SiO_2 Poly (butylnorbornene) (PNB)	Nanofluidic channels	100 nm× 100 nm	λ-phage DNA (48.5 kbp/16.5 μm)	Li *et al.*, 2003
DNA molecules can be stretched by reducing the entropy of the system	Nanoimprint lithography and reactive ion dry etching	Si substrate mold; PMMA	Meniscus-shaped nanochannels	300 nm× 700 nm 300 nm× 500 nm 75 nm×120 nm	T5 phage DNA (103 kbp, 35 μm) labeled with YOYO-1 (base pair:dye 5:1)	Guo *et al.*, 2004
DNA linearization in a nanochannel is length-dependent—confirming deGennes theory	Nanoimprint lithography narrowed and sealed by non-uniform deposition	Fused silica	Nanofluidic channels	100 nm (width) × 200 nm (depth)	λ-DNA (48.5 kbp/22 μm)	Tegenfeldt *et al.*, 2004
The best-fit model for DNA extension transitions from Odijk modeling (smaller channels) to power-law fit (larger channels) around a critical dimension (~2× persistence length)	Nanoimprint lithography and electron beam lithography	Fused silica	Nanofluidic channels	30 × 40 nm and 60×80 nm with periodicity: 200 nm	λ-DNA (48.5 kbp/18.6 μm) and T2 phage DNA (164 kbp/63 μm) labeled with TOTO-1 (pair:dye 10:1)	Reisner *et al.*, 2007
DNA extension modeled under three experimental conditions: (1) stretching with ensuing relaxation, (2) relaxed recoil, and (3) stretched recoil	Electron beam lithography and optical lithography	Fused silica	Nanofluidic channel	Channels: 90 nm wide; walls separating channels: 910 nm wide	T4 phage DNA (169 kbp/70.7 μm) labeled with YOYO-1 (base pair:dye 5:1)	Mannion *et al.*, 2006
Low ionic-strength buffers increase DNA persistence length enabling DNA linearization in channels with larger, more easily fabricated channel dimensions	Soft lithography with dry etching of 100-nm features	PDMS	Nanoslits	100 nm× 1 μm	λ-DNA (48.5 kbp) T4 phage DNA (166 kbp) *E. coli* genomic DNA (×432 kbp)	Jo *et al.*, 2007
System with a dynamically modulated cross-sectional area. By applying perpendicular pressure, DNA could be stretched and migration controlled	Nanoscale fracturing of oxidized PDMS	PDMS	Nanofluidic channels	Uncompressed condition is isosceles triangle with bas length: 688±79 nm Height: 78±18 nm	λ-DNA (48.5 kbp)	Huh *et al.*, 2007
At low ionic strengths, self-avoidance from reducing screening of electrostatic charges increases the effective width of DNA confined in a nanochannel	e-beam lithography transferred to silica via reactive ion etching	Fused silica	Nanofluidic channels	-50 nm (62×44 nm^2) -100 nm (107×91 nm^2) -200 nm (232×173 nm^2)	λ-DNA (48.5 kbp/21 μm) labeled with YOYO-1 (base pair:dye 5:1)	Reisner *et al.*, 2007

Table AI.1. Historical Development of Biophysical Studies in Nanochannels.

Guo and colleagues began to characterize DNA linearization due to nanoconfinement in a poly(methyl methacrylate) (PMMA) polymer channel fabricated using nanoimprint lithography (NIL). Using T5 phage DNA of 103 kb (contour length 35 μm) stretched in channels of various dimensions, the authors demonstrated that the degree of stretching is inversely proportional to the channel dimensions [Guo *et al*., 2004].

Tegenfeldt and colleagues conducted experimental DNA stretching using a ladder of concatamers of the 48.5 kbp λ-monomer [Namasivayam *et al*., 2002]. They fabricated 100 nm width x 200 nm depth using nanoimprint lithography pioneered by Chou and coworkers and measured the end-to-end distances of a DNA molecule captured by a camera in 100-ms duration. Their data showed clear maxima at the first four peaks (L_z = 8 ± 1 μm; 16 ± 1μm; 24 ± 1 μm; 32 ± 1 μm). Because the contour length of a single λ-monomer is 22 μm, the extension factor for λ-monomers in 100-nm channels is ε=0.36 (L_z/L). Their work demonstrated a resolution of 400 bp in 1 min.

Reisner and colleagues showed that DNA molecule stretching is a function of channel width [Reisner *et al*., 2007]. In channels above a critical dimension (approximately twice the persistence length of the DNA), extension can be well modeled by the power law-experimentally fit as a function of $D^{-0.85}$. In channels below this critical dimension, the extension is best estimated by the Odijk model. They fabricated nanochannels with widths ranging from 30-400 nm, on fused silica, using both electron-beam and nanoimprint lithography. λ-phage DNA (48.5 kbp) and T2 DNA (164 kbp) dyed with TOTO-1 were stretched in nanochannels ranging from 30–400 nm. The Odijk and power-law models converge at a critical dimension 110 nm, approximately twice the persistence length of dsDNA.

Reccius and colleagues were the first to quantitatively investigate DNA relaxation from a compressed, rather than stretched state [Reccius *et al*., 2005]. Using high-precision optical equipment, they studied the behavior of λ-phage DNA compressed inside nanochannels, confirming that DNA molecules confined within a nanochannel behave as predicted by deGennes's polymer model.

DNA molecules loaded into a nanoarray by electric force, recoil upon removal of the electric field. Confinement of DNA to a nanochannel, unlike a nanoarray, allows entropic recoil in a single axis of motion. Mannion and colleagues capitalized on this property, using nanochannels to study the molecular motion and folding properties of DNA in 100 nm nanochannels [Mannion *et al*., 2006]. They drove T4-bacteriophage DNA (169 bp) stained with YOYO-1 entirely into nanochannels fabricated in fused silica via nanoimprint and electron beam lithography. They then tested the molecular response of DNA to a variety of conditions including *stretching with ensuing relaxation*, *relaxed recoil*, and *stretched recoil*. Their best-fit model for the three experimental conditions is summarized in Table A.2.

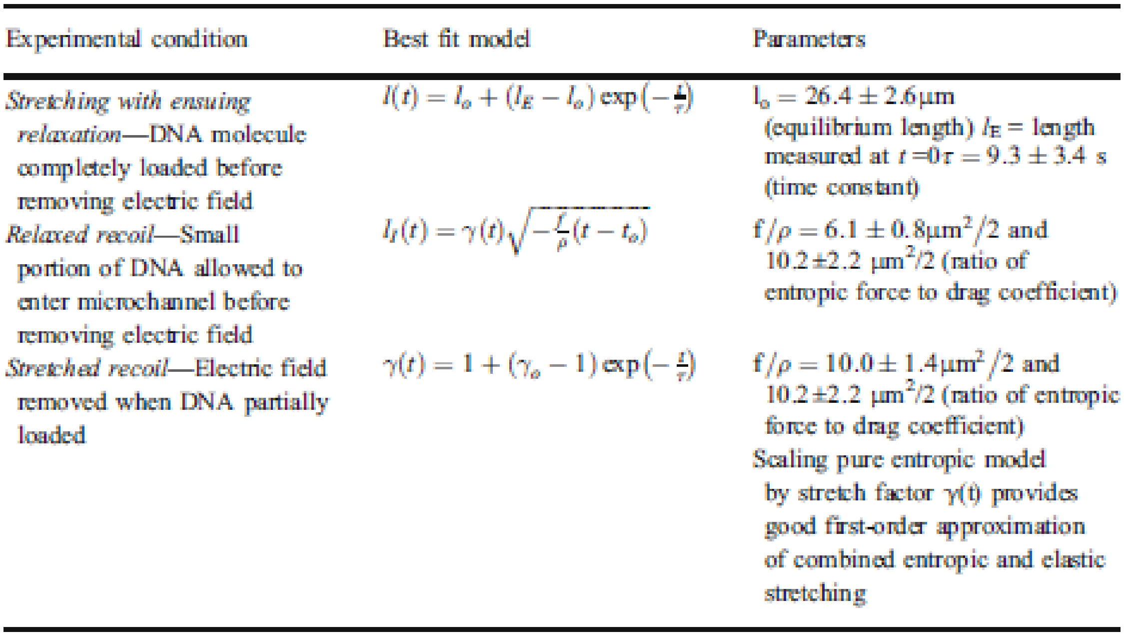

Experimental condition	Best fit model	Parameters
Stretching with ensuing relaxation—DNA molecule completely loaded before removing electric field	$l(t) = l_o + (l_E - l_o)\exp\left(-\frac{t}{\tau}\right)$	$l_o = 26.4 \pm 2.6\mu m$ (equilibrium length) l_E = length measured at $t = 0$ $\tau = 9.3 \pm 3.4$ s (time constant)
Relaxed recoil—Small portion of DNA allowed to enter microchannel before removing electric field	$l_l(t) = \gamma(t)\sqrt{-\frac{f}{\rho}(t - t_o)}$	$f/\rho = 6.1 \pm 0.8\mu m^2/2$ and 10.2 ± 2.2 $\mu m^2/2$ (ratio of entropic force to drag coefficient)
Stretched recoil—Electric field removed when DNA partially loaded	$\gamma(t) = 1 + (\gamma_o - 1)\exp\left(-\frac{t}{\tau}\right)$	$f/\rho = 10.0 \pm 1.4\mu m^2/2$ and 10.2 ± 2.2 $\mu m^2/2$ (ratio of entropic force to drag coefficient) Scaling pure entropic model by stretch factor $\gamma(t)$ provides good first-order approximation of combined entropic and elastic stretching

Table AI.2 Summary of the Results of Mannion *et al*., 2006. Improved modeling of DNA response allows a better separation of long DNA molecules (kb-Mb).

Riehn, Austin, and Sturm transitioned from studying one-dimensional or isotropic two-dimensional systems to an asymmetric lattice of nanochannels [Riehn *et al*., 2005]. They designed a system with intersecting perpendicular nanochannel arrays with different cross-sectional dimensions. Under DC voltage, λ-DNA was stretched and aligned within the wider of the two channel dimensions (130 nm width). When AC voltage was added to the DC bias, the DNA molecule turned 90°, aligning and stretching along the smaller channel dimensions (100 nm width). This orientation resulted because local electric field strength within the channels is inversely related to their cross-sectional area. AC electric fields reverse the sign of the net force driving the DNA molecule into the smaller channels. Upon removal of the AC current, the DNA molecule slowly relaxed into the wide channel. The ability to dynamically modulate the orientation of DNA molecules confined within nanochannels increases the potential to target, sort, and control DNA molecules.

Because DNA persistence length is inversely proportional to the ionic strength of the buffer solution, Jo and colleagues developed a novel method for stretching DNA molecules in larger, more easy to fabricate, systems [Jo *et al*., 2007]. By lowering the salt-concentration of the buffer solution, the authors were able to linearize T4 DNA molecules in 100 nm x 4 μm channels. Their results agreed with stretching data obtained by Reisner and colleagues in much smaller 30 nm x 40 nm channels. While a useful technique for studying the biophysical properties of DNA, lowering buffer concentration greatly limits the biological applications by decreasing the spectrum of enzymes that can be employed and modeling non-physiological conditions.

Huh and colleagues introduced a system capable of dynamically and reversibly modulating the entropy of a single DNA molecule [Huh *et al*., 2007]. Their system comprised elastomeric nanochannels whose cross-sectional dimensions could be modified by the addition of perpendicular force. The channel character was optimized so that addition of this force allowed the selective passage of molecules or nanoparticles. In an uncompressed channel, fluorescently labeled λ-phage DNA molecules (48.5 kbp) were stretched to ~30% of their contour length and traveled through the length of the nanochannel without any additionally changes in length. When 22 kPa of perpendicular pressure was applied to the nanochannel, the cross-sectional area was reduced causing further elongation of the DNA molecule (~75% of contour length). Although the upstream end demonstrated no electrophoretic movement, the downstream end showed continued extension, reaching an equilibrium length of ~13.6 μm at which point electrophoretic movement through the channel resumed. When compressive force resumed, the λ-phage DNA shrank to its original length within 1 minute.

Nanochannel confinement of DNA has evolved immensely over the past decade. Early processes required expensive and equipment-intensive electron-beam lithography of SiO_2 molds. Newer techniques have turned to polymers such as PDMS and PMMA, enabling more rapid and less expensive fabrication. Innovative fabrication techniques have continued to shrink the channel dimensions that can be accurately fabricated. Research efforts also have focused on continuing to improve DNA loading techniques to match this decrease in channel size.

BIOLOGICAL APPLICATIONS

The most common biological uses of DNA linearization in nanochannels are physical gene mapping and fragment separations. Biological applications of DNA linearization are described in Table A.3.

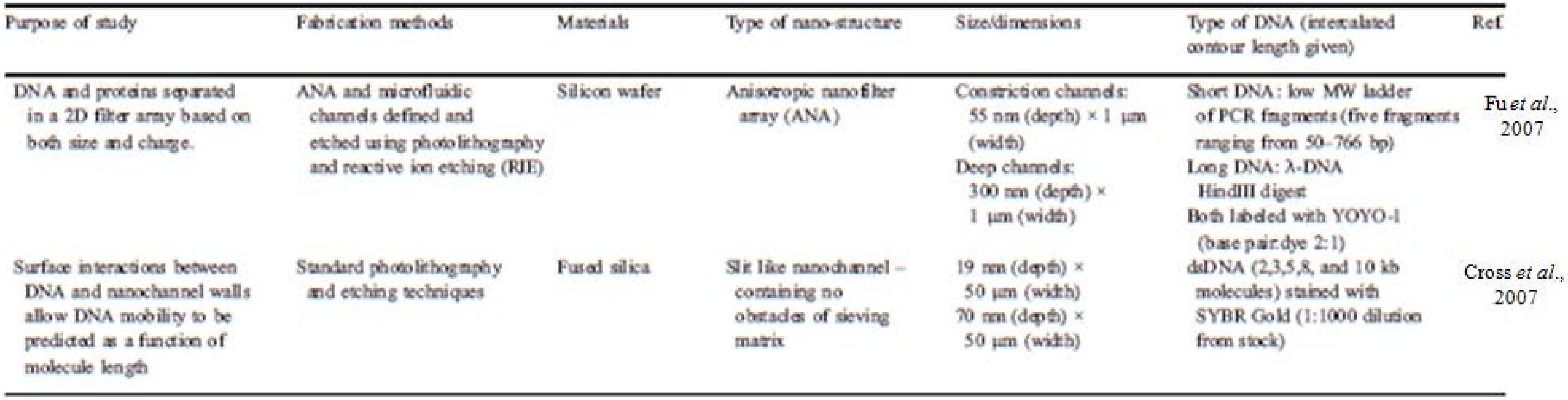

Purpose of study	Fabrication methods	Materials	Type of nano-structure	Size/dimensions	Type of DNA (intercalated contour length given)	Ref.
DNA and proteins separated in a 2D filter array based on both size and charge.	ANA and microfluidic channels defined and etched using photolithography and reactive ion etching (RIE)	Silicon wafer	Anisotropic nanofilter array (ANA)	Constriction channels: 55 nm (depth) × 1 μm (width) Deep channels: 300 nm (depth) × 1 μm (width)	Short DNA : low MW ladder of PCR fragments (five fragments ranging from 50–766 bp) Long DNA: λ-DNA HindIII digest Both labeled with YOYO-1 (base pair:dye 2:1)	Fu *et al.*, 2007
Surface interactions between DNA and nanochannel walls allow DNA mobility to be predicted as a function of molecule length	Standard photolithography and etching techniques	Fused silica	Slit like nanochannel – containing no obstacles of sieving matrix	19 nm (depth) × 50 μm (width) 70 nm (depth) × 50 μm (width)	dsDNA (2,3,5,8, and 10 kb molecules) stained with SYBR Gold (1:1000 dilution from stock)	Cross *et al.*, 2007

Table AI.3. The Two Major Applications of DNA Linearization in Biological Research are for Physical Gene Mapping and Molecular Separation.

Physical gene mapping

Foquet and colleagues used nanochannels to resolve the size of restriction fragments and measure the total concentration of DNA within a sample [Foquet *et al*., 2002]. Although they demonstrated the ability to distinguish *Hind*III digested restriction fragments greater than 564 bp, they were unable to resolve the smallest fragment at a size of 130 bp using fluorescence correlation spectroscopy (FCS) [Foquet *et al*., 2002]. In etched fluidic channels <1 μm in size fabricated using the sacrificial layer technique, Foquet and colleagues achieved analysis speeds as high as 5 mm s^{-1}, corresponding to only milliseconds of analysis per molecule.

A DNA molecule stretched within a nanochannel is able to relax and fluctuate around its equilibrium state, enabling multiple statistically independent observations from a single confined molecule. This higher reliability reads even from single molecules, enables restriction mapping of a much smaller quantity of DNA than is required in traditional biological techniques, and eliminates some of the bias introduced during the amplification of DNA. By first stretching DNA, Riehn and colleagues correlated the spatial and genomic position of DNA [Riehn *et al*., 2005]. In this work, shown in Figure AI.5B, the linearization and cutting of DNA were divided into separate steps by dynamically varying the concentration of Mg^{2+}, an enzymatic cofactor necessary for restriction enzyme function. Riehn and colleagues successfully cut and mapped λ-DNA (48.5 kbp) with SmaI and Sac I restriction enzymes to a resolution of 1.5 kbp. In their experiments, the authors showed that SmaI cut λ-DNA into four fragments which were all observed in their expected order while SacI cut the λ-DNA into three fragments of which the longer two were capable of being observed while the smallest fragment was not. Because DNA relaxation time in a channel scales with the square of molecular weight, cut DNA fragments relax at a faster rate than overstretched long molecules. Additionally, if data are collected over statistically independent Brownian fluctuations, precise length measurements can be made based on a single confined molecule, reducing initial sample size and amplification requirements. Therefore the work of Riehn and colleagues provides a procedure to potentially perform more rapid and reliable restriction maps using nanoconfinement.

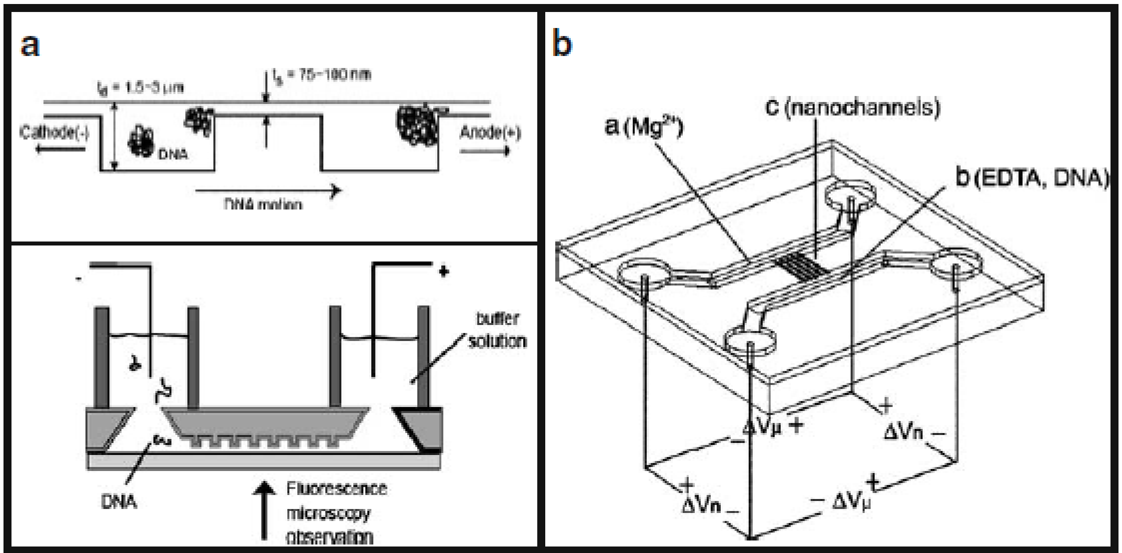

From Han J, Craighead HG. (2000) Science. 28: 1026-1029. Reprinted with Permission from AAAS.

From Riehn R, Lu M, Wang Y, Lim SF, Cox EC, Austin RH. (2005) PNAS. 102.29: 10012-10016. Copyright (2005) National Academy of Sciences, U.S.A. Reprinted with Permission.

Table AI.5. Biological Applications of DNA Nanoconfinement: Device Schematics. (a.) Han and Craighead created an entropic trap for separating DNA molecules based on size. Molecules pass through an alternating array of thin and thick regions. Larger DNA molecules have greater area in contact with interface therefore have a greater probability of escaping entrapment and move more quickly through the system. (b.) Riehn, Austin, and colleagues designed a nanofluidic device for restriction mapping DNA molecules. DNA and EDTA were loaded into one of two microfluidic channels. Mg^{2+} was loaded into a second microfluidic channel, linked by a sequence of ten nanochannels. DNA and Mg^{2+} moved through the nanochannels via electrophoresis. Mg2+ serves as cofactor for restriction digestion of DNA within nanochannels.

Schwartz and colleagues combined improved optical mapping capabilities with advances in PDMS microfluidic channels to stretch DNA on to positively charged surfaces enabling rapid mapping of human DNA >1 mm long [Dimalanta *et al*., 2004]. Their system linearized DNA due to the hydrodynamic flow in a microchannel, as opposed to directly due to the confinement effect of a nanofluidic channel. After elongation, DNA was adsorbed on to a surface in a configuration parallel to the flow. The authors demonstrated the ability to load

DNA on to the optimal mapping surface in aligned, non-overlapping segments via microfluidic channels. The advantage of this system is user-friendliness.

As can be seen from the examples described above, use of nanochannels for physical gene mapping is still at the demonstration stage. Nanoconfinement has the potential to provide more consistent DNA linearization and more precise information compared with methods that use microchannels to hydrodynamically stretch DNA. The experimental procedures, however, are more difficult. Thus, the method that is more used in a practical setting is optical mapping where DNA is linearized using flow in a microchannels and the stretched DNA is immobilized on to a surface. The larger microchannels allow easier manipulations which make up for the less precise stretching of DNA molecules.

Separation

Huang and colleagues developed a method for separating bacterial DNA based on the laminar flow profile around microfabricated asymmetric obstacles [Huang *et al*., 2004]. Using this procedure, they separated bacterial DNA (×40 kb) in approximately 10 min with a resolution of ~12%, faster and with better resolution than standard separation techniques. While not yet applied to nano-scale applications, asymmetric bifurcation of laminar flow could be used to improve the speed and resolution of biological molecules including DNA and protein.

Han and Craighead fabricated an entropic trap, consisting of alternating thick and thin regions capable of constricting individual DNA molecules, using photolithography and etching techniques on a Si substrate [Han and Craighead, 2000]. A schematic diagram of their entropic trap is shown in Figure AI.5A. The thin regions were designed to be smaller than the radius of gyration of a DNA molecule, allowing them to function as a “molecular sieve”, while the thick regions were designed to be greater than the radius of gyration of a DNA molecule, allowing DNA to assume spherical equilibrium shape. Because larger molecules have a greater surface area in contact with the boundary of the trap, they have a higher probability of escaping the entropic trap. This leads to the somewhat counterintuitive principle that larger molecules have increased mobility compared with smaller molecules. Using their entropic trap, Han and Craighead were able to separate larger T2 DNA from smaller T7 DNA in about 15 min-two orders of magnitude faster than using conventional pulsed-field gel electrophoresis. Next, they separated several dsDNA samples ranging from 5-164 kbp.

The Craighead group conducted further work optimizing their entropic trap for separating individual DNA molecules. Advances in entropic trapping for separation of DNA molecules are included in Table A.3.

Campbell and colleagues designed a system of nanofabricated capillaries for studying the electrophoretic behavior of DNA [Campbell *et al*., 2004]. The authors fabricated four channels with dimensions ranging from 900x600 nm down to 150x180 nm using a focused ion beam. The three smallest channels were connected to larger capillaries with dimensions 1000x1200 nm. Upon confinement in the small nanocapillaries, DNA uncoiled into a partially extended form. DNA was observed to migrate electrophoretically toward the anode, overcoming the electro-osmotic flow of the buffer toward the cathode. At voltages between 100 mV and 2 V, DNA successfully entered the capillary system at the cathodic side of the channel and exited at the anodic side. Furthermore, migration direction was immediately reversed, upon changing electrode polarity. The total mobility of DNA within a structure is the vector sum of the electrophoretic mobility and electroosmotic mobility of the buffer. Because electroosmotic counter-flow increases with larger channel size, DNA mobility was shown to have an inverse relationship to capillary cross-section [Campbell *et al*., 2004].

Fu and colleagues developed an anisotropic nanofilter array (ANA) for continuous separation of DNA and proteins based on size and charge [Fu *et al*., 2007]. The structural anisotropy of the ANA enables continuous-flow separation not possible with random isotropic mediums like gels, liquid gels, or ampholytes. Because this system incorporates different sieving mechanisms for small and large DNA molecules, the ANA can separate biomolecules covering a much broader range of biological sizes. The system designed by Fu and colleagues sorts short DNA molecules via Ogston sieving and long DNA molecules via entropic trapping. DNA molecules are driven at an angle through an obstacle array. Because DNA molecules of different length have different probabilities of escaping the shallow regions of the array, molecules of different length demonstrate different trajectory angles relative to the initial direction of flow. ANA also has the potential to sort proteins based on size and charge. The authors showed that the transition from Ogston sieving to entropic trapping occurs between 1000-2000 bp, concurrent with the transition from a rodlike DNA conformation to a coiled conformation. Furthermore the size selectivity of the ANA was shown to be of the order of 5 nm, DNA length of 20 bp.

Cross, Strychalski, and Craighead found that in channels 19 nm high, dsDNA (2-10 kb) could be separated by length, but in larger, 70 nm high, channels no length dependent separation was detected [Cross *et al*., 2007]. These results indicated that as the degree of nanoconfinement increases, surface friction between the channel walls and the confined DNA molecule plays a larger role in the mobility of a DNA molecule and that the rules of free-solution DNA electrophoresis are no longer valid. The experimental results agreed with the $N^{-1/2}$ model of DNA length-dependent mobility. As nanofluidic device dimensions continue to decrease and more easily interface with lab-on-a-chip devices the potential for separating DNA molecules based on length using wall surface friction will expand.

As can be seen from the examples described above, using nanochannels for separations offers the potential for more rapid separation of DNA molecules of much wider size distribution. This can be accomplished because molecules of different sizes behave differently when confined-with Ogston sieving used to separate short molecules and entropic trapping used to separate short molecules. Future research will focus on separating DNA molecules based upon both size and charge while continuing to improve the speed and resolution of sorting.

Other

Ying and colleagues developed a nanopipet capable of delivering small numbers of DNA molecules through the precise control of palatial voltage changes [Ying *et al*., 2002]. The applied voltage drop preferentially occurs almost entirely in the tip of the pipet enabling highly concentrated electric field strength with very low applied potential. The authors used Single Molecule Detection techniques and Fluorescence Correlation Spectroscopy (FCS) to determine the number of molecules delivered.

CONCLUSION

Nanoconfinement has proven to be a feasible process for physical gene mapping and separations. Avariety of potential benefits relative to traditional techniques have been demonstrated including manipulating longer DNA fragments, more rapidly, and with greater reliability. At the present, however, nanoconfinement techniques have not been readily incorporated into biological applications. Whether nanotechnology for the linearization of DNAwill remain merely an interesting biophysical research tool or grow to fill critical needs in the fields of genetics, medicine, and biology remains unseen. Because DNA and nanochannels have similarly matched width and length dimensions the potential for continued innovative applications remains obvious. More importantly, the confluence of timing between emerging biomedical problems, such as long-range haplotyping and single molecule genetic mapping [Michalet *et al*, 1997], and improvements in nanofabrication enables unique solutions to these needs. Only time will tell which properties of DNA will be revealed through nanoconfinement;

however, if these techniques are to live up to their potential many daunting challenges will need to be to overcome and exciting opportunities grasped.

Appendix II

Modifications to DNA-Histone Complexescan be Resolved through Nanoconfinement-based Linearization

Nicholas J. Douville[*], Toshiki Matsuoka[*], Byoung Choul Kim, Jessie Huang, M.D. Thouless, and Shuichi Takayama

INTRODUCTION

Single pieces of chromatin have been stretched through a variety of techniques including optical tweezers [Bennink *et al*., 2001] and nanoconfinement [Streng *et al*., 2009]. These techniques allow more precise analysis of the DNA-protein interactions occurring within a single strand of chromatin, than can be resolved with traditional techniques such as Chromatin Immunoprecipitation (ChIP), which require relatively large amounts of homogenous chromatin [Buck and Lieb, 2004] Current techniques are limited by difficulty loading protein-DNA structures into systems with dimensions small enough for DNA linearization. Because channel size cannot be modulated, loading and migration of chromatin-complexes in nanofluidic channels must be controlled via electric field [Douville *et al*., 2008]. Confinement of reconstituted chromatin within an elastomeric, adjustable nanochannel enables DNA-protein binding to be analyzed over a broader range of chromatin states at the level of single-chromatin complexes. To demonstrate this capability, we compared differences in nanoconfinement-based linearization between phage-DNA reconstituted with different histone core proteins. By dynamically modulating elastomeric nanochannel we have linearized the longest reported fragments of reconstituted-DNA (T4-phage DNA is >3x longer than λ-DNA), without the need for electrophoretic loading. Using this technique, we have specifically investigated changes in degree of linearization resulting from: (i) epigenetic-based histone-modifications (hyperacetylation of HeLa histone) and (ii) the removal of H1, linker histone.

Acetylation of the histone core in HeLa cells leads to a decondensation of the chromatin structure making the underlying DNA structure more accessible to larger molecules and protein-complexes [Fejes *et a*l., 2004; Gorlsch *et al*., 2005]. Chromatin can be forced into a state of hyperacetylation by inhibitors of histone deacetylases, such as Trichostatin A (TSA), making acetylation-state an appealing epigenetic change to resolve by nanoconfinement based linearization. Linker histone, H1, also plays a well-established role condensing chromatin into a more compact, stable structure [Allan *et al*., 1986; Grigoryev *et al*., 2001; Ramakrishnan, 1997; Brown, 2003] and generally inhibiting transcription [Wolfe, 1992]. Because H1 can easily be stripped through perchloric acid treatment, H1-state is another attractive to reconstitution condition to study via nanoconfinment.

Traditional nanoconfinement-based systems are limited in ability to linearize longer DNA sequences and protein-DNA complexes by the ability to load DNA into channels with dimensions small enough for linearization [Douville *et al*., 2008]. Dynamic modulation enables larger channel dimensions in the “open” configuration and smaller channel dimensions in the “closed” configuration compared to traditional systems, longer strands of reconstituted DNA, as well as, strands contain bound fluorescent antibodies (to distinguish histone proteins from the DNA backbone) can be linearized and imaged. We used our system to characterize differences in the degree of nanoconfinement-elongation as a function of chromatin state for (i) an epigenetic histone modification and (ii) the binding of linker histone H1, an inhibitor of transcription whose regulation and binding remains poorly understood . The methods presented in this paper, specifically co-fluorescent antibody labeling of histone subunits and single molecule resolution of histone modifications, provide an opportunity to expand studies on protein-DNA complexes to single chromatin level, potentially advancing the understanding of how these interactions govern replication, transcription, and enzyme catalysis.

RESULTS

A. Reconstitution of Phage DNA. We confirmed the success of our reconstitution protocol using: (1) micrococcal nuclease (MNase) digestion of λ-phage DNA (Supporting Information, Figure AII.5) and (2) co-fluorescence staining of reconstituted DNA (Figure AII.2). MNase induces double stranded breaks only within nucleosome linker regions, enabling us to confirm reconstitution protocol from the increased number of restriction fragments in reconstituted DNA (lanes 3,4,5,6,7) compared to the single restriction fragment found in non-reconstituted λ-DNA (lane 1) or reconstituted λ-DNA not digested by MNase (lane 2).

FigureAII.1 Overview/Background

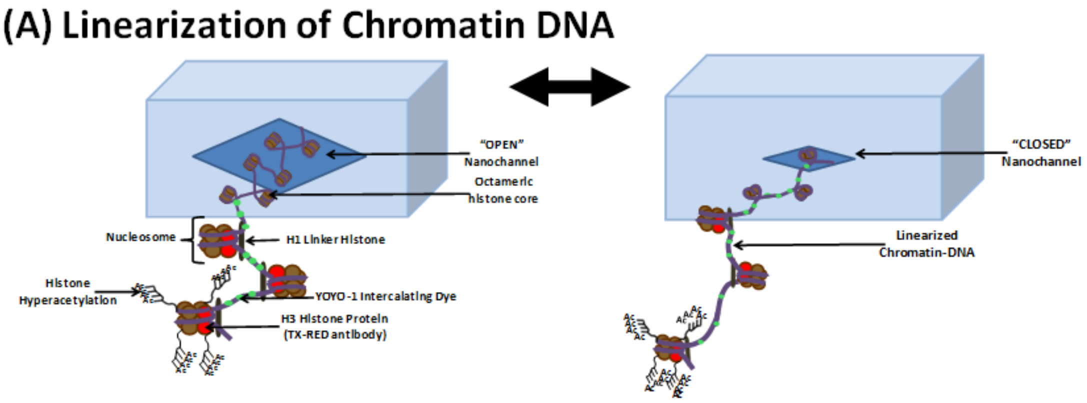

(B) Linearization of Reconstituted Chromatin DNA (λ-phage)

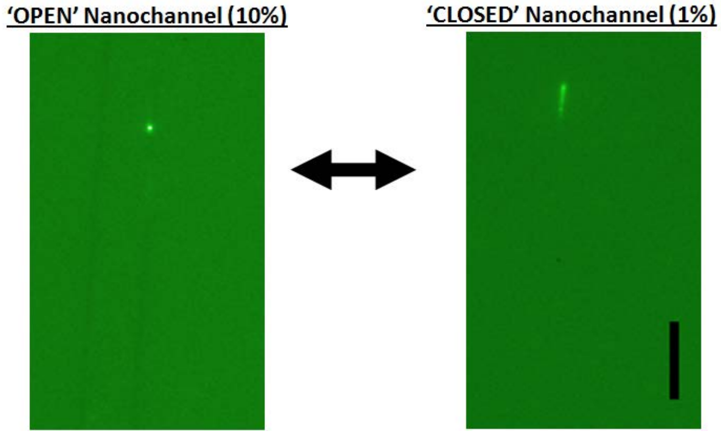

(C) Comparison of Reconstituted and Bare λ-Phage DNA

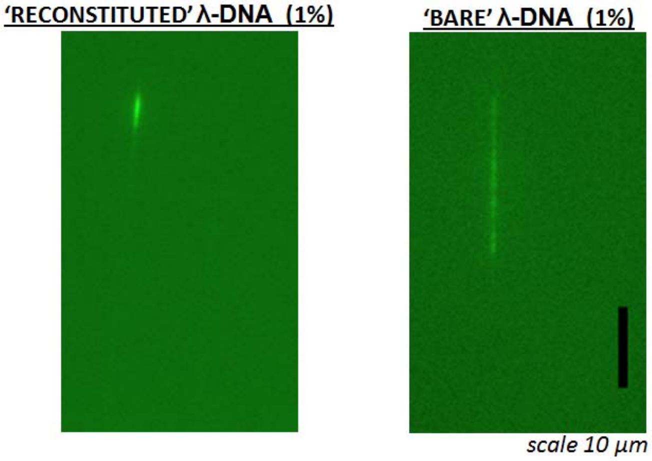

(D) Comparison of Reconstituted and Bare T4-Phage DNA

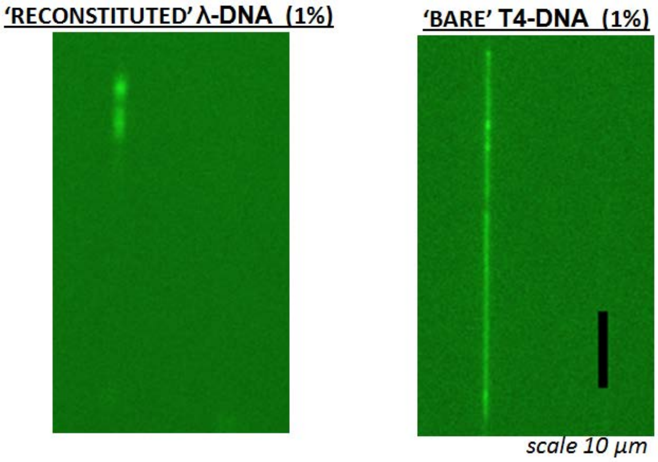

B. Linearization of Reconstituted DNA. λ- and T4-DNA were reconstituted with histone protein containing linker histone protein (H1) and histone protein stripped of H1 (both calf thymus histone and histone protein isolated from HeLa Cells). Figure AII.2 shows a co-fluorescence micrograph demonstrating the successful reconstitution of λ (Figure AII.2A) and T4 (Figure AII.2B) DNA with calf thymus histone proteins. The histone proteins were visualized by Antibody to Histone protein H3 (Abcam) labeled with Texas-red fluorescent stain (Biotium). The underlying DNA molecule was stained using YOYO-1 FITC fluorescent stain (Invitrogen). After verifying the reconstitution procedure, YOYO-1 stained chromatin fragments (λ- and T4-) were loaded into “open” nanochannel systems (10% strainbefore the channels were gradually closed to a tensile strain of 5% then 1%. The length of DNA molecules were measured in both the open (10% tensile strain) and closed (1% tensile strain) corresponding to a channel width and height of approximately 1228.43 nm x 55.48 nm and 333.21 nm x 47.78 nm, respectively. Gaussian probability density functions were also fit to the data demonstrating the “linearization states” (folded, fully stretched, and multiple fragments) simultaneously occurring within different nanochannels at the same strain condition. The impact of H1 and acetylation state were compared by analyzing the 2nd linearization state proposed by Streng and colleagues corresponding to whole molecules of reconstituted chromatin (while the smaller maxima corresponds to fragments and the larger maxima corresponds to poorly reconstituted molecules) [Buck and Lieb, 2004].

Figure AII.2. Co-fluorescence Micrograph of Reconstituted DNA.

(A) λ-DNA

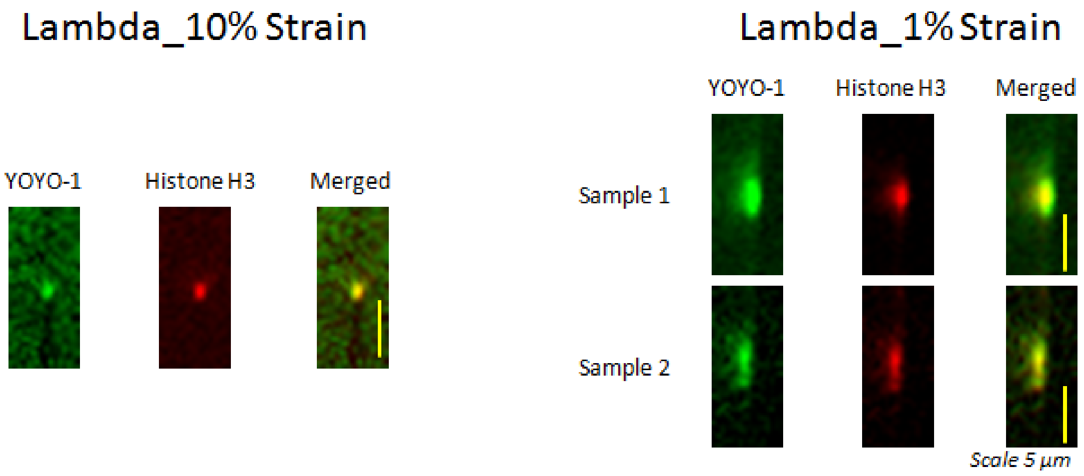

(B) T4-DNA

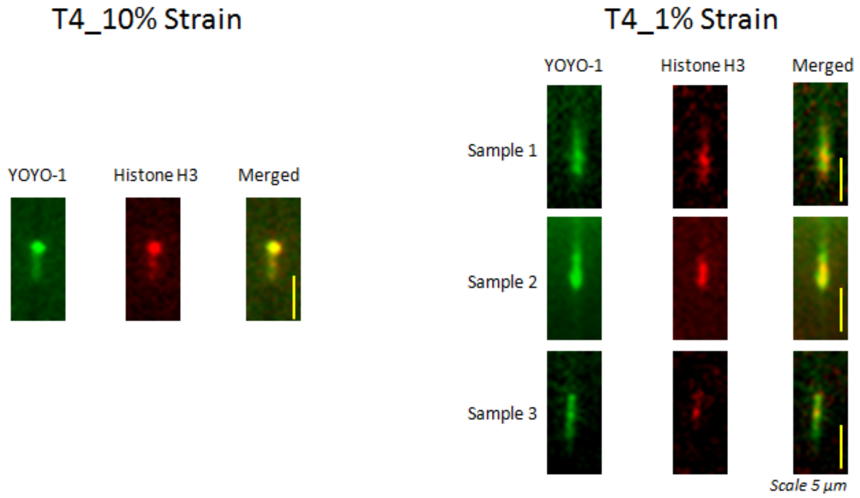

C. Impact of Linker Histone H1 on Linearization. λ-DNA was reconstituted around histone proteins (both calf-thymus and HeLa cell-isolated) (i) containing H1 and (ii) stripped of H1. Reconstituted chromatin was loaded in the “open” configuration (10% tensile strain), before being “closed” to 1% tensile strain for confinement and linearization of the trapped structures. The length of the confined chromatin structures was measured using fluorescent microscopy. Figure AII.3 compares the length of λ-DNA reconstituted with histone-proteins isolated from (A) HeLa cells and (B) calf-thymus. A probability density function fit to the fully stretched data (second linearization state) data as described by Streng *et al*., 2009 shows a clear increase in the degree of linearization following the removal of H1 from the core histone protein (Figure AII.3A/B). A *Kolmogorov-Smirnov* statistical analysis of the full datasets (all three linearization states: (i) folded, (ii) fully stretched, and (iii) multiple fragments) also shows significant increase in linearization in the chromatin lacking H1 (Supplementary Information).

Figure AII.3. Impact of Linker Histone H1 on Degree of Linearization

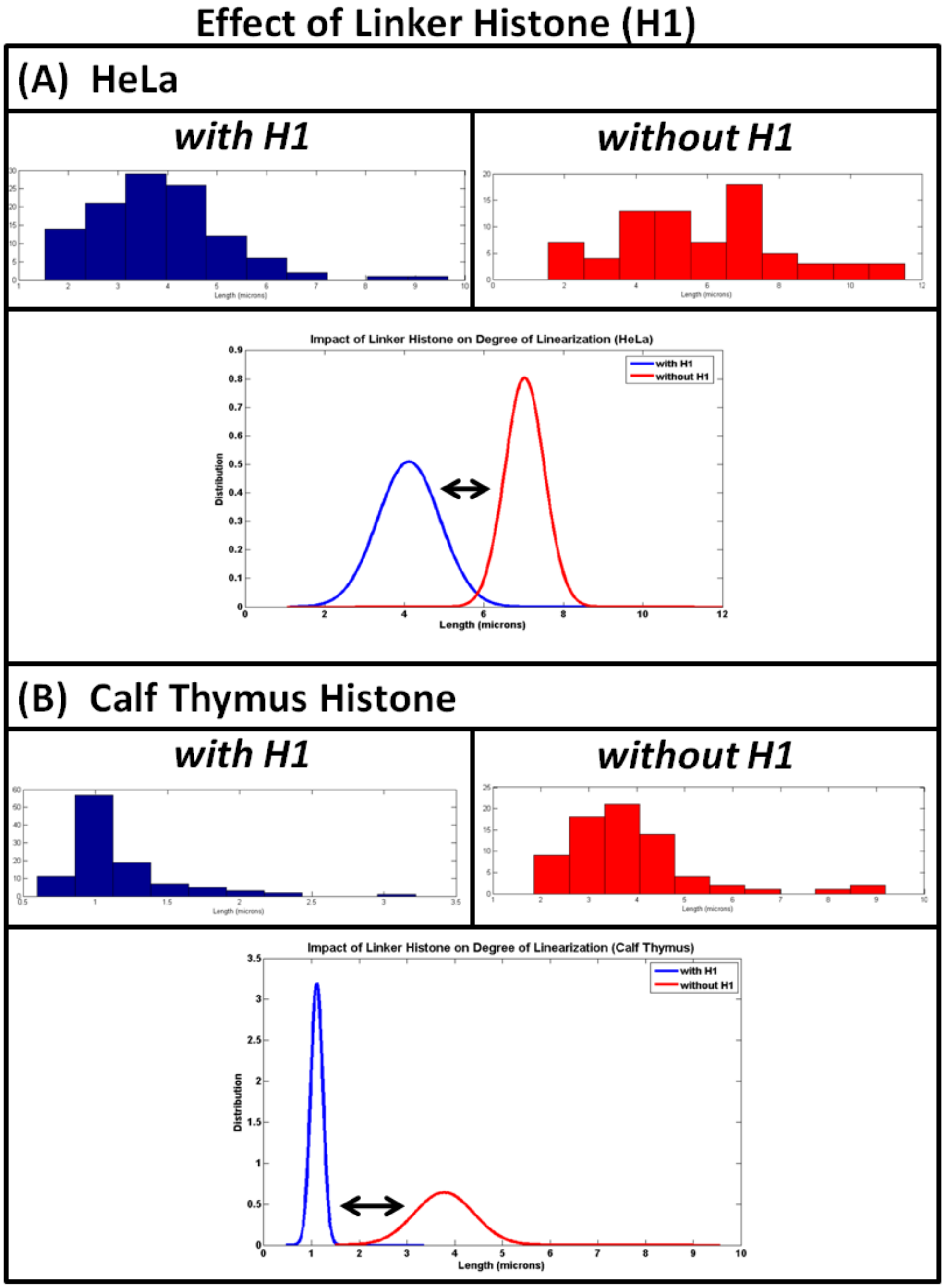

D. Impact of Acetylation State on Linearization. Histone proteins were isolated from HeLa cells treated with Trichostatin A (TSA) and from un-treated HeLa cells (control). λ-DNA was reconstituted with the isolated histone proteins, linearized using our nanochannel system, and length analyzed via fluorescent microscopy. Probability Density Function fit to the second linearization state (Figure AII.4C) show that hyperacetylation increases the degree of linearization. The increase in linearization from this epigenetic modification was much more subtle than the change resulting from the removal of linker histone, H1 and there is significant overlap resulting from variability in channel dimensions and other factors, but statistical analysis using the *Kolmogorov-Smirnov* test resolved a significant difference with P=0.002 (Figure AII.6).

Figure AII.4. Impact of Acetylation State on the Degree of Linearization

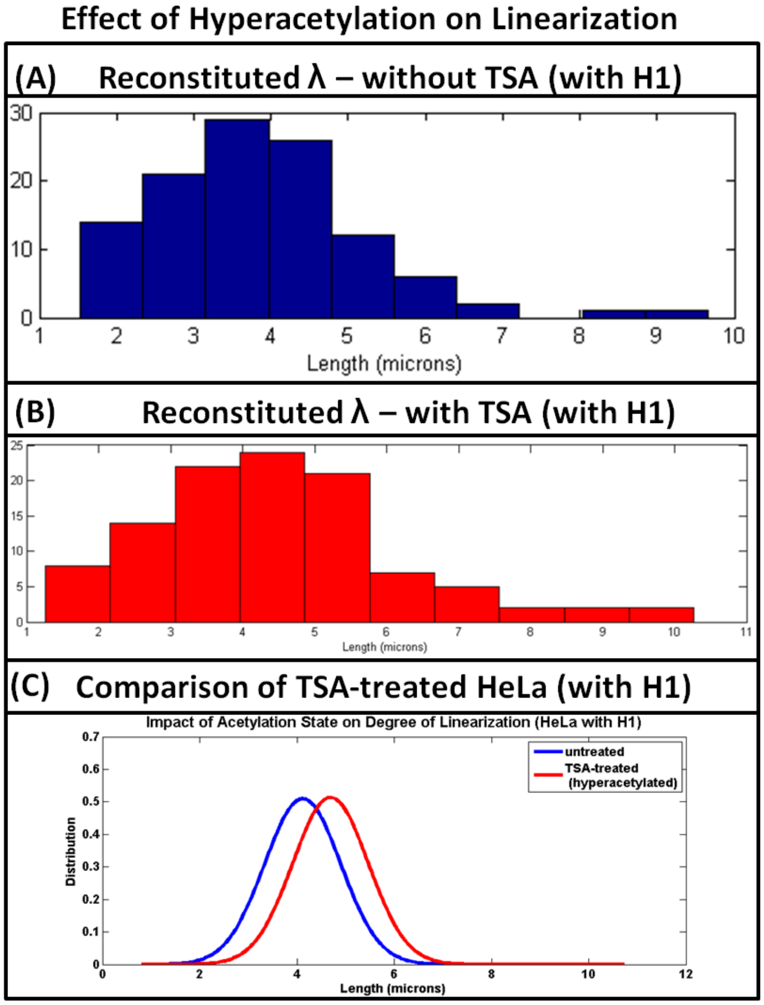

METHODS

A. Reconstitution of Phage DNA. Phage DNA was reconstituted using a protocol first described by Steger *et al*.[Steger *et al.*, 1998]

Initial Reconstitution Solution. 2 μL of phage DNA [λ-phage=4.0 μg/mL (Invitrogen); T4-phage=14 μg/mL (Wako)] and 1 μL of histone from calf thymus [2.2 mg/mL and 7.3 mg/mL, respectively] were added to 1 μL of 100X BSA, 4 μL of 5 M NaCl and 2 μL of Deionoized Water yielding 10 μL of total solution. This solution (containing phage DNA and histone protein) was incubated at 37 °C for 15 minutes.

Serial Dilution Solution. *Serial Dilution Solution* [500 mM HEPES, pH 7.5; 1 mM Ethylenediaminetetraacetic acid (EDTA); 5 mM Dithiothreitol (DTT); 0.5 mM phenylmethylsulfonyl fluoride (PMSF)] was added to the initial solution in a series of dilution steps (3.3, 6.7, 5.0, 3.6, 4.7, 6.7, 10.0, 30.0, and 20.0 μL) every 15 minutes at 30 °C.

Final Dilution Solution. 100 μL of *Final Dilution Solution* [10 mM Tris-HCl (pH 7.5); 1 mM EDTA; 0.1% Nonidet P-40; 5 mM DTT, 0.5 mM PMSFT, 1% BSA] were added to the previous solution bringing the total volume to 200 μL. This solution was incubated at 30 °C for an additional 15 minutes.

YOYO-1 Intercalation Solution. 0.5 μM YOYO-1 solution was added to yield an intercalation ratio of 10:1 (base pairs: fluorophores) [2.4 μL added to the λ-DNA solution; 7.2 μL added to the T4-DNA solution]. The solution was covered at room temperature for 30 minutes then kept covered and refrigeratored between experiments.

B. MNase Digestion and Gel Electrophoresis.

The reconstituted chromatin was divided into six parts and MNase (BioLabs) was added (0, 0.2, 2, 20, 200, 2000 Gel Units per tube). After incubate at 37°C for 15 min, add adjust 0.1% SDS to the reaction samples, which were loaded on 1.2%

agarose gel in 0.5X TBE buffer. The gel was stained in ethidium bromide and viewed under UV.

C. Co-fluorescence of DNA and Histone. Following reconstitution and YOYO-1 intercalation, the reconstituted DNA was labeled with H3 antibody (H3 antibody from Abcam; Mix-n-Stain labeling kit from Biotium) to verify successful reconstitution.

D. Hyper-acetylation through TSA-treatment of HeLa Cells. Trichostatin-A (TSA) inhibits the activity of histone deacetylase (HDAC) [Yoshida *et al*., 1990]. HeLa cell were cultured to 80-90% confluence in CO2 incubator, then treated with 300nM TSA for 8 hours. Following TSA treatment, histone proteins were isolated from HeLa cells according to the procedure described (E.), then phage DNA was reconstituted on the isolated histone proteins according to the procedure described in (A).

E. Isolation of histone proteins from HeLa Cells (*same protocol for TSA-treated and non-treated conditions*). HeLa cells were washed with pre-warmed FBS free DMEM medium 2 times. Then, the cells were trypsinized. Cold extraction buffer was added and rotated at 4 degree C for 30min to 2 hours. Next the cell mixture was spun at 12000 rpm at 4 ^{o}C for 5 min. The supernatant was transferred to new tube, and 1/4 volume of 5x Neutralization buffer was added. The sample was then transfered to the equilibrated column, spun at 2300 rpm, 4 °C for 3 min. Histone wash buffer was added to the column, and spun at 2300rpm, 4 °C for 3 min. The washing step was repeated 3 times, then the column was transfered to new tube, histone elution buffer was added to the column, and spun again at 2300rpm, 4 ^{o}C for 3 min.

F. Removing linker-histone, H1 from the isolated Histone Core. 70% perchloric acid was added to the isolated histone core, bringing the final concentration to 4%. This histone-acid mixture was incubated overnight at 4 ^{o}C, then, spun at 12000 rpm, 4 ^{o} C for 1 hour, then the supernatant was carefully removed. 4% perchloric acid was used to slowly wash the pellet, then spun again at 12000 rpm, 4 °C for 5 min. This washing step (4% perchloric acid) was repeated 2 times. Next, the pellet was slowly washed with 0.2% HCl in acetone, and spun at 12000 rpm, 4 °C for 5 min. This washing step (0.2% HCl in acetone) was also repeated 2 times. The pellet was slowly washed with acetone and spun at 12000 rpm, 4 °C for 5 min. This washing step (acetone) was also repeated 2 times. The acetone was allowed to evaporate from the at room temperature for ~10-20 min. The remaining histone was eluted with histone elution buffer and stored at -20 °C.

FigureAII.5. Confirmation of Reconstitution Protocol through MNase Digestion. We confirmed reconstitution of λ-DNA through digestion with Micrococcal nuclease (MNase), a nuclease which induces double-stranded breaks within nucleosome linker regions and single-stranded breaks within the nucleosome. Non-reconstituted λ-DNA (Lane 1) and reconstituted λ-DNA without MNase (Lane 2) show a single electrophoresis band. Because reconstituted λ-DNA contains nucleosomes, digestion with varying concentrations of MNase (Lanes 3, 4, 5, 6, 7) show multiple electrophoresis bands. The reconstituted lambda DNA chromatin by MNase treatment is digested to the length corresponding to mono-, di-, and tri-nucleosomes.

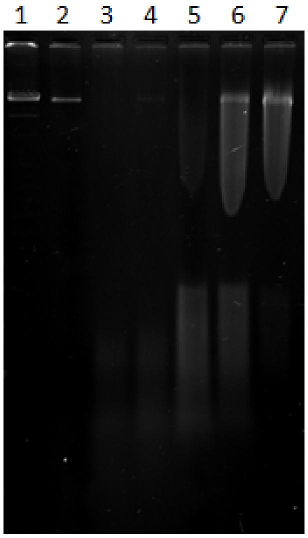

1: Lambda DNA
2: Reconstituted lambda DNA chromatin without MNase
3: Reconstituted lambda DNA chromatin with MNase 2000 gel units
4: Reconstituted lambda DNA chromatin with MNase 200 gel units
5: Reconstituted lambda DNA chromatin with MNase 20 gel units
6: Reconstituted lambda DNA chromatin with MNase 2 gel units
7: Reconstituted lambda DNA chromatin with MNase 0.2 gel units

Figure AII.6. Statistical Differences between Data Sets were Resolved using the Kolmogorov-Smirnov Test.

Comparison of Gaussian Probability Density Functions (PDFs) revealed that λ-DNA reconstituted on nucleosomes without linker histone, H1 could be stretched to a much greater lengths than λ-DNA reconstituted on nucleosomes containing linker histone, H1 (Figure AII.3A/B). Comparison of PDFs fit to λ-DNA appeared to show that λ-DNA reconstituted on hyperacetylated histone proteins could be stretched to greater lengths than those reconstituted with normally acetylated histone proteins; however, these datasets shared substantial overlap, making these differences more difficult to ascertain (Figure AII.4C). To determine whether hyperacetylation altered "linearization state" of the reconstituted chromatin, we applied the *Kolmogorov-Smirnov Test* to the full datasets (all three linearization states: (i) folded, (ii) fully stretched, and (iii) multiple fragments). This contrasts to the graphical comparisons (Figure AII.3A/B and Figure AII.4C) which depict only the Gaussian Probability Density Functions fit to the second linearization state (fully stretched). Our data shows significant differences in the degree of linearization resulting from (A) the removal of linker histone, H1 (on both calf-thymus and HeLa-isolated histone proteins) and (B) hyper-acetylated HeLa-isolated histone protein. The statistical comparisons of these two experiments are summarized below.

A. Effect of Histone Protein H1.

i. Calf-Thymus Histone Proteins. The maximum difference between the cumulative distributions, D, is 0.9581 with a corresponding $P < 0.001$.

with H1 (n=105):

Mean=1.167 (95% CI for Mean: 1.092-1.242)
Standard Deviation=0.387
Median=1.040
Average Absolute Deviation from Median=0.241

no H1 (n=75):

Mean=3.822 (95% CI for Mean: 3.515-4.128)
Standard Deviation=1.33
Median=3.460
Average Absolute Deviation from Median=0.890

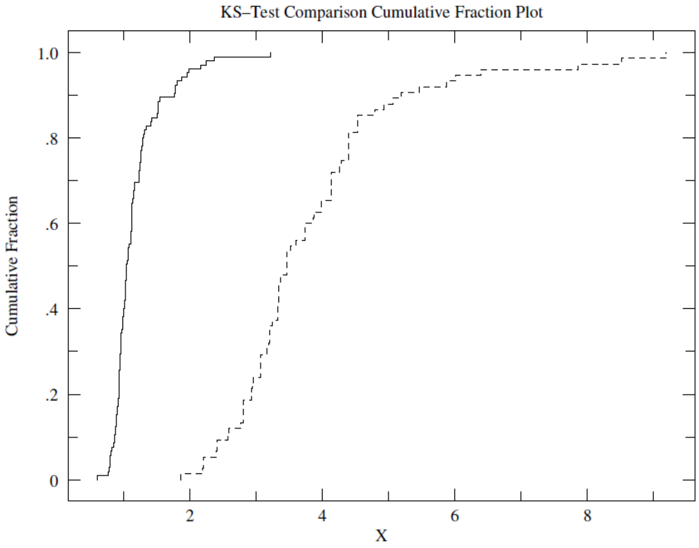

ii. **HeLa-Isolated Histone Proteins**. The maximum difference between the cumulative distributions, D, is 0.4610 with a corresponding P < 0.001.

with H1 (n=112):
Mean=3.820 (95% CI for Mean: 3.562-4.078)
Standard Deviation=1.38
Median=3.430
Average Absolute Deviation from Median=1.05

no H1 (n=75):
Mean=6.725 (95% CI for Mean: 4.910-8.539)
Standard Deviation=7.99
Median=6.120
Average Absolute Deviation from Median=2.76

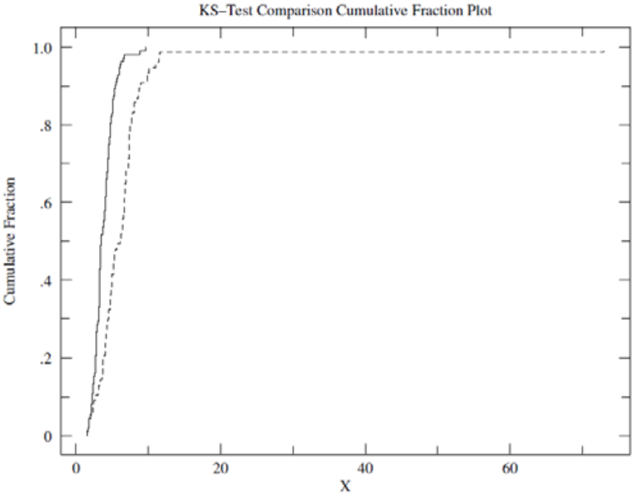

B. **Effect of Hyperacetylation (TSA-treatment)**. The maximum difference between the cumulative distributions, D, is 0.2424 with a corresponding P of 0.002.

No TSA-treatment (n=112):
Mean=3.791 (95% CI for Mean: 3.534-4.048)
Standard Deviation=1.37
Median=3.425
Average Absolute Deviation from Median=1.04

TSA-treatment 9 (n=109):
Mean=4.452 (95% CI for Mean: 4.119-4.784)
Standard Deviation=1.75
Median=4.260

Average Absolute Deviation from Median=1.32

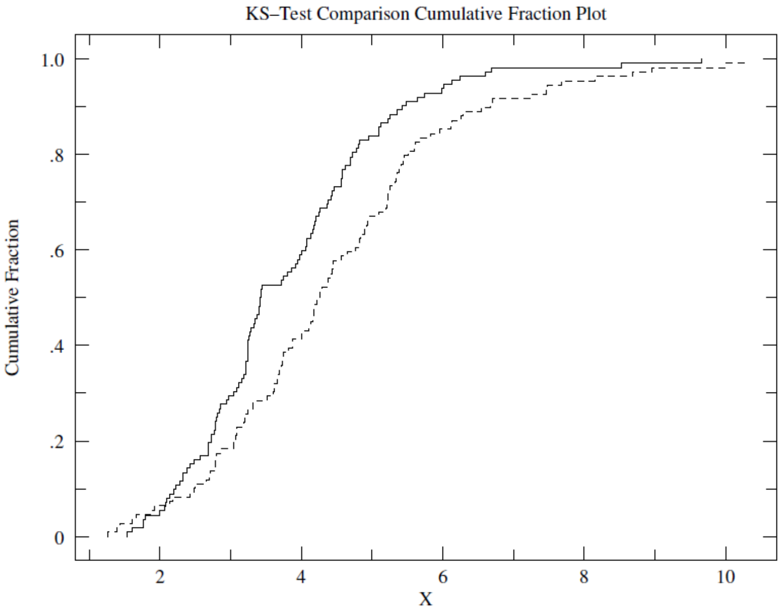

Bibliography

Adelung R, Aktas OC, Franc J, Biswas A, Kunz R, Elbahri M, Kanzow J, Schurmann U, Fapel F. *Nat Mater*. **2004**. 3: 375–379

Akogwu O, Kwabi D, Midturi S, Eleruja M, Babatope B, and Soboyejo WO/ *Mater. Sci. Eng., B*, **2010**, 170: 32–40.

Allan J, Mitchell T, Harborne N, Bohm L, and Crane-Robinson C. Roles of H1 Domains in Determining Higher Order Crhomatin Structure and H1 Location. *J. Mol. Biol*. **1986**. 187: 591-601.

Allen HG. Analysis and Design of Structural Sandwich Panels, Pergamon, New York, **1969**.

Anzueto A, Baughman RP, Guntupalli KK,,. Weg JG, , Weidemann HP, and. Raventos AA, et al., *N. Engl. J. Med*., **1996**, 334: 1417–1421.

Atencia, J.; Beebe, D. J. *Nature* **2005**, *437*: 648–655.

Ayliffe, H. E.; Frazier, A. B.; Rabbit, R. D. *J. MEMS* **1999**, *8*: 50–57.

Bakajin OB, Duke TAJ, Chou CF, Chan SS, Austin RH, Cox EC. *Phys Rev Lett*. **1998**. 80.12:2737–2740

Balda MS, Whitney JA, Flores C, Gonzalez S, Cereijido M, and Matter K. *J. Cell Bio*. **1996**, 134: 1032-1049.

Bao, N.; Wang, J.; Lu, C. *Anal. Bioanal. Chem.* **2008**, *391*: 933–942.

Begley MR and Bart-Smith H. *Int. J. Solids Struct*., **2005**, 42: 5259– 5273.

Begley MR, Bart-Smith H, Scott ON, Jones MH, and Reed ML, *J. Mech. Phys. Solids*, **2005**, 53: 2557–2578.

Bretherton FP. *J. Fluid Mech*., **1961**, 10(2): 166–188.

Bennink ML, S.H. Leuba, G.H. Leno, J. Zlatanova, B.G. deGrooth, and J. Greve. *Nature Struct. Biol*, **2001**, 8(7): 606-610.

Beuth JL, Jr, *Int. J. Solids Struct*. **1992**, 29: 1657–1675.

Bian S, Tai CF, Halpern D, Zheng Y, and Grotberg JB. *J. Fluid Mech*., **2010**, 647: 391–402.

Bilek AM, Dee KC, and Gaver DP. *J. Appl. Physiol*., **2003**, 94:770–783.

Birks EK, Mathieu-Costello O, Fu Z, Tyler WS, West JB. *Respir. Physiol*. **1994**, 97: 235-246.

Birukov KG, Jacobson JR, Flores AA, Ye SQ, Birukova AA, Verin AD, Garcia JGN. *Am. J. Physiol. Lung Cell Mol. Physiol*. **2003**, 285: L785-L797.

Boas S and Winnie GB. Kliegman: Nelson Textbook of Pediatrics, 18th ed. Chapter 389: Emphysema and Overinflation. **2007** Saunders.

Bowden N, Brittain S, Evans AG, Hutchinson JW, and Whitesides GM, *Nature*, **1998**, 393: 146–149.

Brochard-Wyart F, Tanaka T, Borghi N, deGennes PG. *Langmuir*. **2005**. 21:4144–4148

Broek D. *Elementary Engineering Fracture Mechanics*, 3rd edn, Martinus Nijhoff Publishers, The Hague, The Netherlands, **1982**.

Brown DT. Histone H1 and the Dynamic Regulation of Chromatin Function. *Biochem. Cell Biol*. **2003***,* 81(3): 221-227.

Brown MG, Zhang J, Du Y, Stoll J, Yokoyama WM, Scalzo AA. *J Immunol*. **1999**. 163:1991–1999

Buck MJ and J.D. Lieb, Genomics, **2004**, 83: 349-360.

Burgess KA, Hu HH, Wagner WR, and Federspiel WJ. Towards microfabricated biohybrid artificial lung modules for chronic respiratory support. *Biomed. Microdevices*. **2009**. 11: 117-127.

Bustamante C, Bryant Z, Smith SB. *Nature*. **2003**, e 421: 423–427

Campbell LC, Wilkinson MJ, Manz A, Camilleri P, Humphreys CJ. *Lab Chip*. **2004**, 4:225–229

Carney D, DiRocco J, and Nieman GA. *Crit. Care Med*., **2005**, 33: S122–S128.

Cao H, Wang J, Tegenfeldt JO, Austin RH, Chen E, Wu W et al. *App Phys Lett*. **2002**. 81(1):74–176

cellZscope: How It Works. NanoAnalytics. http://www.nanoanalytics.com/en/hardwareproducts/cellzscope/literature/index.php.

Cereijido, M.; Robbins, E. S.; Dolan, W. J.; Rotunno, C. A.; Sabatini, D. D. *J. Cell Biol.* **1978**, *77*: 853–880.

Chan EY, Goncalves NM, Haeusler RA, Hatch AJ, Larson JW, Maletta AM et al. *Genome Res*. **2004**, 14:1137–1146

Chapman KE, Sinclair SE, Zhuang D, Hassid A,. Desai LP, and Waters CM. *Am. J. Physiol. Lung Cell. Mol. Physiol*., **2005**, 289: L834–L841.

Chen X and Hutchinson JW. *J. Appl. Mech*., **2004**, 71: 597–603.

Cheung, K.; Gawad, S.; Renaud, P. *Cytometry, Part A* **2005**, *65A*: 124–132.

Chou SY, Krauss PR, Renstrom PJ. *Science*. **1996**, 272.5258:85–87

Chueh, B.-H.; Huh, D.; Kyrtsos, C. R.; Houssin, T.; Futai, N.; Takayama, S. *Anal. Chem.* **2007**, *79*: 3504–3508.

Chu J, Clements JA,, Cotton EK, , Klaus MH, ,. Sweet AY, and Tooley WH. *Pediatrics*, **1967**, 40: 709–782.

Chung S, Lee JH, Moon MW, Han J, and Kamm RD. *Adv. Mater*., **2008**, 20: 3011–3016.

Christensen PJ, Du M, Moore B, Morris S, Toews GB, and Paine RP, III. *Am. J. Physiol. Lung Cell. Mol. Physiol*., **2004**, 286: L68–L72.

Clark AR, Burrowes KS, Tawhai MH. *J. Appl. Physiol*. **2010**, 108: 1116-1126.

Cook KE, Perlman CE, Seipelt R, Backer CL, Mavroudis C, Mockros LF. *ASAIO Journal*. **2005**. 51(4): 404-411.

Copland IB and Post M. *Journal of Cellular Physiology*. **2007**, 210: 133-143.

Copland IB, Reynaud D, Pace-Asciak C, and Post M. *Am. J. Physiol. Lung Cell Mol. Physiol*. **2006**, 291: L487-L495.

Cordill MJ, Taylor A, Schalko J and Dehm G.. *Metall. Mater. Trans. A*, **2010**, 41: 870–874.

Correa-Meyer E, Pesce L, Guerrero C, and Sznajder JI. *Am. J. Physiol. Lung Cell Mol. Physiol*. **2002**. 282: L883-L891.

Crosby LM, and Waters CM. **2008**, 295: L958-L965.

Cross JD, Strychalski EA, Craighead HG. *J Appl Phys*. **2007**. 102: 024701-1–5

deGennes PG. Scaling concepts in polymer physics. Cornell Univ Press, Ithaca, NY. **1979**.

Deli, M. A.; Abraham, C. S.; Kataoka, Y.; Niwa, M. *Cell. Mol. Neurobiol.* **2005**, *25* (1): 59–127.

Dimalanta ET, Lim A, Runnheim R, Lamers C, Churas C, Forrest DK et el. *Anal Chem*. **2004**. 76: 5293–5301

Douville NJ, Huh D, and Takayama S. *Anal. Bioanal. Chem*. **2008**. 391: 2395-24009.

Douville NJ, Li Z, Takayama S., and Thouless MD. *Soft Matter*., **2011**, DOI: 10.1039/c1sm05140g

Douville NJ, Moraes C, White J, Park C, Kinney A, Simon A, Kaylan K, Christiansen P, and Takayama S. **2011**. In preparation.

Douville NJ, Tung YC, Li R, Wang JD, El-Sayed MEH and Takayama S. *Anal. Chem*., **2010**, 82: 2505–2511.

Douville NJ, Zamankhan P, Tung YC, Li R, Vaughan BL, Tai CF, White J, Christensen PJ, Grotberg JB, and Takayama S. *Lab Chip*. **2011**, 11: 609-619.

Dundurs J. *J. Appl. Mech*., **1969**, 36: 650–652.

Egan EA. *J. Appl. Physiol.: Respir., Environ. Exercise Physiol*.,**1980**, 49: 1032–1036.

Erben, M.; Decker, S.; Franke, H.; Galla, H.-J. *J. Biochem. Biophys. Methods* **1995**, *30*: 227–238.

Esteban A, Anzueto A, Alia I, Gordo F, Apezteguia C, Palizas F, Cide D, Goldwaser R, Sota L, Bugedo G, Rodrigo C, Pimental J, Raimoni G, and Tobin MJ. *Am. J. Respir. Crit. Care Med*., **2000**, 161: 1450–1458.

Fan R, Karnik R, Yue M, Li D, Majumdar A, Yang P. *Nano Lett*. **2005**. 5.9:1633–1637

Farinas, J.; Chow, A. W.; Wada, H. G. *Anal. Biochem.* **2001**, *295*: 138–142.

Fejes TK, Knoch TA, Wachsmuth M, Frank-Stohr M, Stohr M, Bacher CP, Muller G, and Rippe K. *J. Cell Sci*. **2004**. 117: 4277-4287.

Fischer JE and Bland KI. Master of Surgery, Vol. 1 Chapter 8: Multiple Organ Dysfunction Syndrome: Pathogenesis, Management, and Prevention. **2007**. pg 117.

Fisher RF and Wakely J. *Proc. R. Soc. Long. B*. **1976**, 193(1113): 335-358.

FlexCell International Corporation. Product Information.

Flory PJ. Principles of polymer chemistry. Cornell Univ Press, Ithaca, NY. **1953**.

Foquet M, Korlach J, Zipfel W, Webb WW, Craighead HG. *Anal Chem*. **2002**. 74.6:1415–1422

Fretschner R, Deusch H, Weitnauer A, and Brunner JX. *Intensive Care Med.*, **1993**, 19: 372–376.

Fritsche CS, Simsch O, Weinberg EJ, Orrick B, Stamm C, Kaazempur-Mofrad MR, Borenstein JT, Hetzer R, Vacanti JP. *Int. J. Artif. Organs*. **2009**, 32: 701-710.

Fu J, Schoch RB, Stevens AL, Tannenbaum SR, Han J. *Nat Nanotechno*. **2007**. l:2121–128

Fung YC and Sobin SS. Theory of Sheet Flow in Lung Alveoli. *J. Appl. Physiol*. **1969**, 26(4): 472-488.

Fu Z, Costello ML, Tsukimoto K, Prediletto R, Elliott AR, Mathieu-Costello O and West JB. *J. Appl. Physiol.*, **1992**, 73: 123–133.

Ganong W. Review of Medical Physiology. 21st Ed. Lange Medical Publications. **2003**. McGraw-Hill Professional.

Garcia, C. D.; Henry, C. S. *Anal. Chem.* **2003**, *75*: 4778–4783.

Garcia, C. D.; Henry, C. S. *Analyst* **2004**, *129*: 579–584.

Gehr P, Bachofen M, and Weibel ER. *Resp. Physiol*. **1978**, 32: 121-141.

Giaever, I.; Keese, C. R. *Proc. Nat. Acad. Sci. U.S.A.* **1984**, *81*: 3761–3764.

Gorlsch SM, Wachsmuth M, Toth KF, Licter P, and Rippe K. **2005**. 118(24): 5825-5834.

Gray, D. S.; Tien, J.; Chen, C. S. *Adv. Mater.* **2004**, *16*: 393–401.

Grigoryev SA. *Biochem. Cell Biol*. **2001**. 79: 227-241.

Grotberg JB and Jensen OE. *Annu. Rev. Fluid Mech.*, **2004**, 36: 121–147.

Gumbiner BM. *J. Cell Bio*. **1993**. 123(6): 1631-1633.

Guo LJ, Cheng X, Chou CF. *Nano Lett*. **2004**. 4.1:69–73

Haefeli-Bleuer B and Weibel ER. *The Anatomical Record*. **1988**, 220: 401-414.

Halpern D and Grotberg JB. *J. Biomech. Eng*., **1993**, 115(3): 271– 277.

Halpern D and Grotberg JB. *J. Fluid Mech*., **1992**, 24: 615–632.

Hamer BG. Clearance of Airway Liquid from the Lung due to Surface Tension Gradients, Master's thesis, Massachusetts Institute of Technology, **1995**.

Han J, Craighead HG. *Science*. **2000**. 28:1026–1029

Han J, Turner SW, Craighead HG. *Phys Rev Lett*. **1999**. 83.8: 1688–1691

Harnett CK, Coates GW, Craighead HG. *J Vac Sci Technol B*. **2001**. 19(62): 842–2845

Harris, S. G.; Shuler, M. L. *Proc. IEEE 2nd Annu. Northeast Bioeng. Conf.* **2002**, *28*: 1–2.

Haubert K, Drier T, and Beebe D. *Lab Chip*., **2006**, 6: 1548–1549.

Hayes CM. Acute Respiratory Distress Sydnrome (ARDS): A Close Look at a Complication of Shock. EMS Village. **2010**.

Hediger, S.; Sayah, A.; Horisberger, J. D.; Gijs, M. A. M. *Biosens. Bioelectron.* **2001**, *16*: 689–694.

Hediger, S.; Sayah, A.; Horisberger, J. D.; Gijs, M. A. M. *Sens. Actuators, B* **2000**, *63*: 63–73.

Heller MJ. *Annu Rev Biomed Eng*. **2002**, 41: 29–153

Hinds WC. Aerosol Technology: Properties, Behavior, and Measurement of Airborne Particles, John Wiley & Sons, New York 2nd edn, **1999**.

Hirschl RB, Conrad S, Kaiser R, Zwischenberger JB, and Bartlett RH , et al., *Ann. Surg*., **1998**, 228: 692–700.

Hirschl RB, Tooley R, Parent A, Johnson K, and Bartlett RH. *Crit. Care Med*., **1996**, 24: 1001–1008.

Hogg JC and Doerschuk CM. Leukocyte Traffic in the Lung. *Annu. Rev. Physiol*. **1995**, 57: 97-114.

Huang LR, Cox EC, Austin RH, Sturm JC. *Science*. **2004**. 304: 987–990

Huang Y, Doershuk CM, and Kamm RD. *J. Appl. Physiol*. **2001**, 90: 545-564.

Hubmayr RD. *Am. J. Resp. Crit. Care*. **2002**, 165: 1647-1653.

Huh, D.; Fujioka, H.; Tung, Y.-C.; Futai, N.; Paine, R.; Grotberg, J. B.; Takayama, S. *Proc. Nat. Acad. Sci.* **2007**, *104*: 18886–18891.

Huh D, Matthews BD, Mammoto A, Montoya-Zavala M, Hsin HY, and Ingber DE. *Science*, **2010**, 328: 1662–1668.

Huh D, Mills KL, Zhu X, Burns MA, Thouless MD and Takayama S. *Nat. Mater*., **2007**, 6: 424–428.

Hu MS, Thouless MD, and Evans AG. *Acta Metall*., **1988**, 36: 1301–1307.

Hurst, R. D.; Fritz, I. B. *J. Cell. Physiol.* **1996**, *167*: 81–88.

Hutchinson JW. private communication, July **2010**

Hutchinson JW and Suo Z. *Adv. Appl. Mech*., **1992**, 29: 63–191.

Iliescu, C.; Poenar, D. P.; Carp, M.; Loe, F. C. *Sens. Actuators, B* **2007**,*123*: 168–176.

Jain A and Munn LL. *PLoS One*. **2009**, 4(9): e7104-1-8.

Jansson NE, Leterrier Y, and Manson JAE. *Eng. Fract. Mech*., **2006**, 73: 2614–2626.

Johnson LR. Essential Medical Physiology, Lippincott-Raven, Philadelphia, 3rd edn, 2003.

Jo K, Dhingra DM, Odijk T, de Pablo JJ, Graham MD, Runnheim R et al. *PNAS*. **2007**. 104.8: 2673–2678

Karl A, Henry FS, and Tsuda A. *J. Biomech. Engin*. **2004**, 126: 420-429

Karlsson A, Karlsson R, Karlsson M, Cans A, Stromberg A, Ryttsen F et al. *Nature*. **2001**. 409:150–152

Kim JH, Shi WX, Larson RG. *Langmuir*. **2007**. 23: 755–764

Kim, K.-J.; Borok, Z.; Ehrhardt, C.; Willis, B. C.; Lehr, C.-M.; Crandall, E. D. *J. Appl. Physiol.* **2004**, *10*: 1152–1180.

Kim HN, Lee SH, and Suh KY*. Lab Chip*, **2011**, 11: 717–722.

Kniazeva T, Hsiao JC, Charest JL, and Borenstein. *Biomed. Microdevices*. **2011**. 13: 315-323.

Kottra, G.; Fromter, E. *Pflugers Arch.* **1984**, *402*: 409–420.

Koto, T.; Takubo, K.; Ishida, S.; Shinoda, H.; Inoue, M.; Tsubota, K.; Okada, Y.; Ikeda, E. *Am. J. Path.* **2007**, *170*: 1389–1397.

Kunii, H.; Kinouchi, Y. *Proc. 20th Annu. Int. Conf. IEEE EMBS* **1998**, *20*: 3108–3111.

Kumar: Robbins and Cotran Pathologic Basis of Disease, Profession Edition, 8th ed. **2009** Saunders.

Lacour, SP.; Tsay, C.; Wagner, S. *IEEE Electron Device Lett.* **2004**, *25*: 792– 794.

Lacour SP, Wagner S, Huang Z, and Suo Z. *Appl. Phys. Lett.,* **2003**, 82: 2404–2406.

Lagally, E. T.; Simpson, P. C.; Mathies, R. A. *Sens. Actuators, B* **2000**, *63*:138–146.

Larson JW, Yantz GR, Zhong Q, Charnas R, D'Antoni CM, Gallo MV, Gillis GA, Neely LA, Phillips KM, Wong GG, Gullans SR, Gilmanshin R. *Lab Chip*. **2006**. 6:1187–1199

Lee D. PhD thesis, University of Michigan, **2008**.

Lee, W. G.; Bang, H.; Yun, H.; Kim, J. A.; Cho, K.; Chung, C.; Chang, J. K.; Han, D.-C. *Curr. Appl. Phys.* **2008**, *8*: 696–699.

Lewis J. , *Mater. Today*, **2004**, 9: 38–45.

Lewis, S. A.; Wills, N. K. *J. Membr. Biol.* **1982**, *67*: 45–53.

Lide DR. CRC Handbook of Chemistry and Physics, 90th Ed. **2009-2010**.

Li T, Huang ZY, Suo Z, Lacour SP, and Wagner S. *Appl. Phys. Lett*., **2004**, 85: 3435–3437.

Li T and Suo Z. *Int. J. Solids Struct*., **2006**, 43: 2351–2363.

Li T, Huang ZY, Xi ZC, Lacour SP, Wagner S and Suo Z. *Mech. Mater*., **2005**, 37: 261–273.

Li W, Tegenfeldt JO, Chen L, Austin RH, Chou SY, Kohl PA, Krotine J, Sturm JC. *Nanotechnology*. **2003**. 14:578–583

Lumelsky VJ, Shur MS, and Wagner S. *IEEE Sens. J*., **2001**, 1: 41–51.

Maina JN and West JB. *Physiol Rev*. **2005***,* 85: 811-844.

Mannion JT, Reccius CH, Cross JD, Craighead HG. *Biophys J*. **2006**. 90.12: 4538–4545

Martin, R. S.; Gawron, A. J.; Lunte, S. M. *Anal. Chem.* **2000**, *72*: 3196– 3202.

McCord MA, Rooks MJ. In: Rai-Choudhury P (ed) SPIE handbook of micromachining and microfabrication, vol 1. PM39. 1997.

Michalet X, Ekong R, Fougerousse F, Rousseaux S, Schurra C, Hornigold N et al. *Science*. **1997**. 277:1518–1523

Mills KL, Huh D, Takayama S, and Thouless MD*. Lab Chip*, **2010**, 10: 1627–1630.

Mills KL, Zhu X, Takayama S. and Thouless MD. *J. Mater. Res*., **2008**, 23: 37–48.

Mishler, D. R.; Kraut, J. A.; Nagami, G. T. *Am. J. Physiol. Renal Physiol.* **1990**, *258* (6): F1561–F1568.

Moon MW, Lee SH, Sun JY, Oh KH, Vaziri A, and Hutchinson JW. *Proc. Natl. Acad. Sci. U. S. A*., **2007**, 104: 1130-1133.

Mrksich M, Chen CS, Xia Y, Dike LE, Ingber DE, and WhitesidesGM*. Proc. Natl. Acad. Sci. U. S. A*., **1996**, 96: 10775– 10778.

Namasivayam V, Larson RG, Burke DT, Burns MA. *Anal Chem*. **2002**. 74:3378–3385

Nicholas TE, Doyle IR, and Bersten AD. *Thorax*, **1997**, 52: 195–197.

Ning QM and Wang XR. **2007***,* 74: 579-585.

Nunn AJ and Gregg I. *Br. Med. J*. **1989***,* 298: 1068-1070.

Ochs M, Nyengaard JR, Jung A, Knudsen L, Voigt M, Wahlers T, Richter J, Gundersen HJG. *Am. J. Respir. Crit. Care Med*. **2004**, 169: 120–124.

Oudin S, and Pugin J. *Am J Respir Cell Mol Biol*. **2002**, 27: 107-114.

Pantoja, R.; Nagarah, J. M.; Starace, D. M.; Melosh, N. A.; Blunck, R.; Bezanilla, F.; Heath, J. R. *Biosens. Bioelectron.* **2004**, *20*: 509.

Paine R, Morris SB, Jin H, Baleeiro CEO, Wilcoxen SE.. *Am J Physiol Lung Cell Mol Physiol*. **2002**, 283:L180-L187.

Pai, R. S.; Walsh, K. M.; Crain, M. M.; Roussel, T. J.; Jackson, D. J.; Baldwin,R. P.; Keynton, R. S.; Naber, J. F. *Anal. Chem.* **2009**, *81*: 4762–4769.

Parker H, Horsfield K, and Cumming G. *J. Appl. Physiol*. **1971**, 31: 386-391.

Pashley DW. *Proc. R. Soc. London, Ser. A*, **1960**, 255: 218–231.

Pelrine R, Kornbluh RD, Joseph J, Heydt R, Pei Q, and Chiba S. *Mater. Sci. Eng., C*, **2000**, 11: 89–100.

Perkins TT, Smith DE, Larson RG, Chu S. *Science*. **1995**. 268:83–87

Polk, B. J.; Stelzenmuller, A.; Mijares, G.; MacCrehan, W.; Gaitan, M. *Sens. Actuators, B* **2006**, *114*: 239–247.

Pugin J, Dunn I, Jolliet P, Tassaux D, Magnenat JL, Nicod LP, and Chevrolet JC. *Am J Physiol Lung Cell Mol Physiol.* **1998***,* 275:1040-1050.

Ramakrishnan V. *Crit. Rev. Eukaryot. Gene Exp*. **1997**. 7: 215-230.

Rand CJ, Sweeney R, Morrissey M, Hazel L and Crosby AJ. *Soft Matter*, **2008**, 4: 1805–1807.

Reccius CH, Mannion JT, Cross JD, Craighead HG. *Phys Rev Lett*. **2005**. 95: 268101.1–4

Reichel, A.; Begley, D. J.; Abbott, N. J. An Overview of In Vitro Techniques for Blood-Brain Barrier Studies. In *The Blood-Brain Barrier: Biology and Research Protocols (Methods in Molecular Medicine)*; Nag, S., Ed.; Springer Protocols: 2003, Vol. 89; pp 307-324.

Reinelt DA, and Saffman PG. *SIAM J. Sci. Stat. Comput*., **1985**, 6(3): 542–561.

Reisner W, Beech JP, Larsen NB, Flyvbjerg H, Kristensen A, Tegenfeldt JO. *Phys Rev Lett*. **2007**. 99: 058302-1–4

Richardson, J. C.; Scalera, V.; Simmons, N. L. *Biochim. Biophys. Acta* **1981**, *673*: 26–36.

Riehn R, Lu M, Wang Y, Lim SF, Cox EC, Austin RH. *PNAS*. **2005**. 102.29: 10012–10016

Rothemund PWK. *Nature*, **2006**, 440: 297–302

Sapoval B, Filoche M, and Weibel ER. *Proc. Natl. Acad. Sci. USA*. **2002**, 99(16): 10411-10416.

Savla U, and Waters CM. *Am J Phsyiol Lung Cell Mol Physiol*. **1998**, 274: L883-L892.

Schittny JC, Mung SI, and Stampanoni M. *Am. J. Phsyiol. Lung Cell Mol. Physiol*. **2008**, 294: L246-L254.

Schreider JP and Raabe OG. *Am J. Anat*. **1981**, 162: 221-231.

Schwartz DC, Li X, Hernandez LI, Ramnarain SP, Huff EJ,Wang Y. *Science*. **1993**. 262.5130:110–114

Seebach, J.; Dieterich, P.; Luo, F.; Schillers, H.; Vestweber, D.; Oberleithner, H.; Galla, H.-J.; Schnittler, H.-J. *Lab. Invest.* **2000**, *80* (12): 1819–1831.

Seeman NC, Belcher AM. *Proc Natl Acad Sci USA*. **2002**, 99: 6451–6455

Shenoy VB, Schwartzman AF, and Freund LB. *Int. J. Fract*., **2000**, 103: 1–17.

Siegel, A. C.; Bruzewicz, D. A.; Weibel, D. B.; Whitesides, G. M. *Adv. Mater.* **2007**, *19*: 727–733.

Sia, S. K.; Whitesides, G. M. *Electrophoresis* **2003**, *24*: 3563–3576.

Simonnet, C.; Groisman, A. *Anal. Chem.* **2006**, *78*: 5653–5663.

Sinclair, J.; Olofsson, J.; Pihl, J.; Orwar, O. *Anal. Chem.* **2003**, *75*: 6718–6722.

Sivanesan P, Okamoto K, English D, Lee CS, Devoe DL. *Anal Chem*. **2005**. 77:2252–2258

Smith BJ and Gaver DP. *J. Fluid Mech*., **2008**, 601: 1–23.

Smith SB, Finzi L, Bustamante C. *Science*. **1992**. 258:1122–1126

Smith WF and Hashemi J. *Foundations of Materials Science and Engineering*, The McGraw-Hill Companies, Inc., New York NY 10020, **2006**, ISBN: 0072953586.

Song, J. W.; Cavnar, S. P.; Walker, A. C.; Luker, K. E.; Gupta, M.; Tung, Y.-C.; Luker, G. D.; Takayama, S. *PLoS ONE* **2009**, *4* (6): e5756–e5756.

Song, J. W.; Gu, W.; Futai, N.; Warner, K. A.; Nor, J. E.; Takayama, S. *Anal. Chem.* **2005**, *77*: 3993–3999.

Stamatovic, S. M.; Keep, R. F.; Wang, M. W.; Jankovic, I.; Andjelkovic, A. V. *J. Biol. Chem.* **2009**, *284*: 19053–19066.

Stavis SM, Edel JB; Li Y, Samiee KT, Luo D, Craighead HG. *J Appl Phys*. **2005**. 98: 44903.1–5

Steger DJ, A. Eberharter, S. John, P.A. Grant, and J.L. Workman. *Proc. Natl. Acad. Sci. USA*, **1998**, 95: 12924-12929.

Streng DE, S.F. Lim, J. Pan, A. Karpusenka, and R. Riehn. *Lab Chip*, **2009**, 9: 2772-2774.

Sweeney NVO, Cummins PM, Cotter EJ, Fitzpatrick PA, Birney YA, Redmond EM, and Cahill PA. *Biochemical and Biophysical Research* Communication, **2005**, 329: 573-582

Sznitman J, Heimsch F, Heimsch T, Rusch D, and Rosgen T. *J. Biomech. Engin*. **2007**, 129: 658-665.

Swindells JF, Coe JR, Godfrey TB. *Journal of Research of the National Bureau of Standards*. **1952**, 48(1): 1-31.

Tai CF, Bian S, Halpern D, Zheng Y, and Grotberg JB. *J. Fluid Mech.*, **2010**, submitted.

Tawhai and Burrowes. Modeling Pulmonary Blood Flow. *Respir. Physiol. Neurobiol*. **2008**, 163: 150-157.

Tavana T, Huh D, Grotberg JB, and Takayama S*. Lab. Med*. (Chicago, IL, U. S.), **2009**, 40: 203–209.

Tavana H, Jovic A, Mosadegh B, Lee QY, Liu X, Luker KE, Luker GD, Weiss SJ, and Takayama S. *Nature Mater*. **2009**. 8: 736-741.

Tegenfeldt JO, Prinz C, Cao H, Chou S, Reisner WW, Riehn R et al. *PNAS*. **2004**. 101(30): 10979–10983

Thouless MD. *Annu. Rev. Mater. Sci*., **1995**, 25: 69–96.

Thouless MD. *J. Am. Ceram. Soc*., **1990**, 73: 2144–2146.

Thouless MD, Li Z, Douville NJ, and Takayama S. *J. Mech. Phys. Solids*, **2011**, DOI: 10.1016/j.jmps.2011.04.009, in press.

Thouless MD, Olsson E, and Gupta A. *Acta Metall. Mater*., **1992**, 40: 1287–1292.

Tiruppathi, C.; Malik, A. B.; Del Vecchio, P. J.; Keese, C. R.; Giaever, I. *Proc. Nat. Acad. Sci. U.S.A.* **1992**, *89*: 7919–7923.

Tschumperlin D and Marulies S. *Am. J. Physiol*., **1998**, 275: L1173–L1183.

Tschumperlin DJ and Margulies SS. *J. Appl. Physiol*. **1999**, 86: 2026-2033.

Tschumperlin DJ, Oswari J, and Margulies SS. *Am. J. Respir. Crit.Care Med*., **2000**, 162: 357–362.

Tsubone D, Hasebe T, Kamijo A, and Hotta A. *Surf. Coat. Technol*., **2007**: 6423–6430.

Tsuda A, Filipovic N, Haberthur D, Dickie R, Matsui Y, Stampanoni M, and Schittny JC. *J. Appl. Physiol*. **2008**, 105: 964-976.

Tung, Y.-C.; Zhang, M.; Lin, C.-T.; Kurabayashi, K.; Skerlos, S. J. *Sens. Actuators, B* **2004**, *98*: 356–367.

Turner SWP, Cabodi M, Craighead HG. *Phys Rev Lett*. **2002.** 88.12:128103.1–4

van de Ven, A. L.; Adler-Storthz, K.; Richards-Kortum, R. *J. Biomed. Opt.* **2009**, *14* (2): 011012-1–10.

Vivoy JL. *Rev Mod Phys*, **2000**, 72: 813–872

Vlahakis NE, Schroeder MA, Limper AH, and Hubmayr RD. *Am. J. Physiol. Lung Cell. Mol. Physiol*., **1999**, 277: 167–173.

Vlahakis NE, Schroeder MA, Pagano RE, and Hubmayr RD. *Am. J. Respir. Crit. Care Med.*, **2002**, 166: 1282–1289.

Walker, G. M.; Zeringue, H. C.; Beebe, D. J. *Lab Chip* **2004**, *4*: 91–97.

Wagner PD, Gale GE, Moon RE, Torre-Bueno JR, Stolp BW, and Saltzman HA. *J. Appl. Physiol*. **1986**, 61: 260-270.

Wang JD, Douville NJ, Takayama S. and El-Sayed MEH. **2011**. In Preparation.

Warren LL and Slutsky LE. Chapter 90 – Acute Respiratory Distress Syndrome. Mason: Murray and Nael's Textbook of Respiratory Medicine, 5th ed. **2010**.

Watz H, Brelthecker A, Rau WS, Krlete A. *Radiology*, **2005**,1053-1058.

Wegener, J.; Sieber, M.; Galla, H.-J. *J. Biochem. Biophys. Methods* **1996**, *32*: 151–170.

Weibel ER. Morphology of the Lung, Springer Verlag, Berlin, 1963.

Weibel ER and Knight BW. *J.Cell Biol*., 1964, 21(3): 367-384. *Respir. Physiol. Neurobiol*. 2005, 148: 3-21.

Weibel, ER, 1963. Morphometry of the Human Lung. SpringerVerlag/Academic Press, Heidelberg, New York.

Wei HH, Fujioka H, Hirschl RB, Grotberg JB. *Physics of Fluids*. **2005**, 17: 031510-1-16.

West JB, Dollery CT, and Naimark A.. *J. Appl. Physiol*. **1964**, 19: 713-724.

West JB and Mathieu-Costello O. *Annu. Rev. Phsyiol*. **1999**, 61:543-572.

West JB and Mathieu-Costello O. *Resp. Physiol.* **1992**, 88: 141-148.

West JB, Tsukimoto K, Matheiu-Costello O, and Prediletoo R. *J. Appl. Physiol*. **1991**, 70(4): 1731-1742.

Wolfe AP. Chromatin Structure and Function. Academic Press, San Diego. **1992**.

Wu, H.; Huang, B.; Zare, R. N. *Lab Chip* **2005**, *5*: 1393–1398.

Yalcin HC, Perry SF, and Ghadiali SN. *J. Appl. Physiol*., **2007**, 103: 1796–1807.

Yao, B.; Luo, G.-A.; Feng, X.; Wang, W.; Chen, L.-X.; Wang, Y.-M. *Lab Chip* **2004**, *4*: 603–607.

Ying L, Bruckbauer A, Rothery AM, Korchev YE, Klenerman D. *Anal Chem*. **2002**. 74:1380–1385

Yoshida M, Kijima M, Akita M, and Beppu T. *J. Biol. Chem*. **1990**. 265(28): 17174-17179.

Zak AK and Williams ML. *J. Appl. Mech*., **1963**, 30: 142–143.

Zamankhan P, Takayama S, and Grotberg,JB. *Phys. Fluids*, **2011**, submitted.

Zhang K, Zhu J, Shendure J, Porreca GJ, Aach JD, Mitra RD, Church GM. *Nat Genet*. **2006**. 38:382–387

Zelig D and Haber S. *SIAM J. Appl. Math*. **2002**, 63(1): 195-221.

Zhu X, Mills KL, Peters PR, Bahng JH, Liu EH, Shim J, Naruse K, Csete ME, Thouless MD, and Takayama S. *Nat. Mater*., **2005**, 4: 403–405.